



# Concept of a polarized positron source for CEBAF

Sami Habet

## ► To cite this version:

Sami Habet. Concept of a polarized positron source for CEBAF. Accelerator Physics [physics.acc-ph]. Université Paris-Saclay, 2023. English. NNT : 2023UPASP170 . tel-04584936

**HAL Id: tel-04584936**

**<https://theses.hal.science/tel-04584936>**

Submitted on 23 May 2024

**HAL** is a multi-disciplinary open access archive for the deposit and dissemination of scientific research documents, whether they are published or not. The documents may come from teaching and research institutions in France or abroad, or from public or private research centers.

L'archive ouverte pluridisciplinaire **HAL**, est destinée au dépôt et à la diffusion de documents scientifiques de niveau recherche, publiés ou non, émanant des établissements d'enseignement et de recherche français ou étrangers, des laboratoires publics ou privés.

# Concept of a polarized positron source for CEBAF

*Conception d'une source polarisée de positrons  
pour CEBAF*

Thèse de doctorat de l'université Paris-Saclay

École doctorale n°576 : particules hadrons énergie et  
noyau : instrumentation, imagerie, cosmos et simulation  
(PHENIICS)

Spécialité de doctorat : Physique des accélérateurs  
Graduate School : Physique. Référent : Faculté des Sciences d'Orsay

Thèse préparée dans l'unité de recherche **IJCLab (Université Paris-Saclay, CNRS)** sous la direction de **Eric VOUTIER**, Directeur de recherche et le co-encadrement de **Joseph GRAMES**, Directeur de recherche

Thèse soutenue à Paris-Saclay, le 4 Décembre 2023, par

**Sami HABET**

## Composition du jury

Membres du jury avec voix délibérative

**Sophie KAZAMIAS**

Professeur, Université Paris-Saclay

**Kurt AULENBACHER**

Professeur, Université de Mainz

**Gudrid MOORTGAT-PICK**

Professeur, Université de Mainz

**Frank ZIMMERMANN**

Chercheur, Conseil européen pour la recherche nucléaire

Présidente

Rapporteur & Examineur

Rapporteur & Examineur

Examineur





**Titre :** Conception d'une source polarisée de positrons pour CEBAF

**Mots clés :** faisceaux de positrons, polarisation, dynamique faisceaux

**Résumé :** Cette thèse se concentre sur le développement de faisceaux de positrons polarisés et non polarisés pour le futur programme expérimental en physique hadronique au Thomas Jefferson National Accelerator Facility (JLab). Le défi principal consiste à produire des faisceaux de positrons polarisés de grand cycle utile à haute intensité et à courant élevé. La source de positrons du JLab, basée sur la technique PEPPo (Polarized Electrons for Polarized Positrons), vise à utiliser un faisceau continu d'électrons de haute intensité (1 mA) et hautement polarisés (90%) d'énergie modérée (120 MeV)

pour produire soit un faisceau de positrons de faible intensité ( $>50$  nA) et hautement polarisés (60%), soit un faisceau de positrons de haute intensité ( $>1$   $\mu$ A) et non polarisés.

L'optimisation de la disposition et des performances de la source de positrons est examinée dans cette thèse. La source est conçue avec un second injecteur spécialisé pour générer, transporter, accélérer et façonner les faisceaux de positrons. Elle est compatible avec l'accélération au Continuous Electron Beam Accelerator Facility (CEBAF), et les résultats de l'investigation sont présentés dans ce document.

**Title :** Conception of a polarized positron source for CEBAF

**Keywords :** Positron beams, polarization, Beam dynamics

**Abstract :** This thesis focuses on the development of polarized and unpolarized positron beams for the future experimental program of hadronic physics at the Thomas Jefferson National Accelerator Facility (JLab). The primary challenge is to produce high-duty-cycle and high-intensity polarized positron beams. The JLab positron source, which is based on the PEPPo (Polarized Electrons for Polarized Positrons) technique, aims to use a high intensity (1 mA) and highly polarized (90%) continuous electron beam of moderate energy (120 MeV) to

produce either a low intensity ( $>50$  nA), highly polarized (60%) positron beam or a high intensity ( $>1$   $\mu$ A), unpolarized positron beam.

The optimization of the layout and performance of the positron source is examined in this thesis. The source is designed with a specialized second injector to generate, transport, accelerate, and shape positron beams. It is compatible with acceleration at the Continuous Electron Beam Accelerator Facility (CEBAF), and the investigation results are presented in this document.

# Abstract

This thesis focuses on the development of polarized positron beams for the future experimental program of hadronic physics at the Thomas Jefferson National Accelerator Facility (JLab). The primary challenge is to produce high-duty-cycle and high-intensity polarized positron beams. The JLab positron source, which is based on the PEPPo (Polarized Electrons for Polarized Positrons) technique, aims to use a high intensity ( $\geq 1$  mA) and highly polarized (90%) continuous electron beam of moderate energy (120 MeV) to produce either a low intensity ( $> 50$  nA), highly polarized ( $\geq 60\%$ ) positron beam or a high intensity ( $> 1$   $\mu$ A), unpolarized positron beam.

The optimization of the layout and performance of the positron source is examined in this thesis. The source is designed with a specialized second injector to generate, transport, accelerate, and shape positron beams. It is compatible with acceleration at the Continuous Electron Beam Accelerator Facility (CEBAF), and the investigation results are presented in this document.

# Acknowledgements

Writing this thesis was a big challenge, but I couldn't have done it without the help and support of many special people. I want to thank each one of them for their part in my journey.

A big thank you to Dr. Eric Voutier, my main advisor. Eric was always there to guide me, especially when things got tough. His patience, good advice, and careful way of solving problems have been a huge part of my work. He pushed me to work hard, keep going, and always do my best. Eric believed in me even when I had doubts, and that really kept me going.

Dr. Joe Grames, serving as my co-advisor, has been an extraordinary mentor. Our discussions, encompassing various scientific aspects and broader concepts, have significantly influenced my thinking. Joe's unwavering belief in my abilities, coupled with the diverse responsibilities he entrusted to me, has been instrumental in my personal and professional growth. His kindness and support were especially valuable when I first arrived in the USA, making my transition much smoother.

Yves Roblin has been a big influence on my thesis. Talking with him was always a learning experience. He master beam dynamics, and his passion made me want to learn more and do better. He was always quick to help when I needed it, and I'm so grateful for everything I've learned from him.

Dr. Ryan has been a great support, helping me with my work and getting used to life in Newport News. He's been really kind and generous, and I'm so thankful for all the help he gave me with my thesis.

A special thanks to Andriy Ushakov. Working together was not only good for my career but we also became real friends. His feedback, ideas, and support were so important, especially when things were hard.

I'm also grateful to Carlos and his wife for their friendship while I was in Newport News. Their kindness made me feel like I was part of a family. Their hospitality brought a lot of happy moments, and I'm so thankful for the feeling of home they gave us.

The Jefferson Lab community deserves my heartfelt thanks for their knowledge, enthusiasm, and collaborative spirit. Interacting with its members offered me diverse perspectives and a deeper appreciation of our field.

Thanks also to the people at IJCLab, Silvia, Dominique, Raphael, Noémie, Mathieu and Mostafa. Working with them really added to my project. Their skills and support meant a lot.

Pierre and Gloria have been more than just helpers with this thesis; they've been true friends. Their support and advice, showed me how wonderful people can be.

To my sister, Linda, your support and belief in me have been a big source of strength. Even from far away, you made me feel supported and lifted my spirits when I needed it.

Thank you to Dr. Antoine Henry for his friendship and support, especially during hard times. I really value our friendship.

I owe so much to my parents. Their sacrifices and teachings have shaped who I am. They've always been there for me, loving and supporting me, giving me the courage to follow my dreams.

Thanks to my parents-in-law, Monique and Giuseppe, for welcoming me into your family and for all your love and support. Your understanding has helped me a lot through this thesis.

To Rebecca, you've been incredible. You understood when I was busy with work and always had patience. Your belief in me gave me the strength to keep going even when it was tough. This thesis is as much about your support and love as it is about my work.

I am deeply grateful to my sister Lilia, my cousin Youba, and everyone else I have mentioned, as well as to all those who have assisted me in various ways. Each one of you has left an indelible mark on this thesis.

This thesis isn't just a bunch of research; it's made up of all the help, guidance, and support from everyone who's been part of this journey. Thank you from the bottom of my heart.

**This project has received funding from the European Union's Horizon 2020 research and innovation program under grant agreement No 824093.**

**This work was supported in part by the U.S. Department of Energy, Office of Science, Office of Nuclear Physics under contract DE-AC05-06OR23177.**

# Dedication

To Ringo

# Contents

<b>1</b>	<b>Introduction</b>	<b>1</b>
<b>2</b>	<b>Positron sources</b>	<b>7</b>
2.1	Past positron sources . . . . .	9
2.1.1	Stanford Linear Accelerator Center . . . . .	9
2.1.2	Large Electron-Positron collider . . . . .	10
2.1.3	Positron-Electron Tandem Ring Accelerator . . . . .	10
2.1.4	Cornell Electron-positron Storage Ring . . . . .	11
2.2	Current positron sources . . . . .	12
2.2.1	DAΦNE $\phi$ -factory . . . . .	12
2.2.2	Beijing Electron Positron Collider . . . . .	13
2.2.3	Kō Enerugī Kasokuki Kenkyū Kikō . . . . .	13
2.3	Future positron sources . . . . .	14
2.3.1	International Linear Collider . . . . .	14
2.3.2	Future Electron-Positron Circular Collider . . . . .	16
2.3.3	Jefferson Lab positron source . . . . .	17
2.4	Comparative summary . . . . .	17
<b>3</b>	<b>Ce<sup>+</sup>BAF positron source concept</b>	<b>21</b>
3.1	CEBAF overview . . . . .	21
3.1.1	The CEBAF polarized electron source . . . . .	23
3.1.2	The electron injector . . . . .	24
3.2	CEBAF acceptance . . . . .	25
3.3	Ce <sup>+</sup> BAF . . . . .	30
3.3.1	Electron injector . . . . .	31
3.3.2	Positron source . . . . .	32
3.3.3	Spin rotator . . . . .	33
3.3.4	Transport line . . . . .	33
<b>4</b>	<b>Positron production optimization</b>	<b>34</b>
4.1	Polarized Bremsstrahlung . . . . .	34
4.1.1	Cross section . . . . .	34
4.1.2	Polarized cross-section . . . . .	35
4.2	Pair-creation . . . . .	37
4.2.1	Unpolarized cross-section . . . . .	37
4.2.2	Polarization Transfer . . . . .	38
4.3	Characteristic parameters of positron production . . . . .	39
4.4	Optimization of production at 120 MeV . . . . .	44
4.4.1	Unpolarized optimization . . . . .	44

4.4.2	Polarized optimization . . . . .	44
4.5	Optimization of production at 1000 MeV . . . . .	47
4.6	Comparison between 120 MeV and 1000 MeV . . . . .	50
4.7	Collection System considerations . . . . .	52
4.8	Target thermal fatigue . . . . .	55
<b>5</b>	<b>Positron capture optimization</b>	<b>58</b>
5.1	Collection system . . . . .	58
5.2	Adiabatic Matching Device . . . . .	59
5.2.1	Phase space admittance . . . . .	60
5.2.2	Transverse acceptance . . . . .	61
5.3	Quarter Wave Transformer . . . . .	61
5.3.1	Longitudinal acceptance . . . . .	63
5.3.2	Transverse acceptance . . . . .	65
5.3.3	Comparison of collection systems . . . . .	66
5.3.4	QWT optimization . . . . .	66
5.4	Capture linac . . . . .	76
<b>6</b>	<b>Positron transport optimization</b>	<b>82</b>
6.1	Chicane design . . . . .	82
6.1.1	Matching section . . . . .	86
6.1.2	Momentum collimation . . . . .	88
6.2	Bunch Length compression . . . . .	92
6.2.1	Investigation of the compression chicane . . . . .	95
<b>7</b>	<b>Conclusion</b>	<b>107</b>
<b>A</b>	<b>Poster contribution to the International Particle Accelerator Conference   IPAC22</b>	<b>110</b>
<b>B</b>	<b>Poster contribution to the International Particle Accelerator Conference   IPAC23</b>	<b>115</b>
	<b>Résumé en français</b>	<b>126</b>



# List of Figures

1.1	DVCS and BH contributions to electro-production of photons. . . . .	3
2.1	The $e^+e^-$ -pair creation process. . . . .	8
2.2	Sketch of the Stanford Linear Collider (SLC) showing the 220 MeV positron return line, the damping ring, and the LinAc-to-ring transport system. The electron bunch intended for the positron production target is extracted from the main LinAc at the two-thirds point with an energy of 30-33 GeV [1]. . . . .	9
2.3	LIL injector layout [2]. . . . .	10
2.4	PETRA LinAc injector [3]. . . . .	11
2.5	Positron channel layout at the CESR [4]. . . . .	11
2.6	Layout of the DAΦNE positron source [5]. . . . .	12
2.7	Positron focusing and accelerating systems at BEPCII [6]. . . . .	13
2.8	The KEKB injector LinAc [7]. . . . .	14
2.9	Layout of the positron source at the KEKB injector LinAc [8]. . . . .	14
2.10	Overview of the proposed ILC positron source [9]. . . . .	15
2.11	Schematic design of the FCC-ee positron source [10]. . . . .	16
2.12	Schematic of the PEPPo concept : a highly polarized electron beam interacts with a target and generates circularly polarized $\gamma$ -rays which then transfer their polarization to the $e^+e^-$ -pairs formed within the nuclear field of target nuclei. . . . .	17
3.1	CEBAF diagram: an overview of the injector gun, superconducting linear accelerators, and recirculating arcs for high-quality electron beam production, with color-coded representations of accelerator modules (red), C100 cryomodules (blue), and upgraded injector module (green). . . . .	22
3.2	A schematic layout of the CEBAF injector at Jefferson Lab. . . . .	24
3.3	Chopper system at the CEBAF injector operating at 499 MHz: three drive lasers generate interleaved pulsetrains at a frequency of 499 MHz. Each beam passes through a corresponding aperture at the master slit [11]. . . . .	25
3.4	Phase space ellipse defining the occupied area of the beam. . . . .	26
3.5	$\beta$ functions along the CEBAF-NL. . . . .	29
3.6	Variation of the beam size $\sigma_{x,y}$ along the CEBAF-NL, accelerating the beam from 123 MeV to approximately 1090 MeV. . . . .	29
3.7	Schematic Layout: Linking LERF and CEBAF Accelerators for High-Energy Positron Beam Acceleration [12] . . . . .	31
3.8	Layout of Polarized Electron and Positron Injectors at LERF [12]. . .	31

3.9	Optimization of Positron Generation from Electron-Target Interaction: Towards Polarized and Unpolarized Positron Beams at CEBAF [13]. . . . .	32
4.1	Bremsstrahlung differential cross-section $\frac{d\sigma_b}{dk, d\theta_k}$ for different electron energies in tungsten at a photon emission angle $\theta = 0.17$ rad . . . .	35
4.2	Angular distribution of the bremsstrahlung differential cross section for different electron beam energies: photon energy fraction dependency of the angle corresponding to the maximum cross-section (left) and of the optimum angle corresponding to the 1- $x$ fraction of the maximum cross-section (right) [14]. . . . .	36
4.3	Circular polarization of bremsstrahlung for electron beam energies: red (10 MeV), blue (100 MeV), green (1000 MeV) with 100% longitudinal polarization. . . . .	37
4.4	Pair-creation cross-section for 100 MeV photon energy within a tungsten material. . . . .	38
4.5	Multiple scattering spread of electron/positron distribution as a function of energy, for various tungsten thicknesses. . . . .	38
4.6	Polarization transfer in Pair creation process for various initial photon energies. . . . .	40
4.7	Energy dependence of positron production efficiency (left) and Figure-of-Merit (right) for a 120 MeV polarized electron beam interacting with a 4 mm thick tungsten target. The curves of different colors demonstrate the influence of energy binning on the shape of the distributions, as defined in Eq. 4.21. . . . .	41
4.8	Positron transverse phase space created using 120 MeV longitudinally polarized electron beam on a 4 mm tungsten target, illustrating the positron transverse phase space at the exit of a 4 mm tungsten target when using a longitudinally polarized 120 MeV electron beam. The figure top left and right sections display the positron transverse space in the $x$ and $y$ directions, respectively. The correlation between the axis ( $x$ , $y$ ) and ( $x_p = \frac{p_x}{p_z}$ and $y_p = \frac{p_y}{p_z}$ ) is shown in the bottom left and right sections. . . . .	42
4.9	Comparison of positron energy distributions: production efficiency (left), average longitudinal polarization (middle), and FoM (right) for 120 MeV incident electrons on a 4 mm thick tungsten target, for different angular acceptances in the positron collection system with a fixed $\pm 5\%$ positron momentum acceptance. . . . .	43
4.10	Dependency of characteristic quantities on target thickness in the polarized mode at 120 MeV with $\pm 5\%$ momentum acceptance and various angular acceptances . . . . .	45
4.11	Dependency of characteristic quantities on target thickness in the polarized mode at 120 MeV with $\pm 5\%$ momentum acceptance and various angular acceptances . . . . .	46
4.12	Target thickness dependence of the characteristic quantities of the unpolarized mode at 1000 MeV and a momentum acceptance of $\pm 5\%$ for different angular acceptances. . . . .	49

4.13	Target thickness dependence of the characteristic quantities of the polarized mode at 1000 MeV and a momentum acceptance of $\pm 5\%$ for different angular acceptances. . . . .	50
4.14	Angular vs momentum positron distribution at the target exit . . . .	52
4.15	Effect of angular acceptance on the optimal target thickness (top panel), maximum positron momentum (middle panel), and positron polarization (bottom panel) in the unpolarized and polarized modes at 120 MeV. . . . .	53
4.16	Angular acceptance dependence of the optimum target thickness (top panel), the positron momentum at maximum (middle panel) and the positron polarization at maximum (bottom panel) of the unpolarized and polarized modes at 1000 MeV. . . . .	54
4.17	Left: energy deposition and temperature profile in a rotating target under electron beam irradiation, Right: heat power density distribution of a 1 mA electron beam at 120 MeV with 1.5 mm rms Size in a 4 mm thick tungsten target [15]. . . . .	56
4.18	Left: cyclic temperature variation in tungsten at a radius of 18 cm with a tangential velocity of 2.3 m/s and 1.5 mm rms beam spot: heating phase (shown in red) followed by cooling phase (extended up to 0.5 s in blue). . . . .	56
4.19	Left; thermal-induced mechanical stressRight, right: temperature distribution in a 17 kW Target. . . . .	57
4.20	Radiation damage in a tungsten target with a diameter of 36 cm. . .	57
5.1	schematic and purpose of the positron collection system symbolized here by the matching device item . . . . .	58
5.2	Effect of AMD length on magnetic field variation . . . . .	59
5.3	QWT magnetic field profile: short and long are two solenoidal field profiles. The target converter is positioned at the origin of the system. In this context, $B_1$ and $B_2$ represent the field strengths of the short and long solenoids, respectively, while $L_1$ and $L_2$ indicate the lengths of these solenoids [16]. . . . .	62
5.4	Variation of the short solenoid length versus the magnetic field at optimum QWT volume acceptance . . . . .	64
5.5	$B_2$ Vs $B_1$ for various $\Delta p/p_0$ . . . . .	65
5.6	QWT volume acceptance shows the strong dependency between the system acceptance and the positron momentum. . . . .	67
5.7	Positron momentum distribution at the exit of the target (blue) and at the exit of the QWT (orange) . . . . .	68
5.8	Longitudinal positron phase space at the QWT exit. . . . .	69
5.9	Positron transverse space x, $x_p$ and y, $y_p$ through the QWT . . . . .	69
5.10	Angular Distribution of Collected Positrons: Left Panel - Positrons Identified at Target Exit, Right Panel - Positrons Transmitted through QWT Exit . . . . .	70
5.11	Longitudinal positron momentum distribution, collecting at the QWT exit 19 MeV/c, the same short solenoid length is kept for this configuration . . . . .	70
5.12	Positron longitudinal phase space at the QWT exit . . . . .	71

5.13	Positron transverse phase space at different locations: at the target exit and at the QWT exit . . . . .	72
5.14	Angular Distribution of Collected Positrons: Left Panel - Positrons Identified at Target Exit, Right Panel - Positrons Transmitted through QWT Exit . . . . .	72
5.15	Longitudinal unpolarized positron collection phase space . . . . .	74
5.16	Longitudinal positron phase space at the re-optimized QWT exit . . .	74
5.17	Positron transverse phase space at different locations : at the target exit and at the re-optimized QWT exit . . . . .	75
5.18	Angular distribution of collected positrons: left panel - positrons identified at target exit, right panel - positrons transmitted through the re-optimized QWT Exit . . . . .	75
5.19	Effect of the QWT on the transverse and angular beam size, top optimized QWT configuration for the polarized mode, bottom: re-optimized QWT for the unpolarized mode . . . . .	76
5.20	Capture linac: energy spread optimization procedure . . . . .	77
5.21	Energy spread of the collected positrons along the capture section . .	78
5.22	Variation of beam parameters along the capture section: top panel shows the beam emittance of the captured positron, and the bottom panel shows the bunch length . . . . .	79
5.23	Variation of beam parameters along the capture section: top panel shows the transverse beam size of the captured positron, and the bottom panel shows the angular transverse component of the captured beam . . . . .	80
6.1	Momentum collimation scheme . . . . .	83
6.2	ELEGANT dispersion generated by the first arm (first two dipoles) with $\theta = -0.3$ mrad, $L = 3.4$ m with $L\theta = -0.0011$ m which agrees with the previous matrix estimation. . . . .	84
6.3	Twiss function variation along one period FODO lattice . . . . .	86
6.4	Twiss parameters variation over the chicane implemented within the designed FODO lattice. . . . .	87
6.5	Acceptance of the designed matching section for three different beta input . . . . .	89
6.6	Acceptance of the designed matching section for three different alphas input . . . . .	90
6.7	Transverse Twiss parameters variation along the designed collimation system . . . . .	91
6.8	Momentum collimation process: Left panel, positron momentum collimation described in the p (MeV/c)-x (m) plane at different locations, right panel, the positron momentum before and after the momentum collimation. . . . .	92
6.9	Energy Chirp Variation Across Accelerating Phase . . . . .	96
6.10	Longitudinal positron phase space before and after the compression process . . . . .	97
6.11	Progression of longitudinal positron beam characteristics in the optimized compression system . . . . .	98

6.12	Longitudinal positron phase space before and after the compression process . . . . .	99
6.13	Progression of longitudinal positron beam characteristics in the optimized compression system . . . . .	99
6.14	Schematic Layout of the Positron Injector Designed for the LERF Facility . . . . .	100
6.15	Twis parameters variation along the designed positron injector for the polarized operational mode . . . . .	102
6.16	Evolution of transverse beam parameters along the positron injector: transverse beam sizes in x and y axes and normalized transverse emittances . . . . .	103
6.17	Evolution of Key Longitudinal Positron Characteristics Along the Designed Injector: Central Momentum $p_0$ (Blue Curve), Bunch Length $\sigma_t$ (Green Curve), and Energy Spread (Red Curve) for Two Distinct Compression Configurations . . . . .	105
6.18	Positron beam physics characteristics along the layout, the central momentum is shown in blue color, and the green current shows the positron current, in the top panel figure, and in the bottom panel figure shows the lost positrons along the beam line . . . . .	106

# List of Tables

2.1	Electron sources performance summary for positron production. The different symbols stand for: Number of $e^-$ per bunches $Ne/b$ , Number of bunches per pulse (b/p), average power ( $PW_a$ ), average $e^-$ current $I_a$ ( $\mu A$ ), peak current $I_{peak}(A)$ , polarization $P_{e^-}$ (%), Repetition rate (Rr) in Hz. . . . .	18
2.2	Positron sources performance summary. . . . .	20
3.1	CEBAF parameters for 12 GeV operation [17]. . . . .	23
4.1	Parameters characterizing the unpolarized mode of a positron source. The source utilizes a 120 MeV polarized electron beam interacting with a 4 mm thick tungsten target. The positron momentum acceptance is $\Delta p/p_0 = \pm 5\%$ , with different angular acceptances considered. . . . .	43
4.2	Parameters characterizing the polarized mode of a positron source. The source utilizes a 120 MeV polarized electron beam interacting with a 4 mm thick tungsten target. The positron momentum acceptance is $\Delta p/p_0 = \pm 5\%$ , with different angular acceptances considered. . . . .	43
4.3	Optimal target thickness $t_\epsilon$ and positron momentum at maximum $p_\epsilon$ for the unpolarized mode at 120 MeV, considering different angular and momentum acceptances. . . . .	45
4.4	Optimum target thickness ( $t_{FoM}$ ) and positron momentum at maximum ( $p_{FoM}$ ) in the polarized mode at 120 MeV, considering various angular and momentum acceptances. . . . .	46
4.5	Optimal target thickness ( $t_\epsilon$ ) and maximum positron momentum ( $p_\epsilon$ ) in the unpolarized mode at 1000 MeV for various angular and momentum acceptances . . . . .	48
4.6	Optimal Target Thickness ( $t_{FoM}$ ) and Maximum Positron Momentum ( $p_{FoM}$ ) in the polarized Mode at 1000 MeV for Various Angular and Momentum Acceptances . . . . .	48
5.1	QWT configuration for 6 MeV momentum capture . . . . .	73
5.2	Different QWT configurations for various positron operational modes . . . . .	81
6.1	Positron beam parameters at the exit of the momentum collimation chicane showing a reduced energy spread . . . . .	92

# List of definitions

$\beta_x, \alpha_x, \beta_y, \alpha_y$	: Twiss parameters describing the optical beam function along the beam line
$\Delta p/p_0$	: Momentum spread
$\epsilon$	: Beam emittance describing the particle phase space
$\gamma$	: Photon
$\sigma_t$	: Bunch length in seconds
$\sigma_x, \sigma_y$	: Beam size in the transverse plane
$\sigma_z$	: Bunch length in meters
$B_1$	: Starting field value in the QWT and AMD
$B_2$	: Weak magnetic field after the QWT or AMD
$c$	: Celerity of light
$L_1$	: Length of the QWT or the AMD
$m_e$	: Electron mass
$p_0$	: Central particle momenta
AMD	: Adiabatic Matching Device
Ce <sup>+</sup> BAF	: Continuous Positron Beam Accelerator Facility
CEBAF	: Continuous Electron Beam Accelerator Facility
CEBAF-NL	: CEBAF North Linac
CEBAF-SL	: CEBAF South Linac
CERN	: European Organization for Nuclear Research
E	: Particle energy
e <sup>+</sup>	: Positron
e <sup>-</sup>	: Electron
JLab	: Jefferson Lab
MAMI	: Mainz Microtron
N	: Nucleon
PEPPo	: Polarized Electrons for Polarized Positrons
QWT	: Quarter Wave Transformer
RF	: Radio Frequency
SRF	: Superconducting Radio Frequency
TJNAF	: Thomas Jefferson National Accelerator Facility

# Chapter 1

## Introduction

Particle accelerators are crucial tools for probing the fundamental laws of the universe. They manipulate charged particles in beams that are used across diverse sectors such as medicine, industry, and research. These applications demand beams of high quality, characterized by their intensity, size, and energy. With the progression of technology over the years, the expectations of beam users have also evolved. In the particle accelerator community, leptons, especially electrons and positrons, play a significant role. They offer a unique window to probe matter at its most fundamental level. The development of accelerated positron beams has seen significant advancements in recent years. This progress is driven by innovation and rigorous research, benefiting from the synergy of knowledge spanning fields such as condensed matter physics, materials science, and high-energy physics for linear electron-positron ( $e^-/e^+$ ) colliders.

The importance of positron experiments is underscored by their profound insights into the interactions of these particles with materials at atomic and subatomic scales. For instance, advanced experiments using positron beams have enabled studies on phenomena like two-photon excitation of positronium [18], positron scattering from alkali metal atoms [19]. A pivotal realization in this field was the tendency of positrons to become trapped in specific defects within solids [20]. This discovery propelled the field of positron annihilation spectroscopy (PAS) as a technique capable of characterizing materials at a granular and a subatomic scale. The introduction of monoenergetic positron beams further increased this capability, allowing scientists to delve into the study of thin films and near-surface regions [21]. These advances have seamlessly integrated with cutting-edge technological applications, playing a crucial role in refining semiconductor devices and offering insights into the novel applications of polymer films. Additionally, exploring new surface spectroscopies, such as low-energy positron diffraction, underscores the versatility and depth of positron-related studies.

Given the ongoing advancements in materials science and high energy physics, there is an increasing demand for specialized sources that can surpass current limitations. In this context, this thesis describes the design of a new polarized positron source for the Thomas Jefferson National Accelerator Facility (JLab) for nuclear physics.

The Jefferson Lab (JLab) Physics Community have a strong interest in using positron beams for experiments. The hadronic physics program at the Thomas Jefferson National Accelerator Facility (TJNAF) aims to study the structure of



hadrons (protons, neutrons, and other particles made of quarks) in detail. One of the tools used to investigate this structure is scattering experiments, where beams of electrons are directed at a target, and the resulting scatter is analyzed. Polarized positrons offer a unique tool for some experiments. One notable example is the Deeply Virtual Compton Scattering (DVCS), a process in which an electron (or positron) scatters off a nucleon, resulting in the emission of a real photon. The process can be expressed as

$$e^{\pm} + N \rightarrow e^{\pm'} + N' + \gamma$$

where  $e^{\pm}$  and  $e^{\pm'}$  represent the incoming and scattered lepton, respectively,  $N$  and  $N'$  represent the initial and final state of the nucleon, and  $\gamma$  is the emitted real photon.

DVCS is particularly interesting because it provides a window into the internal structure of the proton, specifically the distribution of quarks and gluons within the nucleon, as a function of both their momentum and their spatial distribution. This is encapsulated in Generalized Parton Distributions (GPDs) which are complex objects that combine features of the more familiar Parton Distribution Functions (PDFs) and Form Factors [22]. Using a polarized electron and positron beam in DVCS experiments offers several advantages. One can measure the beam-spin asymmetry [23] which represents a difference in scattering rates based on the spin orientation of the positron. This asymmetry in DVCS is intrinsically tied to specific GPDs, shedding light on the quark and gluon distributions inside the nucleon. Additionally, the Bethe-Heitler (BH) process [24], another means by which real photons emerge in lepton-proton scattering, can interfere with the DVCS process.

The polarized positron beam facilitates the separation of DVCS and BH amplitudes through certain measurable asymmetries, a crucial step for gleaning GPDs from the data. The polarization inherently grants an enhanced sensitivity to the scattering process, enabling high-precision measurements of polarized observables, like asymmetries, which can often be measured with high precision and can be sensitive to small effects or subtle details of the proton structure that might be hard to access otherwise. Furthermore, using polarized positrons in DVCS experiments complements data taken with polarized electrons. Comparing measurements using both  $e^{-}$  and  $e^{+}$  allows to separate the DVCS and BH contributions to the cross section of electro-production of photons.

In summary, polarized positrons enhance the DVCS experiments at JLab by allowing for the precise measurement of certain observables, like beam-spin asymmetries, which provide direct insights into the complex internal structure of the proton encapsulated in the GPDs.

After establishing the significance of polarized positrons in enhancing DVCS experiments, it becomes pertinent to delve into the techniques and advancements in generating such positron beams.

Previous studies explored the feasibility of introducing a Continuous Wave (CW) positron source for the Continuous Electron Beam Facility (CEBAF). Three design options for a positron injector were investigated [25]. Each of these options is distinguished by how positrons are captured and transported. Positron sources built already have common characteristics due to the pulsed nature of linacs. Firstly, they use pulsed electron beams as the primary means to produce positrons. Once generated, these positrons are captured using solenoidal fields. Directly after this,

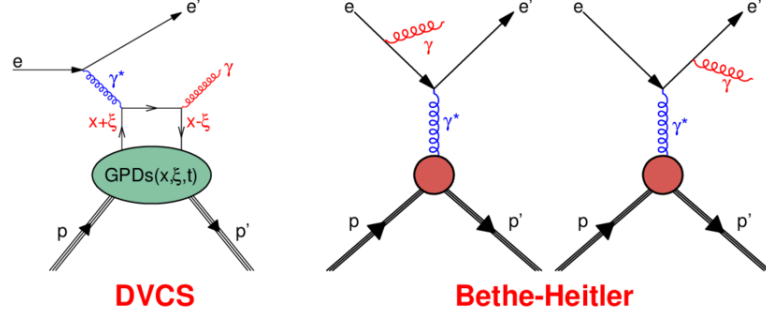


Figure 1.1: DVCS and BH contributions to electro-production of photons.

they are accelerated using RF accelerating cavities.

Studies have shown that the emittance of the positron beam is anticipated to be larger than the existing electron beam. An optimal energy range was identified for positron output, pinpointing an energy peak of 15-25 MeV/c, when using the 120 MeV CEBAF electron beam. Various design solutions yielded a positron current of 1  $\mu$ A reaching the North LinAc.

The design of the converter target is also a significant challenge, given that a notable portion of the incoming electron beam power gets deposited in the production target. Proposed solutions involved either a rotating target wheel or a liquid target. Due to radiation concerns, the suggestion was made to house the Continuous Electron Beam Accelerator Facility (CEBAF) positron injector in a separate tunnel. Ultimately, while handling the large amount of power deposited on the target presents an R&D challenge, it is believed that with the appropriate modifications, achieving a positron current of 1  $\mu$ A is within reach.

The JLab 12 GeV electron beam upgrade underscores the significance of advanced accelerator facilities, offering a more detailed understanding of nucleon structures. In the context of positron program, the most prominent method considered for the production of such positrons is the polarization transfer from sub-GeV polarized electrons via bremsstrahlung and pair production. This led to the conception of the Polarized Electron for Polarized Positron (PEPPo) experiment at JLab [26]. PEPPo aimed to experimentally validate the production technique of polarized positrons using bremsstrahlung of polarized electrons. The Polarized Electrons for Polarized Positrons (PEPPo) experiment successfully demonstrated the efficient transfer of polarization from electrons to positrons generated through the bremsstrahlung radiation process in a high-Z target. Positron polarization levels of up to 82% were achieved, limited only by the polarization of the initial electron beam with a momentum of 8.19 MeV/c. Technical design of the experiment has evolved over time, incorporating innovative diagnostic tools, enhancing its capability to potentially offer critical insights into the underlying physics of polarization transfers. While prior research and developments have laid a solid foundation in this field, they also reveal a number of intricate challenges that this thesis aims to actively address by developing a beam injector.

Developing a CW positron injector for CEBAF introduces a unique and challenging approach that is fundamentally different from previous facilities that have produced positrons using pulsed mode operation. The transition from pulsed to continuous mode operation not only offers several advantages but also poses significant

challenges:

- **Collection and injection:** In pulsed mode operation, positrons are generated and collected in batches before being injected into the accelerator. Continuous mode demands innovative techniques to efficiently capture and transport positrons without interrupting the beam.
- **Beam dynamics:** In continuous mode, constant control and adjustment of beam parameters such as emittance, energy spread, and bunch length are required to maintain stability. In pulsed mode, beam dynamics are tailored and optimized for the specific pulse characteristics, necessitating careful control and tuning for each pulse.
- **Power density management:** A continuous positron beam implies higher power density than its pulsed equivalent, necessitating effective cooling systems to prevent potential damage to the accelerator components, especially crucial when dealing with a low number of generated positrons.
- **RF power needs:** Continuous positron sources demand a consistent high-power RF supply. This constant RF provision can be technically intricate and costly, unlike in pulsed sources where RF is intermittently required.
- **Damping ring:** Employing a damping ring, a feature in many pulsed mode facilities, is impractical for CEBAF continuous mode due to the unceasing inflow of positrons. Alternate methods to optimize beam quality are essential.

While these challenges are substantial and require thoughtful solutions, the continuous mode of operation presents a series of advantages that underscore its potential benefits:

- **Enhanced beam utilization:** Continuous beams offer a higher duty cycle, enabling efficient and consistent data collection, maximizing the physics reach of the accelerator.
- **Time structure flexibility:** Continuous beams can be more easily adjusted to meet specific experimental needs.
- **Reduced beam-related backgrounds:** The continuous nature of the beam offers a stable environment, beneficial for precision experiments demanding high signal-to-background ratios.

Research and development efforts are required to address these challenges and limitations. The primary focus should be enhancing positron generation efficiency, refining beam accumulation techniques, preserving polarization, managing power density, and ensuring compatibility with accelerator systems. Overcoming these hurdles is key for successfully operating future electron-positron accelerators and other experiments that rely on high-intensity, polarized positron beams.

Given the significance of these challenges, this thesis expands on the broader context of positron research and innovation to provide a comprehensive overview. Building on the foundational research in the field, the methodology used in this work is based on the approach of Olsen and Maximov [27]. They detailed the polarization

transfer process. In the context, the longitudinally polarized electron beam at 120 MeV hitting a target composed of tungsten ( $Z=74$ ) is studied. The passage of the beam through the target enables efficient polarization transfer, first producing a circularly polarized photon by the bremsstrahlung process. These photons then create electron-positron pairs in the same target. The mechanisms behind this polarization transfer are used in this thesis.

One of the key considerations in this context is that the same target and thickness can yield either a useful polarized current or an unpolarized current, with each beam being suitable for acceleration at CEBAF. The thickness of the tungsten target plays a pivotal role in ensuring both high positron yields and polarization. To this end, an automated GEANT4 routine was instituted to simulate positron production across varied tungsten thicknesses. This simulation led to the identification of an optimal thickness, a finding that has potential implications for future research and applications.

These results led to two different design approaches: Polarized Mode, emphasis on optimizing polarization and Unpolarized Mode, which focus on maximizing positron yield.

The secondary nature of the positron beam involves particles exhibiting significant transverse momentum. To address this, two strategies were examined for capturing  $e^+$ : an adiabatic variation of the solenoidal magnetic field and an abrupt variation of the magnetic field. Both aimed to reduce the transverse component of the positron momentum. An analytical study was undertaken to refine the magnetic field and capture system dimensions. Subsequently, the parameters from these analytical methods were tested in a beamline modeled in ELEGANT [28] to simulate the effects of the optimized capture system. With the methodological foundation laid:

- Chapter 2 provides a summary of positron sources worldwide. It aims to offer a technical comparison of these sources, organizing them into three categories: past, present, and future positron source projects. It describes the state of the art in global positron projects and introduce the unique features of the positron source at JLab, highlighting both its similarities and differences with other initiatives.
- Chapter 3 focuses on the CEBAF accelerator facility, detailing the electron injector from the generation of electrons to their injection into the North LinAc (CEBAF-NL). The aim is to provide insights into the typical beam parameters used for injection at CEBAF. Additionally, the chapter estimates the maximum phase space acceptance of the CEBAF-NL. These factors serve as crucial parameters for the design and optimization of the positron source.
- Chapter 4 delves into the production of the positron beam at CEBAF, focusing on the interaction between a polarized electron beam and a high- $Z$  target. The chapter breaks down the two-step production process first, photon emission through bremsstrahlung radiation, and second, the creation of  $e^+e^-$ -pairs from these photons. In the latter part of the chapter, the focus shifts to identifying the optimal target thickness for improving either positron production efficiency ( $\epsilon$ ) or polarization (FoM). This is done with respect to specified incident electron beam energy and target  $Z$ . Extensive GEANT4

simulations with a pencil electron beam have been performed for these investigations. The simulations investigate positron efficiency and polarization over a range of momentum and angular acceptances of the collection system.

- Chapter 5 provides an overview of collection systems, focusing in particular on the solenoid combinations used to refine and capture positrons emitted from the production target. The chapter studies two collection systems — the Adiabatic Matching Device (AMD) and a Quarter Wave Transformer (QWT) — evaluating their effectiveness in capturing and focusing positrons. Overall, the chapter provides deep insights into the importance and functioning of collection systems. These systems are critical components of the CEBAF positron source. They ensure that particles emitted with large transverse momentum are appropriately focused, which is essential for efficient and optimal operations.
- Chapter 6 explores how the captured positron distribution is managed and refined. Initially, the chapter explains the role of the magnetic chicane system in directing positrons, selecting only those with desired energy range. The focus then shifts to efforts to improve the quality of the longitudinal positron energy. The ultimate goal is to adjust this energy and increase it to 123 MeV, which is the required injection energy for CEBAF. To achieve this, the chapter introduces a second magnetic chicane designed to ensure longitudinal compression. It explores how this second chicane interacts with the accelerating section to optimize the longitudinal quality of the positron beam.

The simulation results of the beam tracking in the capture system agreed with the initial analytical predictions, confirming the optimization approach. The positron injector was elaborated step-by-step, and these results are presented in detail in this thesis.

In summary, this thesis represents a significant achievement in the design and optimization of a positron source for CEBAF. Through detailed simulations, a simulated positron polarization of over 65% was achieved, along with a positron current exceeding 170 nA. These results not only demonstrate the practical feasibility of the positron project but also highlight its potential impact on the JLab facility. By systematically addressing challenges and limitations, this research has the potential to advance the field of positron studies and enhance facilities like CEBAF, thereby contributing to a deeper understanding of the structure of matter. With this introduction, the path is now clear for the upcoming chapters, which will present the specifics of this work and explore its potential for the future of positron research.

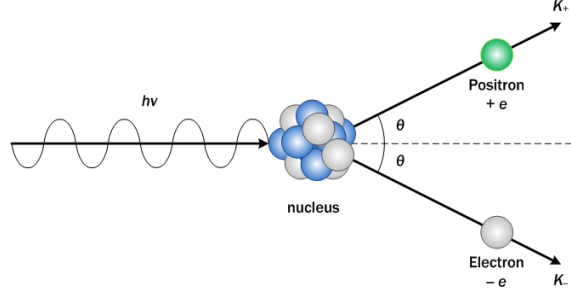
# Chapter 2

## Positron sources

Positron sources have been essential for various applications, including fundamental physics research, medical imaging, and material science. The need for high-quality, polarized positron beams has only increased with the advancement of these fields. This chapter provides an overview of the current state-of-the-art positron sources, including the various techniques used to produce positrons and their associated challenges.

There are essentially two methods to obtain positrons : the  $\beta^+$ -decay, an electroweak process, and the  $e^+e^-$ -pair creation, an electromagnetic process.

The  $\beta^+$ -decay is the most common natural process in which a proton of a nucleus converts into a neutron while emitting a positron and a neutrino. This process is used in imaging techniques as positron annihilation spectroscopy [29] and positron emission tomography [30]. These are based on the annihilation of the positron with an electron of the medium it is crossing. The positron loses energy primarily through collisions with atomic electrons down to a few electron volts where it is captured by electrons. The two particles undergo annihilation emitting preferentially two 511 keV  $\gamma$ -rays in opposite directions. The Coulomb interaction between positrons and electrons is so strong that the typical path-length of  $\beta^+$ -decay positrons does not exceed a few millimeters. This short range ensures that the annihilation of positrons occurs within a few nanoseconds [31]. However, this method remains of limited intensity and restricted polarization capabilities because of the intensity of available radioactive sources and of the parity violating nature of the  $\beta^+$ -decay. It is consequently only of limited use in accelerator physics. For instance, positron generators used for medical applications involve a radioactive isotope as a source coupled to accelerating and focusing devices [32]. The  $e^+e^-$ -pair creation process involves the interaction of a high-energy  $\gamma$ -ray with the electric field of a nucleus or an atomic electron. This interaction converts the photon energy into more generally two leptons of opposite charges. The  $\gamma$ -ray energy,  $E_\gamma$ , is an important parameter of this process. It must be high enough to produce an  $e^+e^-$ -pair ( $E_\gamma \geq 2m_e c^2 = 1.022$  MeV) but not too high such that photons pass through the material without interacting. The kinetic energy of the positrons produced in the reaction ranges from 0 up to the maximum  $E_\gamma - 2m_e c^2$ . The pair-creation process is a highly efficient way to produce positrons, with each high-energy photon capable of producing an  $e^+e^-$ -pair. As the process occurs into a material, the produced electrons and positrons participated in additional  $\gamma$ -ray production and interactions, leading to the development of an electromagnetic shower. This shower induces the loss of the characteristics


 Figure 2.1: The  $e^+e^-$ -pair creation process.

of the primary beam depositing heat and the subsequent mechanical stress in the target material. Several sources, including radionuclides, linear accelerators, and cyclotrons can produce the high-energy photons required for the  $e^+e^-$ -pair creation. In medical imaging, radionuclides such as  $^{18}\text{F}$  are commonly used as a source of high-energy photons [33]. In cancer treatment, linear accelerators and cyclotrons produce the required photons [34]. In particle and nuclear physics applications, they are produced by high energy electrons. This technique provides the ability to produce secondary positron beams with high intensities and high spin polarization.

The production of positron beams for particle and nuclear physics experiments follows a basic scheme where a primary electron beam is accelerated to a desired energy and directed onto a high  $Z$  target, where  $\gamma$ -rays are generated through the bremsstrahlung of initial electrons. A focusing system immediately after the target reduces the large angular spread of the secondary positrons resulting from the electromagnetic shower development and multiple scattering effects. This system uses a strong axial magnetic field  $B_1$ , typically in the order of a few Tesla, focusing the positrons within a desired transverse size. Two main focusing systems with different longitudinal field profiles have been and are still used: the AMD, where the field decreases adiabatically to a small constant value  $B_2$  serving to contain particles along the capture section, and the QWT where the transition to  $B_2$  is abrupt [16]. Following the high-field magnetic system, a Radio Frequency (RF) section enclosed in the low magnetic field system  $B_2$  reduces the positron beam emittance. After separation from the primary electron beam, the positrons can be post-accelerated to enter a damping ring at a desired energy. The purpose of this ring, which is typical but not present in every positron source, is to reduce the transverse emittance of the positron beam using the effect of energy loss through synchrotron radiations, therefore preparing the beam for further acceleration via the main accelerator complex.

The next subsections review some of the most important and renowned facilities that have been/are/will be used to generate positron beams for particle and nuclear physics experiments. Each of these facilities employs different schemes of production and transport of the positrons. It is the purpose of this chapter to compare them and position the Ce<sup>+</sup>BAF positron source in this global positron accelerator environment.

## 2.1 Past positron sources

### 2.1.1 Stanford Linear Accelerator Center

The Stanford Linear Collider (SLC) [35] was a linear accelerator located at the Stanford University in California (USA). It was originally designed for high-energy physics experiments but also served other various applications. A schematic layout of the SLC facility is shown in Fig. 2.2.

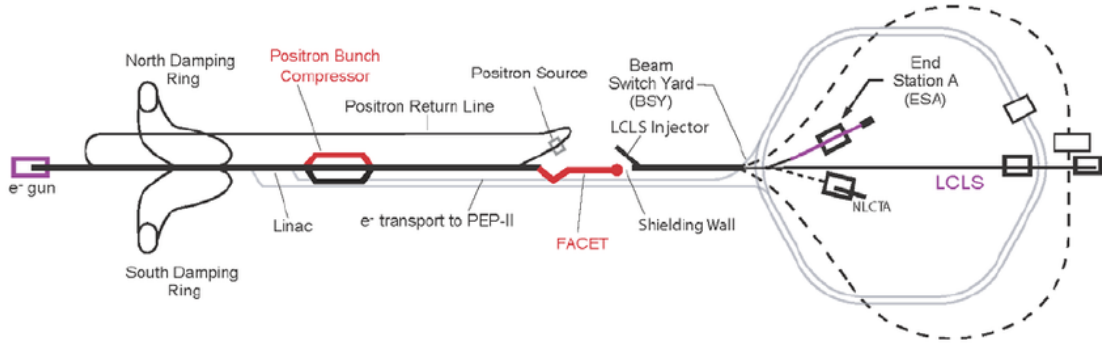


Figure 2.2: Sketch of the Stanford Linear Collider (SLC) showing the 220 MeV positron return line, the damping ring, and the LinAc-to-ring transport system. The electron bunch intended for the positron production target is extracted from the main LinAc at the two-thirds point with an energy of 30-33 GeV [1].

The path of positrons at SLC starts at the end of the LinAc section, where 30-33 GeV electrons are extracted towards the positron production target. The most common target material used at SLC is a Tantalum-Tungsten (90%Ta+10%W) alloy [36]. The positrons produced in the target material have a broad range of energies, but are produced preferentially in the 2-20 MeV range [36]. The quantity of generated positrons is abundant, about  $31 e^+/e^-$  in the energy range of interest, and thus would be the beam intensity if they can be successfully captured and accelerated. The efficiency of the positron collection system, and consequently the positron beam intensity, depends on the energy range of the collected positrons as well as the design of the system. SLC has adopted a Flux Concentrator (FC) collection system, which was designed to accept the 2-20 MeV range optimally. It includes a series of solenoid magnets creating a peak field of 5.8 T ( $B_1$ ) at the target and regurly decreasing to a lower uniform 0.5 T ( $B_2$ ), which reduces the positron angular divergence and improve particles transport. A yield of  $2.5 e^+/e^-$  has been measured at the exit of the SLC collection system [37]. The positrons are then accelerated up to 200 MeV in a booster and transported to the injection point of the main accelerator. Here, they are further accelerated up to 1.2 GeV and extracted to a damping ring. This element is an essential component of the SLC positron source, as it allows to match the transverse size of the beam with transverse acceptance of the main accelerator. Positrons stay up to 11.1 ms in the damping ring, reducing the transverse emittance by a factor 300 [36].



### 2.1.2 Large Electron-Positron collider

The Large Electron-Positron (LEP) collider with a 27 km circumference was the largest ever constructed accelerator for electron-positron collisions, marking a monumental civil-engineering project in Europe only rivaled by the Channel Tunnel. This collider was initially designed for the investigation of electroweak physics.

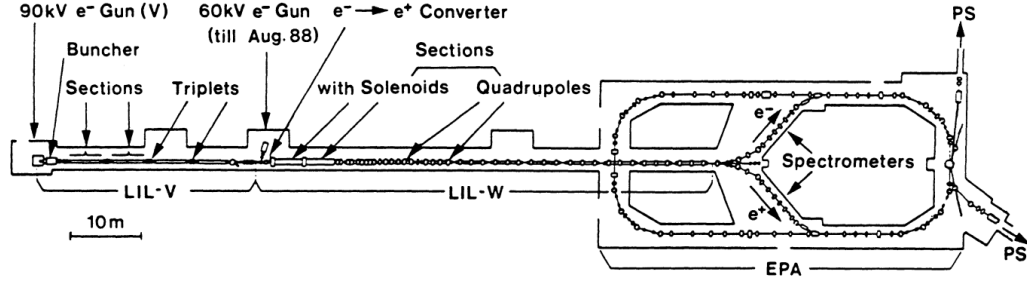


Figure 2.3: LIL injector layout [2].

The LEP Injector LinAc (LIL) shown in Fig. 2.3 comprises two Linacs in series: a high-current electron LinAc (V) with a nominal energy of 200 MeV used for positron generation and a lower-current LinAc (W) that accelerates either positrons or electrons up to 600 MeV [38]. The LEP positron production target is a 7 mm (two radiation lengths) tungsten target. The mean energy of emitted positrons is 8.5 MeV [39] and is captured within a  $2.4^\circ$  angular domain. The expected positron yield in this configuration amounts to  $4.3 \times 10^{-3} e^+/e^-$  at the 200 MeV incident beam energy. Immediately after the target, the positron beam is matched to the acceptance of the accelerating sections by a QWT system. A short-pulsed solenoid of approximately 1.6 T ( $B_1$ ) is employed, followed by a long solenoid with a field strength of 0.3 T ( $B_2$ ) [2]. This solenoid is mounted on the first two accelerating sections, the 0.3 T field being determined by the 18 mm iris diameter of the cavities. This system converts the beam from a small radius with large divergence ( $2 \times 160$  mm-mrad) to a larger radius with smaller divergence ( $8 \times 40$  mm-mrad). The accelerating gradient in these sections is chosen to be smaller than the nominal (7 MeV/m instead of 12 MeV/m) as a precaution against potential breakdown issues in the high-field radiation environment near the converter. The beam exits the matching and first two accelerating sections at approximately 95 MeV. Three quadrupole matching and accelerating sections follow that increase the beam energy up to 550 MeV that is the final positron energy at the exit of the injector [40], before entering the Electron-Positron Accumulator (EPA) ring and the main accelerator complex.

### 2.1.3 Positron-Electron Tandem Ring Accelerator

The Positron-Electron Tandem Ring Accelerator (PETRA) is a particle accelerator at the Deutsches Elektronen-Synchrotron (DESY) in Hamburg. It was initially built as a storage ring electron-positron collider for elementary particle physics studies. The third phase of PETRA (PETRA III) operates since 2009 as a brilliant storage-ring-based X-ray source.

The positron production at PETRA (Fig. 2.4) is based on a fixed target scheme: a 400 MeV electron beam hits a tungsten target which is followed by collection



The electron beam used for this purpose has an energy of 150-200 MeV, a pulse duration of  $2.5 \mu\text{s}$ , and a repetition rate of 60 Hz. Each pulse comprises 52 bunches, each containing approximately  $6 \times 10^{10}$  electrons. The instantaneous and average electron currents hitting the target are respectively 0.2 A and  $30 \mu\text{A}$ , resulting in an average beam power of 6 kW. A QWT collects the generated positrons [44]. The first solenoid has a magnetic field strength of 2.5 T over a 4.5 cm length, while the second solenoid has a field strength of 0.5 T. This QWT setup achieves a positron collection efficiency of approximately 1%.

## 2.2 Current positron sources

### 2.2.1 DAΦNE $\phi$ -factory

The DAΦNE accelerator complex at Frascati is an  $e^+e^-$  collider dedicated to the study of CP symmetry violation in  $\phi$ -meson decay [45]. It comprises a high-current electron and positron LinAc, a 510 MeV electron and positron accumulator, and two 510 MeV storage rings equipped with two interaction regions. The LinAc generates an electron-positron beam stacked and damped in the accumulator ring, further extracted and injected into the main rings. When the injector system is not supplying beams to the accumulator, the LinAc beams can be directed to a beam test area through a dedicated transfer line known as the Beam Test Facility (BTF) line [46].

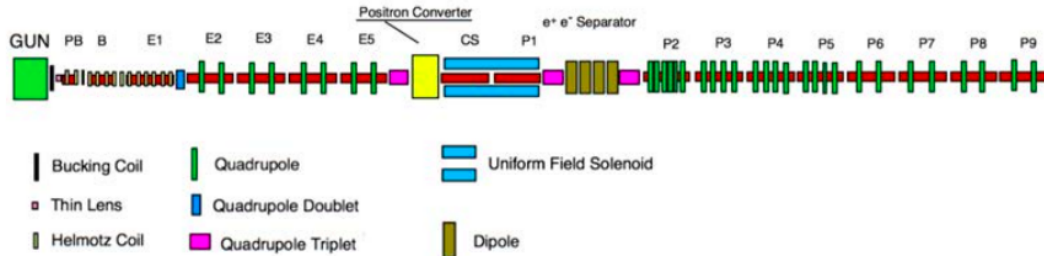


Figure 2.6: Layout of the DAΦNE positron source [5].

The positron beams at DAΦNE are generated from the interaction of a 200-250 MeV electron beam with a peak current of 5.5 A into 2 radiation length thick tungsten-rhenium target. Right after the production target, positrons are collected using a SLAC-type flux concentrator in conjunction with DC solenoid magnets. These magnets produce a peak magnetic field of 5 T, decreasing to 0.5 T over the capture section [47]. Downstream the capture section, a magnetic chicane consisting of four dipoles separates secondary positrons and electrons into two distinct paths. Electrons are directed toward a beam stopper while positrons undergo momentum selection through a  $45^\circ$  dipole and collimators in the horizontal plane. This process significantly reduces the beam intensity, which depends on the chosen central value of the secondary beam energy (ranging from approximately 50 MeV up to nearly the primary beam energy). The momentum spread  $\Delta p/p_0$ , is typically better than 1%, depending on the collimator setting [46].

### 2.2.2 Beijing Electron Positron Collider

The Beijing Electron Positron Collider (BEPC) is a double ring accelerator developed to serve both fundamental high-energy physics research and applied physics research using light-sources produced by synchrotron radiation of the lepton beams [48].

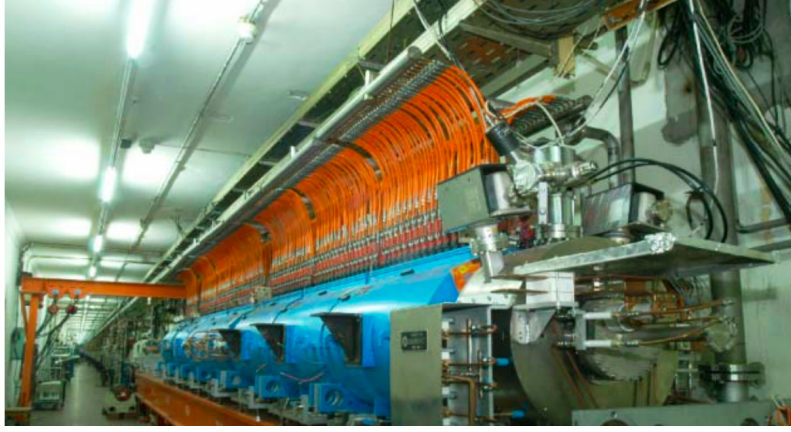


Figure 2.7: Positron focusing and accelerating systems at BEPCII [6].

At the upgraded BEPCII, positrons are produced from a 240 MeV electron beam, focused into a 3-5 mm spot diameter, interacting with a 8 mm thick tungsten target [49]. A SLAC-type flux concentrator (AMD) captures the positrons. This capture device consists of a 12-turn copper coils, 10 cm in length, with a cylindrical outside radius of 53 mm. The inside radius of the flux concentrator is conical in shape, gradually increasing from 3.5 mm to 26 mm. The peak magnetic field ( $B_1$ ) at the entrance face of the flux concentrator is 4.5 T and gradually decreases down to 0.5 T at its exit. Downstream of the flux concentrator, seven DC-focusing solenoid modules are wrapped around RF structures. Each solenoid module is 1 m long and generates a magnetic field of 0.5 T. These solenoid modules are responsible for further focusing and matching of the positron beam into the downstream quadrupole focusing system. A positron yield of  $7.3 \times 10^{-2}$  ( $e^+/e^- \cdot \text{GeV}$ ) was reported at the commissioning of the upgraded facility [6].

### 2.2.3 Kō Enerugī Kasokuki Kenkyū Kikō

The High Energy Accelerator Research Organization, also known as KEK [50], is investigating since 1999 the CP symmetry violation in the  $B$ -meson decay. The KEKB accelerator is an asymmetric electron-positron collider with 3.5 GeV positron and 8 GeV electron storage rings. Its upgraded version, known as SuperKEKB features 4 GeV positron and 7 GeV electron beams.

The injector LinAc (Fig. 2.8) directly injects single-bunch positron and electron beams into the KEKB rings. The design aimed for beam charges of 0.64 nC/bunch for positrons and 1.3 nC/bunch for electrons at the end of the LinAc, with a maximum repetition rate of 50 Hz for both beams. High-current primary electron beams (about 10 nC/bunch) are required to generate sufficient positrons [8]. The layout of the KEKB positron source is represented in Fig. 2.9. It consists of a positron-production target and a positron-capture section. Positrons are generated from a

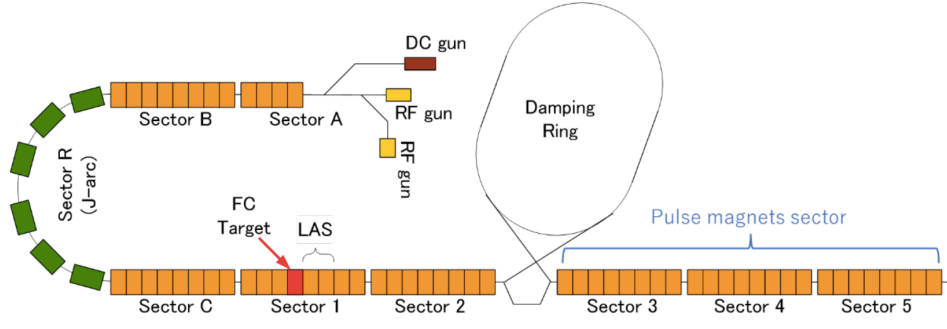


Figure 2.8: The KEKB injector LinAc [7].

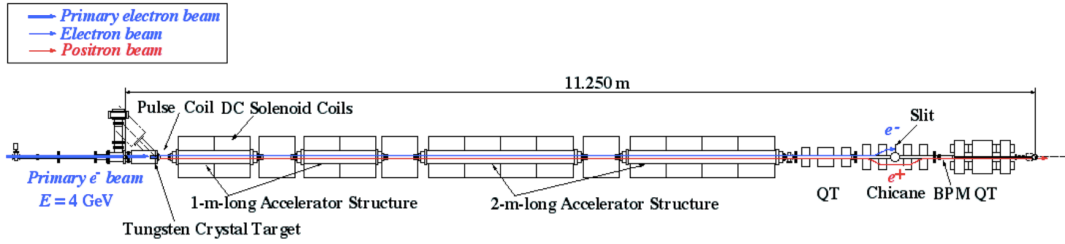


Figure 2.9: Layout of the positron source at the KEKB injector LinAc [8].

500 nA  $e^-$  beam current with an energy of 4 GeV interacting with a 10.5 mm thick tungsten crystal target. The average beam power reaches 2 kW, producing about 4 nC  $e^+$  at the end of the injector LinAc for a 10 nC primary beam charge. The typical transverse beam size is 0.7 mm (rms) in radius, and the average horizontal and vertical normalized emittances are 660 and 360 mm-rad (rms) at the target. The estimated horizontal(vertical) angular spread at the target is 0.2(0.1) mrad (rms).

The positron collection system is based on a QWT. It comprises a 45-mm long pulsed solenoid with a field strength of 2 T, an 8 m long DC solenoid with a field strength of 0.4 T, and two accelerating sections all installed inside the DC solenoid. This system captures the positrons generated from the target and accelerates them from captured  $e^+$  at 10 MeV to an energy of about 70 MeV. To separate electrons generated alongside the positrons, a positron/electron separator (chicane) consisting of four rectangular magnets and a beam stopper is employed at the center of the chicane.

## 2.3 Future positron sources

### 2.3.1 International Linear Collider

The International Linear Collider (ILC) is a proposed future electron-positron collider, necessitating a robust positron source capable of delivering highly longitudinally spin polarized positrons. The ILC aims to achieve a center-of-mass energy of 500 GeV at the interaction point, using a series of accelerating cavities operating at an average gradient of 31.5 MV/m [51].

The major components of the ILC positron source and its operational principles are illustrated in Fig 2.10. The source operates through a multi-stage process that encompasses positron production, subsequent positron capture and cooling. The

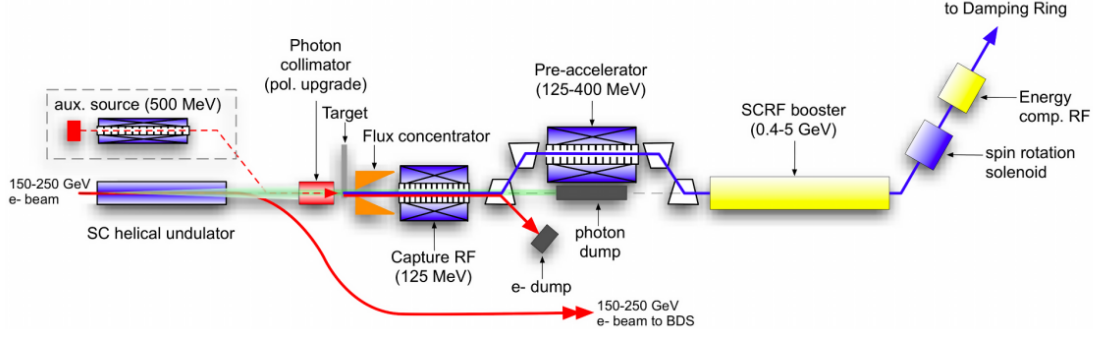


Figure 2.10: Overview of the proposed ILC positron source [9].

positron source employs a photoproduction technique to produce positrons. Initially, the primary electron beam is accelerated in the main LinAc and directed into a 147 m superconducting helical undulator. This undulator generates photons within a range of approximately 10 MeV to 30 MeV, depending on the energy of the electron beam. The photons are separated from the electron beam through a low-emittance chicane and directed towards a titanium alloy target (0.4 radiation length thick) situated approximately 500 m downstream. The interaction between the photons and the target leads to the creation of electron-positron pairs. Following the target, these pairs are guided through an optical-matching device (OMD) which features a magnetic field that initiates at less than 0.5 T near the target, rapidly increases to 3 T within approximately 2 cm, and subsequently decreases to 0.5 T over a length of 14 cm. This unique OMD design offers a broad energy acceptance and optimizes the matching of the beam phase-space with the capture L-band RF cavities.

Directly after the OMD, capture RF cavities operating at an average gradient of 9 MV/m and within 0.5 T solenoids accelerate the positron beam up to 125 MeV. Then, positrons are directed through a dipole magnet located at the entrance of an achromatic chicane, effectively separating them from electrons and photons. Within the chicane, collimators are strategically placed to eliminate positrons with large incoming angles and those deviating significantly from the desired energy. Downstream of the chicane, the pre-accelerator takes charge, propelling the positron beam from 125 MeV to 400 MeV. This acceleration occurs within normal-conducting RF structures immersed in a constant solenoid field of 0.5 T over a 35 m long accelerating section. At the exit of the chicane, superconducting RF structures are employed to achieve further acceleration up to 5 GeV. Before injection into the damping ring, superconducting solenoids are used to rotate the spin vector of the positrons into the vertical plane. Energy compression is achieved using a separate superconducting RF structure. The baseline design of the positron source provides a polarization of 30%. Provisions have been made for a potential upgrade to achieve a polarization of 60% in the future. This would require a photon collimator upstream of the target and a new 220 m long helical undulator [9].

An auxiliary positron source is provided for commissioning and tuning purposes to generate low-intensity positron beams when the high-energy electron beam is unavailable [52]. This auxiliary source uses a 500 MeV warm LinAc to produce an electron beam toward the positron production target. The resulting beam provides a small percentage of the nominal positron current.

### 2.3.2 Future Electron-Positron Circular Collider

The Future Electron-Positron Circular Collider (FCC-ee) is a proposed collider aiming to enhance the understanding of fundamental physics through high-energy electron and positron collisions. The FCC-ee envisions a circular collider capable of achieving  $e^+e^-$ -collision energies of up to 182.5 GeV, as part of the large Future Circular Collider project.

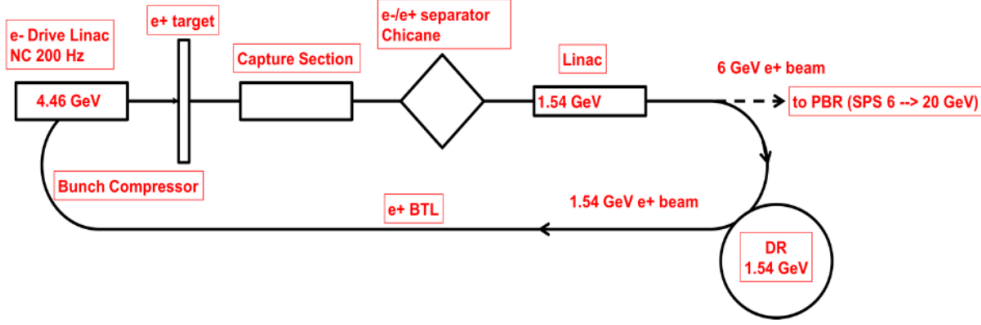


Figure 2.11: Schematic design of the FCC-ee positron source [10].

The FCC-ee positron source schematic design is shown in Fig. 2.11. A first approach involves a conventional positron source where high-energy electrons interact with a thick target of high nuclear charge. A second approach employs thin crystal targets to generate numerous photons. Electrons passing through the crystal at specific angles are channeled and collectively emit soft photons due to interactions with numerous nuclei. This hybrid approach combines a thin-oriented crystal with an amorphous converter and a magnet to damp charged particles emitted in the crystal, allowing only photons to reach the converter [53]. The final choice will be guided by optimizing performance while considering constraints like power density limits, target thickness, and the desired positron beam intensity and emittance. A 6 GeV electron LinAc is intended to serve as a source for positron generation, with a bunch intensity of  $4.2 \times 10^{10} e^-/\text{bunch}$  at a repetition rate of 200 Hz [54]. Optimization studies involving positron yield and deposited power [55] led to the adoption of a 16 mm thick tungsten target in the conventional scheme while the hybrid scheme combines a 1.4 mm tungsten crystal with a 12 mm thick amorphous tungsten target.

The design of the capture section in both investigated schemes relies on an AMD. This facilitates the transformation of the positron beam phase space at the target, initially characterized by a significant transverse divergence, to align with the acceptance of the capture LinAc. A Flux Concentrator (FC) device is employed to achieve an adiabatically decreasing magnetic field. One FC model considered is 14 cm long, starting with a longitudinal magnetic field ranging from 5-7 T and gradually decreasing to 0.5 T and 0.7 T, respectively. In the hybrid scheme, the capture LinAc comprises 1.5 m long L-band structures operating at 17 MV/m and 2 GHz. In contrast, the conventional scheme employs 3 m long S-band cavities with a large aperture, operating at 20 MV/m and 2856 MHz. The entire capture LinAc is surrounded by a solenoid that generates an axial magnetic field of 0.5-0.7 T preventing losses until the positron transverse momentum is sufficiently mitigated.

### 2.3.3 Jefferson Lab positron source

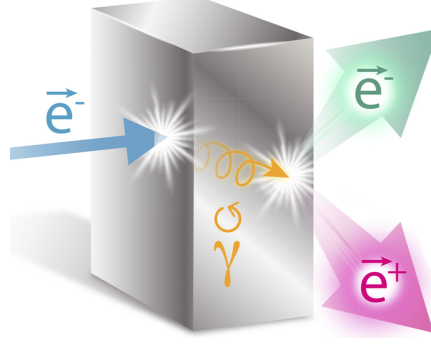


Figure 2.12: Schematic of the PEPPo concept : a highly polarized electron beam interacts with a target and generates circularly polarized  $\gamma$ -rays which then transfer their polarization to the  $e^+e^-$ -pairs formed within the nuclear field of target nuclei.

A novel approach known as the Polarized Electrons for Polarized Positrons (PEPPo) technique (Fig. 2.12), has been demonstrated at the Thomas Jefferson National Accelerator Facility for the production of polarized positrons [26]. The PEPPo technique exploits the bremsstrahlung radiation of longitudinally polarized electrons within a high- $Z$  target to generate polarized photons, producing polarized  $e^+e^-$ -pairs. By using high-intensity ( $\geq 1$  mA) and high-polarization ( $\geq 80\%$ ) electron sources it is expected that the PEPPo concept can efficiently produce polarized positrons with high intensity ( $\geq 100$  nA) and high polarization ( $\geq 60\%$ ).

The PEPPo experiment was conducted with low energy electrons (8.2 MeV/ $c$ ) free of activation issues, minimizing the detector footprint and ensuring robust measurements of the polarization of positrons. The PEPPo collaboration reported polarization as high as 82%, indicating a nearly 100% transfer of the initial polarization [26]. The present work aims to build on this experiment and propose a high duty-cycle positron source capable of reaching high intensities and high polarization.

While these innovative approaches represent the future of positron sources, it is also pertinent to compare the current state-of-the-art facilities stack up against each other. One notable facility that emerges in this context is CEBAF.

## 2.4 Comparative summary

Based on Tab. 2.1, the comparison of CEBAF with other facilities reveals several significant distinctions:

- Firstly, CEBAF has a notably low number of electrons per bunch ( $N_e/b$ ), approximately on the order of  $8.13 \times 10^6$ , in contrast to other facilities which typically range from  $10^9$  to  $10^{11}$ .
- Secondly, CEBAF has a 100% Duty Cycle (DC), meaning continuous operation, unlike other facilities that predominantly operate in pulsed mode.
- Furthermore, CEBAF exhibits much lower electron energy ( $E_{e^-}$ ) at 0.123 GeV compared to facilities like the ILC which requires energies of up to 250 GeV.



	$N_{e^-}$ ( $\times 10^6\ e^-/b$ )	$n_b$ (b/p)	Duty Cycle	$P_{e^-}$ (%)	$p_{e^-}$ (GeV/c)	PW <sub>a</sub> (kW)	I <sub>ap</sub> ( $\mu$ A)	I <sub>peak</sub> (A)	Rr (Hz)	Bunch length (ns)	
SLAC	[36]	$5 \times 10^4$	1	$3.6 \times 10^{-7}$	No	33	47.5	1.44	4	180	2
LEP	[40]	$1.875 \times 10^5$	4	$1.2 \times 10^{-6}$	No	0.2	2.4	12	2.5	100	12
PETRA	[56, 57, 58]	$1 \times 10^5$	1	$4 \times 10^{-7}$	No	0.3	0.24	0.8	2	50	8
CESR	[3]	$6 \times 10^4$	52	$0.18 \times 10^{-6}$	No	0.2	5.99	30	3.2	60	3
DAFNE	[47, 5]	$1 \times 10^5$	1	$5 \times 10^{-7}$	No	0.25	0.2	0.8	1.6	50	10
BEP2	[48]	$5.4 \times 10^3$	2	$5 \times 10^{-8}$	No	0.24	0.02	0.086	0.84	50	1
KEKB	[8, 59]	$6 \times 10^4$	2	$5 \times 10^{-11}$	No	4	4	793	6.31	50	$1 \times 10^{-3}$
ILC	[51]	$3 \times 10^4$	1312	$1 \times 10^{-11}$	No	250	60	31.5	1.83	5	$2 \times 10^{-3}$
FCC e <sup>+</sup> e <sup>-</sup>	[53]	$4.20 \times 10^4$	2	$2 \times 10^{-4}$	No	6	16.1	2.69	2.68	200	$1 \times 10^3$
Ce <sup>+</sup> BAF	[12]	8.13	1	1	90	0.123	123	1000	$5.2 \times 10^{-4}$	$1.50 \times 10^{09}$	$2 \times 10^{-3}$

Table 2.1: Electron sources performance summary for positron production. The different symbols stand for: Number of  $e^-$  per bunches  $N_e/b$ , Number of bunches per pulse (b/p), average power ( $PW_a$ ), average  $e^-$  current  $I_a$  ( $\mu A$ ), peak current  $I_{peak}(A)$ , polarization  $P_{e^-}$  (%), Repetition rate (Rr) in Hz.

Regarding the average power, CEBAF values are significantly lower than those of other facilities due to the lower electron beam energy. CEBAF also stands out with a very high repetition rate of  $1.50 \times 10^9$  Hz, in contrast to other facilities. Finally, CEBAF bunch length is very short, of the order of a few ps, shorter than many other facilities. These distinctions have implications for positron production at CEBAF:

1. The smaller the electron energy, the lower number of electrons per bunch and the low pulse energy density at CEBAF may lead to reduced positron production compared to other facilities;
2. The CEBAF potential for continuous operation may result in a more constant production of positrons compared to facilities operating in pulsed mode;
3. The very high repetition rate could have implications for beam quality, stability or other characteristics crucial for positron production.

In summary, CEBAF has unique characteristics, such as its lower number of electrons per bunch, low pulse energy density, and continuous operation potential, may have implications for the positron production efficiency and method when compared to other facilities notably, polarized.

Table 2.2 presents an overview of various positron sources, detailing their essential parameters and performance metrics used in various accelerator facilities worldwide, each tailored to specific experimental requirements. The key takeaways from this table are summarized hereafter.

The selection of target material and thickness varies across sources, encompassing tantalum-tungsten (Ta-10W) to titanium-aluminum (Ti-Al), with CEBAF planning for a 4 mm thick tungsten (W) target thinner than other sources. This choice significantly impacts positron yield and polarization, with CEBAF target designed to maximize positron production, potentially at the expense of polarization or yield. Different sources utilize various collection systems, including AMD and QWT. CEBAF stands out by utilizing a specialized QWT. This selection deviates from sources that opt for AMD, potentially impacting the capture and focus of positrons, especially within distinct energy spectra. With positron polarization exceeding 65%, CEBAF is particularly suited for experiments, such as DVCS, which necessitate polarized positron beams. However, CEBAF shares common challenges with other sources, including issues related to beam dumping, power density, integration of technical effects into simulations, and the need for external collaboration. Addressing these challenges through ongoing research and collaboration is crucial to maintaining beam quality and facility operations. This comparison of positron sources underscores CEBAF unique characteristics and potential advantages, emphasizing its significance in positron research and the ongoing efforts required to tackle shared challenges.

Delving deeper into the distinctiveness of CEBAF offers an understanding of its foundational structure and the pivotal role the facility plays in nuclear physics. This sets the stage for the subsequent discussions.

Positron sources	Target		Collection system			$N_{e^+}$ ( $\times 10^{10} e^+/\text{bunch}$ )	P (%)
	Material	Thickness (mm)	Type	$B_1$ (T)	$B_2$ (T)		
SLAC	Ta-10W	24	AMD	5.8	0.5	2 – 20	No
LEP	W	7	QWT	1.6	0.3	8	No
PETRA	W	7	QWT	2	0.4	10	No
CESR	W	7	QWT	2.5	0.5	10	No
DAFNE	W	7	AMD	5	0.5	20	No
BEP2	W	8	AMD	4.5	0.5		No
KEKB	W	10.5	AMD	2	0.4	10	No
ILC	Ti-Al	0.4/1.4	AMD	3.2	0.5	20	30
FCC	W-Re	16	AMD	7	0.5		No
Ce <sup>+</sup> BAF	W	4	QWT	2.5	0.05	60	$\geq 65$

Table 2.2: Positron sources performance summary.

# Chapter 3

## $Ce^+$ BAF positron source concept

### 3.1 CEBAF overview

CEBAF is a remarkable facility that has contributed significantly to advancing nuclear physics research. An important feature of CEBAF is that it provides a continuous electron beam, which allows for precision measurements of nuclear physics phenomena. Since its birth, CEBAF has been upgraded in energy twice to improve its capabilities. In 1994, the accelerator was built to accelerate the electron beam to 4 GeV and has been upgraded to 6 GeV thanks to cavity performances. In 2012, 6 GeV operation ended, and the machine was upgraded up to 12 GeV. In 2013, beam turned back on in CEBAF, and was eventually able to send beam to four experimental halls simultaneously, reaching 11 GeV to Halls A, B, and C, and 12 GeV in the new Hall D. This increased energy enables to explore new frontiers in nuclear physics. CEBAF is home to four experimental halls (A, B, C, D) equipped with detectors and instrumentation to capture and analyze the results of experiments. Each hall is specialized for a specific area of research.

Fig. 3.1 shows the different components of the CEBAF accelerator chain; at the starting point, the gun section continuously emits the electron beam. Four beams are simultaneously delivered to the halls. Halls A, B, and C receive beams using four lasers operating at either 249 MHz or 499 MHz, while Hall D receives only beams delivered at 249 MHz. Downstream of the gun is a bunching/chopping system which defines the longitudinal emittance, then another buncher to compress the beam to a few picoseconds for acceleration to 7 MeV in an SRF booster. The laser spot size and GaAs photocathode defines the transverse beam emittance. However, the maximum transverse emittance is limited by a pair of emittance filter apertures. The beam enters the CEBAF-NL at 123 MeV and gains an additional 1090 MeV through a series of cryomodules. The beam then makes a  $180^\circ$  turn through the East Arc and continues through the second linear accelerator (South LinAc (CEBAF-SL)), providing a similar accelerating gradient (1090 MeV). After exiting the CEBAF-SL, either extracted or recirculated. The West Arc finishes the recirculation, bringing the beam back to the NL. From here, the beam can continue recirculating for any number of passes up to and including 5 passes to Halls A, B, and C (achieving 11 GeV), and 5.5 passes for Hall D (achieving 12 GeV).

In order to separate the beams and achieve multi-hall beam delivery, radiofrequency (RF) separators operating at 499 MHz are used to send beams to the three Halls A, B, and C at 1,2,3 and 4 passes. Additional 748.5 MHz RF separators are

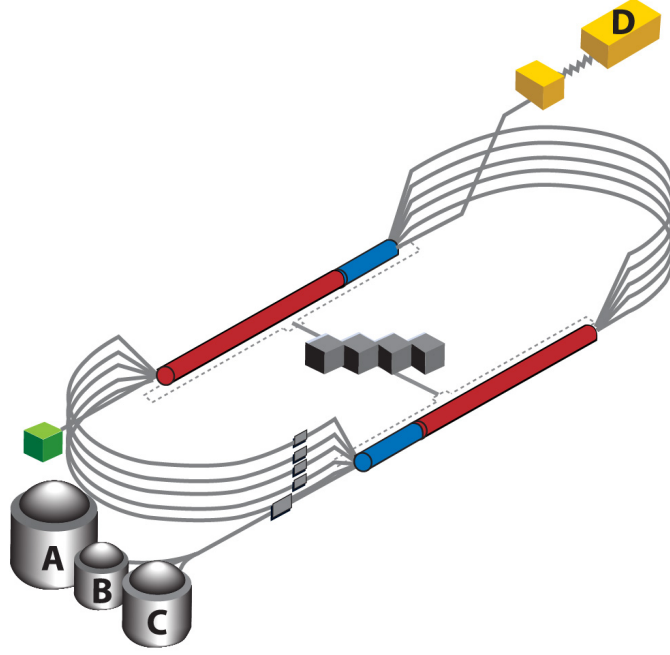


Figure 3.1: CEBAF diagram: an overview of the injector gun, superconducting linear accelerators, and recirculating arcs for high-quality electron beam production, with color-coded representations of accelerator modules (red), C100 cryomodules (blue), and upgraded injector module (green).

used to send the beam to Hall D at 5.5 passes, while Hall A, B, and C receive beams after 5 passes. Hall A can accommodate a maximum beam current of  $120 \mu\text{A}$ , due to the 900 kW beam dump limit for higher passes. This corresponds to a bunch repetition rate of 249.5 MHz, approximately equivalent to a charge of 480 fC per bunch. Hall B can receive up to 160 nA of beam current at 249.5 MHz beam repetition rate, giving a charge per bunch of up to 0.64 fC. Hall C can receive the same amount of current as Hall A, as they both share the same 900 kW beam dump limitation. The guaranteed RMS energy spread delivered to the halls at the final pass is approximately  $5 \times 10^{-4}\%$  with a high beam polarization of 85% - 90% [17].

The accelerator chain at CEBAF is a complex system that requires precise control and monitoring to maintain high CW beam quality and stability. The accelerator instrumentation includes beam position monitors, current transformers, and diagnostic devices, which monitor the beam parameters in real-time [60]. Tab. 3.1 [17] shows various parameters of the CEBAF accelerator in the current 12 GeV setup, including the electron beam energy, current, and polarization. If Hall D is not operational, Halls A, B, and C can use the 499 MHz beam repetition rate during pass 5. However, the delivered current is restricted to the capacity of the beam dump.

Parameter	Value
Electron beam energy (A, B, C)	11 GeV
Electron beam current Hall A	1 - 120 $\mu$ A
Electron beam current Hall B	1 - 160 nA
Electron beam current Hall C	1 - 120 $\mu$ A
Electron beam current Hall D @ 12.1 GeV	2000 nA
Beam polarization	85% – 90%
Bunch Charge (Min-Max)	$4 \times 10^{-3}$ fC – 600 pC
Energy spread (5 <sup>th</sup> pass)	$5 \times 10^{-4}$ %
Maximum limited beam power (5 <sup>th</sup> pass)	900 kW
Operating frequency	249.5 Halls D On / 499 MHz
Hall D Off at 5th pass	
Cryomodule type	C100 and C75
Duty factor	CW

Table 3.1: CEBAF parameters for 12 GeV operation [17].

### 3.1.1 The CEBAF polarized electron source

The creation of positron beams at CEBAF depends on the quality of the polarized electron beam used to create the positrons. This process starts with a GaAs photogun. The GaAs wafer is placed in a vacuum chamber. It is essential to keep this chamber extremely clean, and at low pressure ( $1 \times 10^{-12}$  Torr). Then, it is heated to perform atomic cleaning on the surface, and activated using a particular method involving cesium and nitrogen trifluoride ( $\text{NF}_3$ ). Cesium increases photoemission on the photocathode until it peaks and begins to decline. After reaching half its maximum,  $\text{NF}_3$  is applied in ten Cs- $\text{NF}_3$  cycles to optimize quantum efficiency for efficient electron emission under laser illumination. The effectiveness of this process is often measured by the Quantum Efficiency (QE), given by

$$QE = \frac{N_{e^-}}{N_\gamma} = \frac{124}{i \times \lambda \times Pw_\gamma}$$

where  $i$  is photocurrent in  $\mu$ A,  $\lambda$  is laser wavelength in nm, and  $Pw_\gamma$  is incident laser power in mW, providing a metric that enables evaluative insights into the efficiency of the photocathode illumination.

To create the polarized electron beam, a circularly polarized laser strikes the GaAs photocathode, preferentially exciting  $e^-$  of one spin state in GaAs, then diffuse to surface and emitted, releasing electrons, which are then formed into a beam. The laser time structure is achieved by using the linac radio-frequency to trigger a 1560 nm diode laser, generating short 50 ps FWHM pulses. Consequently the laser repetition rates (249.5 or 499 MHz) are synchronous with the frequency of the linac (1497 Mhz).

Polarized-beam experiments demand a precise electron spin orientation at the target, typically parallel to the beam motion direction, and capability for the spin direction to change at a determined frequency. This is achieved through the use of a Pockels cell, which modulates the polarization direction of the electron beam, typically at 30 Hz but, under certain techniques, even reaching up to 1000 Hz [61]. This modulation is essential to maintain a consistent and high degree of polarization in the electron beam as it travels to the experimental halls.

A Wien filter is employed with the specific goal of rotating the total polarization component of the electron beam so it arrives at the experiment in the desired direction. This orientation is crucial because as the beam progresses through the CEBAF machine, it undergoes precession. The aim is to compensate for this precession effect so that the electron beam achieves a nearly fully longitudinal polarization, closely aligned with the beam axis, as it enters a designated experimental Hall. It is important to note that the electron beam is already longitudinally polarized before entering the Wien filter (From the gun).

The fundamental principle here is based on the fact that electrons leaving the photocathode initially have their spin direction aligned either parallel or antiparallel to the direction of beam motion. This alignment is determined by the helicity of the laser circular polarization, which can be either right or left circular and is controlled by the Pockels cell. However, as the electron beam traverses the arcs and transport lines to the experimental halls, its spin direction precesses in the horizontal plane due to various factors. A spin manipulator is employed at the injector to ensure that this net spin precession is effectively cancelled and the desired spin orientation is maintained. Therefore, a Wien filter is used for this spin manipulation [62]. It operates by employing static electric and magnetic fields that are perpendicular not only to each other but also to the velocity of the charged particles passing through it. Thus, charged particles with a velocity of  $\beta c = E/B$  remain undeflected when passing through the Wien filter. However, the important aspect is that the spin of these particles is rotated within the plane of the electric field, allowing precise control over the final orientation of the electron beam spin.

Strategically applying these methods forms the foundation for achieving high electron beam polarization at CEBAF.

### 3.1.2 The electron injector

The CEBAF injector begins with the electron gun operating at 130 kV to produce a polarized electron beam from a photo-cathode. The beam has the same time structure as the lasers, which operate at 499 MHz for Halls A, B, and C, and a fourth laser operating at 249.5 MHz for Hall D. It is important to note that The A, B and C lasers are tunable to 249.5 as well. Its is needed when either of the halls are at pass 5 and Hall D is running.

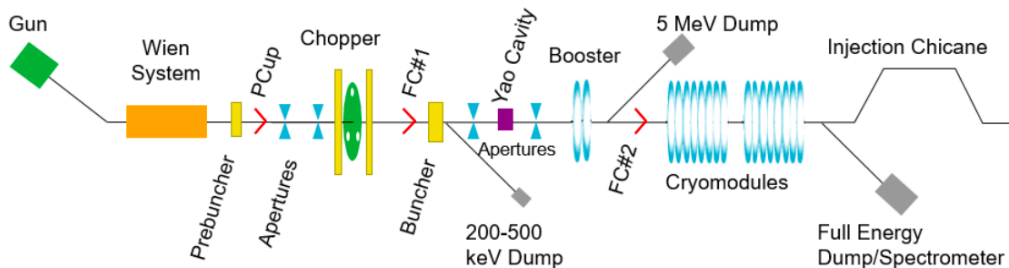


Figure 3.2: A schematic layout of the CEBAF injector at Jefferson Lab.

Downstream from the gun, the pre-buncher cavity bunches the beam and compensates for bunch lengthening. The beam is then directed into the chopper section,

located 7.6 m away from the gun. The chopper system, operating at 499 MHz, deflects the beam transversely using three holes placed 120 degrees apart. Triangular slits control bunch length (0 to 110 ps) and beam current. After passing through the chopper, the process reverses with another solenoid and a another deflecting cavity.

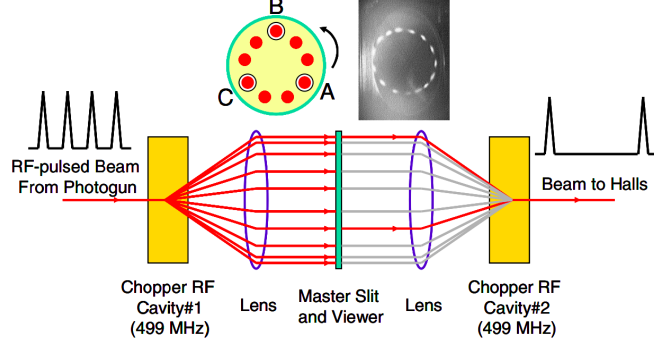


Figure 3.3: Chopper system at the CEBAF injector operating at 499 MHz: three drive lasers generate interleaved pulsetrains at a frequency of 499 MHz. Each beam passes through a corresponding aperture at the master slit [11].

The chopper phase has to be synchronized with the gun and the pre-buncher.

After the Chopper, the beam passes through another buncher and a five-cell capture cavity. The buncher provides the important main bunching to the beam, and the capture cavity provides an acceleration of up to 650 keV. Continuing downstream, the beam enters the two superconducting cryo-unit (booster), where more bunching is provided and the beam gets accelerated to approximately 6 MeV. After the booster, it passes through a pair of cryomodules, accelerating up to 123 MeV. The energy needed depends on the experimental program since it dictates what the gradient in the linacs should be. The injector is set to be:

$$E_i \text{ [MeV]} = \frac{123}{1090} \times E_{\text{LinAc}} \quad (3.1)$$

## 3.2 CEBAF acceptance

After exiting the injector, the beam must be matched into the CEBAF-NL. This matching process involves adjusting the beam phase space to align with the optics phase space, typically performed between beamline sections. Beam phase space is typically described by an ellipse and its associated Twiss parameters. This section details the phase space at the entrance to the CEBAF-NL, where positrons are to be injected.

Defining the beam emittance is crucial for understanding the acceptance of the CEBAF accelerator. This concept illustrates the area in phase space occupied by the particle distribution, a foundational idea in accelerator physics. A smaller emittance value indicates a greater ability to guide the beam through the beam pipe where beam size goes like  $\sqrt{\epsilon n}$  where  $\epsilon$  represents the beam geometric emittance.

The area enclosed by the ellipse is called beam emittance  $\epsilon$  or acceptance, described by

$$A = \int_{xx_p} dx dx_p = \pi \epsilon \quad (3.2)$$



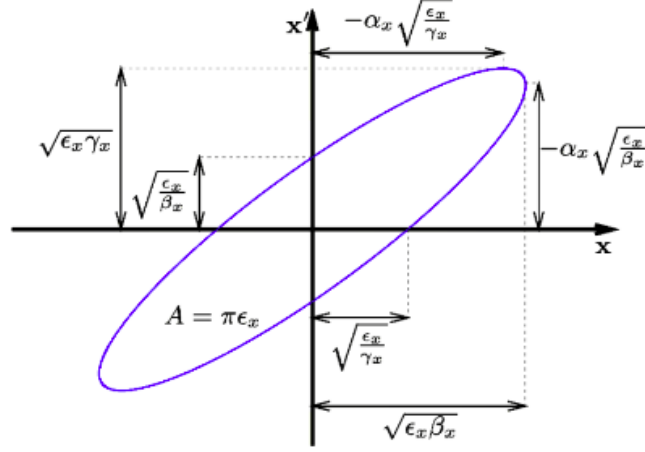


Figure 3.4: Phase space ellipse defining the occupied area of the beam.

where  $x$  and  $x' = x_p$  are the particle phase space coordinates. Eq. 3.2 describes that all particles enclosed by this phase ellipse stay within that ellipse (Liouville theorem). The emittance  $\epsilon$  can be described as

$$\epsilon = \gamma x^2 + 2\alpha x_p + \beta x_p^2 \quad (3.3)$$

where  $\alpha$ ,  $\beta$ , and  $\gamma$  are the Twiss parameters, which determine the shape and the orientation of the beam ellipse. At the CEBAF injector, when the beam exits the chicane injection located before the CEBAF-NL, it has to be within the acceptance of the CEBAF-NL to get accelerated with no loss. From Tab. 3.1 the energy spread at 12 GeV beam energy is about  $5 \times 10^{-4}\%$ . A measurement has been done by [63] to determine the accepted momentum spread at a variety of locations in CEBAF. At the entrance of the NL before acceleration, the energy spread at 123 MeV is approximately  $\Delta p/p_0 \leq 5 \times 10^{-4}\%$  and ten times smaller at the extraction region,  $\Delta p/p_0 \leq 5 \times 10^{-5}\%$ .

The accelerator has a set limit to the particles it can contain, denoted as the accelerator acceptance, represented by  $\epsilon_{\max}$ . This can be imagined as a distinct region in phase space. Within this domain, particles follow an elliptical trajectory, defined by the coordinates  $(x_{\max}, x_p^{\max})$ . The size and shape of the beam are described by the Twiss parameters.  $\beta$  is related to the size of the beam by

$$d = \sqrt{\epsilon_{\max} \beta_{\max}} \quad (3.4)$$

where  $\beta_{\max}$  is the maximum extent of the transverse  $\beta$ . When there is no dispersion ( $\eta = 0$ ), and  $\beta$  reaches its maximum value, the beam achieves its largest transverse size for the same emittance.

The maximum accepted transverse emittance in the accelerator is called the transverse acceptance. As illustrated in Fig. 3.4, the transverse acceptance is defined as:

$$A_T = \epsilon_{\max} = \frac{d^2}{\beta_{\max}}. \quad (3.5)$$

Eq. 3.2 describes the beam phase space expected to be accepted at the injection region at the entrance of the CEBAF-NL. To determine the acceptance, the  $\beta$  function value at the entrance of the CEBAF-NL during injection is considered. The

average  $\beta$  value at the injection point measures  $\beta_x=18$  m. Given an accelerating cavity aperture of 35 mm, the radius is  $d = 17.5$  mm. The resulting transverse acceptance for the first pass at the injection becomes

$$A_T = \frac{(17.5)^2}{18 \times 10^3} = 18 \text{ mm} \cdot \text{mrad}. \quad (3.6)$$

This estimate may seem simplistic because there are other magnets in the CEBAF-NL, such as focusing and defocusing quadrupoles, and those cause chromatic effects. These magnets can influence the acceptance. The following will explain how to calculate the normalized transverse emittance using the maximum geometric transverse emittance  $\epsilon_{\max}$ .

$$\epsilon_N = \gamma \epsilon_{\max} \quad (3.7)$$

$$\epsilon_N = \gamma A_T \quad (3.8)$$

The beam energy at the injection region is  $E=123$  MeV, and the Lorentz factor  $\gamma = 240$ , which leads to a normalized transverse emittance

$$\epsilon_N = 4.3 \text{ mm} \cdot \text{rad} \quad (3.9)$$

To estimate the beam size at the injection region

$$\sigma_x = \sqrt{\epsilon_{\max} \beta_x} = 0.018 \text{ m}. \quad (3.10)$$

To predict the  $\beta$ -value at the exit of the CEBAF-NL, the matrix formalism is used. The transfer matrix of the CEBAF-NL needs to be defined. The linear differential matrix of a LinAc when the Rosenzweig and Serafini (R-S) model is applied, is given by [64]

$$\begin{bmatrix} T_{11} & T_{12} \\ T_{21} & T_{22} \end{bmatrix} \quad (3.11)$$

where

$$T_{11} = \cos \tau - \sqrt{2} \cos \phi \sin \phi \quad (3.12)$$

$$T_{12} = \sqrt{8} \frac{\gamma_i}{\gamma_f} \cos \phi \sin \tau \quad (3.13)$$

$$T_{21} = -\frac{\gamma'}{\gamma_f} \left[ \frac{\cos \phi}{\sqrt{2}} - \frac{1}{\sqrt{8} \cos \phi} \right] \quad (3.14)$$

$$T_{22} = \frac{\gamma_i}{\gamma_f} \left[ \cos \tau + \sqrt{2} \cos \phi \sin \tau \right] \quad (3.15)$$

with  $\tau = \log(\gamma_f/\gamma_i)/\sqrt{8} \cos \phi$ ,  $\gamma_f = \gamma_i + \gamma' L$  is the final lorentz factor ( $L$  is the LinAc section length),  $\gamma' = eV_0 \cos \phi / m_e c^2$  is the normalized energy gradient in the LinAc,  $V_0$  is the maximum accelerating gradient, and  $m_e$  is the electron mass. The Twiss transport of the beam along the LinAc can be described by

$$\begin{bmatrix} \beta_{xE} \\ \alpha_{xE} \\ \gamma_{xE} \end{bmatrix} = T \begin{bmatrix} \beta_{xi} \\ \alpha_{xi} \\ \gamma_{xi} \end{bmatrix} \quad (3.16)$$

where  $\beta_{xE}$ ,  $\alpha_{xE}$  and  $\gamma_{xE}$  are the Twiss parameters at the extraction region (LinAc exit), and  $\beta_{xi}$ ,  $\alpha_{xi}$  and  $\gamma_{xi}$  are the Twiss parameters at the injection region (LinAc entrance).

The CEBAF transverse geometrical emittance of the electron beam has been measured at the exit of the injection chicane to be [63]

$$\epsilon_x = 2.5 \text{ nm} \cdot \text{rad} \quad (3.17)$$

$$\epsilon_y = 1.9 \text{ nm} \cdot \text{rad} \quad (3.18)$$

At the LinAc exit, the beam transitions through the first Arc (Arc 1) see Fig. 3.1. The transverse emittance, measured as  $\epsilon_x=0.43 \text{ nm} \cdot \text{rad}$ , indicates an emittance reduction by a factor of approximately eight, given by  $\epsilon_{chicane}/\epsilon_{Arc\ 1} = 8$ . Using Eq. 3.16, the maximum value of the beta function at the CEBAF-NL end can be estimated. Given the parameters  $\phi = 0$ ,  $f = 1497 \text{ MHz}$ , and  $\omega = 2\pi f$ , Eq. 3.16 can be represented in the Twiss matrix form

$$\begin{bmatrix} \beta_E \\ \alpha_E \\ \gamma_E \end{bmatrix} = T' \begin{bmatrix} \beta_i \\ \alpha_i \\ \gamma_i \end{bmatrix} \quad (3.19)$$

where

$$T' = \begin{bmatrix} C^2 & -2CS & S^2 \\ -CC' & SC' + S'C & -SS' \\ C'^2 & -2S'C' & S'^2 \end{bmatrix} \quad (3.20)$$

knowing that

$$\begin{bmatrix} C & S \\ C' & S' \end{bmatrix} = \begin{bmatrix} -0.69 & 4.17 \\ -0.02 & 0.15 \end{bmatrix}. \quad (3.21)$$

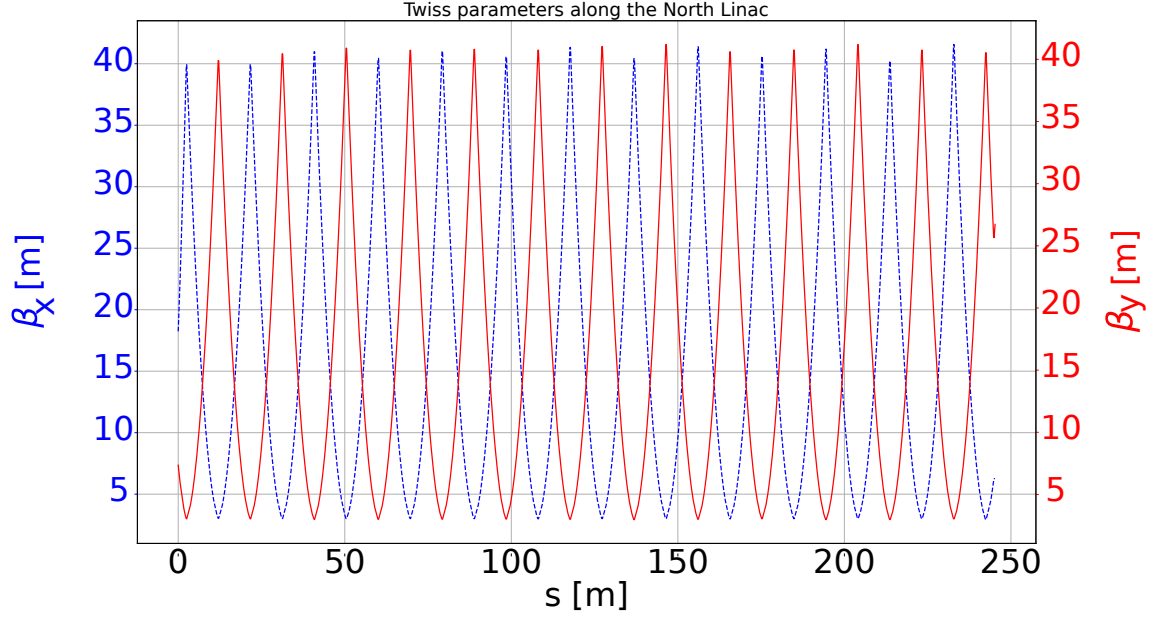
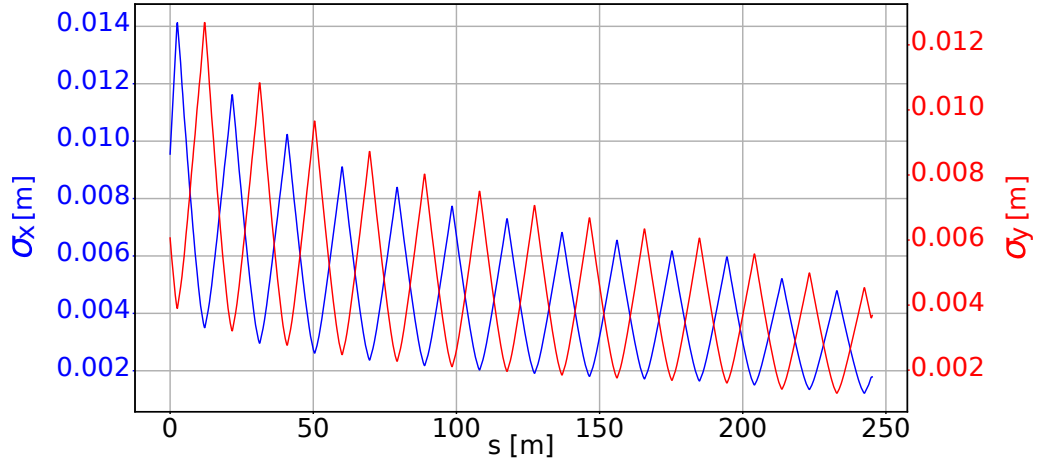
At the CEBAF-NL exit, the value is given by  $\beta_E=6.3 \text{ m}$ . With 9.6 m quadrupole channels between the cryomodules in the CEBAF-NL, the Twiss parameters exhibit periodic behavior. Using the same emittance reduction throughout the CEBAF-NL, the beam size at the extraction region can be estimated as

$$\sigma_{xE} = \sqrt{\beta_E \frac{A_T}{8}} = 3 \text{ mm}. \quad (3.22)$$

In Fig. 3.5, the maximum  $\beta$ -function for the CEBAF-NL is around 40 m. Using an initial setting of  $\beta_x=18 \text{ m}$ , the  $\beta$ -function remains energy-independent and retains its periodicity across the CEBAF-NL, facilitating a consistent decline in electron emittance. Considering the calculated geometrical transverse emittance and the standard beta injection value at CEBAF  $\beta_x=18 \text{ m}$ , the beam size, denoted as  $\sigma_{x,y}$  decreases. This decrease occurs as the  $\beta_{max}$  stays steady and the geometric emittance shrinks while the beam progresses through the CEBAF-NL.

As illustrated in Fig. 3.6, the beam size at the CEBAF-NL entrance corresponds to the estimated injection value of  $\sigma_x=0.018 \text{ m}$  (Eq. 3.10), considering the peak emittance in the injection region. This suggests that by selecting the appropriate value for  $\beta$ , the CEBAF-NL maintains its periodicity. This consistent periodicity facilitates continuous control of the beam size, ultimately reducing it to 3 mm at the LinAc exit.

These findings indicate that when the beam is injected with a value of  $\beta_x=18 \text{ m}$ , the beam size reduces effectively. This value aligns with the estimated acceptance


 Figure 3.5:  $\beta$  functions along the CEBAF-NL.

 Figure 3.6: Variation of the beam size  $\sigma_{x,y}$  along the CEBAF-NL, accelerating the beam from 123 MeV to approximately 1090 MeV.

of the CEBAF-NL. By injecting the beam with this calculated maximum transverse emittance, no losses are observed along the LinAc. These calculations are corroborated by simulations using ELEGANT. However, a more accurate measurement of this acceptance is strongly recommended.

For estimating the required bunch length at the injection region, it is important to note that the CEBAF-NL operates at 1497 MHz. Consequently, the energy spread depends on bunchlength. This necessitates determining the maximum acceptable bunch length. As previously mentioned, the energy spread required at the first ARC

is approximately  $10^{-3}$ :

$$\frac{E - E_0}{E_0} \leq \pm 10^{-3} \quad (3.23)$$

$$|\omega\sigma_t| \leq 1 - 10^{-3} \quad (3.24)$$

$$\sigma_t \leq \frac{0.99}{2\pi f} \quad (3.25)$$

$$\sigma_t \leq 4ps \quad (3.26)$$

when a beam is injected with a bunch length of  $\sigma_t \leq 4$  ps, it ensures the beam acceleration at the highest energy gradient.

Another constraint which must be applied is the ratio of the injection energy to the LinAc energy. Changing this ratio necessitates changing the optics of the spreaders and recombiners, and impacts the transport of the beam throughout the machine (See Eq. 3.1)

where  $E_i$  and  $E_L$  are the injector and the LinAc energy, respectively, To achieve the 12.1 GeV condition, the CEBAF-NL provides acceleration to 1090 MeV, then the injection energy according to Eq. 3.1 must be  $E_i = 123$  MeV.

Summarizing the requirements for  $e^-$  the following beam parameter limits have been identified:

Parameters	Unit	Value
Injection momentum	MeV/c	123
Injection transverse size $\sigma_x$	m	0.018
Injection geometric emittance $\epsilon_x$	mm·mrad	18
Injection Normalized emittance $\epsilon_{xN}$	mm·rad	4.3
Bunch length $\sigma_t$	ps	$\leq 4$
Energy dispersion	%	$\pm \leq 1$

Those parameters are the design requirements for a CW positron source at CEBAF.

### 3.3 $Ce^+BAF$

In the earlier section, different positron sources of existing and upcoming facilities were described, along with a discussion on their characteristics and limitations. The unique and demanding requirements of this project were also highlighted, emphasizing the development of a CW positron injector at CEBAF. A proposed solution for positron injection at Jefferson Lab is described, involving the utilization of the Low Energy Research Facility (LERF) for positron ( $e^+$ ) generation, described here.

The combination of LERF and CEBAF offers an advantage. This approach allow reusing the experimental building and staging the available apparatus there for continuous positron generation.

The LERF acts as an introductory phase of the positron injector with a design specifically adapted for sustained positron production. This facility comprises an polarized electron gun, a dedicated positron source, and a transport system that optimizes  $e^+$  beam quality. LERF distinct features facilitate the production of powerful, uninterrupted positron beams.

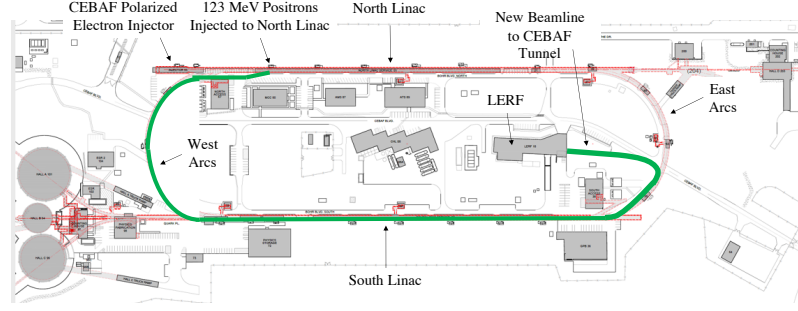


Figure 3.7: Schematic Layout: Linking LERF and CEBAF Accelerators for High-Energy Positron Beam Acceleration [12]

Fig. 3.7 presents the idea of linking LERF to the CEBAF accelerator, emphasizing the addition of a new 123 MeV transport beamline. This transport beamline acts as a bridge, from LERF to CEBAF. In the diagram, the green line symbolizes this transport beamline, underscoring its role in the smooth transport and acceleration of positron beams within the combined system.

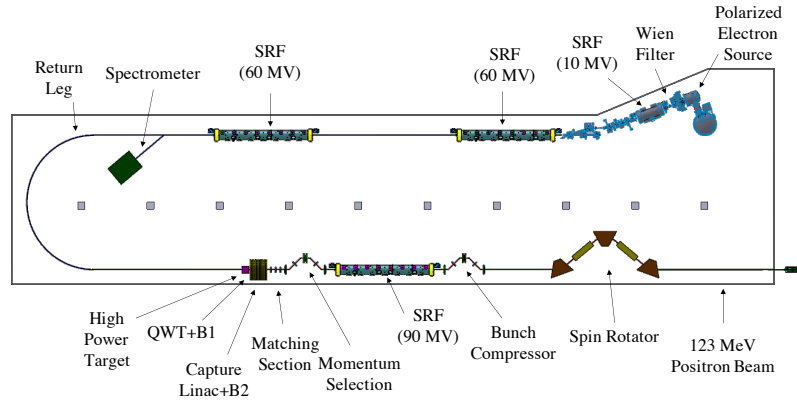


Figure 3.8: Layout of Polarized Electron and Positron Injectors at LERF [12].

Key components of the LERF injector include the superconducting quarter cryomodule, collection system, polarized electron source, Wien spin rotator, buncher cavity, electron gun, accelerating SRF cryomodules, positron source, and the dedicated positron transport line leading to the CEBAF injection region.

### 3.3.1 Electron injector

The LERF injector design is similar to that of the CEBAF injector. It begins with a polarized electron source, then progresses to a Wien spin rotator, and is equipped with a buncher cavity for longitudinal alignment with the 10 MV SRF.

Central to the LERF injector is the superconducting cryomodule. Operating at 1497 MHz, this section can boost 10 mA CW  $e^-$  beams up to 9 MeV/c.

Downstream of the SRF section, a three-dipole magnet chicane injects the electron beam into the first of two full-length accelerating SRF cryomodules, each with a capacity of 60 MV. The LERF electron gun, which needs to be designed and built, is intended to operate within the 300-350 kV range. It represents an up-scaled version of the 130 keV gun used at CEBAF, with specific modifications to accommodate the

demanding requirements of higher beam current ( $\geq 1$  mA) and bunch charge ( $\geq 2$  pC) essential for efficient positron generation.

In the LERF injector, it is planned specific measures to ensure beam quality, especially with higher bunch charges. Minimizing the distance between the gun and the initial accelerating component helps reduce space charge effects that might disrupt bunching. It is particularly crucial to limit bunch lengthening, primarily occurring at the shorter distance, by controlling the beam voltage. The electron bunch is also compressed from 40 ps to about 2 ps within a short distance before it enters the SRF quarter cryomodule.

The final section of the electron injector matches the Twiss parameters into the acceptance of the two CEBAF-style cryomodules, which boost the beam to 123 MeV.

### 3.3.2 Positron source

Building upon the discussions from previous section, this section describes the formation of  $e^+$  beams before being transported to the CEBAF accelerator.

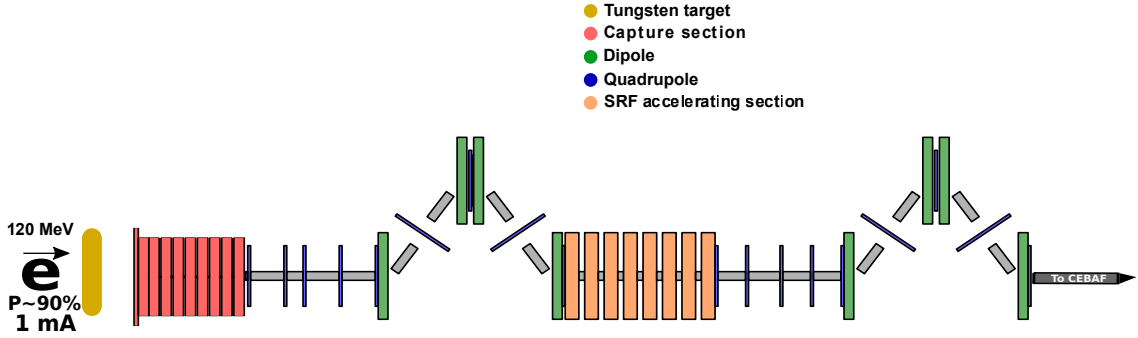


Figure 3.9: Optimization of Positron Generation from Electron-Target Interaction: Towards Polarized and Unpolarized Positron Beams at CEBAF [13].

The LERF positron injector has been designed to deliver a sufficient number of positrons to the CEBAF, while also ensuring the proper match and beam parameters required for positron injection at the CEBAF-NL. A crucial positron injector component is the positron collection system, which uses high magnetic field lenses [65] to mitigate the significant transverse angular divergence at the exit face of the  $e^+/e^-$  production target.

Figure. 3.9 illustrates the conceptual layout of the injector. Initially, a CW  $e^-$  beam of 120 MeV and a 1 mA interacts with a rotating tungsten target (W), generating polarized  $\bar{\gamma}$  and polarized  $e^+/e^-$  in the same target. A four-quadrupole matching section and a magnetic chicane further refine the positron population central momentum and desired spread of allowable momenta. Subsequently, a decelerating/accelerating section (DeAc) reduces the momentum dispersion. A chirping cavity is employed to correlate the momentum dispersion with the positron time-of-flight to ensure precise synchronization. A second chicane then compress the positron bunch length, matching it with the CEBAF injection acceptance. The maximum acceptance for the bunch length is determined to be 4 ps, and the design strategy is to further minimize it through the implementation of compression techniques. The comprehensive layout and compression techniques, which will be

detailed in chapters 5 and 6, are designed to deliver a highly optimized and well-controlled positron beam for injection into CEBAF.

### 3.3.3 Spin rotator

Experiments at CEBAF often require specific longitudinal or transverse spin polarizations at the target. CEBAF employs a  $4\pi$  spin rotator comprising two Wien filters with solenoid magnets in between to control the final spin polarization at the experiment [66]. This setup works well for lower energies ( $\leq 30$  KeV) for modest field strengths. However, for positron beam production at the LERF with energies  $\geq 1$  MeV, it becomes impractical.

For CEBAF, a higher energy spin rotator concept is under study. The scheme, consists of alternated dipole and solenoid fields. Due to the small anomalous gyromagnetic factor of positrons (or electrons), the spin rotation is more effective in the solenoids at lower energies. However, the dipole magnetic field is necessary to establish the desired spin rotation axis. By rotating the spin around the longitudinal solenoid and radial dipole fields, this spin rotator enables a net spin rotation around the vertical axis in the horizontal plane. Importantly, the dipole fields are arranged to have a net zero bending angle, preserving the beam trajectory and minimizing orbit perturbations.

### 3.3.4 Transport line

Once the 123 MeV CW positron beam is formed and its spin is oriented, it is ready for acceleration to higher energies. A new tunnel connects the east side of LERF to the southeast corner of CEBAF, near the entrance of the South LinAc.

The beamline uses a double-bend achromat (DBA) in order to minimize the dispersion and therefore allows for transporting a high momentum spread beam. This ensures the beam aligns with the elevation of the CEBAF South LinAc tunnel, near the ceiling.

The beam is carried through a lengthy FODO channel fixed to the South LinAc ceiling, leading it to CEBAF west side. Here, it makes a 180-degree turn using a Double Bend Achromat (DBA)-like structure that has minimal dispersion. Once the transport line concludes, a combination of a vertical achromat translator and horizontal bending magnets directs the beam to the start of the CEBAF-NL for injection. Each beamline also features a dedicated Twiss matching section. This beamline is primarily designed to accommodate a 123 MeV/c positron beam. The CEBAF accelerator limits the maximum transverse emittance that can be transported due to reduced acceptance at the extraction corners. It is estimated that a normalized emittance of 4.3 mm-rad can be injected at the front of the CEBAF-NL. Regarding longitudinal acceptance, the optics configuration for the first two recirculation arcs (east and west sides) to feature smaller dispersion functions and easily tunable momentum dispersion. This modified optics, is expected to allow injection of up to  $\Delta p/p_0 = \pm 1\%$  at the front of the CEBAF-NL and transport a beam with a longitudinal bunch length of approximately  $\sigma_t \leq 4\text{ps}$ .



# Chapter 4

## Positron production optimization

The production of positron beams at CEBAF relies on the interaction of a polarized electron beam with a high  $Z$  target [13]. This method has been chosen for its ability to efficiently transfer the polarization of the initial electron beam to the secondary positron beam [14]. The process consists of two separate steps. Initially, photons are emitted via bremsstrahlung radiation caused by the electron beam. Thereafter,  $e^+e^-$  pairs form from these generated photons.

The present study focuses on optimizing the two-step production process, specifically for a single-target scheme, intending to generate polarized and unpolarized positron beams. The following sections show the fundamentals of polarized bremsstrahlung and pair creation processes, particularly examining their angular distributions. Subsequent sections focus on the effects of thick targets and the parameters used to characterize positron production. An optimization procedure is then proposed and applied using electron beam kinetic energies of 120 MeV and 1 GeV.

### 4.1 Polarized Bremsstrahlung

#### 4.1.1 Cross section

The bremsstrahlung process, which involves the emission of a photon during the scattering of an electron from a nucleus, is generally well understood. However, previous experimental and theoretical comparisons [67] have focused on the emitted photons alone, overlooking the decelerated outgoing electrons. This approach results in integrated results across all electron scattering angles, leading to the loss of important characteristics and weakening the validity of the theoretical work.

The positron source at CEBAF aims to adopt the conventional positron generation technique inspired by the findings of the PEPPo experiment. This method involves the generation of both unpolarized and polarized photons through the bremsstrahlung process, using either unpolarized or polarized electrons, and is examined using the ultrarelativistic approach developed by Y.S. Tsai [68]. This approach aligns with previous calculations by H. Olsen and L.C. Maximon [69].

The bremsstrahlung radiation emitted by a lepton beam interacting with a nucleus can be described by the energy-angle distribution given by Equation (4.1),

where  $l = (E \sin(\theta_k)/m_e)^2$  represents the angular dependency,  $E$  the lepton energy of the distribution and  $y = k/E$  is the photon energy fraction [68].

$$\frac{d\sigma_b}{dk d\Omega_k} = A_0 \left[ \frac{2y-2}{(1+l)^2} + \frac{12l(1-y)}{(1+l)^4} \right] + A_1 \left[ \frac{2-2y+y^2}{(1+l)^2} - \frac{4l(1-y)}{(1+l)^4} \right] \quad (4.1)$$

The terms  $A_0$  and  $A_1$  in Equation (4.1) are related to the nuclear and electronic contributions to the cross-section and screening effects. The angular distribution can be expressed as

$$\frac{d\sigma_b}{dk d\theta_k} = 2\pi \sin(\theta_k) \frac{d\sigma_b}{dk d\Omega_k}, \quad (4.2)$$

which is maximum at an angle  $\theta_{max}$  approximately given by  $\frac{1}{2}m_e/E$ .

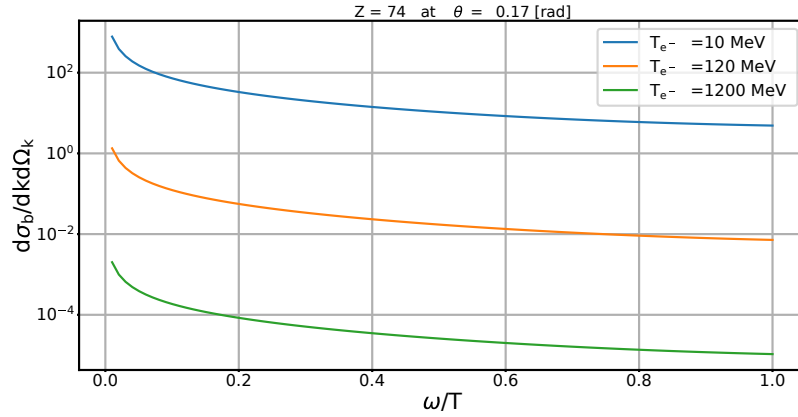


Figure 4.1: Bremsstrahlung differential cross-section  $\frac{d\sigma_b}{dk, d\Omega_k}$  for different electron energies in tungsten at a photon emission angle  $\theta = 0.17$  rad

The optimal angle  $x$  denoted as  $\theta_x$  is determined when the energy-angle differential cross section at this angle is a fraction  $1 - x$  of the maximum value  $\theta_{max}$ . The right panel of Figure 4.2 illustrates how  $\theta_x$  varies with photon momentum. This variation is relatively independent of the photon momentum, yet highly sensitive to the parameter  $x$ . For instance, at 100 MeV, a 1.5-degree cone encompasses 90

#### 4.1.2 Polarized cross-section

The bremsstrahlung radiation of a polarized electron beam is one one additional mechanism for the production of circularly polarized photons [69].

The usual description of polarization is based on the density matrix using Stokes parameters, which allows to write the ordinary polarization cross sections in matrix form [70]. The transfer of electron beam polarization to photons generated in the bremsstrahlung process can be described by the following matrix equation:

$$\begin{pmatrix} I \\ P_1 \\ P_2 \\ P_3 \end{pmatrix} = T_{Brem}^\gamma \begin{pmatrix} 1 \\ S_1 \\ S_2 \\ S_3 \end{pmatrix} \quad (4.3)$$

where  $I$  represents the unpolarized cross section,  $S_i$  are the electron polarization components, and  $P_i$  are the photon polarization components.

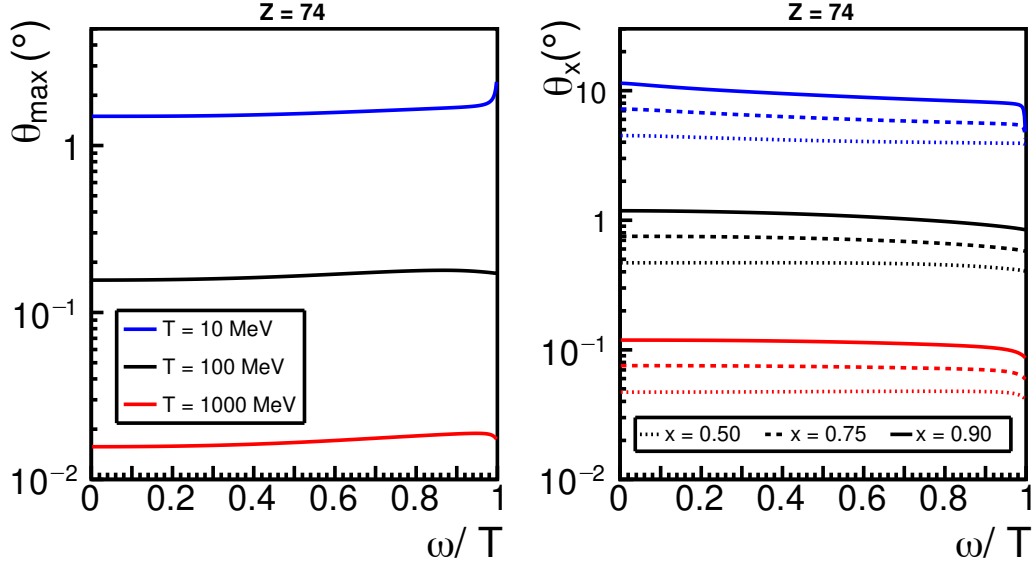


Figure 4.2: Angular distribution of the bremsstrahlung differential cross section for different electron beam energies: photon energy fraction dependency of the angle corresponding to the maximum cross-section (left) and of the optimum angle corresponding to the  $1-x$  fraction of the maximum cross-section (right) [14].

- $S_1$  : transverse polarization in the plane of interaction along the  $x$ -axis;
- $S_2$  : polarization component perpendicular to the interaction plane ( $y$ -axis);
- $S_3$  : longitudinal polarization along  $z$ -axis;
- $P_1$  : linear polarization with respect to  $x$ -axis;
- $P_2$  : linear polarization with respect to the axis oriented at  $45^\circ$  to the right of the  $x$ - and  $y$ -axis;
- $P_3$  : right circular polarization.

The coefficients  $I_0$ ,  $D$ ,  $T$ , and  $L$  in the matrix equation are given by the equations:

$$I_0 = (E_1^2 + E_2^2)(3 + 2\Gamma) - 2E_1E_2(1 + 4u^2\epsilon^2\Gamma) \quad (4.4)$$

$$D = 8E_1E_2u^2\epsilon^2\Gamma/I_0 \quad (4.5)$$

$$T = -kE_2\epsilon(1 - 2\epsilon)u\Gamma/I_0 \quad (4.6)$$

$$L = k[(E_1 + E_2)(3 + 2\Gamma)] - 2E_2(1 + 4u^2\epsilon^2\Gamma)]/I_0 \quad (4.7)$$

Here,  $\Gamma$  includes the Coulomb and screening effects,  $\epsilon$  is the photon energy fraction ( $\omega/E$ ),  $E_1$  and  $E_2$  are the total initial and final electron energies,  $k$  is the photon energy,  $u$  is a variable related to the scattering angle, and  $\Gamma$  describes the Coulomb and screening corrections.

The matrix  $T_{Brem}^\gamma$  is given by:

$$T_{Brem}^\gamma = \begin{pmatrix} I_0 & 0 & 0 & 0 \\ D & 0 & 0 & 0 \\ 0 & 0 & 0 & 0 \\ 0 & -T & 0 & -L \end{pmatrix} \quad (4.8)$$

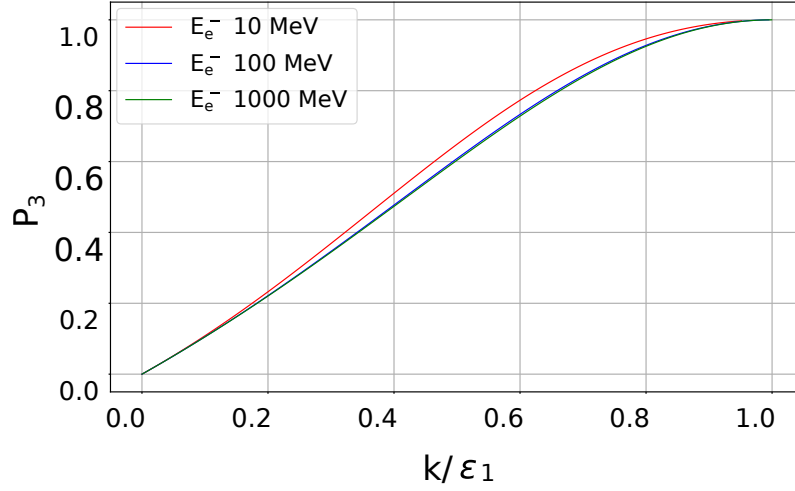


Figure 4.3: Circular polarization of bremsstrahlung for electron beam energies: red (10 MeV), blue (100 MeV), green (1000 MeV) with 100% longitudinal polarization.

From the matrix equation, the Stokes vector of the emitted photon can be expressed as:

$$\begin{pmatrix} I \\ P_1 \\ P_2 \\ P_3 \end{pmatrix} = \begin{pmatrix} 1 \\ D \\ 0 \\ -S_1 T - S_3 L \end{pmatrix} \quad (4.9)$$

This indicates bremsstrahlung radiation generated by an polarized electron beam is partially polarized perpendicular to the interaction plane. However, to obtain a circularly polarized photon beam, both the transverse and longitudinal components of the incoming polarized electron beam may be transferred. Figure 4.3 illustrates the circular polarization of the emitted photons, demonstrating that the circular polarization increases with photon energy.

## 4.2 Pair-creation

### 4.2.1 Unpolarized cross-section

Producing positrons from primary electrons involves combining bremsstrahlung and pair creation processes in a single or multiple target system. In a single-target production scheme, the thickness of the targets can be optimized to improve performance.

Due to generating a lepton pair, the cross-section (Fig. 4.4) is flat. In the case of thick targets, multiple scattering effects dominate the angular distribution of the secondary particles and result in significant transverse momentum. Fig. 4.5 shows the energy-dependent of a multiple scattering spread of an electron/positron distribution influenced by multiple scattering for different thicknesses of tungsten material. Multiple scattering effects cause low-energy particles to be spread over a wide angular range while high-energy particles remain within a relatively narrow angular domain.

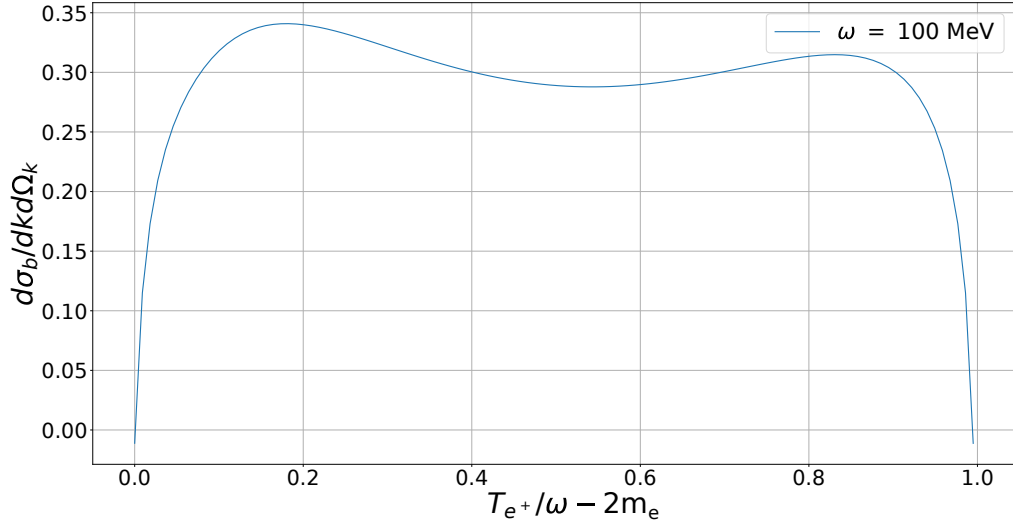


Figure 4.4: Pair-creation cross-section for 100 MeV photon energy within a tungsten material.

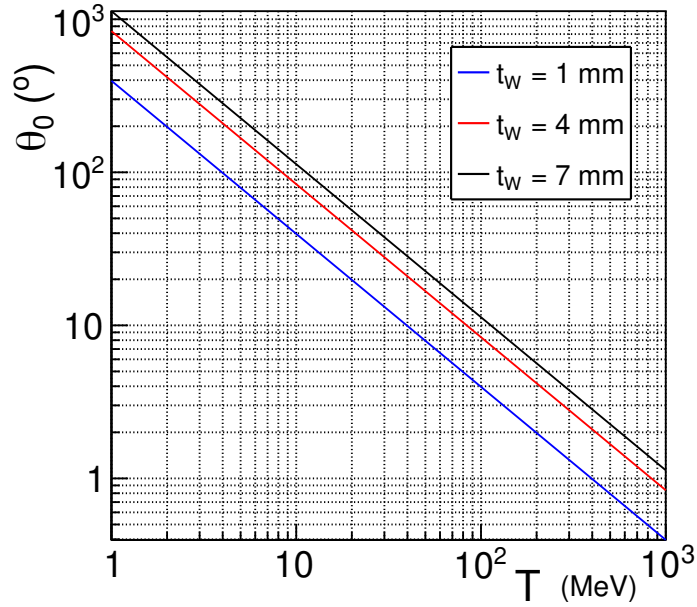


Figure 4.5: Multiple scattering spread of electron/positron distribution as a function of energy, for various tungsten thicknesses.

### 4.2.2 Polarization Transfer

The pair creation process generates longitudinally polarized positrons, depending on the polarization of the incident photons. It enables the transfer of circular polarization from photons to  $e^+e^-$  pairs when the photon energy exceeds 1.022 MeV. By employing the same polarization framework discussed earlier and recognizing the reciprocal nature of the pair creation and Bremsstrahlung reactions, we can express it as follows:

$$E_2^{Beam} = -E_2^{Pair} \quad (4.10)$$

Hence, the bremsstrahlung radiation  $k_B = E_1 - E_2$  undergoes a transformation to  $k_{pair} = E_1 + E_2$ . By substituting the previous formula into Stokes parameters [70], we obtain the following expression for the pair production process:

$$I_0 = (E_1^2 + E_2^2)(3 + 2\Gamma) + 2E_1E_2(1 + 4u^2\epsilon^2\Gamma) \quad (4.11)$$

$$D = 8E_1E_2u^2\epsilon^2\Gamma/I_0 \quad (4.12)$$

$$T = -kE_2\epsilon(1 - 2\epsilon)u\Gamma/I_0 \quad (4.13)$$

$$L = k[(E_1 - E_2)(3 + 2\Gamma)] + 2E_2(1 + 4u^2\epsilon^2\Gamma)/I_0 \quad (4.14)$$

By using the transfer matrix of the pair creation process, we can apply the following transformation:

$$\begin{pmatrix} I \\ S_1 \\ S_2 \\ S_3 \end{pmatrix} = T_{Pair}^e \begin{pmatrix} 1 \\ P_1 \\ P_2 \\ P_3 \end{pmatrix} \quad (4.15)$$

And:

$$T_{Pair}^e = \begin{pmatrix} 1 & D & 0 & 0 \\ 0 & 0 & 0 & T \\ 0 & 0 & 0 & 0 \\ 0 & 0 & 0 & L \end{pmatrix} \quad (4.16)$$

The Stokes vector for the emitted positron-electron ( $e^+e^-$ ) pair is determined as follows:

$$\begin{pmatrix} I \\ S_1 \\ S_2 \\ S_3 \end{pmatrix} = \begin{pmatrix} 1 \\ P_3T \\ 0 \\ P_3L \end{pmatrix} \quad (4.17)$$

This equation reveals that only the circular polarization of photons ( $P_3$ ) is transferred to the positron-electron ( $e^+e^-$ ) pairs. The pairs resulting polarization will consist of transverse ( $S_1$ ) and longitudinal ( $S_3$ ) components.

The outcomes of the polarization transfer during the pair creation process are illustrated in the figure

As depicted in Fig. 4.6, significant polarization degrees are observed at both ends of the positron energy spectra. Furthermore, there is a correlation with the photon energy, as higher photon energies correspond to increased maximum positron polarization.

### 4.3 Characteristic parameters of positron production

In a single target production scheme, the efficiency of generating secondary positrons is a key parameter. This efficiency  $\varepsilon \equiv \varepsilon(p, \theta, \phi)$  measures the number of positrons  $N_p(p, \theta, \phi)$  at a specific momentum  $p$  and spherical angle  $(\theta, \phi)$  relative to the incident number of electrons ( $N_{e^-}$ ). It can be expressed as

$$\varepsilon(p, \theta, \phi) = \frac{N_p(p, \theta, \phi)}{N_e}. \quad (4.18)$$

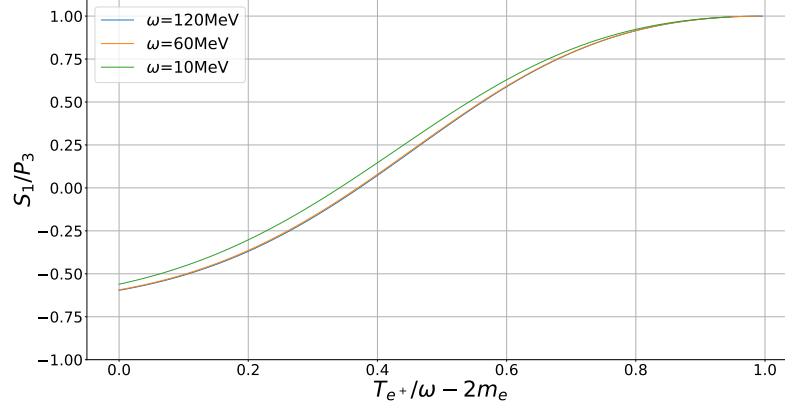


Figure 4.6: Polarization transfer in Pair creation process for various initial photon energies.

The positron yield is calculated as the following:

$$N_p(p, \Delta p, \Delta\theta) = N_e \int_{p-\Delta p}^{p+\Delta p} d\xi \int_0^{\Delta\theta} d\theta \int_0^{2\pi} d\phi \frac{d\varepsilon(\xi, \theta, \phi)}{d\xi d\theta d\phi}. \quad (4.19)$$

The positron yield is determined by considering the effective fixed (0.6 MeV) or variable (0.05p) momentum acceptance represented by  $\Delta p$  and the corresponding  $\Delta\theta$ . On the other hand, the performance of a polarized source is better defined using the Figure-of-Merit (*FoM*), which considers both the efficiency and the average particle polarization ( $S_3$ ). The expression for the Figure-of-Merit is given by

$$FoM = FoM(p) = \epsilon(p) P_3^2. \quad (4.20)$$

$$FoM(p, \Delta p, \Delta\theta) = \frac{N_p(p, \Delta p, \Delta\theta)}{N_e} \langle S_3^2 \rangle = \int_{p-\Delta p}^{p+\Delta p} d\xi \int_0^{\Delta\theta} d\theta \int_0^{2\pi} d\phi \frac{d\varepsilon(p, \theta, \phi)}{d\xi d\theta d\phi} S_3^2(p, \theta, \phi). \quad (4.21)$$

where  $p$  represents the momentum.

The bremsstrahlung and pair creation processes combine within a single target to generate a positron flux. Low-energy positrons are more likely to escape the target material than high-energy positrons since the latter have a higher probability of being involved in the electromagnetic shower. Consequently, the flux of secondary particles exhibits a maximum at a specific low positron energy.

In the left panel of Fig. 4.7, the momentum distribution of the positron production efficiency is shown for a 120 MeV polarized electron beam interacting with a 4 mm thick tungsten target. The distribution is restricted to positrons emitted within a  $10^\circ$  cone angle, representing a collection system angular acceptance. The maximum value observed in the distribution determines the energy range of the positrons that can be effectively collected.

The Figure-of-Merit, as shown in the right panel of Fig. 4.7, follows a similar trend but with a shift in the positron momentum at the maximum. This shift is a consequence of the energy dependence of the positron polarization. An important observation can be made: using a variable bin width results in a different effect than

a constant bin width. The variable bin width was introduced to mimic the impact of a magnetic collection system on the positron yield. This change in bin width is related to the momentum with which the system accepts the positrons. Specifically in that example the system accepts positron momentum within a range of  $\pm 5\%$ . This variation significantly distorts the energy distribution compared to the constant bin width. Furthermore, it indicates that optimal efficiency and Figure-of-Merit are achieved at different positron momenta.

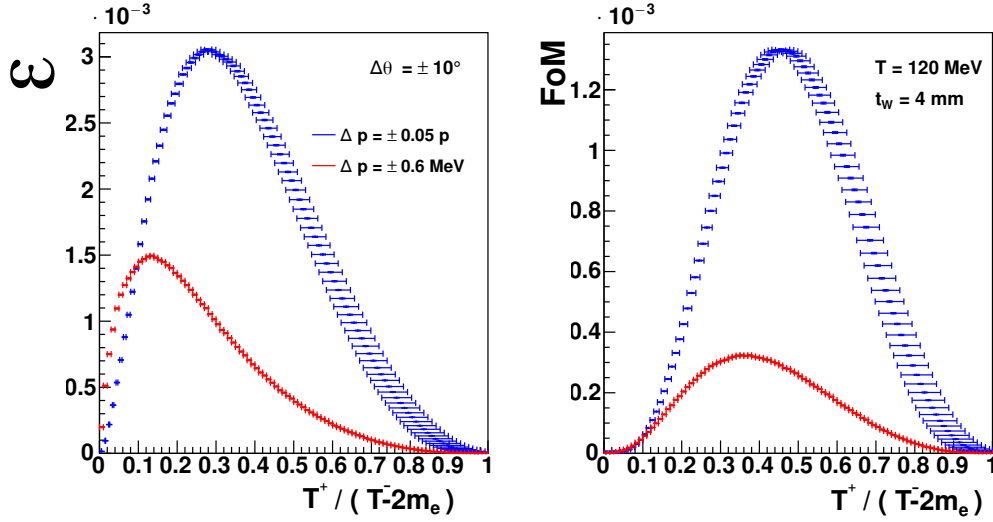


Figure 4.7: Energy dependence of positron production efficiency (left) and Figure-of-Merit (right) for a 120 MeV polarized electron beam interacting with a 4 mm thick tungsten target. The curves of different colors demonstrate the influence of energy binning on the shape of the distributions, as defined in Eq. 4.21.

Fig. 4.8 introduces the challenges associated with the high transverse momentum at the target exit. A notable feature is the positron transverse angular divergence at the target exit. This high transverse momentum spread poses challenges in designing an efficient collection system for the positrons. The sizeable transverse angular divergence makes it more difficult to accurately collect and manipulate the positrons, requiring careful consideration in the design of the collection device.

The goal of the optimization is to determine the target thickness that maximizes the positron production efficiency ( $\epsilon$ ) and Figure-of-Merit (FoM) for a given incident electron beam energy and target  $Z$ .

Extensive GEANT4 simulations are performed, considering a pencil beam of electrons and investigating the positron yield and Figure-of-Merit for different momentum and angular acceptances of the collection system. For the unpolarized mode, the following quantities are associated with the maximum efficiency ( $\epsilon_{max}$ ):

- $\epsilon_{max}$ : the maximum positron production efficiency
- $\text{FoM}_\epsilon$ : the Figure-of-Merit at  $\epsilon_{max}$



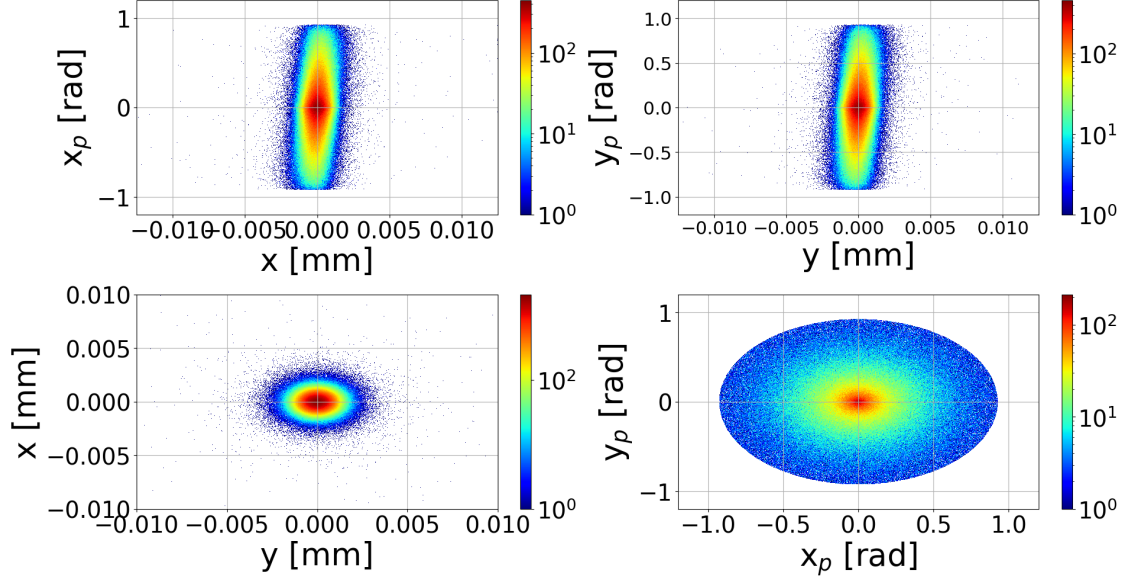


Figure 4.8: Positron transverse phase space created using 120 MeV longitudinally polarized electron beam on a 4 mm tungsten target, illustrating the positron transverse phase space at the exit of a 4 mm tungsten target when using a longitudinally polarized 120 MeV electron beam. The figure top left and right sections display the positron transverse space in the  $x$  and  $y$  directions, respectively. The correlation between the axis ( $x, y$ ) and ( $x_p = \frac{p_x}{p_z}$  and  $y_p = \frac{p_y}{p_z}$ ) is shown in the bottom left and right sections.

- $p_\varepsilon$ : the positron momentum at  $\varepsilon_{max}$
- $P_\varepsilon$ : the longitudinal polarization of positrons at  $\varepsilon_{max}$

Similarly, for the polarized mode, the following quantities are associated with the maximum Figure-of-Merit ( $FoM_{max}$ ):

- $FoM_{max}$ : the maximum Figure-of-Merit
- $\varepsilon_{FoM}$ : the positron production efficiency at  $FoM_{max}$
- $p_{FoM}$ : the positron momentum at  $FoM_{max}$
- $P_{FoM}$ : the longitudinal polarization of positrons at  $FoM_{max}$

These parameters are determined from the energy distribution spectra of efficiency, average longitudinal polarization, and Figure-of-Merit.

The obtained parameters are reported in Tab. 4.1 and Tab. 4.2, including statistical and systematic uncertainties.

When compared, the optimized unpolarized and polarized modes show clear differences. These differences matter less as the angle of acceptance grows. At larger angles, more low-energy positrons are accepted because of scattering effects, making the system most efficient at low energies where there's a small polarization.

On the other hand, the Figure-of-Merit maximizes at higher positron energy due to the energy dependence of positron polarization. Reducing the angular acceptance,

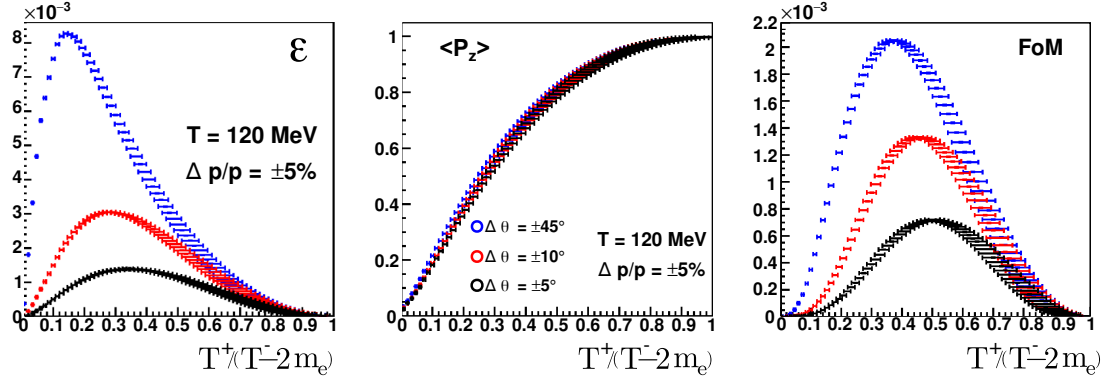


Figure 4.9: Comparison of positron energy distributions: production efficiency (left), average longitudinal polarization (middle), and FoM (right) for 120 MeV incident electrons on a 4 mm thick tungsten target, for different angular acceptances in the positron collection system with a fixed  $\pm 5\%$  positron momentum acceptance.

$\Delta\theta$ ( $^\circ$ )	$\varepsilon_{max}$ ( $\times 10^{-3}$ )	$p_\varepsilon$ (MeV/c)	$P_\varepsilon$ (%)	$FoM_\varepsilon$ ( $\times 10^{-3}$ )	$\delta\varepsilon_{max}$ ( $\times 10^{-6}$ )	$\delta p_\varepsilon^-$ (MeV/c)	$\delta p_\varepsilon^+$ (MeV/c)	$\delta P_\varepsilon^-$ (%)	$\delta P_\varepsilon^+$ (%)	$\delta FoM_\varepsilon$ ( $\times 10^{-6}$ )
45	8.27	17.2	29.4	0.72	8.91	1.80	1.80	2.58	2.56	1.20
10	3.05	33.0	50.9	0.79	5.40	2.29	3.58	2.18	4.23	1.66
5	1.39	41.0	59.9	0.50	3.64	2.59	3.77	2.00	3.74	1.45

Table 4.1: Parameters characterizing the unpolarized mode of a positron source. The source utilizes a 120 MeV polarized electron beam interacting with a 4 mm thick tungsten target. The positron momentum acceptance is  $\Delta p/p_0 = \pm 5\%$ , with different angular acceptances considered.

$\Delta\theta$ ( $^\circ$ )	$FoM_{max}$ ( $\times 10^{-3}$ )	$p_{FoM}$ (MeV/c)	$P_{FoM}$ (%)	$\varepsilon_{FoM}$ ( $\times 10^{-3}$ )	$\delta FoM_{max}$ ( $\times 10^{-6}$ )	$\delta p_{FoM}^-$ (MeV/c)	$\delta p_{FoM}^+$ (MeV/c)	$\delta P_{FoM}^-$ (%)	$\delta P_{FoM}^+$ (%)	$\delta\varepsilon_{FoM}$ ( $\times 10^{-6}$ )
45	2.05	44.1	66.2	4.68	3.16	2.72	3.87	1.76	3.33	6.69
10	1.33	55.2	76.2	2.30	2.81	4.21	4.21	2.96	2.76	4.68
5	0.72	60.0	79.3	1.15	2.13	3.39	4.37	1.29	2.48	3.30

Table 4.2: Parameters characterizing the polarized mode of a positron source. The source utilizes a 120 MeV polarized electron beam interacting with a 4 mm thick tungsten target. The positron momentum acceptance is  $\Delta p/p_0 = \pm 5\%$ , with different angular acceptances considered.

rejects more low-energy particles, favoring the high-energy part of the positron spectra and reducing the significance of the difference between unpolarized and polarized modes. The unpolarized mode strongly correlates with the angular acceptance, although a non-zero polarization remains at the maximum efficiency.

Tab. 4.1 summarizes the key parameters that characterize the unpolarized mode of a positron source. These parameters are obtained from simulations involving a 120 MeV polarized electron beam interacting with a 4 mm thick tungsten target. The positron momentum acceptance is set to a constant  $\Delta p/p_0 = \pm 5\%$ , while different angular acceptances are considered.

## 4.4 Optimization of production at 120 MeV

In this study, the investigation focuses on how the efficiency of producing positrons is affected by the thickness of the target. A range of target thicknesses up to 16 mm is used, and different angular acceptances are considered. The maximum efficiency ( $\varepsilon_{\max}$ ), the Figure-of-Merit at maximum production ( $FoM_\varepsilon$ ), the positron momentum at maximum production ( $p_\varepsilon$ ), and the positron polarization ( $P_\varepsilon$ ) are measured. These results are shown in Fig.4.10 and Fig.4.11.

Initially, when the target is thin, the production efficiency is low. However, as the thickness increases, the efficiency improves and reaches an optimal region where it changes slowly. Beyond this point, further increasing of the thickness reduces the efficiency because the positron flux is attenuated and not compensated by additional positrons. The Figure-of-Merit shows a similar trend, mainly influenced by changes in efficiency, and indicates a nearly constant positron polarization. Only when the target is thin, and the angular acceptance is significant we obtain an almost unpolarized positron flux. However, achieving large angular acceptances in practice is difficult, so the optimized unpolarized mode ultimately results in a polarized flux.

### 4.4.1 Unpolarized optimization

The optimal target thickness ( $t_\varepsilon$ ) for maximizing positron production is presented in Table 4.3. The value of  $t_\varepsilon$  strongly depends on the angular acceptance, while its dependence on the momentum acceptance is less significant. The reported errors in the table are a combination of simulation statistics based on a large number of pencil electron beams and the shape of the distribution in the region of maximum efficiency. These errors are determined by comparing the lower edge of the maximum efficiency ( $\varepsilon_{\max}(t_\varepsilon) - \delta\varepsilon_{\max}(t_\varepsilon)$ ) with the upper edge of other values at different thicknesses ( $\varepsilon_{\max}(t) + \delta\varepsilon_{\max}(t)$ ). The distribution flatness around the optimal thickness leads to values larger than the simulation step (0.1 mm). The uncertainty in the positron momentum at the maximum also reflects this characteristic.

### 4.4.2 Polarized optimization

We are examining how the Figure-of-Merit ( $FoM_{\max}$ ) is affected by the thickness of the target in the polarized mode. The same conditions as in the unpolarized case are used for this investigation. We explore target thicknesses up to 16 mm and present the results ( $FoM_{\max}, \varepsilon_{FoM}, p_{FoM}, P_{FoM}$ ) in Fig. 4.11. The optimization method in the polarized mode closely resembles that of the unpolarized mode, except for thin targets where there is initially a high maximum positron momentum and beam polarization. When considering realistic angular acceptances, we observe a similar trend to what has been observed at lower beam energies. The maximum  $FoM$  is achieved at approximately half of the electron beam energy, corresponding to a polarization transfer of about 80%.

Importantly, a high level of polarization remains nearly constant regardless of the target thickness. This phenomenon was observed in the PEPPo experiment [26] and can be attributed to multiple scattering effects. These effects cause a reduction

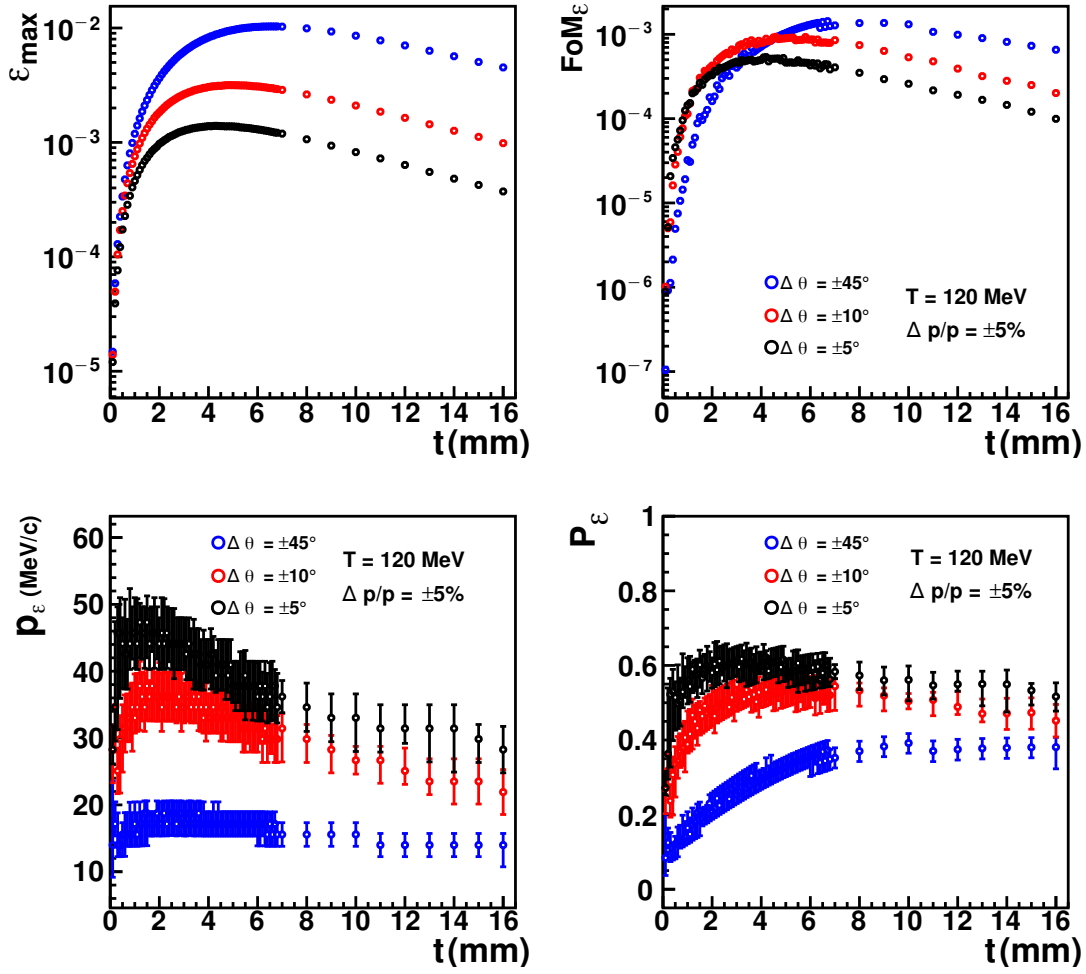


Figure 4.10: Dependency of characteristic quantities on target thickness in the polarized mode at 120 MeV with  $\pm 5\%$  momentum acceptance and various angular acceptances

$\Delta\theta$ (°)	$\Delta p/p_0 = \pm 5\%$						$\Delta p/p_0 = \pm 10\%$					
	$t_\epsilon$ (mm)	$\delta t_\epsilon^-$ (mm)	$\delta t_\epsilon^+$ (mm)	$p_\epsilon$ (MeV/c)	$\delta p_\epsilon^-$ (MeV/c)	$\delta p_\epsilon^+$ (MeV/c)	$t_\epsilon$ (mm)	$\delta t_\epsilon^-$ (mm)	$\delta t_\epsilon^+$ (mm)	$p_\epsilon$ (MeV/c)	$\delta p_\epsilon^-$ (MeV/c)	$\delta p_\epsilon^+$ (MeV/c)
45	6.5	0.2	0.5	17.2	3.29	1.80	5.8	0.4	0.3	25.1	2.02	2.02
10	4.8	0.2	0.5	33.0	3.58	3.58	4.8	0.2	0.5	33.0	3.58	3.58
5	4.3	0.2	0.2	39.4	2.53	3.73	4.3	0.2	0.2	39.4	2.53	3.73

Table 4.3: Optimal target thickness  $t_\epsilon$  and positron momentum at maximum  $p_\epsilon$  for the unpolarized mode at 120 MeV, considering different angular and momentum acceptances.

in the energy of positrons while preserving their polarization. Consequently, even positrons produced at a specific momentum in the first part of a thick target lose energy as they travel through the second part, contributing to an approximately constant average polarization.

Like the unpolarized mode, the optimal target thickness does not depend on the momentum acceptance but is highly dependent on the angular acceptance. These results are summarized in Table 4.4.

Tab. 4.1 presents the parameters characterizing the unpolarized mode of the

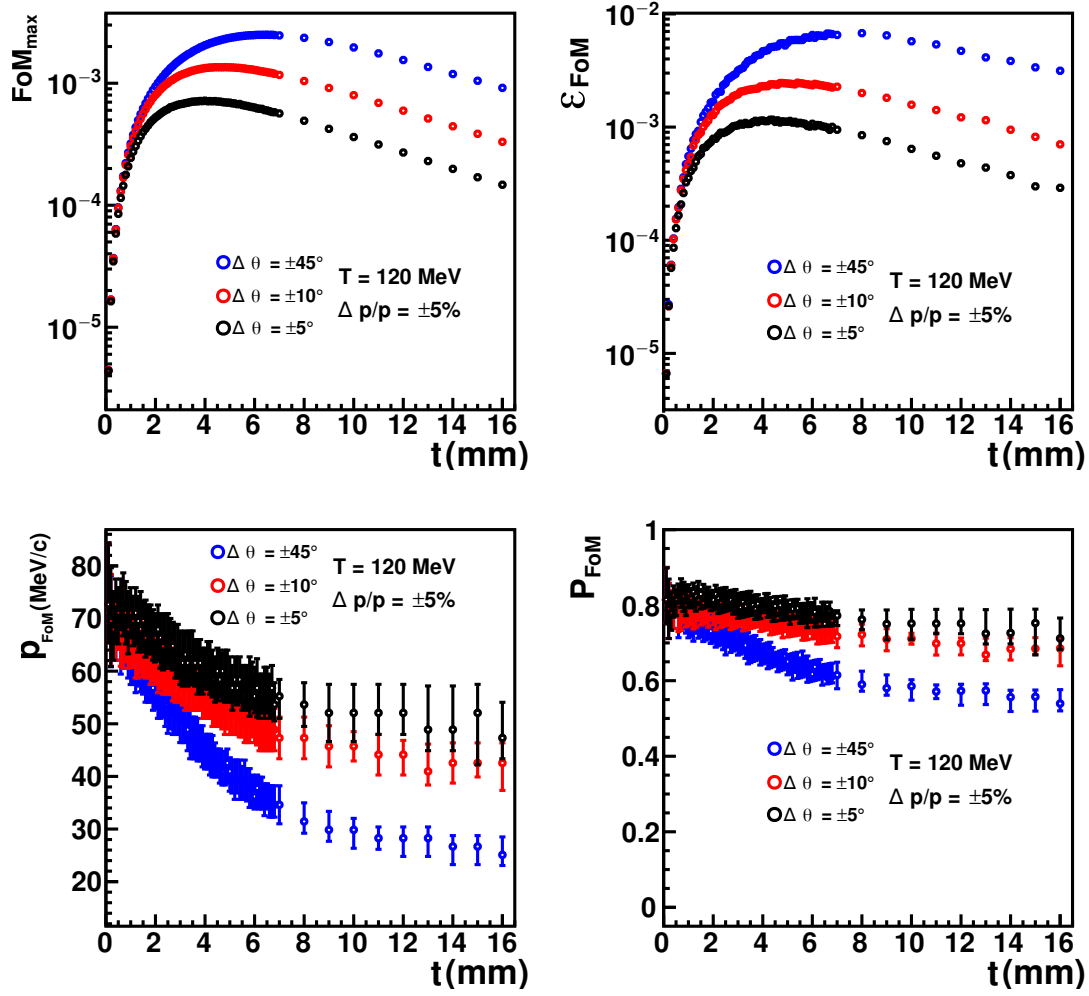


Figure 4.11: Dependency of characteristic quantities on target thickness in the polarized mode at 120 MeV with  $\pm 5\%$  momentum acceptance and various angular acceptances

$\Delta\theta$ (°)	$\Delta p/p_0 = \pm 5\%$						$\Delta p/p_0 = \pm 10\%$					
	$t_{FoM}$ (mm)	$\delta t_{FoM}^-$ (mm)	$\delta t_{FoM}^+$ (mm)	$p_{FoM}$ (MeV/c)	$\delta p_{FoM}^-$ (MeV/c)	$\delta p_{FoM}^+$ (MeV/c)	$t_{FoM}$ (mm)	$\delta t_{FoM}^-$ (mm)	$\delta t_{FoM}^+$ (mm)	$p_{FoM}$ (MeV/c)	$\delta p_{FoM}^-$ (MeV/c)	$\delta p_{FoM}^+$ (MeV/c)
45	6.5	0.3	0.1	36.2	2.41	2.41	5.5	0.3	0.5	44.1	2.72	3.87
10	4.8	0.5	0.3	52.1	4.10	4.10	4.8	0.5	0.3	52.1	4.10	4.10
5	4.0	0.5	0.7	60.0	3.39	4.37	4.0	0.5	0.7	60.0	3.39	4.37

Table 4.4: Optimum target thickness ( $t_{FoM}$ ) and positron momentum at maximum ( $p_{FoM}$ ) in the polarized mode at 120 MeV, considering various angular and momentum acceptances.

positron source, while the second table Tab. 4.2 presents the parameters for the polarized mode. Based on these tables, the major differences and similarities between the two modes can be summarized. Differences:

1. **Maximum efficiency:** The unpolarized mode achieves higher efficiency values compared to the polarized mode.
2. **Figure-of-merit (FoM):** The FoM values for the unpolarized mode are generally lower than those for the polarized mode. This suggests that the polarized

mode achieves better overall performance in terms of positron polarization.

3. **Momentum acceptance:** The polarized mode exhibits higher positron momentum values compared to the positron momentum at optimum efficiency.

Similarities:

1. **Angular acceptance:** Both modes show similar trends in terms of angular acceptance. As the it increses, the maximum efficiency and FoM values generally increase for both modes.
2. **Sensitivity to acceptance parameters:** Both modes exhibit similar sensitivities to acceptance parameters such as angular acceptance.

Tab. 4.3 and Tab. 4.4 provide information about the optimal target thickness ( $t$ ) and positron momentum ( $p$ ) at maximum efficiency for both the unpolarized and polarized modes at 120 MeV, considering different angular and momentum acceptances. Let us discuss the significant differences and similarities between the two tables:

1. **Optimal target thickness ( $t$ ):** In both the unpolarized and polarized modes, the optimal target thickness decreases as the angular acceptance decreases. This observation suggests that specific setups can apply the same target thickness for both polarized  $e^+$  and unpolarized  $e^+$  production. Despite the decline in thickness with increasing angular acceptance, considering simulation binning and error margins, a 4.3 mm and 4.0 mm thickness might be nearly equivalent at 5 degrees. Therefore, achieving an angular acceptance slightly higher than 5 degrees, possibly between 7.5 and 10 degrees, could standardize the thickness for both modes. Achieving this would also result in lower  $e^+$  momentum, facilitating further acceleration and manipulation to address the energy spread.
2. **Positron momentum:** The positron momentum at optimum of the two production modes differs between the unpolarized and polarized modes. Generally, the polarized mode exhibits higher positron momentum values than the unpolarized mode at the same angular acceptance.

The optimal target thickness generally decreases as the angular acceptance decreases for both modes. The polarized mode tends to achieve higher positron momenta than the unpolarized mode, indicating a potential advantage in collecting higher polarization. The results suggest the feasibility of designing a production target with an optimal thickness suitable for both polarized and unpolarized  $e^+$ . With an approximate angular acceptance of around 7° and a thickness close to 4 mm, such a target would be instrumental. Identifying the optimum target thickness is important for improving the positron production as it aims to support both polarized and unpolarized modes efficiently.

## 4.5 Optimization of production at 1000 MeV

To explore the advantages of increasing the electron beam energy to enhance positron yield, and to understand its implications on the collection system, a study

on positron production using a 1000 MeV electron beam was conducted. This section explores the optimization of positron production at this beam energy, considering both unpolarized and polarized modes.

The dependence of maximum positron production efficiency on target thickness is studied in the unpolarized mode. The results show similarities to the 120 MeV case, where larger beam energy leads to a more focused positron distribution and a reduced optimum angular domain. Higher production rates can be achieved with more considerable beam energies, but this comes at the cost of a more technologically demanding collection system. The target thickness is found to be minimally sensitive to the momentum acceptance but strongly dependent on the angular acceptance as shown in Fig. 4.12.

$\Delta\theta$ (°)	$\Delta p/p_0 = \pm 5\%$						$\Delta p/p_0 = \pm 10\%$					
	$t_\varepsilon$ (mm)	$\delta t_\varepsilon^-$ (mm)	$\delta t_\varepsilon^+$ (mm)	$p_\varepsilon$ (MeV/c)	$\delta p_\varepsilon^-$ (MeV/c)	$\delta p_\varepsilon^+$ (MeV/c)	$t_\varepsilon$ (mm)	$\delta t_\varepsilon^-$ (mm)	$\delta t_\varepsilon^+$ (mm)	$p_\varepsilon$ (MeV/c)	$\delta p_\varepsilon^-$ (MeV/c)	$\delta p_{FoM}^+$ (MeV/c)
20	11.0	0.4	1.0	33.8	13.4	13.4	10.8	0.8	1.2	33.8	13.7	13.7
5	7.4	0.4	0.6	113.7	14.5	14.5	7.4	0.2	0.6	113.7	17.5	17.5
1	5.1	0.3	0.2	300.2	30.6	20.1	5.1	0.5	0.2	300.2	40.1	40.1

Table 4.5: Optimal target thickness ( $t_\varepsilon$ ) and maximum positron momentum ( $p_\varepsilon$ ) in the unpolarized mode at 1000 MeV for various angular and momentum acceptances

Similarly, in the polarized mode, the dependence of characteristic parameters ( $FoM$ ,  $\varepsilon_{FoM}$ ,  $p_{FoM}$ ,  $P_{FoM}$ ) on target thickness is investigated under the same conditions as the unpolarized mode on Fig. 4.13. The results show no significant differences between low and high beam energies, except for higher optimum  $FoM$  values, indicating improved production efficiency at higher energies. As previously observed, the established rule of thumb for the optimum thickness remains valid. However with an enhanced sensitivity to the angular acceptance primarily due to the focusing effects of the initial electron beam.

$\Delta\theta$ (°)	$\Delta p/p_0 = \pm 5\%$						$\Delta p/p_0 = \pm 10\%$					
	$t_{FoM}$ (mm)	$\delta t_{FoM}^-$ (mm)	$\delta t_{FoM}^+$ (mm)	$p_{FoM}$ (MeV/c)	$\delta p_{FoM}^-$ (MeV/c)	$\delta p_{FoM}^+$ (MeV/c)	$t_{FoM}$ (mm)	$\delta t_{FoM}^-$ (mm)	$\delta t_{FoM}^+$ (mm)	$p_{FoM}$ (MeV/c)	$\delta p_{FoM}^-$ (MeV/c)	$\delta p_{FoM}^+$ (MeV/c)
20	7.4	1.6	4.6	246.9	18.2	29.4	8.2	2.2	2.8	233.6	35.4	35.4
5	7.2	1.0	0.8	300.2	42.7	30.6	7.2	0.8	0.4	300.2	40.1	40.1
1	4.4	0.6	0.9	500.0	36.5	36.5	4.9	1.0	0.5	486.7	55.5	55.5

Table 4.6: Optimal Target Thickness ( $t_{FoM}$ ) and Maximum Positron Momentum ( $p_{FoM}$ ) in the polarized Mode at 1000 MeV for Various Angular and Momentum Acceptances

The study results suggest that using a drive beam with greater momentum leads to the creation of more positrons, when considering a 1 GeV drive beam for generating positrons. However, incorporating this into the CEBAF presented various difficulties. Nonetheless, analysis with a 120 MeV electron beam for positron production yielded results comparable to the 1 GeV scenario. This implies that a 120 MeV electron beam is an effective alternative for producing positrons in CEBAF. It offers the advantage of being easier to integrate into the system while still achieving satisfactory levels of polarization and yield of positrons.

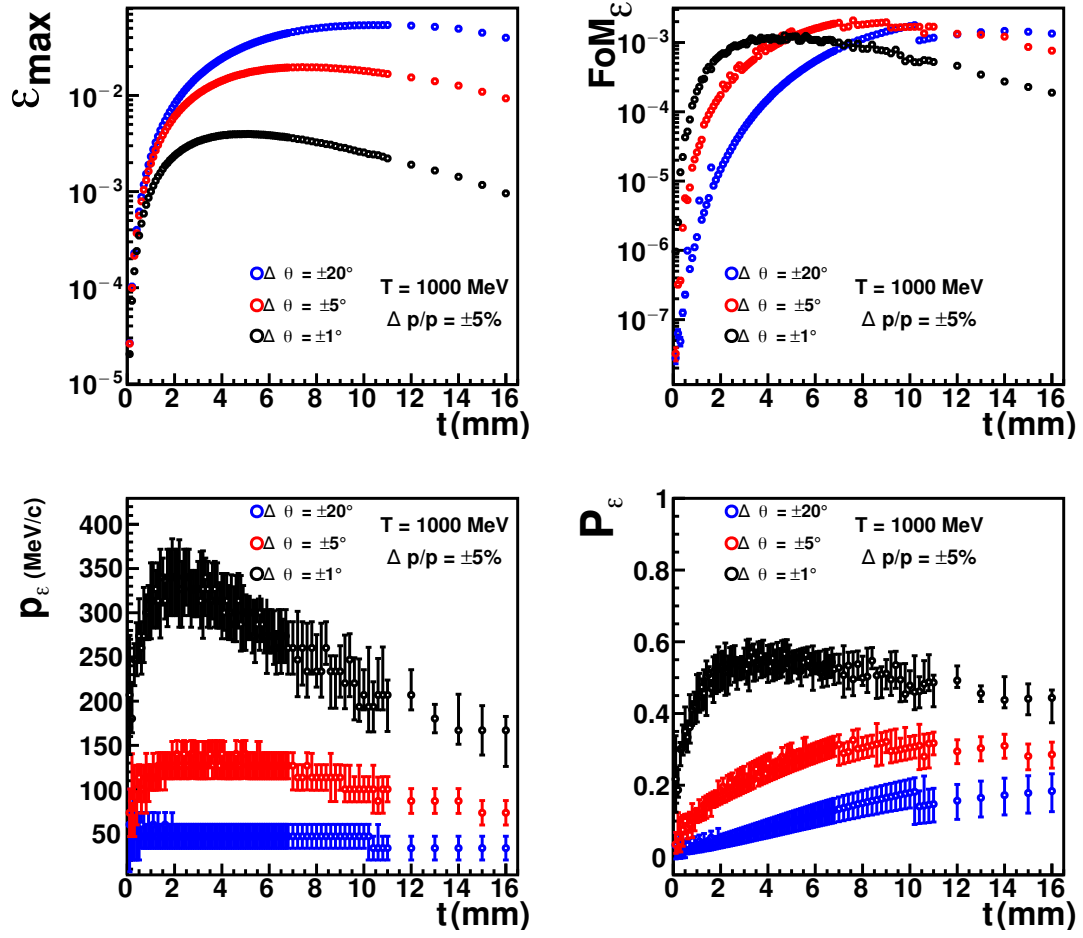


Figure 4.12: Target thickness dependence of the characteristic quantities of the unpolarized mode at 1000 MeV and a momentum acceptance of  $\pm 5\%$  for different angular acceptances.



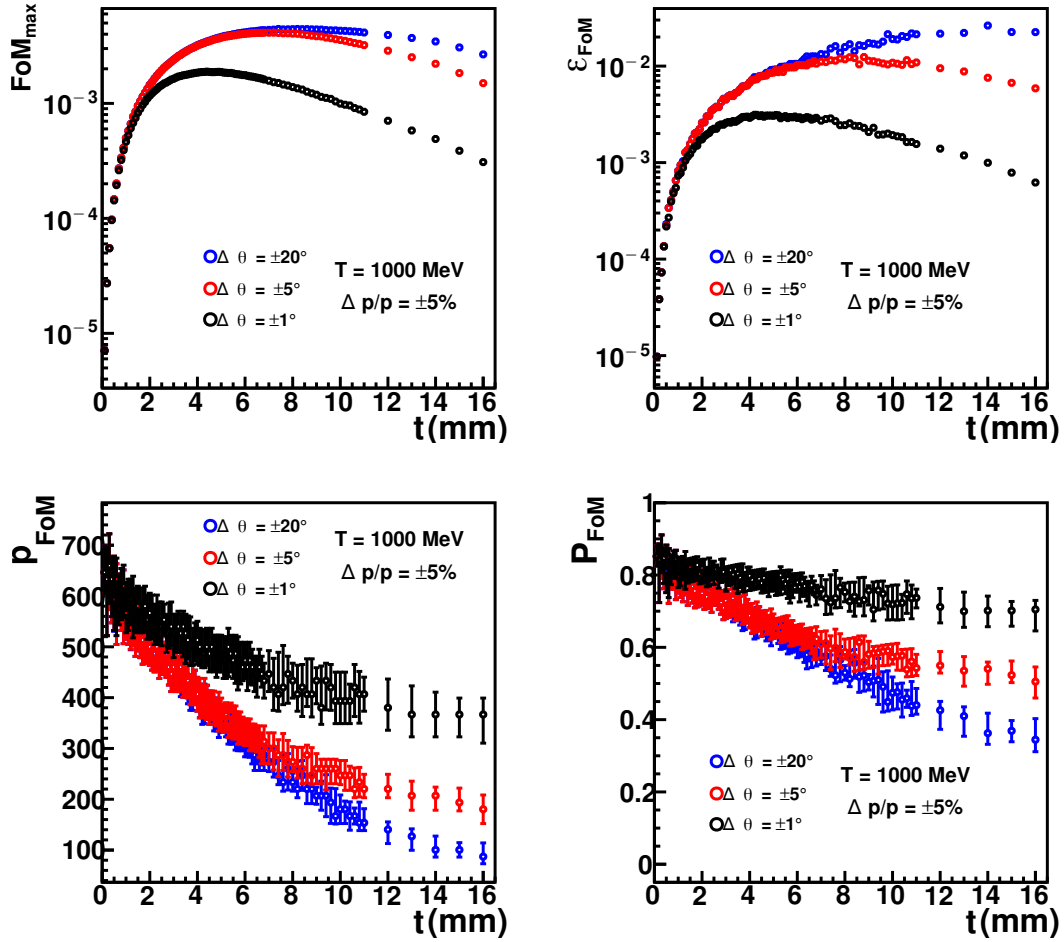


Figure 4.13: Target thickness dependence of the characteristic quantities of the polarized mode at 1000 MeV and a momentum acceptance of  $\pm 5\%$  for different angular acceptances.

## 4.6 Comparison between 120 MeV and 1000 MeV

The simulations results has been presented previously; the comparison between 120 MeV and 1000 MeV results can be summarized as follows:

### 1. Optimal Target thickness:

- At 120 MeV, the thickness varies from 6.5 mm at  $\Delta\theta = \pm 45^\circ$  to 4 mm at  $\Delta\theta = \pm 5^\circ$ .
- At 1000 MeV, the thickness varies from 11 mm at  $\Delta\theta = \pm 20^\circ$  to 5 mm at  $\Delta\theta = \pm 1^\circ$ .

The optimal target thickness increases at higher energies for similar angular acceptances, but the range of angular acceptances are different between the two energies.

### 2. Positron momentum $p_0$ :

- At 120 MeV, the normalized momentum varies from 0.14 at  $\Delta\theta = \pm 45^\circ$  to 0.32 at  $\Delta\theta = \pm 5^\circ$ .
- At 1000 MeV, the normalized energy increases drastically, ranging from 0.033 at  $\Delta\theta = \pm 20^\circ$  to 0.3 at  $\Delta\theta = \pm 1^\circ$ .

1. **Optimal target thickness:**

- At 120 MeV, the thickness ranges from 6.5 mm at  $\Delta\theta = \pm 45^\circ$  to 4 mm at  $\Delta\theta = \pm 5^\circ$ .
- At 1000 MeV, the thickness ranges from 7.4 mm at  $\Delta\theta = \pm 20^\circ$  to 4.4 mm at  $\Delta\theta = \pm 1^\circ$ .

Thickness values are quite similar between 120 MeV and 1000 MeV.

2. **Positron momentum  $p_0$ :**

- At 120 MeV, the positron normalized energy ranges from 0.3 at  $\Delta\theta = \pm 45^\circ$  to 0.5 at  $\Delta\theta = \pm 20^\circ$ .
- At 1000 MeV, the momentum drastically increases, ranging from 0.24 at  $\Delta\theta = \pm 20^\circ$  to 0.5 at  $\Delta\theta = \pm 1^\circ$ .

Again, the positron momentum significantly rises at 1000 MeV for all angular acceptances.

1. **Efficiency in positron production:** Higher electron beam energy (1000 MeV) leads to a noticeable increase in the momentum of produced positrons in both polarized and unpolarized modes.
2. **Optimal target thickness:** In the unpolarized mode, the thickness generally increases with higher energy, while in the polarized mode, the thickness remains roughly consistent between the two modes for the given angular acceptances. This suggests that thinner targets might suffice at 120 MeV, which can be advantageous regarding target longevity, cost, deposited power, or other factors related to the target physical properties.
3. **Polarization:** The results indicate that producing positrons at 120 MeV in a polarized mode yields polarization levels similar to those achieved at 1000 MeV. This similarity in polarization outcomes means that using 120 MeV for positron production aligns well with the polarization objectives of the CEBAF involving the production of highly polarized positron beams.

It's important to note that the range of angular acceptances differs between 120 MeV and 1000 MeV. This difference is crucial for a fair comparison, especially when considering the effects of the Lorentz boost. As energy increases, the angular distribution of positrons narrows. Hence, positrons are more tightly focused at higher energies than at lower energies.

## 4.7 Collection System considerations

In Fig. 4.14, the angular positron distribution at the target exit is shown. It highlights that high positron yields correspond to low energies. Consequently, optimizing a positron injector for low polarization and high yield emphasizes capturing the maximum positrons at low energies. The main challenge is capturing low-momentum positrons at wide angles. The figure also contrasts the design approaches for collection systems in polarized and unpolarized modes. For high polarization, a small angular acceptance satisfies capture of the majority of positrons at the optimum FoM. In contrast, the unpolarized mode requires a different design approach due to its extended transverse size at low momenta, with peak positron density observed at a  $50^\circ$  angle.

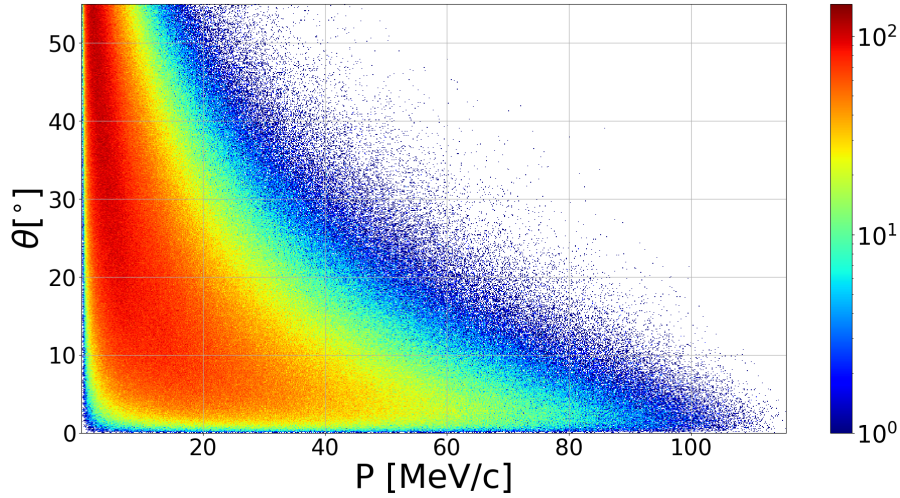


Figure 4.14: Angular vs momentum positron distribution at the target exit

The sensitivity to the momentum and angular acceptances was investigated within the  $\Delta p/p_0$  range from  $\pm 1\%$  to  $\pm 15\%$  and  $\Delta\theta$  from  $\pm 1^\circ$  to  $\pm 35^\circ$ . Consistent with previous sections, the optimum thickness dependence on  $\Delta p/p_0$  at a fixed  $\Delta\theta$  can be approximated as a constant.

The fitted values resulting from the analysis of the  $\Delta p/p_0$  distributions at fixed  $\Delta\theta$  are presented in Figure 4.15 (top panel) across the investigated angular range and fitted using a 3rd-order polynomial. It is worth noting that the smallest  $\Delta\theta$  values exhibit larger statistical fluctuations, which lead to a normalized  $\chi_r^2$  larger than 1. Overall, there is a systematic difference between the optimum target thickness for the unpolarized and polarized modes, which declines with increasing angular acceptance. Similarly, the positron momentum and polarization at the optimum point do not depend on  $\Delta p/p_0$  but are strongly influenced by the angular acceptance. The inverse of a 3rd-order polynomial function successfully fits the  $\Delta\theta$  dependencies, as shown in Figure 4.16 (middle and bottom panels). However, these observations cannot be directly extended to the optimum efficiency and FoM, as these quantities depend on momentum and angular acceptances. Nevertheless, it is evident that both the efficiency and FoM increase with larger values of  $\Delta\theta$ .

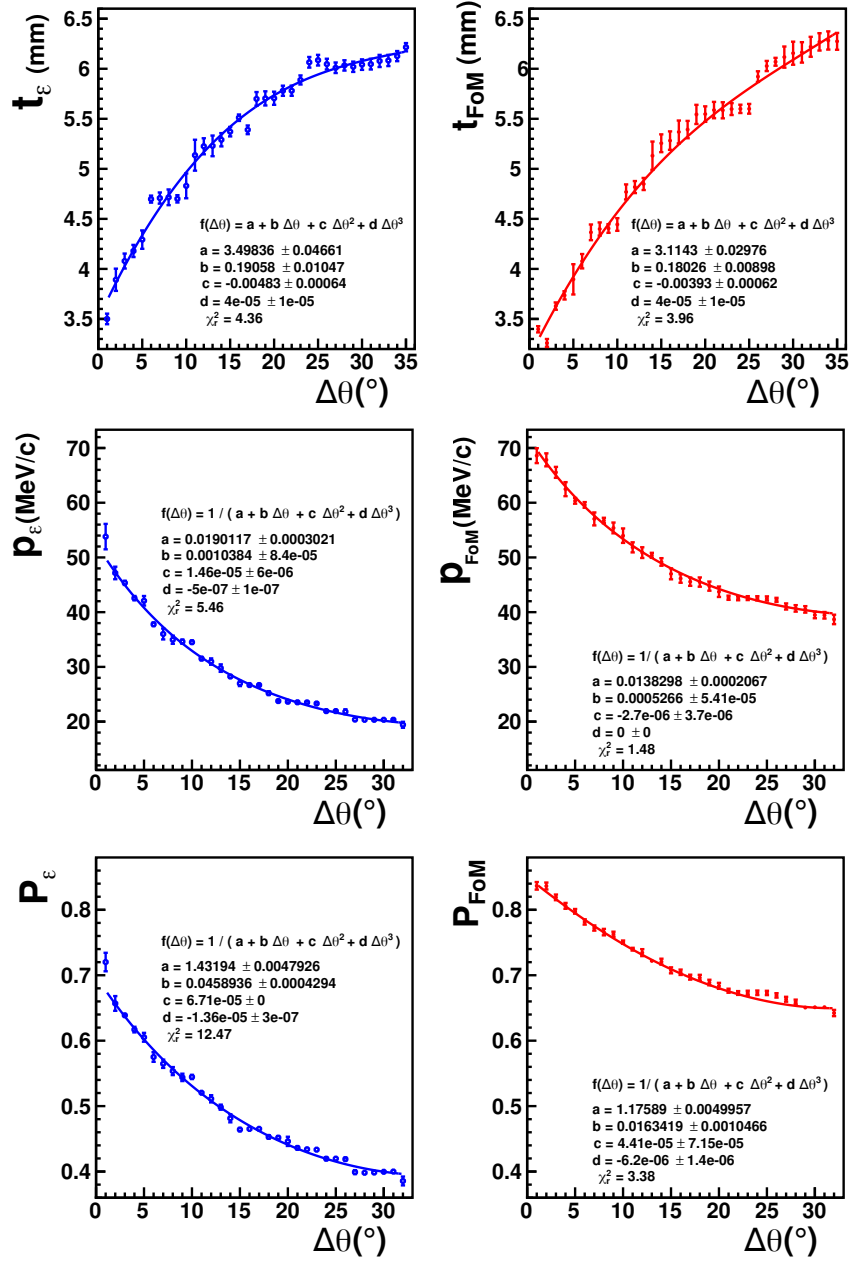


Figure 4.15: Effect of angular acceptance on the optimal target thickness (top panel), maximum positron momentum (middle panel), and positron polarization (bottom panel) in the unpolarized and polarized modes at 120 MeV.

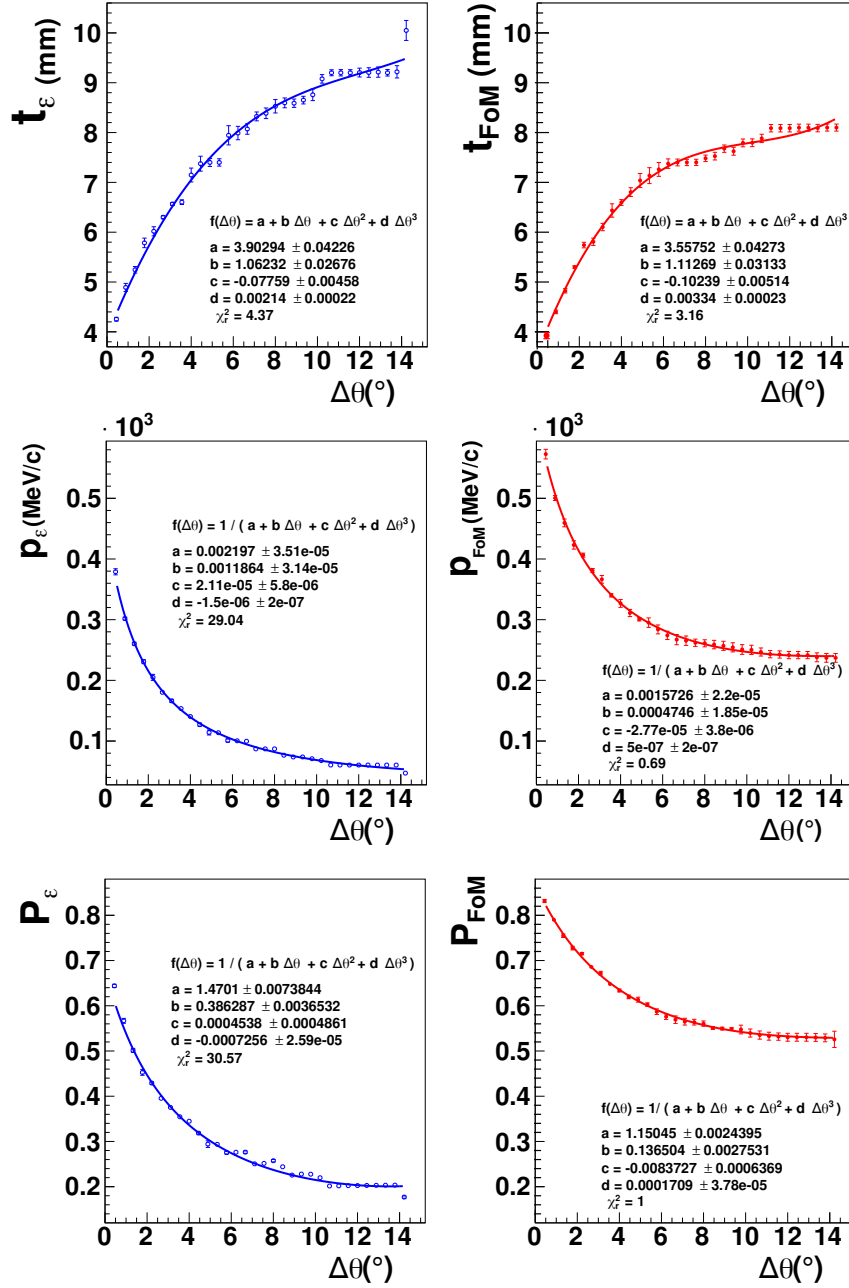


Figure 4.16: Angular acceptance dependence of the optimum target thickness (top panel), the positron momentum at maximum (middle panel) and the positron polarization at maximum (bottom panel) of the unpolarized and polarized modes at 1000 MeV.

In conclusion, the optimization and analysis of the positron production target have provided valuable insights. The investigation focused on the sensitivity of the maximum positron production efficiency and Figure-of-Merit (FoM) to various parameters, including target thickness, momentum acceptance, and angular acceptance.

The results revealed that the optimization patterns in the polarized and unpolarized modes are similar, with some notable differences. However, an interesting

observation is that a high level of polarization is achieved regardless of the target thickness.

The optimum target thickness was found to be dependent on the angular acceptance, while its sensitivity to the momentum acceptance was relatively minor. The study revealed that the optimum thickness maximizing positron production efficiency in the unpolarized mode is consistently different from the optimum target thickness for maximizing the Figure of Merit (FoM) in the polarized mode. However, this discrepancy decreases as the angular acceptance increases.

The study also investigated the sensitivity to the collection system, represented by momentum and angular acceptances. The demonstrated that the optimum target thickness remains relatively constant with varying momentum acceptance but strongly depends on the angular acceptance. Similarly, the positron momentum and polarization at the optimum point were found to be independent of the momentum acceptance but highly sensitive to the angular acceptance.

Overall, the optimization and analysis highlighted the complex interplay between target thickness, momentum acceptance, and angular acceptance in maximizing positron production efficiency and achieving high positron polarization. This guides the design and optimization of positron production targets in practical applications, improving the efficiency and control of positron beams.

## 4.8 Target thermal fatigue

In this section, the focus shifts to a critical aspect of this process studying the thermal fatigue of the target material. When employing a 120 MeV electron beam to interact with a tungsten target of 4 mm thickness for positron production, it becomes imperative to estimate the deposited power on the target. The reason for this lies in the potential heat generation during the interaction process. The electron beam, carrying substantial energy, can result in a significant power deposition within the target material. Therefore, understanding how to effectively dissipate this heat within the production region is important to ensuring the target durability.

To delve into this matter, FLUKA software was employed to simulate and analyze the energy deposition patterns when subjecting a 120 MeV electron beam, characterized by a 1.5 mm rms spot size, to a 4 mm thick tungsten target. The insights gained from this study will provide invaluable information for devising strategies to manage the thermal challenges associated with positron production targets.

The electron beam energy deposition in the target was investigated using FLUKA software [15]. Fig. 4.17 illustrates the energy distribution of a 120 MeV electron beam with a 1.5 mm RMS spot size in a 4 mm thick tungsten target. For a CW beam with a current of 1 mA, the peak power density is  $324 \text{ MeV/e}^- \text{mm}^3$ .

The heat generated by the beam needs to be distributed over a larger volume. A 4 mm thick tungsten rim is mounted on a water-cooled copper disk. The calculations for temperature were based on the following parameters: The target rotates at a frequency of 2 Hertz (Hz), and the beam moves across the target at a tangential speed of 2.3 meters per second (m/s). Additionally, the copper disk that houses the target contains a water channel, which has a radius of 8 millimeters (mm). This information pertains to the design and operational conditions of the system

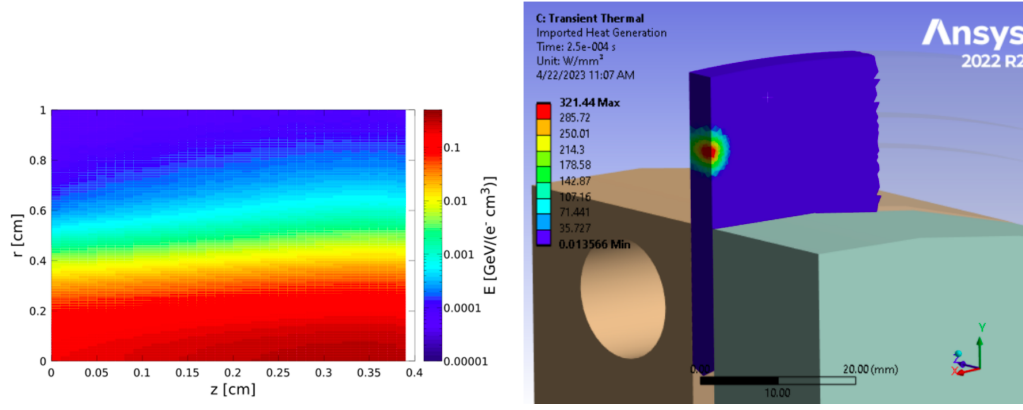


Figure 4.17: Left: energy deposition and temperature profile in a rotating target under electron beam irradiation, Right: heat power density distribution of a 1 mA electron beam at 120 MeV with 1.5 mm rms Size in a 4 mm thick tungsten target [15].

being analyzed. Simulation results indicate that the water cooling system effectively dissipates heat from the copper disk and tungsten rim, with an increase in water temperature of approximately  $30^\circ\text{C}$  and a peak temperature in the copper disk below  $100^\circ\text{C}$  for a beam power deposited in the tungsten of 17 kW. This suggests that more than 100 kW of beam power will still be present after the target.

To simulate the heating of tungsten by the electron beam, the heat power density distribution was shifted along a circular path with a radius of 18 cm in 0.25 ms time steps. The temperature at the selected point on the target (at  $R = 18$  cm) increases during 4.5 ms, reaching a maximum of  $681^\circ\text{C}$ . The time evolution of temperature during the first 10 ms of the 0.5 s cycle is shown in Fig. 4.18.

The temperature distribution is then used to calculate the mechanical stress from

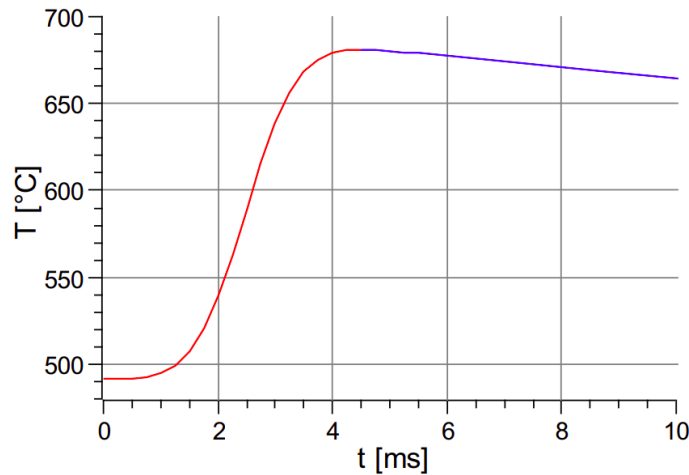


Figure 4.18: Left: cyclic temperature variation in tungsten at a radius of 18 cm with a tangential velocity of 2.3 m/s and 1.5 mm rms beam spot: heating phase (shown in red) followed by cooling phase (extended up to 0.5 s in blue).

the ANSYS static structural module. The equivalent Von Mises stress [71], which

indicates the proximity to material failure, shows a maximal stress of 878 MPa in tungsten as shown in Fig.4.19.

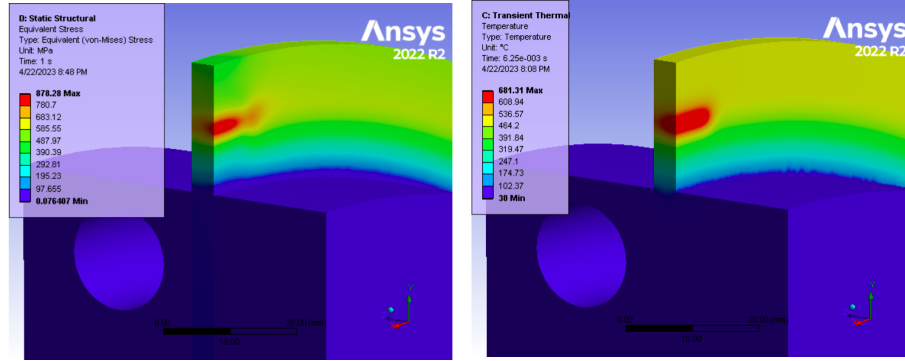


Figure 4.19: Left; thermal-induced mechanical stressRight, right: temperature distribution in a 17 kW Target.

FLUKA is employed to simulate the radiation damage incurred by tungsten. Within FLUKA, radiation damage effects are taken into account for all particles, including recoils that possess sufficient energy to cause material damage. Fig. 4.20 displays the radiation damage at various depths within the rotating target, which has a diameter of 36 cm, after 5000 hours of irradiation. The calculated peak damage reaches 0.21 displacements per atom (dpa) .

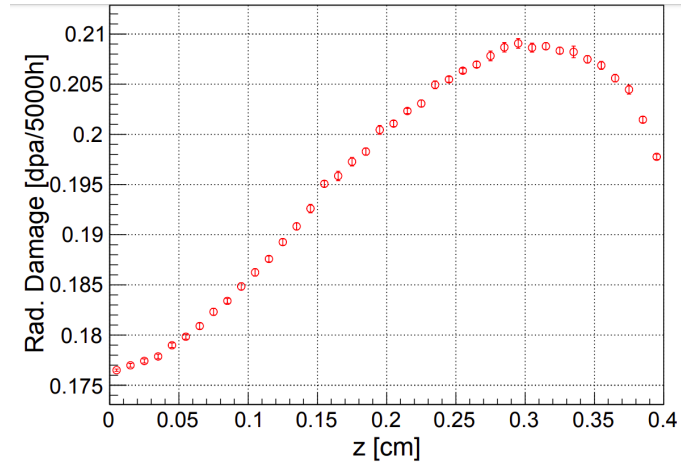


Figure 4.20: Radiation damage in a tungsten target with a diameter of 36 cm.

Experimental Tests have begun using tungsten and tantalum to study radiation damage on these materials. They are exposed to a  $50 \mu A$ , 3.5 MeV electron beam at Mainz Microtron (MAMI). Additionally, fatigue tests with a high-power laser are under investigation, similar to those for the APEX target at Jefferson Lab. The goal is to determine the target stress limits and understand the impact of radiation on the material.



# Chapter 5

## Positron capture optimization

### 5.1 Collection system

The positron beam, generated from the conversion target, exhibits unique properties: a diverse energy spectrum, a pronounced angular spread, and a compact radius, which strongly tied to the choice of the incoming  $e^-$  beam. These intrinsic characteristics, especially the significant angular divergence, complicate its straightforward acceleration or transportation to experimental halls. This is where the collection system becomes indispensable, effectively transforming the widely distributed positrons at the target into the accelerator, a parallel beam with minimal transverse momentum. To attain a high degree of polarization ( $\text{FoM}_{\text{max}}$ ) and an optimal positron yield ( $\epsilon_{\text{max}}$ ), it is essential to selectively harness positrons based on their angular and momentum attributes, ensuring they have reduced transverse momentum.

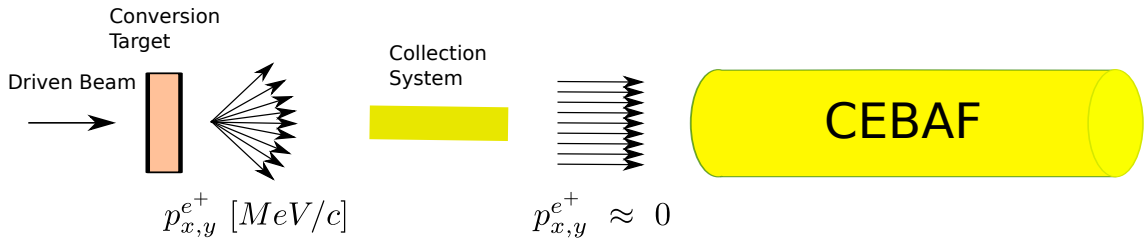


Figure 5.1: schematic and purpose of the positron collection system symbolized here by the matching device item

Magnetic solenoids are pivotal in particle accelerator systems due to their effectiveness in managing the transverse momentum of charged particle beams. Essentially, a solenoid creates a near-uniform axial magnetic field. This causes charged particles to spiral due to the fringe field at the solenoid entrance. However, when these particles exit the solenoid and cross the fringe fields, their spiral trajectory stops. This intrinsic property offers a dual-directional 'focusing effect' that centers drifting particles in x and y planes, contrasting with quadrupole magnets which focus in only one direction at once. Moreover, while changing the beam characteristics, solenoids conserve its overall emittance. Solenoids adeptly reduce transverse momentum by providing multidirectional focus and conserving the beam inherent quality.

In this work, two different solenoid approaches are investigated for collecting positrons at the exit of the production target [16]: the Quarter Wave Transformer

(QWT) solenoid and the Adiabatic Matching Device (AMD) solenoid. The AMD is a device capable of accepting a broad range of energy, while the QWT is designed for a small energy acceptance.

Since both devices are meant to focus particles, understanding the nuances and functionalities of the two primary solenoids, the Quarter Wave Transformer and the Adiabatic Matching Device, is essential to effectively harnessing the collection system potential. This study will explore incorporating both devices with a weak magnetic field at their exits. This strategy is adopted to avoid losing particles post-focusing. After the focusing solenoids, there are also accelerating cavities, which are important for further enhancing the particle beam. The following sections will present a detailed exploration of both these devices. Furthermore, a comparative analysis will characterize each system-accepted particle phase space, illustrating their distinct advantages and optimal use cases for CEBAF.

## 5.2 Adiabatic Matching Device

The term "adiabatic" refers to processes that occur slowly enough such that certain properties stay unchanged. In the context of an AMD, an adiabatic process would slowly change the properties of the axial magnetic field  $B_z$ , allowing the beam emittance to be transformed in a controlled manner without inducing unwanted oscillations or other perturbations. The Adiabatic Matching Device (AMD), features a slow variation in a magnetic field between the maximum  $B_1$  and the minimum  $B_2$  values, along the  $z$ -axis (Fig. 5.2), this device can focus a large momentum range because of the adiabatic variation of the magnetic field. The magnetic field distribution of the AMD can be described by the expression [72]:

$$B(z) = \frac{B_1}{1 + \mu z} \quad (5.1)$$

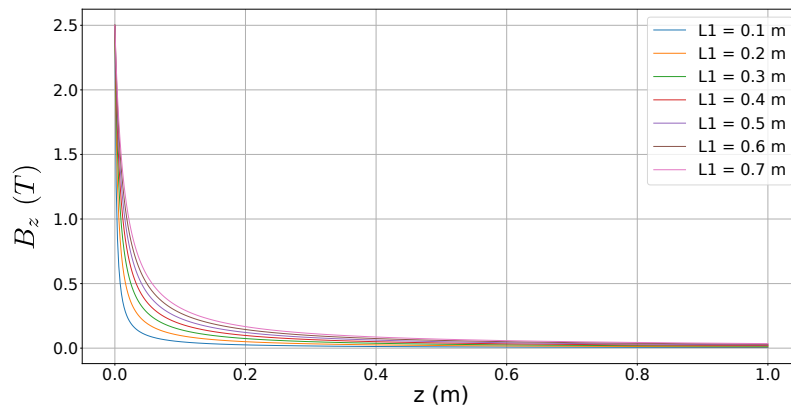


Figure 5.2: Effect of AMD length on magnetic field variation

where  $\mu = \frac{\epsilon B_1}{p_0}$ , and  $p_0$  is a specific central scalar momentum. The adiabaticity of the system can be characterized by a smallness parameter [72] defined as:

$$\int_0^L \frac{\epsilon}{p_0} dz = \int_{B_1}^{B_2} \frac{dB}{B^2} \quad (5.2)$$

Then:

$$\epsilon = \frac{p_0}{eB^2} \frac{dB}{dz} \quad (5.3)$$

The system is adiabatic only if ( $\epsilon \ll 1$ ). The parameter  $\mu$  become:

$$\mu[\text{m}^{-1}] = \frac{\epsilon e B_1}{p_0} = \frac{e}{L_1} \frac{B_1 - B_2}{B_2} \quad (5.4)$$

resulting in:

$$B(z) = \frac{B_1 B_2 L_1}{B_2 L_1 + (B_1 - B_2) z}. \quad (5.5)$$

Fig. 5.2 illustrates the longitudinal magnetic field profile of the AMD with respect to the length  $L_1$  of the first field region, considering  $B_1 = 2.5$  T and  $B_2 = 0.05$  T. It shows that the choice of the AMD length is important to keep a slow variation of  $B_z$ , indeed, the longer is the length, the smaller is the  $\epsilon$ , the better is the adiabaticity.

The matrix transfer of the AMD region can be expressed using the equations of motion [16]:

$$\begin{pmatrix} \xi \\ P_\xi \end{pmatrix} = \begin{pmatrix} \sqrt{\frac{B_1}{B}} \cos \chi & \frac{2}{e\sqrt{B_1 B}} \sin \chi \\ -\frac{e\sqrt{B_1 B}}{2} \sin \chi & \frac{B}{B_1} \cos \chi \end{pmatrix} \begin{pmatrix} \xi_0 \\ P_{\xi_0} \end{pmatrix}. \quad (5.6)$$

The rotation angle represents the Larmor angle followed by the particle in a solenoidal field and can be expressed by :

$$\chi = \int_0^l \frac{eB}{2p} dz \quad (5.7)$$

where  $l$  is the length of the solenoid.

Here,  $B \equiv B(z)$  represents the AMD magnetic field, and  $B_1$  corresponds to the field intensity at  $z = 0$ . When combined with the long section of constant weak field  $B_2$  (equivalent to  $B(L_1)$ ), the complete transfer matrix can be written [16]:

$$\begin{pmatrix} X \\ P_X \end{pmatrix} = e^{-\chi} \begin{pmatrix} \sqrt{\frac{B_1}{B_2}} \cos \chi & \frac{2}{e\sqrt{B_1 B_2}} \sin \chi \\ -\frac{e\sqrt{B_1 B_2}}{2} \sin \chi & \frac{B_2}{B_1} \cos \chi \end{pmatrix} \begin{pmatrix} X_0 \\ P_{X_0} \end{pmatrix}. \quad (5.8)$$

### 5.2.1 Phase space admittance

Making Eq. 5.8 in quadratic form, and since the emittance is conserved in solenoids, the positron accepted phase space links to the condition:

$$XX^* + \left[ \frac{2}{eB_2} \right]^2 P_X P_X^* = \frac{B_1}{B_2} X_0 X_0^* + \frac{4}{e^2 B_1 B_2} P_{X_0} P_{X_0}^* = \text{Cte}. \quad (5.9)$$

where  $X \equiv x + iy$  and  $P_X \equiv p_x + ip_y$ , and  $X^*$  and  $P_X^*$  are the conjugate values. Positron emitted at the converter with phase space coordinates  $(X_0, P_{X_0})$  will be captured into the downstream acceptance of the accelerating section; Within its aperture  $a$ , and, immersed in a solenoidal magnetic field  $B_2$  if its coordinates and angles satisfy the following conditions:

$$XX^* \leq a^2. \quad (5.10)$$

This leads to the corresponding volume acceptance of the transmitted particles [72]:

$$V_{AMD} = \int_{XX^* \leq a^2} dx dy dp_x dp_y = \frac{2\pi^2}{3} \left[ \frac{eB_2 a^2}{2} \right]^2. \quad (5.11)$$

The adiabatic variation of the solenoid field is advantageous, as the phase space volume does not depend on longitudinal momentum. Accordingly, the AMD exhibits broad momentum acceptance, constrained by the adiabatic condition (Eq. 5.3).

### 5.2.2 Transverse acceptance

The analytical formula [16] is derived from Eq. 5.9 in cylindrical coordinates:

$$\left[ \frac{B_1}{B_2} \right] \left( \frac{r_0}{a} \right)^2 + \left( \frac{P_{r0}}{\frac{1}{2}e\sqrt{B_1 B_2}a} \right)^2 + \left( \frac{P_{\phi_0}}{\frac{1}{2}eB_2 a^2} \right)^2 \left[ \frac{B_1}{B_2} \frac{1}{\left[ \frac{r_0}{a} \right]^2} - 1 \right] \leq 1 \quad (5.12)$$

Here,  $a$  represents the aperture radius of the accelerator channel (capture section),  $B_1$  and  $B_2$  are the peak and constant magnetic fields as defined. The distance from the central axis at the target is denoted as  $r_0$ :

$$r_0 = \sqrt{x_0^2 + y_0^2} \quad (5.13)$$

Notably, only initial positrons  $(x_0, y_0, p_{x0}, p_{y0})$  satisfying the formula (5.12) are accepted. The maximum extension in the spatial dimension, that is, the axis of the ellipsoid in the position space, is determined at  $P_{r0}=P_{\phi_0}=0$  providing the radial acceptance of the AMD, and  $r_0 = P_{\phi_0} = 0$  provide the maximum angular acceptance of the AMD, thus, the acceptance of the AMD is deduced accordingly:

$$r_0^{max} = \sqrt{\frac{B_2}{B_1}} a \quad (5.14)$$

$$\theta^{max} = \frac{1}{2p_0} e a \sqrt{B_2 B_1} \quad (5.15)$$

## 5.3 Quarter Wave Transformer

The second approach involves a QWT based on a strong solenoid magnetic field,  $B_1$ , which focuses particles over a short length,  $L_1$ . In order to use an accelerating cavity structure subsequently, this QWT will be integrated with a longer second solenoid,  $L_2$ , possessing a weaker magnetic field,  $B_2$ . The extended region,  $L_2$ , houses the positrons and is designed to contain the accelerating section for positron capture. This design ensures the positron transverse emittance aligns with the narrow transverse angular acceptance of the capture section, introducing a correlation between the system acceptance and the positron momentum.

For this study scope, the combination of  $B_1$  and  $B_2$  will be approximated using the hard edge model. Subsequent sections will delve deeper into the QWT transfer matrix, its acceptance, and the maximum emittance exiting the high field region.

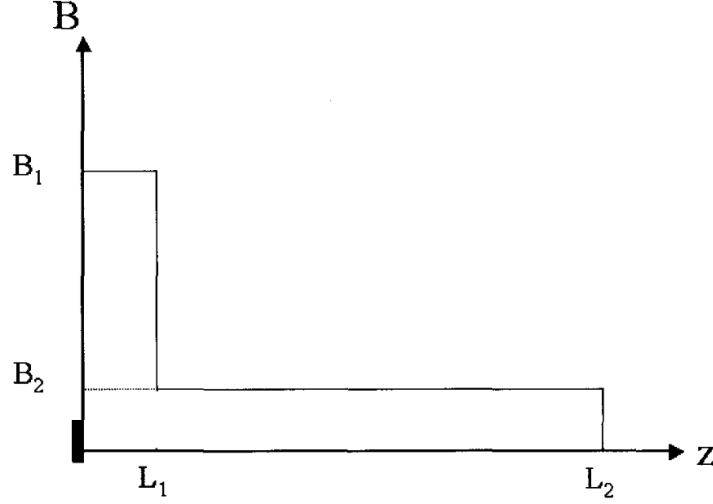


Figure 5.3: QWT magnetic field profile: short and long are two solenoidal field profiles. The target converter is positioned at the origin of the system. In this context,  $B_1$  and  $B_2$  represent the field strengths of the short and long solenoids, respectively, while  $L_1$  and  $L_2$  indicate the lengths of these solenoids [16].

### Phase space acceptance

The transfer of a particle from the target to the exit of the long weak solenoid section can be represented by a matrix, denoted as  $M$ . The equation describes this transfer matrix:

$$\vec{q}_B = M(z_s|z_0) \vec{q}_0. \quad (5.16)$$

And

$$M(z_s|z_0) = R_2 M_2 R_1 M_1. \quad (5.17)$$

where  $\vec{q}$  represents the position vector of a particle in the phase space. The transfer matrix  $M(z_s|z_0)$  can be written as the product of individual matrices:  $R_2, M_2, R_1, M_1$ , where  $M_1$  and  $M_2$  are the transfer matrices for the first and second solenoids under magnetic fields  $B_1$  and  $B_2$ , respectively.  $R_1$  and  $R_2$  are rotation matrices that decouple the particle motion into two-dimensional spaces.

Thus, in a simplified 2-dimensional space, the transfer equation becomes:

$$\begin{pmatrix} X \\ P_X \end{pmatrix} = e^{-i(\xi_1 + \xi_2)} \begin{pmatrix} M_{11} & M_{12} \\ M_{21} & M_{22} \end{pmatrix} \begin{pmatrix} X_0 \\ P_{X_0} \end{pmatrix}. \quad (5.18)$$

where  $X$ ,  $P_X$ ,  $X_0$ , and  $P_{X_0}$  represent the phase space coordinates of the particle. Specific equations give the individual elements of the matrix  $M$ , and  $\xi_1$  and  $\xi_2$  represents the rotation angles.

where

$$M_{11} = \cos \chi_1 \cos \chi_2 - \frac{B_1}{B_2} \sin \chi_1 \sin \chi_2 \quad (5.19)$$

$$M_{12} = \frac{2}{eB_1} \sin \chi_1 \cos \chi_2 + \frac{2}{eB_2} \cos \chi_1 \sin \chi_2 \quad (5.20)$$

$$M_{21} = -\frac{eB_2}{2} \cos \chi_1 \sin \chi_2 - \frac{eB_1}{2} \sin \chi_1 \cos \chi_2 \quad (5.21)$$

$$M_{22} = -\frac{B_2}{B_1} \sin \chi_1 \sin \chi_2 + \cos \chi_1 \cos \chi_2. \quad (5.22)$$

Using the quadratic form of Eq. 5.18:

$$\begin{aligned} XX^* + \left(\frac{2}{eB_2}\right)^2 P_X P_X^* &= \left[ \cos^2 \chi_1 + \left(\frac{B_1}{B_2}\right)^2 \sin^2 \chi_1 \right] x_0 x_0^* \\ &+ \left[ \left(\frac{2}{eB_1}\right)^2 \sin^2 \chi_1 + \left(\frac{2}{eB_2}\right)^2 \cos^2 \chi_1 \right] p_{x_0} p_{x_0}^* \\ &+ \frac{2}{eB_1} \sin \chi_1 \cos \chi_1 \left[ 1 - \left(\frac{B_1}{B_2}\right)^2 \right] (x_0^* p_{x_0} + x_0 p_{x_0}^*). \end{aligned} \quad (5.23)$$

where  $X \equiv x + iy$  and  $P_X \equiv p_x + ip_y$ .  $X^*$  and  $P_X^*$  are the conjugate values. The same transformation can be applied in the (y,y') - plane.

In a solenoid, the particles are held in an ellipse in  $[x \ x_p; y \ y_p]$  planes; this volume is constant due to the Liouville theorem; thus, This may be expressed as:

$$\left(\frac{eB_2}{2}\right)^2 XX^* + P_X P_X^* = \left(\frac{eB_2}{2}\right)^2 (x^2 + y^2) + (p_x^2 + p_y^2) = \text{Cte}. \quad (5.24)$$

and since  $B_2$  is constant along the second solenoid

$$XX^* + \left(\frac{2}{eB_2}\right)^2 P_X P_X^* = \text{Cte}. \quad (5.25)$$

Using (Eq. 5.24) and (Eq. 5.10), it can be written

$$\text{Cte} - \left(\frac{2}{eB_2}\right)^2 P_X P_X^* \leq a^2. \quad (5.26)$$

### 5.3.1 Longitudinal acceptance

The volume acceptance  $V$  (acceptance ellipses in the phase space) of the QWT is then defined from the integrated points of the phase space that satisfy (Eq. 5.10)

$$V_{QWT} = \int_{XX^* \leq a^2} dx \, dy \, dp_x \, dp_y. \quad (5.27)$$

and can be written [16]

$$V(\chi_1) = \frac{2\pi^2}{3} \left(\frac{eB_2 a^2}{2}\right)^2 \left[ 1 - \left( 1 - \frac{1}{\sin^2 \chi_1 + \left(\frac{B_1}{B_2}\right)^2 \cos^2 \chi_1} \right)^{\frac{3}{2}} \right]. \quad (5.28)$$

The QWT can be optimized to collect positrons effectively at specific momenta by adjusting its parameters ( $B_1$ ,  $L_1$ ,  $B_2$ ). The collection depends on the longitudinal momentum ( $p_0$ ) and is represented by the volume acceptance  $V(\chi_1)$ , as shown in equation Eq. 5.28. To locate the maximum QWT volume acceptance  $V_{\max}$ , the following equation is solved::

$$\frac{dV(\chi_1)}{d\chi_1} = 0. \quad (5.29)$$

The maximum value for the QWT volume acceptance is achieved when the rotation angle in the short solenoid  $\chi_1 = \frac{\pi}{2}$ . At this point, the longitudinal particle momentum is optimized:

$$p_0 = \frac{eB_1L_1}{n\pi}. \quad (5.30)$$

Eq. 5.30 reveals the dependency of the positron momentum with the magnetic field  $B_1$  and the high field region  $L_1$ , the QWT volume acceptance is maximized for a particular rotation angle  $\chi_1 = \frac{\pi}{2}$  which corresponds to particles completing half a helical period within the short lens (in a helix, one period correspond to  $2\pi$ ), therefore at this particular rotation angle, the maximized QWT volume acceptance is given by:

$$V\left(\frac{\pi}{2}\right) = \frac{2\pi^2}{3} \left( \frac{eB_2a^2}{2} \right)^2. \quad (5.31)$$

The acceptance volume expression of the quarter-wave transformer is closely affected by both the size of the cavity iris  $a$  and the strength of the solenoid magnetic field  $B_2$ . It's important to note that at a specific central momentum  $p_0$ , the volume acceptance of the QWT is equivalent to that of the AMD. Alternatively, using the derivative of the QWT volume acceptance, the correlation between the length of the high field region  $L_1$  and the magnetic field intensity  $B_1$  can be established to optimize the longitudinal acceptance for a specific momentum, as illustrated in Fig. 5.4. For different positron momenta, the solenoid length shortens as the magnetic field,  $B_1$ , strengthens. Consider a QWT designed to have a field limit of 2.5 T to bypass the need for superconductive solenoids. At a momentum of 60 MeV/c, this results in a solenoid length of 0.25 m, as shown in Fig. 5.4. The magnetic field strength,  $B_1$ , directly affects the value of the collected  $p_0$ . As an illustration, a momentum of 10 MeV/c requires a field of about 0.5 T, as depicted in Fig. 5.4.

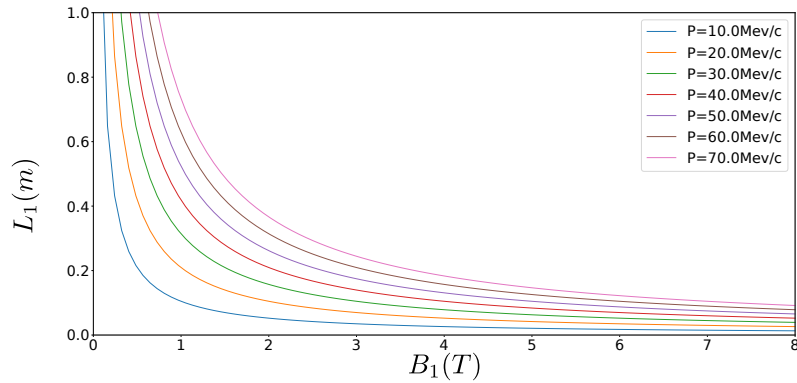


Figure 5.4: Variation of the short solenoid length versus the magnetic field at optimum QWT volume acceptance

With this understanding of the solenoid parameters and their impact, the primary objective becomes clear. The aim is to optimize the transmitted positron yield at 60 MeV/c while ensuring a high positron polarization, as detailed in Table 4.4, especially when operating in the polarized mode for maximum Figure of Merit.

Having established the significance of solenoid parameters and their influence on the system, it is crucial to delve into specific metrics that quantify the system efficiency. Notably, the QWT volume acceptance half-width is an important metric. It defines the accepted momentum spread and can be described by:

$$\frac{\Delta p}{p_0} = \frac{4}{\pi} \frac{B_2}{B_1}. \quad (5.32)$$

Equation (5.32) highlights the significance of selecting the optimum central momentum  $p_0$ : as  $p_0$  increases, so does  $B_1$ ; contrarily, for low momentum collection, the small  $p_0$  corresponds to a reduced  $B_1$ , resulting in a comparable momentum spread at a fixed  $B_2$ .

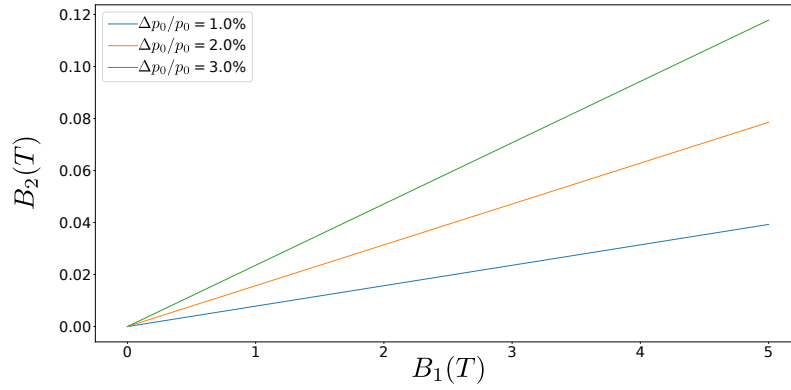


Figure 5.5:  $B_2$  Vs  $B_1$  for various  $\Delta p/p_0$

Figure 5.5 illustrates the connection between the magnetic region  $B_1$  and the magnetic field  $B_2$ . An increased  $B_2$  corresponds to a broader energy spread. Given the prior explanation of CEBAF longitudinal injection requirement, the objective is to use the QWT to efficiently capture a considerable number of positrons within a concise energy spread while maintaining a higher polarization ( $\text{FoM}^{\text{max}}$ ). Subsequent sections will delve into the transverse acceptance characteristics of the QWT.

### 5.3.2 Transverse acceptance

The first accelerating section downstream of the target will house solenoids with weak magnetic field  $B_2$  to keep the positron trajectories focused; the accelerating section imposes a transverse acceptance that the QWT must match. From Eq. 5.28 and considering a rotation angle  $\chi_1 = \frac{\pi}{2}$ , the following expression is derived:

$$X X^* + \left[ \frac{2}{e B_2} \right]^2 = \left[ \frac{B_1}{B_2} \right]^2 X_0 X_0^* + \left[ \frac{2}{e B_1} \right]^2 P_{X_0} P_{X_0^*} = \text{Cte}. \quad (5.33)$$

which can be expressed in a cylindrical coordinate system as

$$\left[ \frac{B_1}{B_2} \right]^2 r_0^2 + \left[ \frac{2}{e B_1} \right]^2 \left[ P_{r_0}^2 + \frac{P_{\phi_0}^2}{r^2} \right] = \text{Cte}. \quad (5.34)$$



where  $(r_0, P_{r_0}, P_{\phi_0})$  are the coordinates of the particles at target. Using Eq.5.10 and Eq.5.26, the following result is obtained:

$$\left[\frac{B_1}{B_2}\right]^2 r_0^2 + \left[\frac{2}{eB_1}\right]^2 \left[P_{r_0}^2 + \frac{P_{\phi_0}^2}{r^2}\right] = a^2 + \left[\frac{2}{eB_2}\right]^2 \frac{P_{\phi_0}^2}{a^2}. \quad (5.35)$$

which defines the hyper-ellipsoid volume of the acceptance. The maximum extension in the spatial dimension, that is, the axis of the ellipsoid in the position space, is determined at  $P_{r_0}=P_{\phi_0}=0$  providing the radial acceptance of the QWT

$$r_0^{max} = \frac{B_2}{B_1} a. \quad (5.36)$$

This relationship indicates that any particle generated at a radial distance from the target greater than  $r_0^{max}$  will not reach the  $(L_1 + L_2)$  exit. Likewise, the acceptance of radial momentum can be described as follows:

$$\theta_{max} = \frac{eB_1 a}{2p_0} \left[1 + \frac{B_2}{B_1}\right]. \quad (5.37)$$

### 5.3.3 Comparison of collection systems

Upon comparing the two systems with identical magnetic fields and optimized lengths, it becomes apparent the AMD does not filter the momentum. Comparing the transverse acceptances of the QWT (Eqs. (5.36)-(5.37)) and the AMD reveals the relationships

$$r_0^{AMD} = \sqrt{\frac{B_1}{B_2}} r_0^{QWT} \quad (5.38)$$

$$\theta_{max}^{AMD} \approx \sqrt{\frac{B_2}{B_1}} \theta_{max}^{QWT}. \quad (5.39)$$

These equations highlight a larger transverse size acceptance for AMD but a smaller transverse momentum acceptance. As a result, this leads to a reduced angular acceptance for a given momentum of interest.

When considering the same technology in both devices (i.e., identical  $B_1$  and  $B_2$  in the QWT and the AMD) for positron collection, selecting the QWT to capture larger angle becomes more aligned with the specific positron source requirements at JLab. This choice offers advantages that address the needs of the positron program.

### 5.3.4 QWT optimization

Given the parameters for the system:

- Magnetic field  $B_1 = 2.5$  T
- Magnetic field  $B_2 = 0.05$  T
- Accelerator aperture  $a = 18$  mm

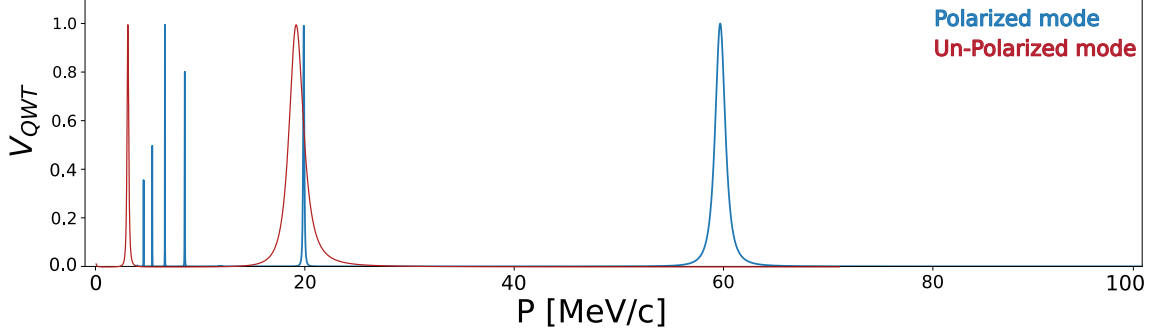


Figure 5.6: QWT volume acceptance shows the strong dependency between the system acceptance and the positron momentum.

The maximum possible radius and angle at the target, which represent the phase space accepted by the QWT, can be defined as:

$$r_0^{\max} = 0.36 \text{ mm} \quad (5.40)$$

$$\Delta\theta^{\max} = \pm 6.3^\circ \quad (5.41)$$

For positrons with momentum  $p_0 = 60 \text{ MeV/c}$ , efficient collection is achieved when confined within an angle  $\Delta\theta^{\max} = \pm 6.3^\circ$ . Fig. 4.14 indicates that most of these positrons are concentrated within this angle. By reducing their transverse angular divergence ( $x_p$  and  $y_p$ ), adjustments are made to their transverse phase space.

A minimal value for  $B_2$ , specifically  $B_2 = 0.05 \text{ T}$ , was selected based on Eq. 5.32. This choice aims to maintain positron polarization at a high level while minimizing energy spread.

According to Tab. 3.2, the expected energy for positron injection at the CEBAF-NL is projected to be 123 MeV. By gathering positrons at 60 MeV, an optimal FoM value is ensured. To reach the target energy of 123 MeV, an acceleration of roughly 63 MeV is required post-capture, which reduces the energy spread.

A criterion of  $\Delta p/p_0 \leq 1\%$  is established for the injection region (NL). The use of  $B_2$  aids in capturing highly polarized positrons in polarized mode while ensuring a minimal energy spread.

### Polarized mode

Building on the parameters established in the preceding discussion, attention is directed to the polarized mode of the system. Using the setup ( $B_1 = 2.5 \text{ MeV/c}$ ,  $L_1 = 0.25 \text{ m}$ ,  $B_2 = 0.05 \text{ T}$ ) in the ELEGANT simulation software, there is an expectation of collecting highly polarized positrons at the peak of the Figure of Merit ( $\text{FoM}_{\max}$ ) within a constrained energy spread.

A primary design objective for this mode is efficiently managing the transverse phase space. Observing the positron distribution right at the target exit exposes characteristics such as compact beam size and pronounced angular divergence. With the system's configurations, the goal is to transform this distribution to have a larger spot size and significantly reduced angular divergence by the time it reaches the QWT exit.

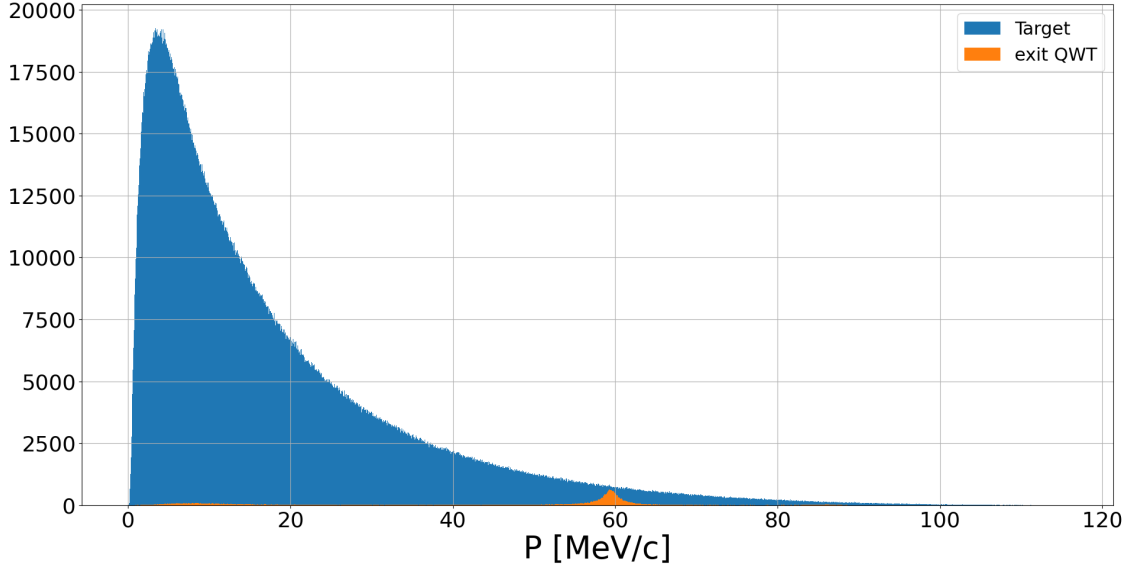


Figure 5.7: Positron momentum distribution at the exit of the target (blue) and at the exit of the QWT (orange)

Fig. 5.7 displays the positron momentum distributions at the target exit (in blue) and the QWT exit (in orange). As anticipated, the results validate the effectiveness of the QWT, particularly when combined with the weaker magnetic field region  $B_2$ . This configuration selectively allows positrons around  $p_0 = 60$  MeV/c to exit from  $L_2$ . The presence of a few positrons at lower momenta can be explained by harmonics within the QWT volume acceptance, as illustrated in Fig. 5.6.

Fig. 5.8, shows the positron longitudinal distribution at the exit of  $L_2$ . The central density around  $p_0 = 60$  MeV/c corresponds to particles fitting the angular divergence at the 60 MeV/c momentum level. Notably, this distribution exhibits minimal momentum dispersion, underscoring the QWT optimization capabilities in the longitudinal phase space plane.

The outcomes highlight not only the efficacy of the QWT in ensuring an optimal phase space rotation ( $\chi = \frac{\pi}{2}$ ) at its exit but also its capability to capture highly polarized positrons.

In Fig. 5.9, the positron transverse plane  $(x, x_p)$  and  $(y, y_p)$  are displayed at two locations: the target exit (in blue) and the QWT exit (in red). The successful achievement of the  $\frac{\pi}{2}$  transverse phase space ellipse is observed by appropriately combining  $B_1$  and  $B_2$ . This configuration effectively reduces the transverse angular divergence (transverse positron momentum  $x_p = \frac{p_x}{p_0}$ ,  $y_p = \frac{p_y}{p_0}$ ). Indeed, the  $\frac{\pi}{2}$  rotation transforms the initial vertically-oriented phase space ellipse, with substantial angular divergence, into a horizontally-oriented one with significantly reduced divergence.

By examining the positrons passing through the QWT from the initial positron distribution at the target, the angular components of the particles become pictured. It becomes apparent that the collected positrons are concentrated within  $\Delta\theta \leq 12^\circ$ , aligning with our earlier estimation (Eq. 5.41).

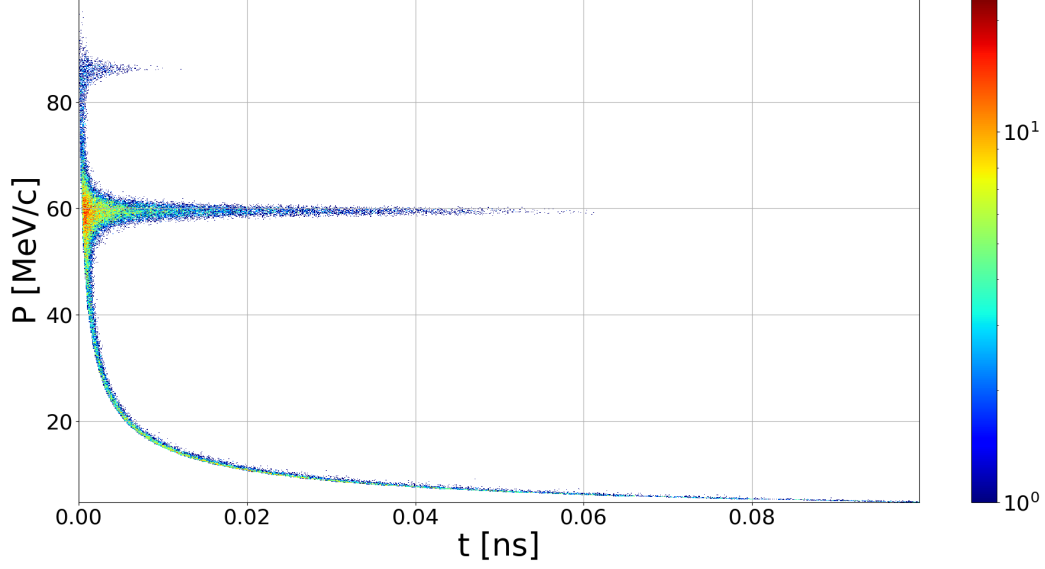
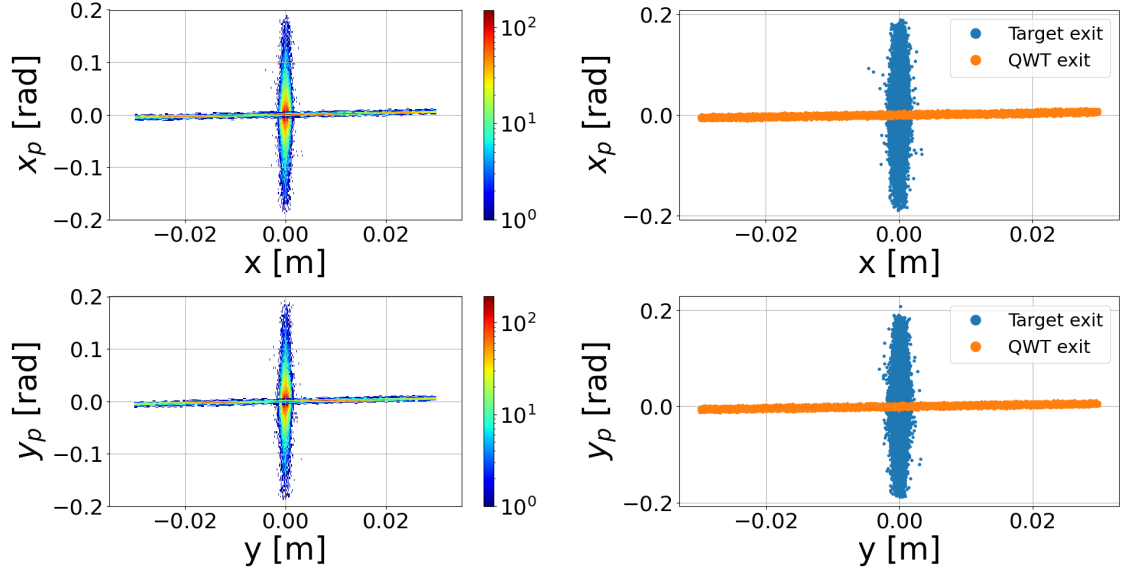


Figure 5.8: Longitudinal positron phase space at the QWT exit.


 Figure 5.9: Positron transverse space  $x$ ,  $x_p$  and  $y$ ,  $y_p$  through the QWT

### UnPolarized mode

To enhance positron collection intensity, adjustments are made to the QWT magnetic field. The goal is to shift the central energy that maximizes the QWT volume acceptance, enabling the collection of positrons at lower momentum values. By adjusting the magnetic field  $B_1$  and maintaining other collection parameters, a new QWT setup emerges:  $B_1 = 1.3$  T,  $L_1 = 0.25$  m, and  $B_2 = 0.05$  T, optimized for capturing positrons at  $p_0 = 19$  MeV/c. The volume acceptance of this configuration can be seen in Fig. 5.6.

Turning to the analysis of Fig. 5.11, the centered positron collection around  $p_0 = 19$  MeV/c becomes evident. Consistent with predictions, the positron momentum distribution showcases not only a heightened yield but also a diminished presence

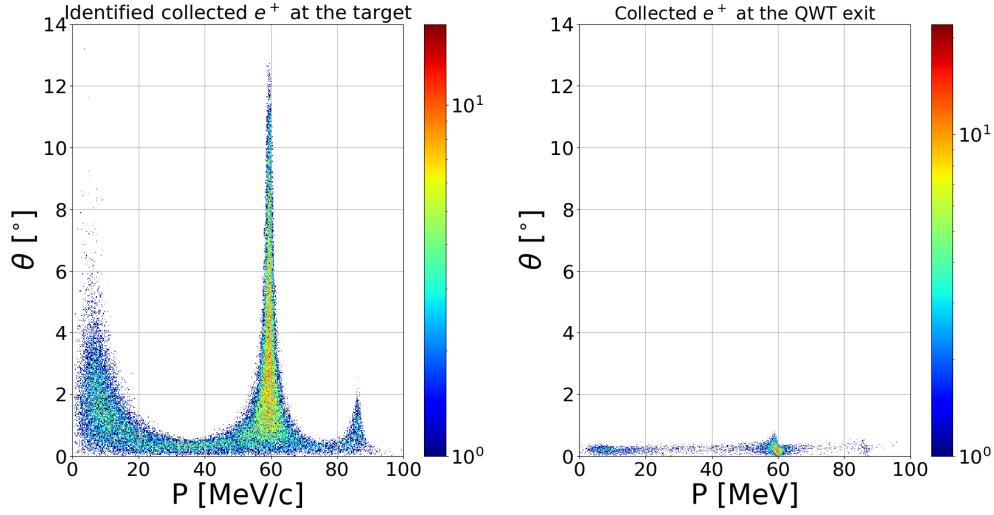


Figure 5.10: Angular Distribution of Collected Positrons: Left Panel - Positrons Identified at Target Exit, Right Panel - Positrons Transmitted through QWT Exit

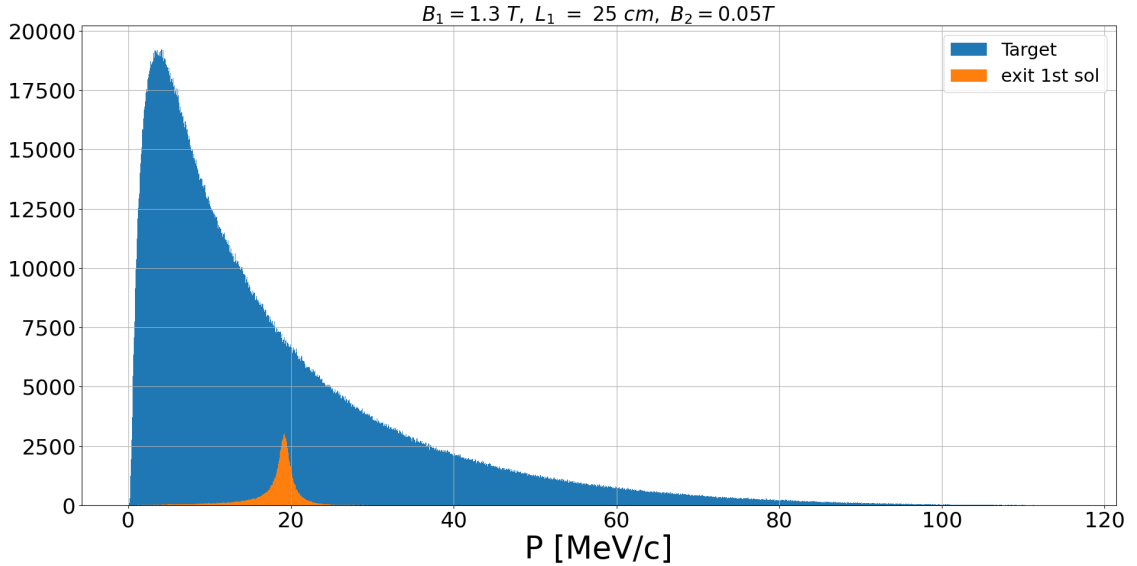


Figure 5.11: Longitudinal positron momentum distribution, collecting at the QWT exit 19 MeV/c, the same short solenoid length is kept for this configuration

of harmonics. This aligns seamlessly with the QWT volume acceptance tailored for the unpolarized operational mode.

Considering the operational modes, the unpolarized mode showcases a distinct approach, with positrons being collected at a notably lower energy. This amounts to roughly a third of the central momentum observed in the polarized mode. Such a shift to a lower energy inherently permits a more expansive energy spread. In juxtaposition, the polarized mode entails the collection of positrons around the 60 MeV, followed by an acceleration process to meet the CEBAF injection energy of 123 MeV. Crucially, this advancement mandates achieving a tightly constrained energy spread, specifically,  $\sigma_{\Delta p/p_0} \leq 1\%$ . This restriction implies that rigorous energy spread requirements bind the jump from 60 MeV to 123 MeV. On the other hand, the unpolarized configuration can accommodate a more generous energy spread,

extending up to  $\sigma_{\Delta p/p_0} \leq 6\%$ . This capacity significantly enhances positron yield following the collection system. At the  $L_2$  exit, the longitudinal positron phase space is represented in Fig. 5.12:

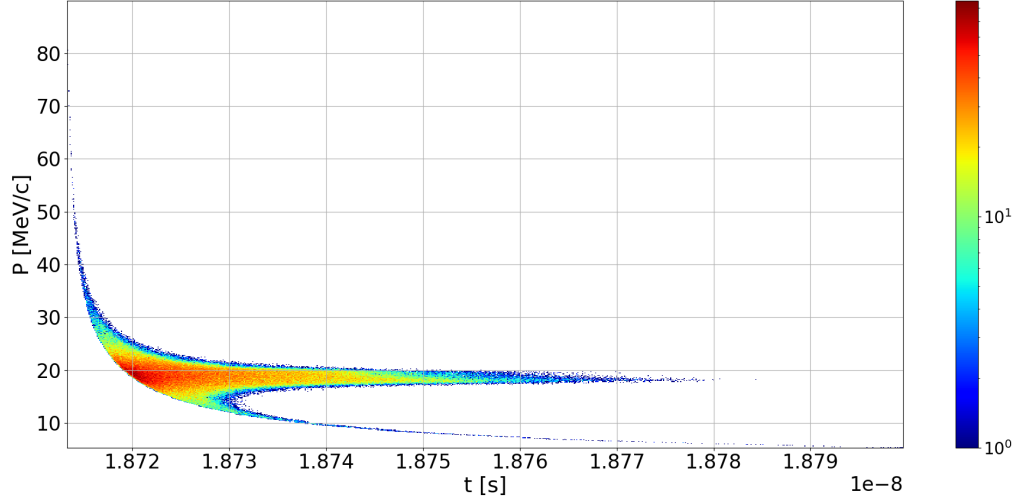


Figure 5.12: Positron longitudinal phase space at the QWT exit

At 19 MeV, the positron density is most concentrated. However, the collection is not maximized, as indicated by Fig. 5.11. This figure distinctly reveals that slightly less than half of the available positron yield at 19 MeV has been captured. This outcome can be attributed to adjusting the collection central momentum, driven by the maximized volume acceptance, towards lower energies. This shift creates a challenge due to the misalignment of the transverse angular divergence acceptance with the wide angular distribution at low energies. The reduction in  $B_1$  results thus in a lower central momentum value, but also in a small  $\Delta\theta^{\max}$  range. However, Fig. 4.14 indicates the need to increase accepted  $\Delta\theta^{\max}$  up to a 60-degree angular QWT acceptance at lower energies. Unfortunately, maintaining the same QWT length limits the flexibility to increase this quantity, leading to a lower-than-expected positron yield at low energy.

With the setup of  $B_1 = 1.3$  T,  $L_1 = 0.25$  m, and  $B_2 = 0.05$  T, the anticipated maximum angle for transverse collection is around  $\Delta\theta^{\max} = \pm 9.16^\circ$ . This angle is quite close to the  $\Delta\theta^{\max} = \pm 6.3^\circ$  seen in the polarized mode. Although a higher positron collection was anticipated at 19 MeV, it is clear that efficient low-energy collection requires a broader angular acceptance. This suggests the need for a specially designed QWT.

Upon examining the positron density at the exit of the tuned QWT, it becomes apparent that the majority of collected positrons are centered around 19 MeV. Owing to the reduced harmonics in this setup, in agreement with the QWT volume acceptance for the unpolarized mode.

As shown in Fig. 5.13, the QWT retains its effectiveness in optimizing transverse phase space rotation. The rotation of both the  $(x, x_p)$  and  $(y, y_p)$  planes by an angle of  $\pi/2$  aligns impeccably with the computed values.

In Fig. 5.14, the angular distribution versus momentum of the collected positrons at the QWT exit is illustrated in the right panel. By correlating this with the same transmitted distribution from the target exit, showcased in the left panel, the angular

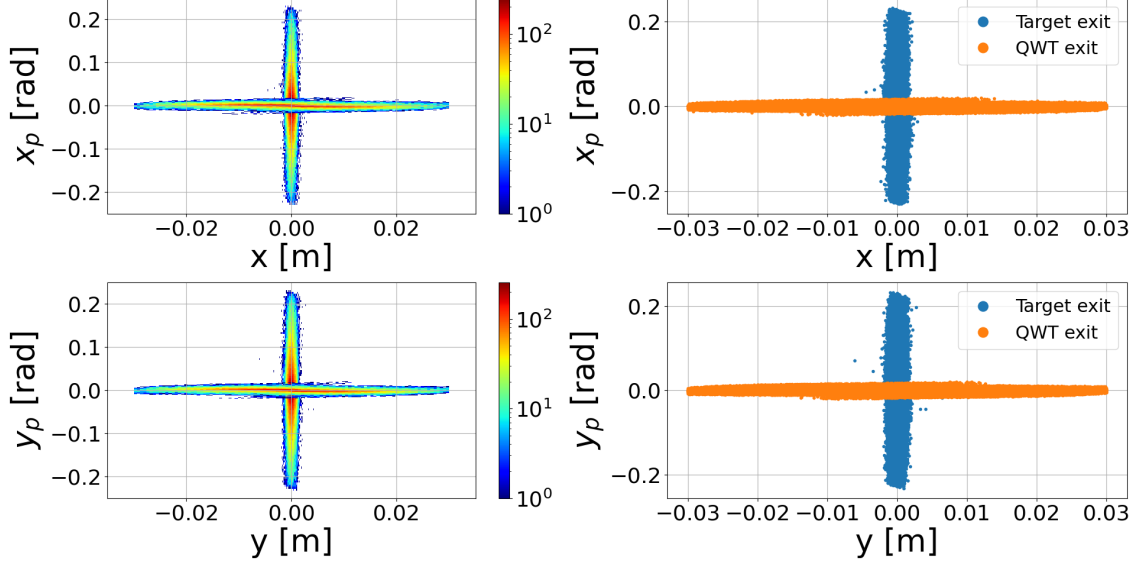


Figure 5.13: Positron transverse phase space at different locations: at the target exit and at the QWT exit

distribution prior to matching emerges.

A key observation from this figure is that the QWT captures the positrons up to a maximum angle of  $\theta = 18$  degrees, in agreement with the previous estimation. This angle is significantly small when overlapped with the polarized mode maximum collection angle. Furthermore, at 19 MeV, there is a notable increase in the positron yield. The right panel underscores the direct impact of the  $\pi/2$  rotation executed by the QWT on diminishing the positrons transverse component. As a result, the positron divergence undergoes a significant reduction, descending from an initial 18 degrees. Given the same positron count, this transverse rotation facilitates a more seamless integration with the subsequent elements of the positron injector.

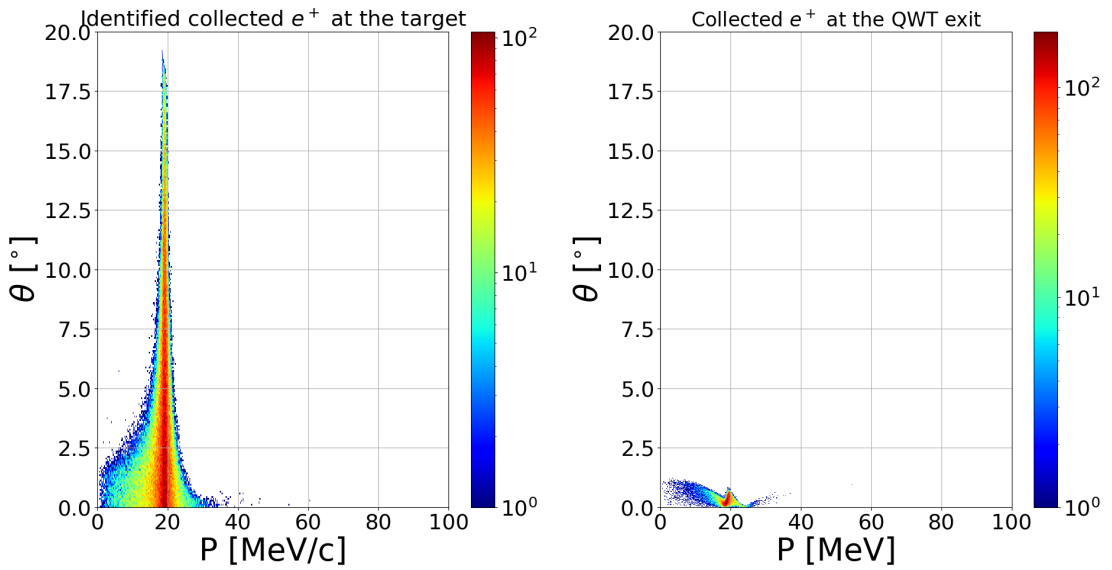


Figure 5.14: Angular Distribution of Collected Positrons: Left Panel - Positrons Identified at Target Exit, Right Panel - Positrons Transmitted through QWT Exit

The decision to set the central QWT volume acceptance momentum at 19 MeV, rather than selecting lower energies with potentially higher positron yield, is based on the same optimized QWT configuration. This configuration was initially designed for the polarized operational mode, specifically for positron collection at 60 MeV. In this setup, the QWT maintains a consistent short solenoid length of  $L_1 = 0.25\text{m}$ . The only possible approach to shifting the central momentum to lower values involves reducing the magnetic field  $B_1$  within the first solenoid. This adjustment in  $B_1$  also reduces the angular acceptance, as governed by Eq. (5.37), which determines the angular acceptance. To achieve a QWT capture centered around 10 MeV, it becomes necessary to adjust  $B_1$  to approximately  $B_1 = 0.5\text{T}$  when keeping the same length  $L_1$  (refer to Fig. 5.4).

Using Eq. 5.37, the maximal collected angle through the QWT will be:

$$\delta\theta^{\max} = \pm 7.4^\circ \quad (5.42)$$

At 10 MeV, the value is too small for efficient positron collection at around 10 degrees. The QWT angular acceptance is considerably distant from the range of high positron yield aimed for (refer to Fig. 4.14).

### Modifying $L_1$ : an alternative approach

An alternative approach involves modifying  $L_1$  to improve the QWT angular acceptance. Considering the potential adjustment of the first solenoid length, the goal is to improve the QWT angular acceptance. The aim is to optimize this revised QWT setup with a central momentum value of  $p_0 = 6\text{ MeV}/c$  to maximize positron collection.

To establish the QWT volume acceptance at 6 MeV, the following configuration is employed:

Parameter	Value
$B_1$	1.27 T
$L_1$	5 cm
$B_2$	0.05 T

Table 5.1: QWT configuration for 6 MeV momentum capture

Using Eq. 5.37 the related angular acceptance is:

$$\Delta\theta^{\max} = \pm 33^\circ \quad (5.43)$$

The newly calculated value for  $\Delta\theta^{\max}$  is found to be  $\pm 33^\circ$ . This value indicates a substantial improvement in angular acceptance within the QWT, achieved by introducing an additional tunable parameter,  $L_1$ , to optimize the QWT configuration.

The resulting positron distribution in Fig. 5.16 illustrates the longitudinal positron phase space at the QWT exit:

The enhanced yield in this reconfigured setup is evident. The QWT efficiently collects all available positron yield within the relevant energy spread, determined by the ratio  $\frac{B_2}{B_1}$  (refer to (Eq. 5.32)). The specific values chosen for  $B_1$  and  $L_1$  are one possible solution among several alternatives that can yield comparable results.

The re-optimization of the QWT configuration significantly enhances the collection efficiency in the angular plane, enabling the capture of the entire available



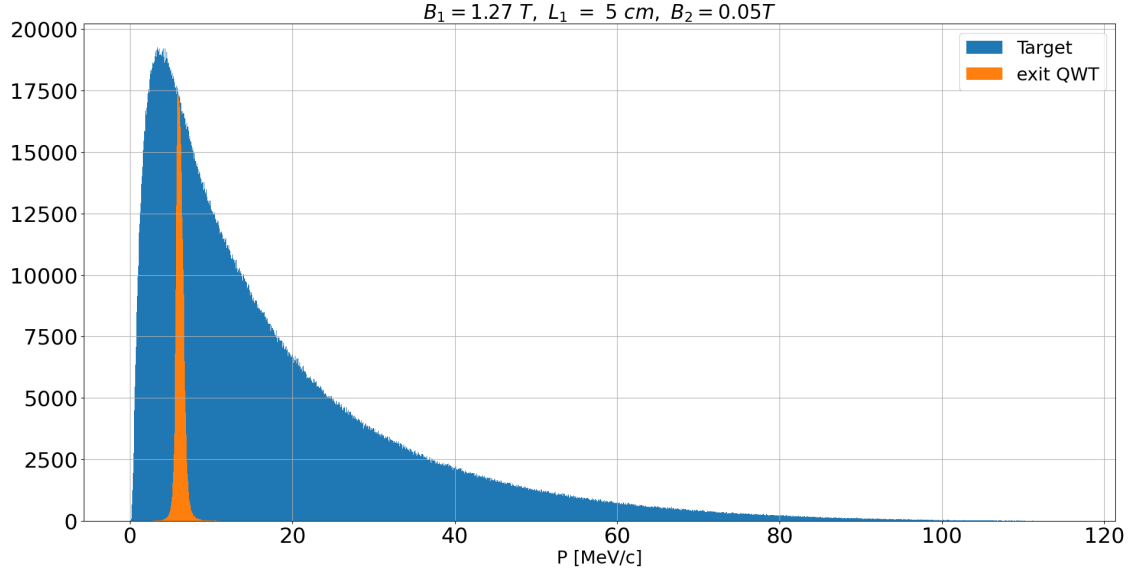


Figure 5.15: Longitudinal unpolarized positron collection phase space

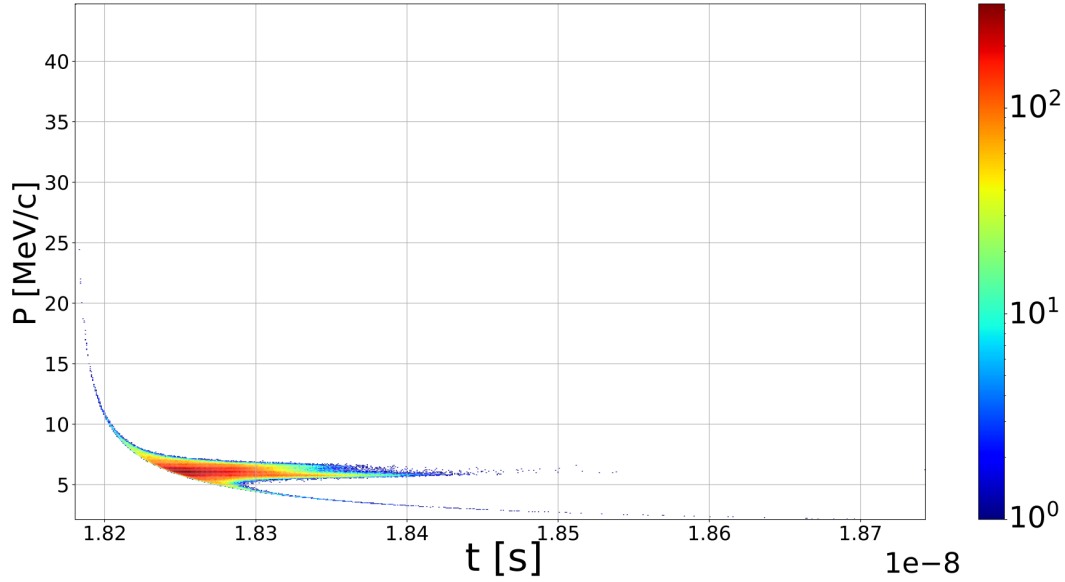


Figure 5.16: Longitudinal positron phase space at the re-optimized QWT exit

positron yield within the accepted angle. This improvement is evident in Fig. 5.16, visually representing the collected positron longitudinal phase space at the QWT +  $L_2$  exit. A notable observation is a considerable increase in positron yield compared to the previous collection at 19 MeV.

The center of the highest positron density is at 6 MeV, which aligns with the observations from Fig. 5.15.

Regarding transverse phase space rotation, the updated QWT configuration achieves a  $\frac{\pi}{2}$  rotation, significantly improving the capture efficiency and alignment with downstream beamline sections. This is supported by Fig. 5.17, where the transverse components  $x_p$  and  $y_p$  (left panel) exhibit a more pronounced phase space distortion along the vertical axis (Angular component) compared to previous QWT configurations. This distortion results from the extensive angular acceptance enabled

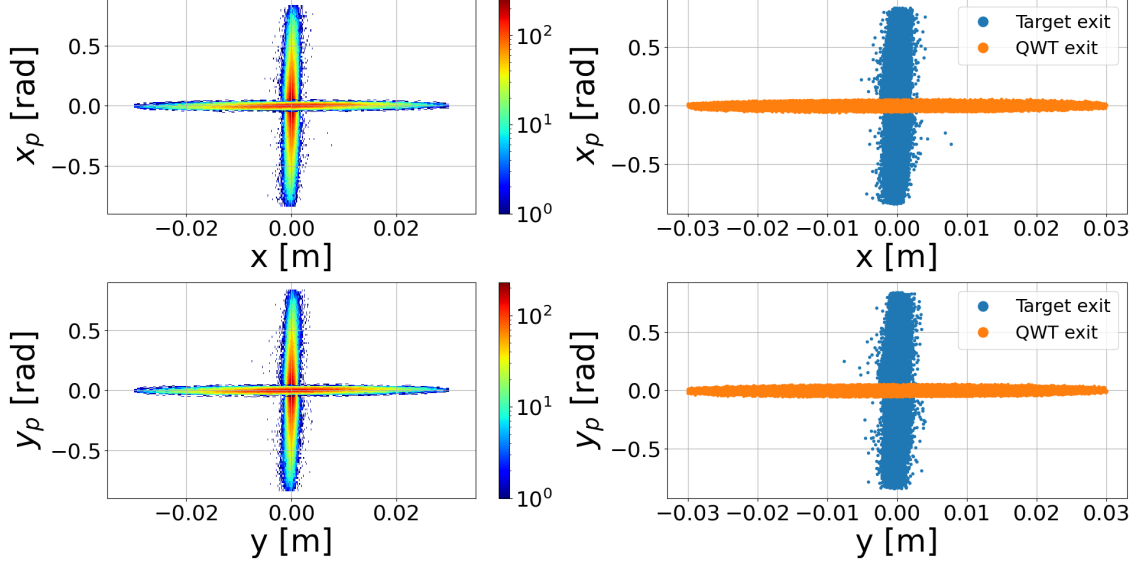


Figure 5.17: Positron transverse phase space at different locations : at the target exit and at the re-optimized QWT exit

by the enhanced QWT. As a result, the new configuration can effectively capture more positrons at wider angles, enabling the accurate  $\frac{\pi}{2}$  phase space rotation and improved matching with subsequent beamline sections.

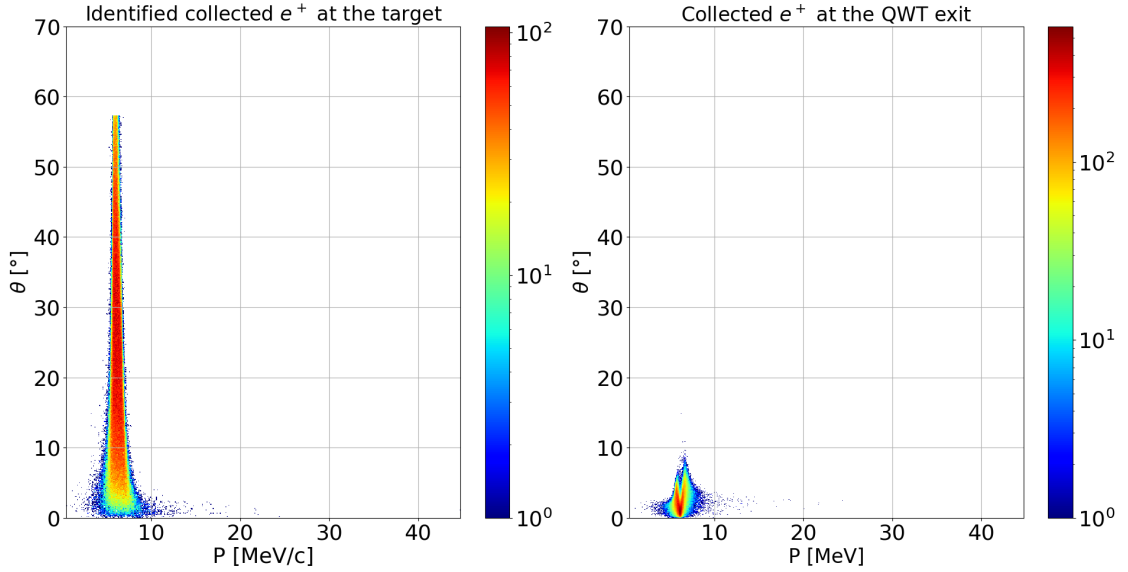


Figure 5.18: Angular distribution of collected positrons: left panel - positrons identified at target exit, right panel - positrons transmitted through the re-optimized QWT Exit

Fig.5.19 Clearly illustrates the QWT remarkable efficiency in reducing angular divergence. The red curve shows the angular transverse expansion of the beam  $\sigma_{x_p}$ , which has substantially reduced from 0.6 rad at the QWT entrance to 0.01 rad at its exit. This reduction arises from the QWT ability to maintain the beam transverse phase space throughout its path. Consequently, the transverse beam size has expanded to approximately  $\sigma_x = 0.013$  m. Additionally, the influence of

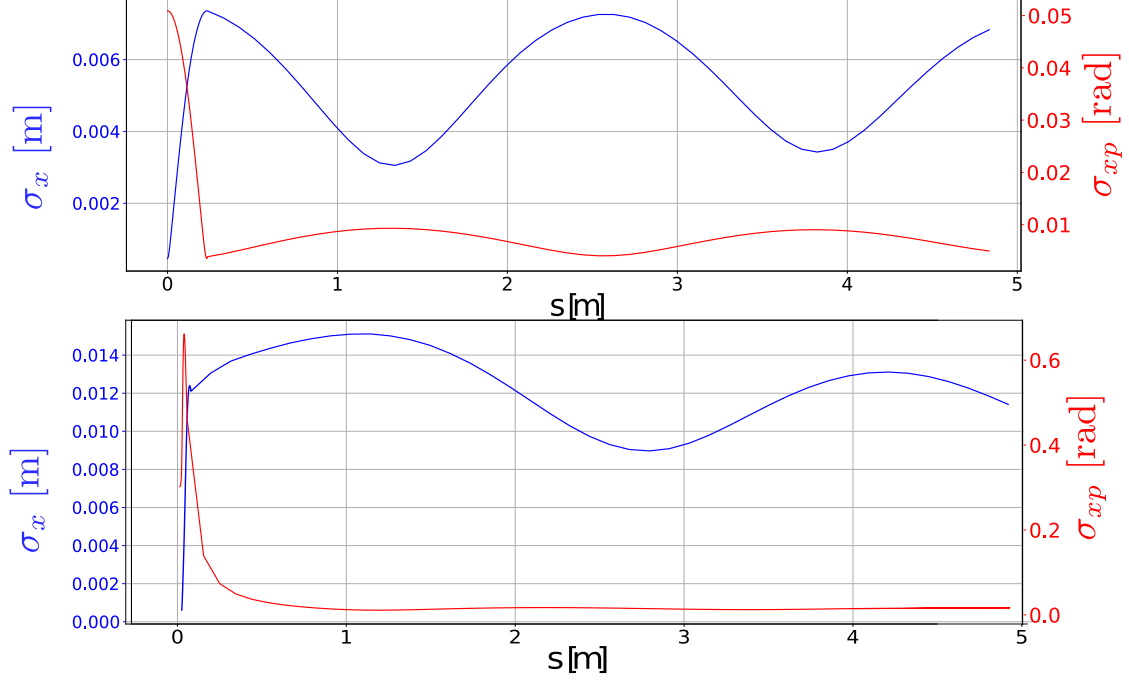


Figure 5.19: Effect of the QWT on the transverse and angular beam size, top: optimized QWT configuration for the polarized mode, bottom: re-optimized QWT for the unpolarized mode

the weak magnetic field  $B_2$  within the long solenoid is evident, as it confines the positron within a limited size while maintaining a consistent focusing effect along the accelerating sections.

## 5.4 Capture linac

A practical method to enhance the collection system involves reducing the quantities  $x_p$  and  $y_p$  through additional acceleration. Introducing an RF structure with a magnetic field  $B_2$  within the long solenoid can further reduce the angular divergence. The RF accelerating gradient can be expressed as:

$$E_f = -\frac{2\pi e V_0}{\lambda h} \sin \phi_{rf} \quad (5.44)$$

Here,  $\lambda$  signifies the RF wavelength,  $V_0$  is the on-crest voltage gain in the accelerating structure,  $E_f$  represents the final energy post-acceleration, and  $h$  denotes the energy chirp. This acceleration boosts the longitudinal component  $p_0$ , leaving the transverse momentum unaltered since the RF structure primarily affects the longitudinal particle component. Consequently, there is a substantial decrease in  $x_p = \frac{p_x}{p_0}$  and  $y_p = \frac{p_y}{p_0}$ , leading to a reduced angular positron distribution along the long solenoid with magnetic field  $B_2$ .

### Off-Crest RF operation for energy spread reduction

The CEBAF RF structure operates at a frequency of 1497 MHz, resulting in an RF period of 660 ps. To minimize the angular component of the beam as effectively as

possible, operating off-crest demonstrates advantageous configuring the beam to use the entire available accelerating gradient resulting in a significant increase in the  $p_0$  component.

Effectively using the RF structure involves leveraging its accelerating effect to reduce the energy spread of transmitted positrons through the second solenoid  $L_2$  in a similar manner. Given the restriction on collecting a wider energy spread, initiating energy spread reduction during capture using the Linac is prudent. Shifting the center of the longitudinal momentum positron distribution slightly in an off-crest setup enhances energy spread reduction from the maximum gradient value. This shift positions the slowest positrons at the peak of the accelerating gradient, prioritizing their acceleration. As a result, they undergo greater acceleration compared to other particles. Conversely, the fastest positrons experience a weaker gradient and undergo less acceleration. This approach converges both sides of the distribution towards a final energy denoted as  $E_f$ .

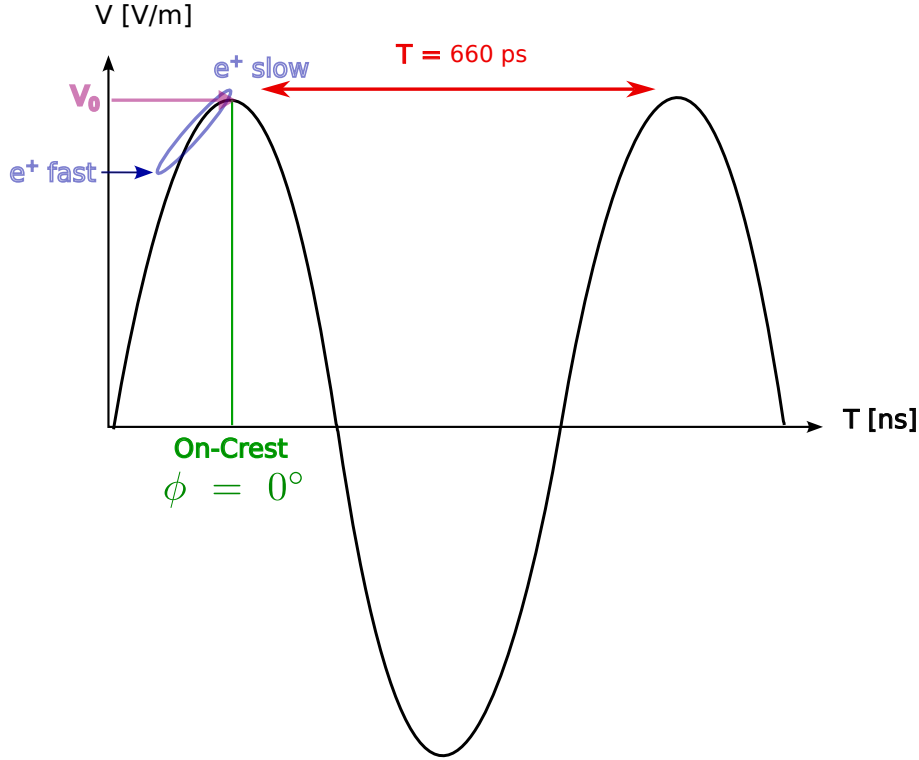


Figure 5.20: Capture linac: energy spread optimization procedure

In CEBAF, the CW beam limited maximum achievable accelerating gradient necessitates using a warm RF structure within the 1 or 2 MV/m limit, due to their heat dissipation limitations. Performing CW operations prevents the use of Superconducting Radio Frequency (SRF) cavities that offer higher gradients within a magnetic field in the long solenoid surrounding the capture linac due to the Meissner effect. This results in a breakdown of the superconducting state, causing increased electrical resistance, energy losses, and degradation of cavity performance. Assuming

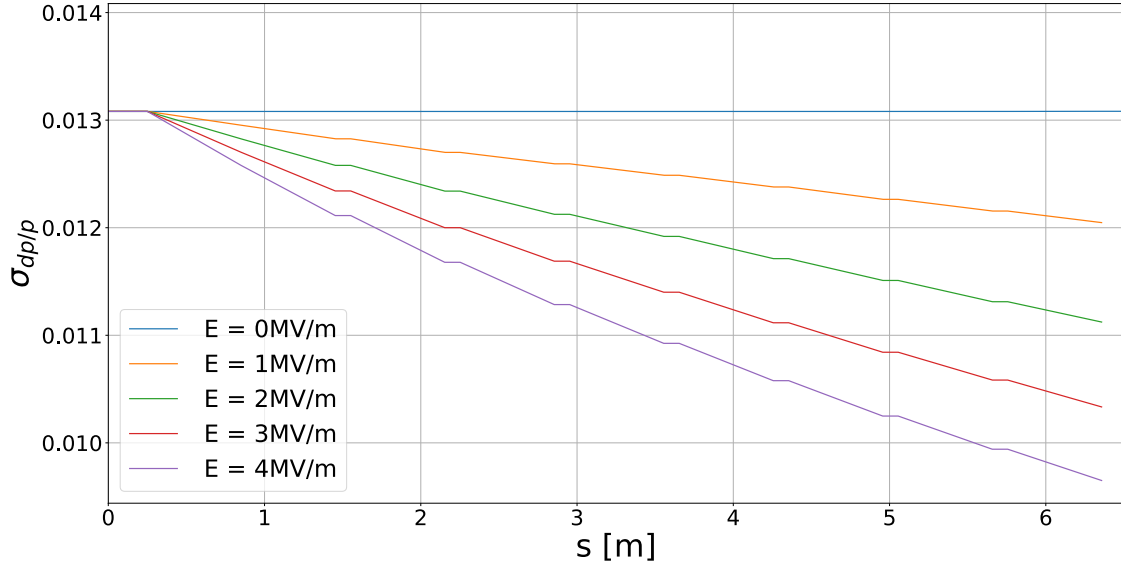


Figure 5.21: Energy spread of the collected positrons along the capture section

the placement of the SRF structure at the QWT exit and considering the short QWT magnetic field  $L_1$ , the high beam power poses a significant risk of inducing a superconducting breakdown.

Another contributing factor to the low available accelerating gradient in CEBAF is the CW mode of operation. With their heat dissipation limitations, normal conductive cavities cannot support a high accelerating gradient due to the potential for material breakdown arising from elevated temperatures.

To assess the impact of using normal conductive RF cavities along the capture section in conjunction with the magnetic field  $B_2$ , ELEGANT simulations were conducted to investigate the effect of the accelerating section on the positron phase space. The simulation results for energy spread reduction are presented in Fig.5.21. Diverse off-crest configurations were employed. For every cavity, a new value of  $\phi_0$  was computed based on the updated acceleration. Subsequently, the cavity phase value was adjusted to align with the position of the slowest positron in the phase of the highest accelerating gradient. Additionally, varying gradient values were used to understand their impact on the beam phase space.

The results from Fig.5.21 reveal that even with a higher gradient (4 MV/m), there is minimal reduction in energy spread after 6 meters. For instance, employing  $V_0 = 1\text{MV/m}$  across 6 meters while assuming the captured distribution is centered around 60 MeV, the final energy is approximately:

$$E_f = 65 \text{ MeV}$$

However, this reduction in energy spread is inadequate to significantly affect the final energy spread. In contrast, a 4 MV/m accelerating gradient yields a more substantial energy spread reduction for the same length. This underscores the significance of employing a high accelerating gradient. Consequently, using a low gradient necessitates very long accelerating sections to achieve notable outcomes in energy spread considerations.

Additionally, the consequences of employing such a low accelerating gradient on various positron phase space parameters are explored, including the transverse

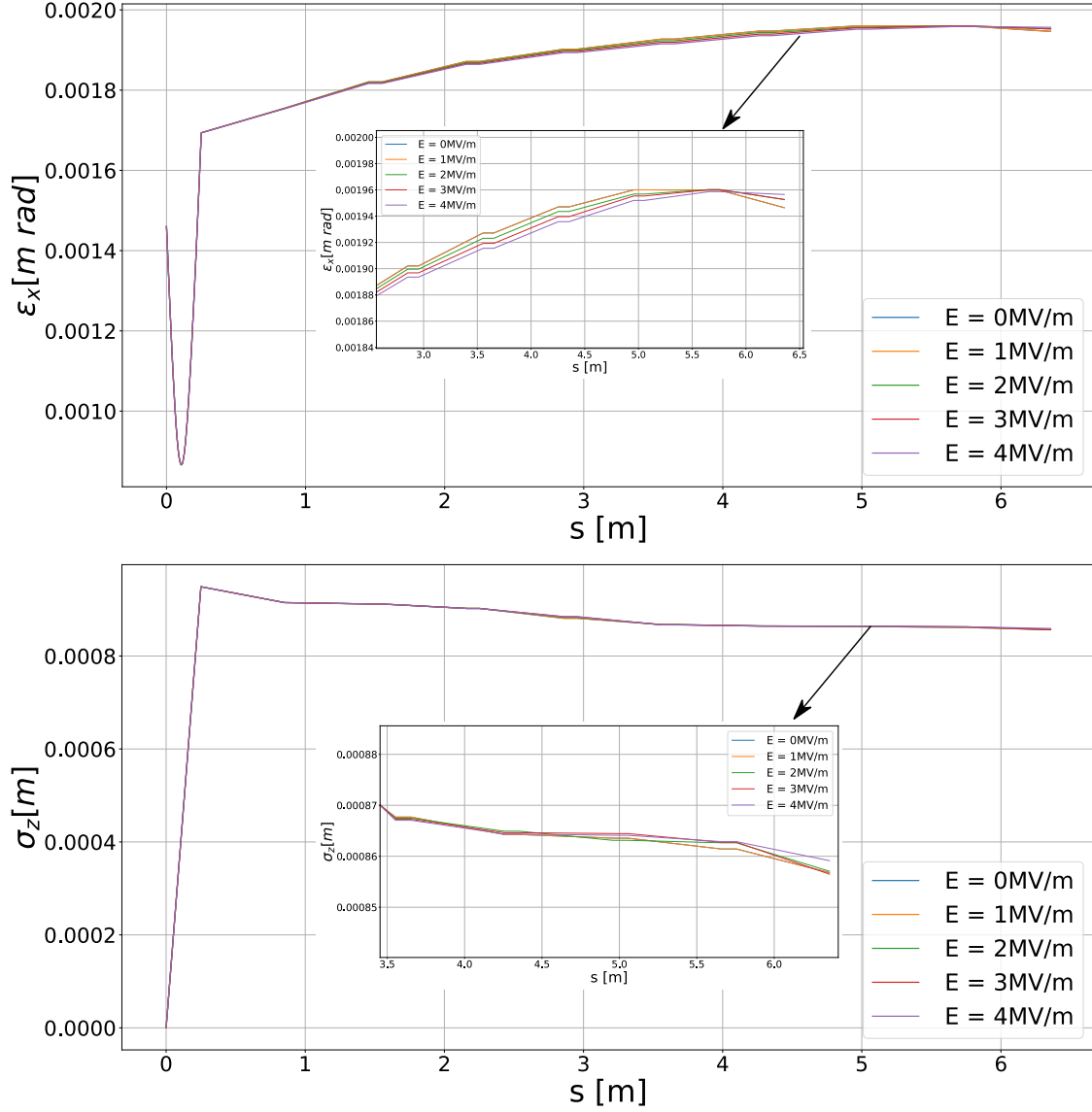


Figure 5.22: Variation of beam parameters along the capture section: top panel shows the beam emittance of the captured positron, and the bottom panel shows the bunch length

beam size  $\sigma_x$ , transverse geometrical emittance  $\epsilon_x$ , angular beam divergence  $\sigma_{x_p}$ , and bunch length. The results of these simulations are illustrated in the subsequent figures.

Fig. 5.22 displays changes in captured beam emittance and bunch length along the capture section, while Fig. 5.23 showcases the angular divergence and corresponding beam size of the captured positron along the QWT and through the capture section.

These results reveal an essential observation: the accelerating cavities affect only the energy spread component. Even when increasing the accelerating gradient, no discernible impact is noted on the transverse positron phase space or the longitudinal bunch length. All transverse quantities behave identically with or without longitudinal acceleration, aligning with the theoretical expectations.

In conclusion, the ELEGANT simulation QWT optimization highlights the key

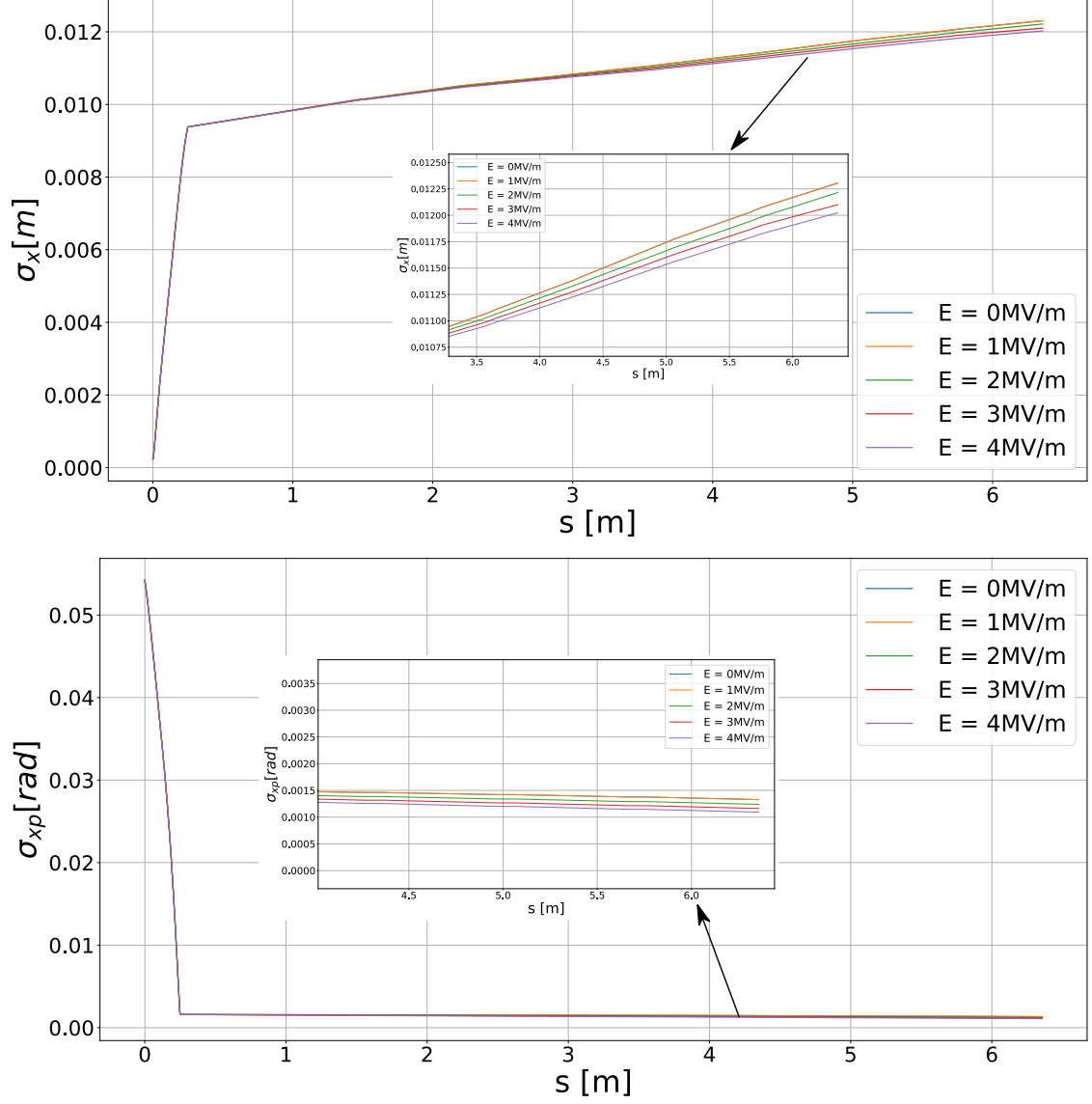


Figure 5.23: Variation of beam parameters along the capture section: top panel shows the transverse beam size of the captured positron, and the bottom panel shows the angular transverse component of the captured beam

role of this short acceptance device in effectively collecting and significantly mitigating the pronounced angular divergence originating from the converter. This device proves highly efficient and necessary after the target to enhance the transverse positron phase space and select the polarization.

Tab. 5.2 shows two different possible QWT setups operating under the polarized and unpolarized operation modes.

Parameters	Polarized mode $p_0 = 60 \text{ MeV}/c$	Unpolarized mode $p_0 = 19 \text{ MeV}/c$	Second approach $p_0 = 6 \text{ MeV}/c$
$B_1 \text{ (T)}$	2.5	1.3	1.27
$L_1 \text{ (m)}$	0.25	0.25	0.05
$B_2 \text{ (T)}$	0.05	0.05	0.05
$r_0^{\text{max}} \text{ (mm)}$	0.36	0.69	0.7
$\Delta\theta^{\text{max}} \text{ (rad)}$	$\pm 6.3^\circ$	$\pm 7.4^\circ$	$\pm 33^\circ$

Table 5.2: Different QWT configurations for various positron operational modes

The chosen QWT design aligns well with PEPPo-like positron sources, facilitating efficient longitudinal energy filtration while favoring angular capture over radial direction, in perfect synchronization with positron production at the converter exit.

Contrarily, enhancing the longitudinal phase space demands a powerful accelerating RF structure. Observations indicate that acceleration exclusively impacts the longitudinal plane and has the potential to enhance the angular positron component with a sufficient accelerating gradient.



# Chapter 6

## Positron transport optimization

### 6.1 Chicane design

The preceding chapters have discussed the generation of the positron distribution and its subsequent characterization. Following this, an optimized collection system was designed to capture and gather positrons based on yield and polarization criteria. Moreover, exploration was carried out into energy spread reduction via a capture linac to minimize losses during injection into the CEBAF-NL.

Upon exiting the capture section the collected positrons with a 60 MeV/c average momentum are accelerated at a rate of 1 MV/m across a 6 meter distance to reach a final momentum of 65 MeV/c. The captured positrons exhibit a notable energy spread post-capture, resulting in a significant positron spectrum energy after traversing the capture linac, necessitating further refinement.

A chicane is proposed within the LERF scheme to enhance the positron momentum distribution. The chicane effectively filters and allows only the highly polarized captured positrons (initially captured at 60 MeV and subsequently accelerated to 65 MeV within the capture section) to proceed through, acquiring the required momentum spread at the chicane exit. Ensuring alignment with the injection requirements of CEBAF-NL is essential to achieve smooth and seamless integration.

Furthermore, the chicane system provides a distinct benefit through its dipole-based design. Since positrons and electrons carry opposite charges, they are deflected in opposite directions when they enter the chicane. This allows for the electrons to be directed into a dump, which still needs to be designed, while the positrons continue along the intended path.

A typical chicane comprises four dipoles. The first component of the chicane (consisting of the first and second dipoles) introduces a dispersion function. This dispersion function transforms the positron momentum spread  $\Delta p/p_0$  from the longitudinal axis  $z$  to the transverse axis  $x$ . Consequently, the possibility arises to incorporate an aperture within the chicane middle. As a collimator, this aperture allows only a beam centered around 65 MeV/c to pass through with a minimal momentum spread. Subsequently, the final two dipoles in the chicane restore the transmitted beam's energy spread from the  $x$ -axis back to the propagation axis  $z$ , thereby returning the dispersion function to its initial state.

To understand the generation of the dispersion function, elaboration on the trans-

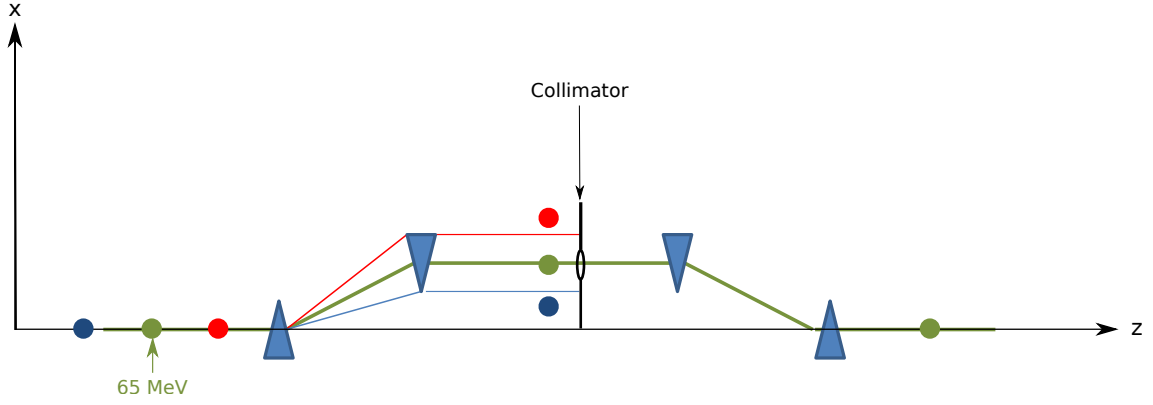


Figure 6.1: Momentum collimation scheme

fer matrix through a dipole is necessary. The sector dipole matrix is defined as :

$$M_d(\rho, \theta) = \begin{bmatrix} \cos \theta & \rho \sin \theta & 0 & 0 & 0 & \rho(1 - \cos \theta) \\ -\frac{1}{\rho} & \cos \theta & 0 & 0 & 0 & \sin \theta \\ 0 & 0 & 1 & \rho\theta & 0 & 0 \\ 0 & 0 & 0 & 1 & 0 & 0 \\ -\sin \theta & -\rho(1 - \cos \theta) & 0 & 0 & 1 & (\frac{\rho\theta}{\gamma^2}) - \rho(\theta - \sin \theta) \\ 0 & 0 & 0 & 0 & 0 & 1 \end{bmatrix} \quad (6.1)$$

Where  $\rho$  is the bend radius,  $\theta$  is the bend angle, and  $L_{dipole} = \rho\theta$ . The first chicane's arm is made of two dipoles with opposite bending angles separated by a drift space; the arm matrix can be calculated using the following:

$$M_{Arm} = M_d(\rho, -\theta) \times M_{drift} \times M_d(\rho, \theta) \quad (6.2)$$

Then the arm matrix can be written as:

$$M_{Arm} = \begin{bmatrix} 1 + \frac{L}{\rho} \cos \theta \sin \theta & L \cos^2 \theta & 0 & 0 & 0 & -L \cos \theta \sin \theta \\ -\frac{L}{\rho^2} \sin^2 \theta & 1 - \frac{L}{\rho} \cos \theta \sin \theta & 0 & 0 & 0 & \frac{L}{\rho} \sin^2 \theta \\ 0 & 0 & 1 & L + 2\rho\theta & 0 & 0 \\ 0 & 0 & 0 & 1 & 0 & 0 \\ -\frac{L}{\rho} \sin^2 \theta & -L \sin \theta \cos \theta & 0 & 0 & 1 & L(1 + \sin^2 \theta) \\ 0 & 0 & 0 & 0 & 0 & 1 \end{bmatrix} \quad (6.3)$$

Assuming free dispersion before the first dipole entrance ( $\eta = 0, \eta' = 0$ ), then the dispersion function at the exit of the second dipole  $D_{Exit}$  is described by:

$$D_{Exit}^{xx'} = M_{Arm}(2 \times 2) \times \begin{bmatrix} \eta_{Entrance} \\ \eta'_{Entrance} \end{bmatrix} + \begin{bmatrix} M_{Arm}(1, 6) \\ M_{Arm}(2, 6) \end{bmatrix} \quad (6.4)$$

It's evident that for small bending angles, the dispersion at the exit of the first arm can be expressed as:

$$D_{Exit}^{xx'} = \begin{bmatrix} -L\theta \\ 0 \end{bmatrix} \quad (6.5)$$

Taking into account that  $M_{Arm}(1, 6)$  and  $M_{Arm}(2, 6)$  describe the  $(x, z)$  and  $(x', z)$  phase space planes, one can use the introduced dispersion by the dipoles.

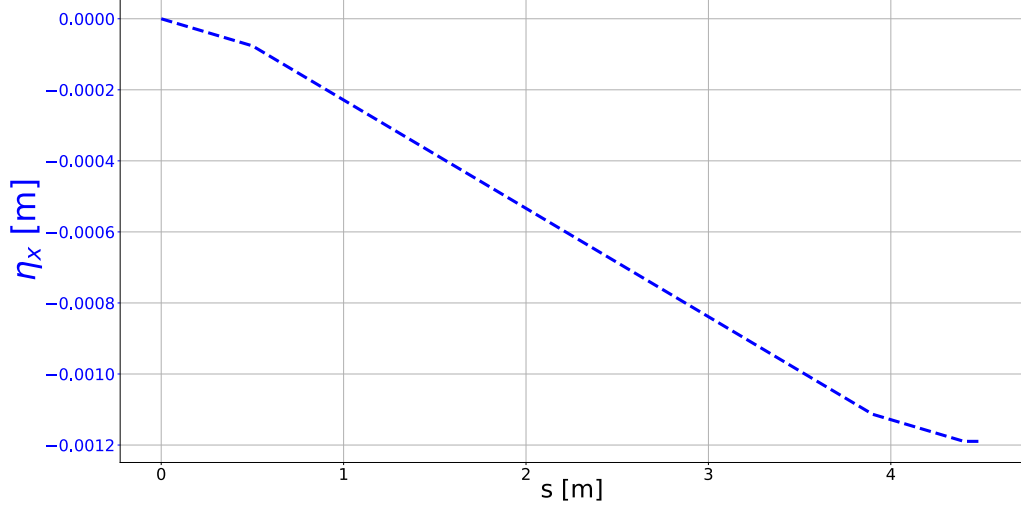


Figure 6.2: ELEGANT dispersion generated by the first arm (first two dipoles) with  $\theta = -0.3$  mrad,  $L = 3.4$  m with  $L\theta = -0.0011$  m which agrees with the previous matrix estimation.

Consequently, the longitudinal energy spread can be transferred to the transverse plane ( $x, x'$ ) via the first arm and canceled using the second arm.

The understanding of dispersion behavior along the dipoles leads to the goal of controlling the beam size within the chicane. Optimizing the dispersion value in the collimation region is essential for facilitating momentum collimation choices. Moreover, maintaining precise control over the beam size at this point is crucial to avoid potential losses.

The idea is to set up the chicane as a periodic system. This periodic behavior keeps the beam size within a specific range across the entire chicane. Therefore, optimizing the optical properties of the system to achieve this periodic behavior becomes highly important.

The optimization relies on the Twiss parameters. Shaping the optical parameters of the beam involves designing a FODO lattice for the chicane. This lattice consists of alternating focusing and defocusing quadrupoles, each separated by a drift space. The quadrupoles impact the transverse phase space, with the transfer matrix for quadrupole focusing represented as:

$$M_{QF} = \begin{bmatrix} \cos \sqrt{K}L_q & \frac{1}{\sqrt{K}} \sin \sqrt{K}L_q \\ -\sqrt{K} \sin \sqrt{K}L_q & \cos \sqrt{K}L_q \end{bmatrix} \quad (6.6)$$

and the defocusing quadrupole matrix is described by:

$$M_{QD} = \begin{bmatrix} \cosh \sqrt{K}L_q & \frac{1}{\sqrt{K}} \sinh \sqrt{K}L_q \\ -\sqrt{K} \sinh \sqrt{K}L_q & \cosh \sqrt{K}L_q \end{bmatrix} \quad (6.7)$$

$K$  is the focusing quadrupole strength,  $L_q$  is the length. Applying the periodicity condition, we have:

$$\begin{bmatrix} \beta_{\text{exit}} \\ \alpha_{\text{exit}} \\ \gamma_{\text{exit}} \end{bmatrix} = \begin{bmatrix} \beta_{\text{entrance}} \\ \alpha_{\text{entrance}} \\ \gamma_{\text{entrance}} \end{bmatrix} \quad (6.8)$$

The half-period FODO matrix can be written as follows:

$$M(s_1 s_2) = \begin{bmatrix} C & S \\ C' & S' \end{bmatrix} \quad (6.9)$$

In a periodic system, the equation of motion in a particle accelerator is stable under the condition [73]:

$$|\text{trace}(M)| < 2 \quad (6.10)$$

The Twiss transformation matrix from point  $s_1$  to  $s_2$  in the lattice is given by :

$$\begin{bmatrix} \beta_{s2} \\ \alpha_{s2} \\ \gamma_{s2} \end{bmatrix} = \begin{bmatrix} C^2 & -2SC & S^2 \\ -CC' & SC' + S'C & -SS' \\ C'^2 & -2S'C' & S'^2 \end{bmatrix} \begin{bmatrix} \beta_{s1} \\ \alpha_{s1} \\ \gamma_{s1} \end{bmatrix} \quad (6.11)$$

And using Eq. 3.21, expressing the beam envelope trajectories, the stability condition described above (Eq. 6.10), the trace of the periodic system is given by:

$$|\text{trace } M(s_1 s_2)| = C + S' < 2$$

Assuming a drift length between quadrupole  $L = 5.55$  m,  $K = 1.7 \text{ m}^{-2}$ ;  $Lq = 0.15$  m, the half period matrix become [73]:

$$M_{\text{Half FODO}} = \begin{bmatrix} 1.77 & 3.79 \\ -0.16 & 0.21 \end{bmatrix}$$

The stability condition is satisfied:

$$|\text{trace } M_{\text{FODO}}| = 0.78$$

Upon entering the FODO lattice, a maximum injection  $\beta_x$  is considered, aligning with  $\alpha = 0$ . In the half period (center of the chicane),  $\beta$  can reach  $\beta_{\text{max}}$  at the focal point of the focusing quadrupole.

Given the matrix determinant condition  $CS' - C'S = 1$ , which indicates that beam emittance  $\epsilon$  remains constant as per Liouville's theorem, there appears a connection between Twiss functions:

$$\gamma_0 = \frac{1 + \alpha^2}{\beta} \quad (6.12)$$

At the entrance of the FODO lattice,  $\alpha = 0$  The ratio between the maximum value of the beta function and its minimum is called the "beat factor" [73], and the equation gives it:

$$m^2 = \frac{C^2}{S'^2} = \frac{\beta_{\text{Max}}^2}{\beta_{\text{Min}}^2} \quad (6.13)$$

Therefore, we end up with:

$$\beta_{\text{Min}} = 1.79 \text{ m} \quad (6.14)$$

$$\beta_{\text{Max}} = 13.8 \text{ m} \quad (6.15)$$

The previous conditions define the periodicity of the system. Specifically, this periodicity remains intact when the maximum required  $\beta_{\text{Max}} = 13.8$  m is introduced at the FODO lattice's entrance. As the system progresses to its midpoint (half period),

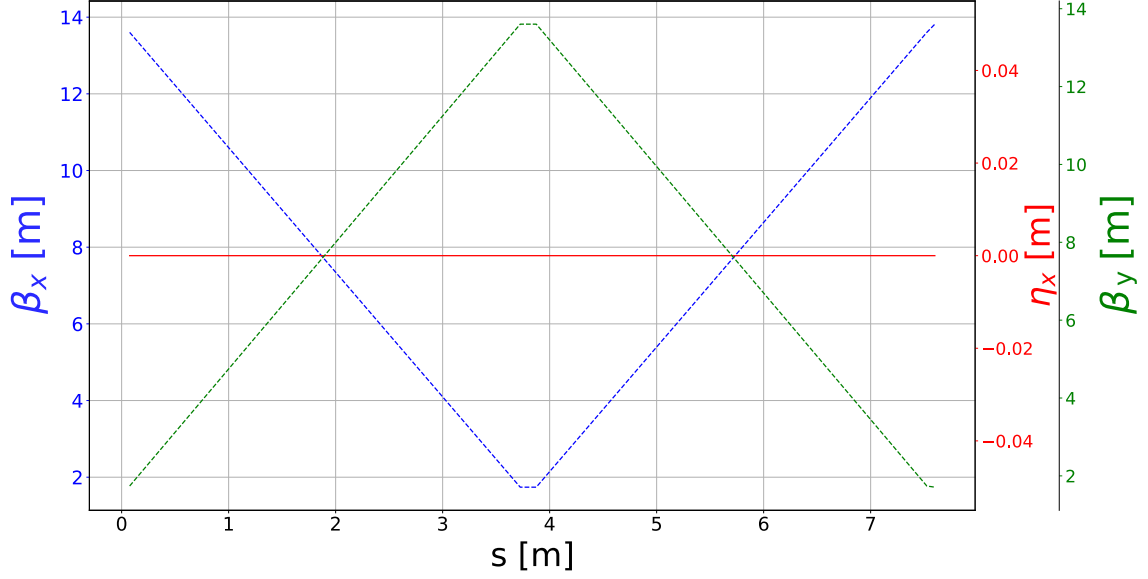


Figure 6.3: Twiss function variation along one period FODO lattice

the beta function is minimized to  $\beta_{\text{Min}} = 1.79$  m. Subsequently, after completing an entire period, the beta function returns to  $\beta_{\text{Max}}$ .

Fig. 6.3 illustrates the change in beta functions throughout a single period of the FODO lattice. The anticipated periodic pattern is achieved by implementing the parameters mentioned earlier in the quadrupoles and employing  $\beta_{\text{Max}}$  at the FODO entrance. Consequently, as the lattice reaches its midpoint, the estimated  $\beta_{\text{Min}}$  value becomes evident. It's worth noting that the dispersion function is null due to the absence of any dispersive magnet in the structure, as indicated by the red curve.

With the establishment of a periodic structure, the previously designed chicane will be incorporated into the ELEGANT FODO model. This chicane is intended to introduce a dispersion function, as clarified earlier. The resulting beta functions are depicted in Fig. 6.4.

The beta functions exhibit perfect periodicity when the FODO lattice is coupled with the chicane. The dispersion function introduced by the first dipole, denoted as  $\eta_x$  (red), is shaped by adding a quadrupole in the middle of the chicane arm (the two first dipoles). This dispersion function achieves its maximum value at the midpoint of the chicane, resulting in  $\eta_x = 0.7$  m. The second chicane arm then adjusts it back to nullify the dispersion at the chicane's exit. The first quadrupole (blue) has a focusing effect in the x plane, allowing to decrease of the  $\beta_x$  function to its minimum when the beam enters the quadrupole located at the middle of the chicane, this quadrupole has a defocusing effect, allowing to the beta function to reach back its initial value at the exit of the chicane.

### 6.1.1 Matching section

With the momentum collimation system now in operation, it's important to ensure its periodicity regardless of the incoming beam parameters. The collected beam from the QWT capture section may exhibit varying Twiss parameter values. It's not feasible to re-optimize the collimation chicane for each incoming beam, con-

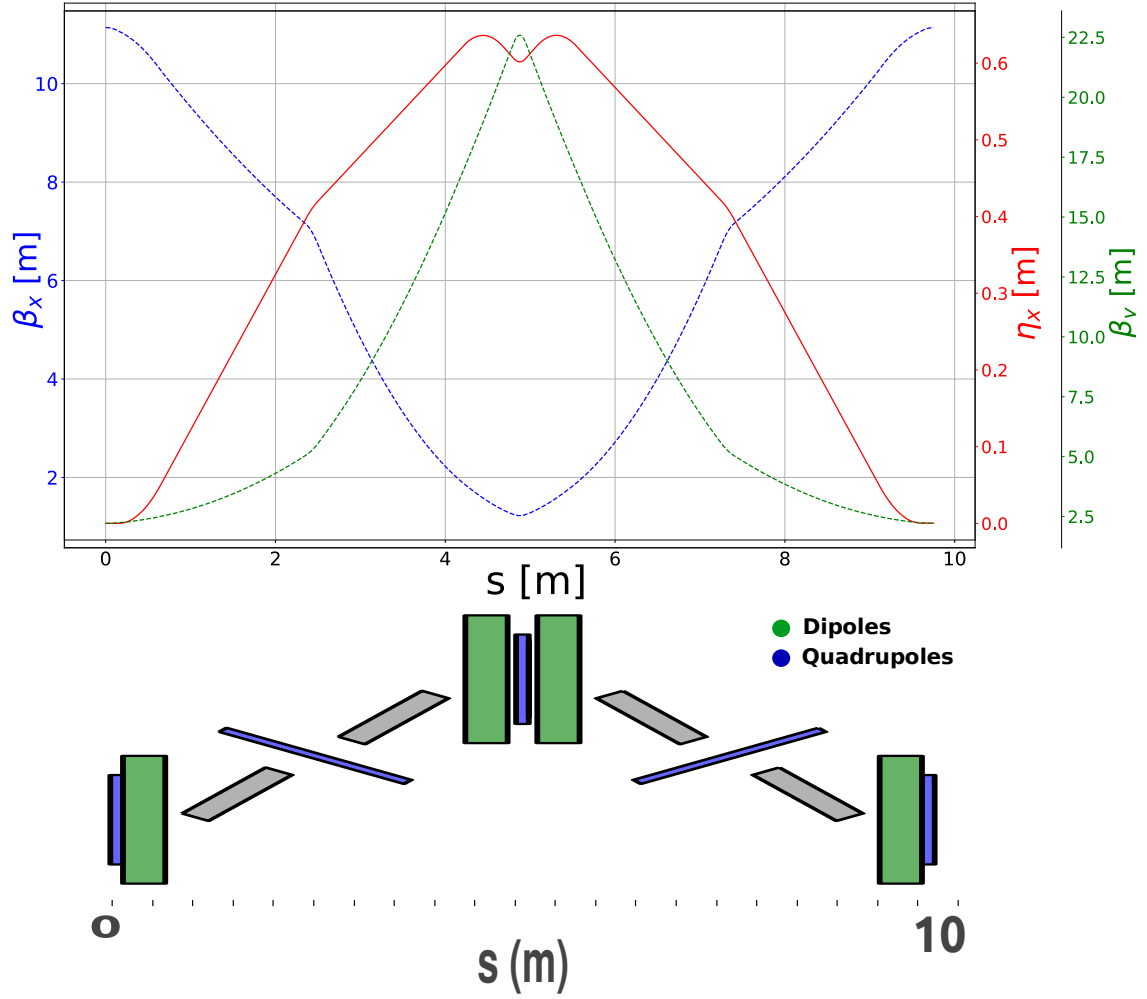


Figure 6.4: Twiss parameters variation over the chicane implemented within the designed FODO lattice.

sidering factors like operational modes, polarization, yield, and the desired central momentum for collection.

A straightforward approach is to incorporate a quadrupole system to align the beam's acceptance with the entrance of the chicane. This system can set the broad range of betas exhibited by the positron beam originating from the QWT. As previously discussed, the collimation chicane maintains periodicity exclusively for specific input parameters:  $\beta_x = 13, \text{m}$ ,  $\alpha_x = 0$ ,  $\beta_y = 1, \text{m}$ , and  $\alpha_y = 0$ . Consequently, an additional setup preceding the chicane is necessary to shape the incoming Twiss parameters from the capture section. This adjustment ensures alignment with the transverse acceptance of the coupled chicane within the FODO lattice. To accomplish this, four quadrupoles have been developed and optimized. These quadrupoles are designed to achieve the necessary Twiss values at the entrance of the initial chicane.

The  $\alpha_{x,y}$  functions are also important to shape since  $\alpha$  is defined as:

$$\alpha = \frac{d\beta}{ds} \quad (6.16)$$

where  $s$  is the longitudinal propagation coordinate.

Equation (6.16) demonstrates how the alpha functions contribute to the propagation of the beta functions. As a result, a minimum of four quadrupoles is necessary to control the transverse Twiss parameters.

This configuration is referred to as a matching section, which serves to mold the optical properties of beams and neutralizes substantial variations in beta and alpha functions that stem from the transverse acceptances of the chicane.

Fig. 6.5 describes the variation of beta and alpha functions along the matching section. The designed matching section accommodates a large range  $\beta_{x,y}$  and  $\alpha_{x,y}$ . This successful adaptation aligns well with the desired Twiss parameters at the chicane entrance.

For instance, the red curve, representing an injection with  $\beta_x = 2.8\text{m}$ ,  $\beta_y = 6.6\text{m}$ ,  $\alpha_x = 0.5$ , and  $\alpha_y = 0.5$ , showcases how the four quadrupoles shape the Twiss functions to attain the requisite betas and alphas at the chicane entrance after traveling approximately 7.5 meters.

The matching section parameters are shown in Tab. 6.1.1

Parameters	$k \text{ (m}^{-2}\text{)}$	$L_1 \text{ (m)}$	Drift (m)
Q1	-2.5	0.15	1.7
Q2	2.95	0.15	1.7
Q3	-0.43	0.15	1.7
Q4	-2	0.15	1.7

To proceed with matching the incoming beam into the chicane, it's essential to know the incoming betas and alphas. While the optics model provides this information, there is no way to determine these parameters in a real-world setting. A method for conducting a quadrupole scan to measure the incoming Twiss parameters is needed, and this aspect has not been addressed in the current work.

## 6.1.2 Momentum collimation

The momentum collimation system is crucial in refining the positron distribution by incorporating the principles developed in earlier work. The previous work established a periodic chicane coupled with a FODO lattice, integrating a set of four quadrupoles to achieve beam Twiss parameter matching. In the subsequent analysis, the simulation and investigation of the transport of the incoming positron distribution will be conducted, starting from the exit of the designed QWT and passing through the designated momentum collimation system.

Figure 6.7 illustrates the control of Twiss parameters as the beam travels along the designed momentum collimation system, which consists of a matching section and a coupled FODO lattice with a magnetic chicane. As the beam exits the capture section, it has approximately  $\beta_x = 17 \text{ m}$  and  $\beta_y = 16 \text{ m}$ , shown by the blue curves in both x and y planes. These  $\beta$  and  $\alpha$  would be mismatched if directly injected into the chicane.

The required parameters which makes the magnetic chicane periodic are met at its entrance (refer to Fig. 6.5). As previously discussed, injecting the necessary Twiss parameters enables the chicane to exhibit periodic behavior. This permits a small  $\beta_x$  value at the middle of the chicane and the maximum dispersion function value at the same point (depicted by the red curve). Additionally, it's noteworthy that

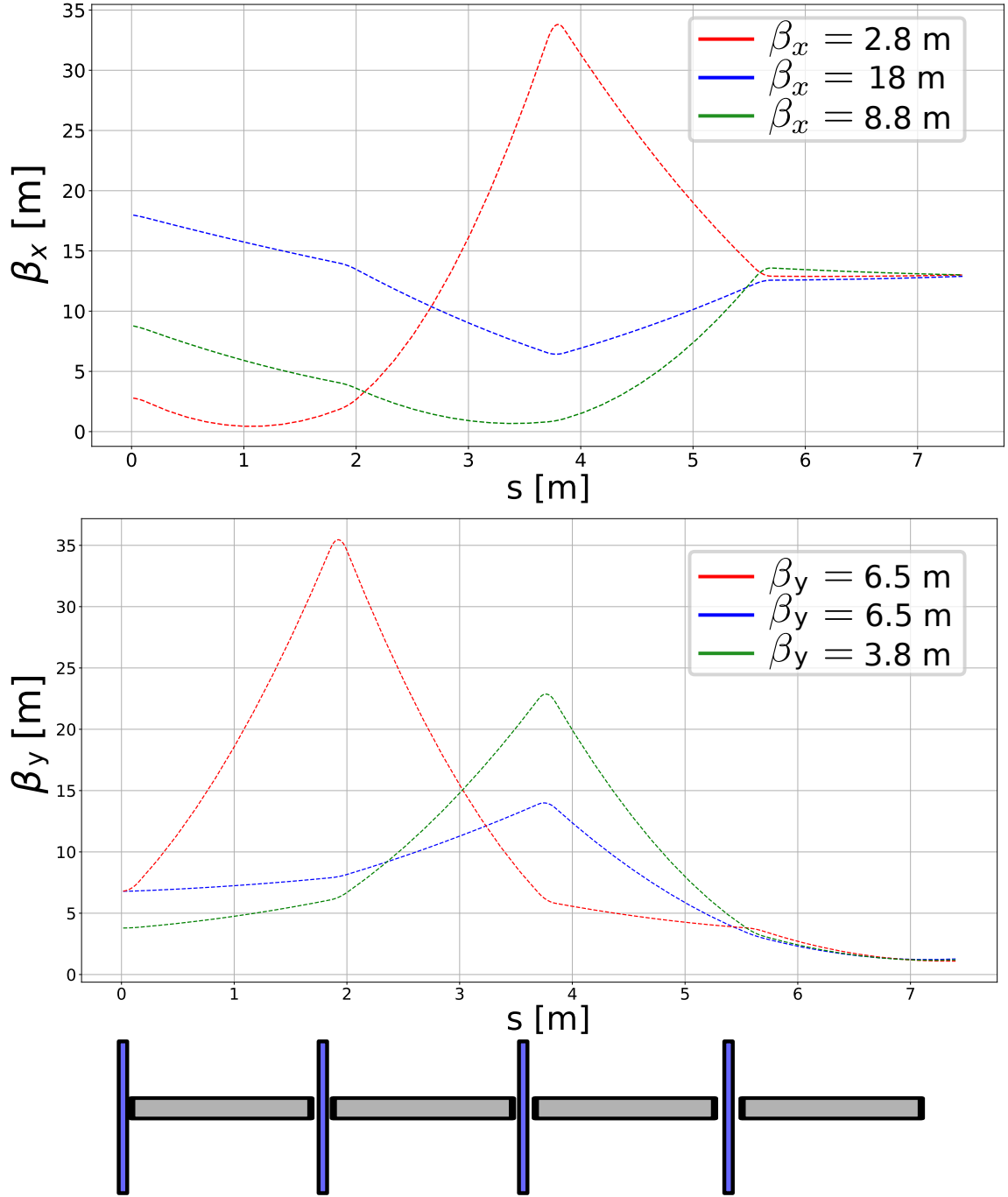


Figure 6.5: Acceptance of the designed matching section for three different beta input

the dipole introduces no dispersion in the y-plane (shown in the bottom figure), ensuring that momentum collimation exclusively takes place within the p-x plane.

Having satisfied the necessary conditions for efficient momentum collimation, the plot in Fig. 6.8 illustrates the positron momentum relative to their x coordinates. This illustration showcases the connected p-x positron phase space during the momentum collimation process at different positions.

The blue dots on the plot represent the positron distribution upon entry into the chicane. In contrast, the orange dots correspond to positrons at the collimator's entrance in the chicane's middle. The green dots denote positrons that have



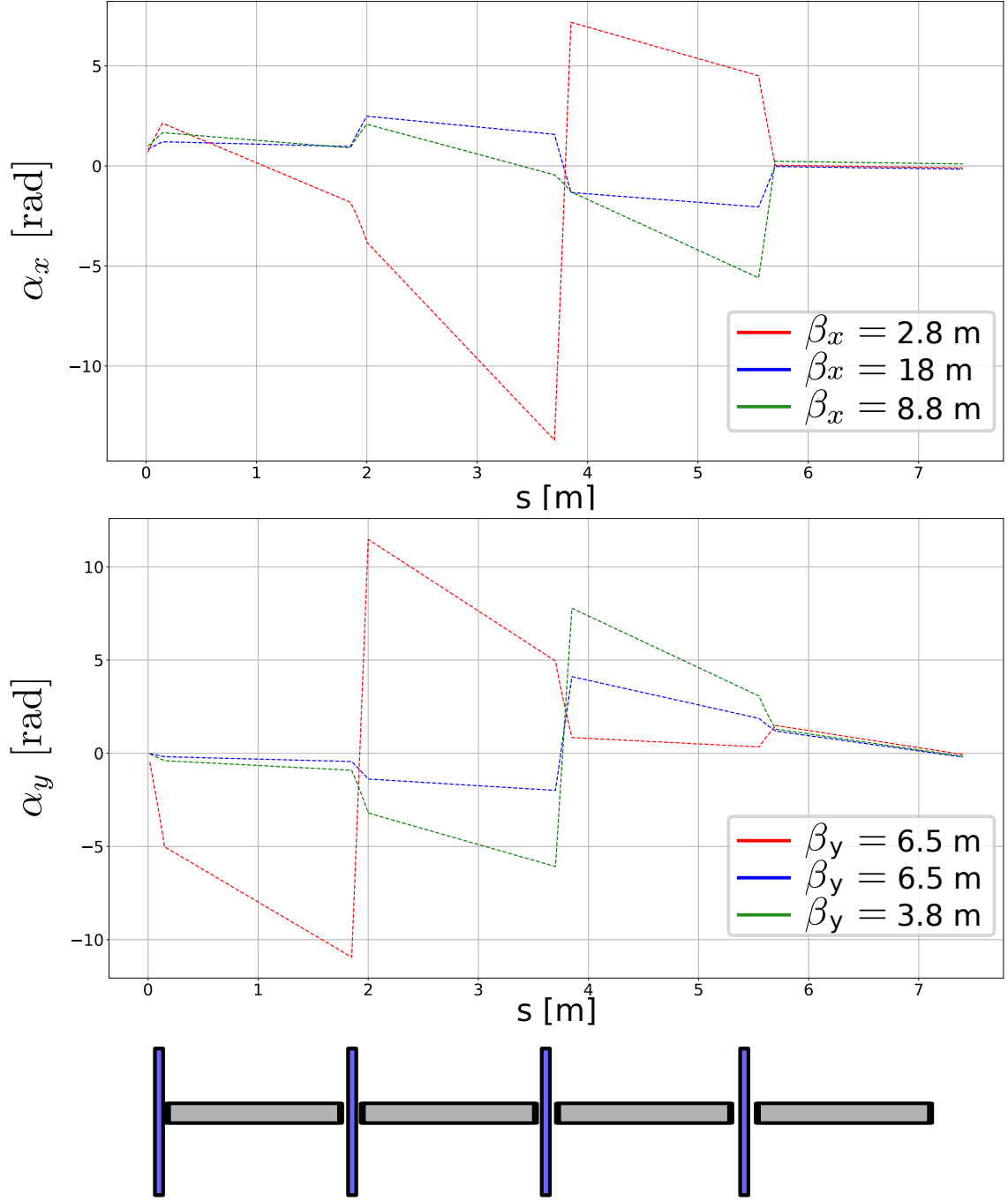


Figure 6.6: Acceptance of the designed matching section for three different alphas input

experienced momentum collimation and are exiting the collimator.

The chicane's design facilitates the conversion of energy spread from the longitudinal axis  $z$  to the transverse axis  $x$ . This transformation is achieved through the dispersion introduced by the dipoles, resulting in a clear correlation between the positron momentum  $p$  and their transverse coordinates  $x$ .

This correlation forms the basis for strategically placing a collimator following the second dipole at the midpoint of the chicane. Adjusting the collimator's aperture makes it possible to capture a narrow portion of the positron energy spread selectively. This captured portion is centered around 65 MeV/c, as visually indicated by

the green distribution.

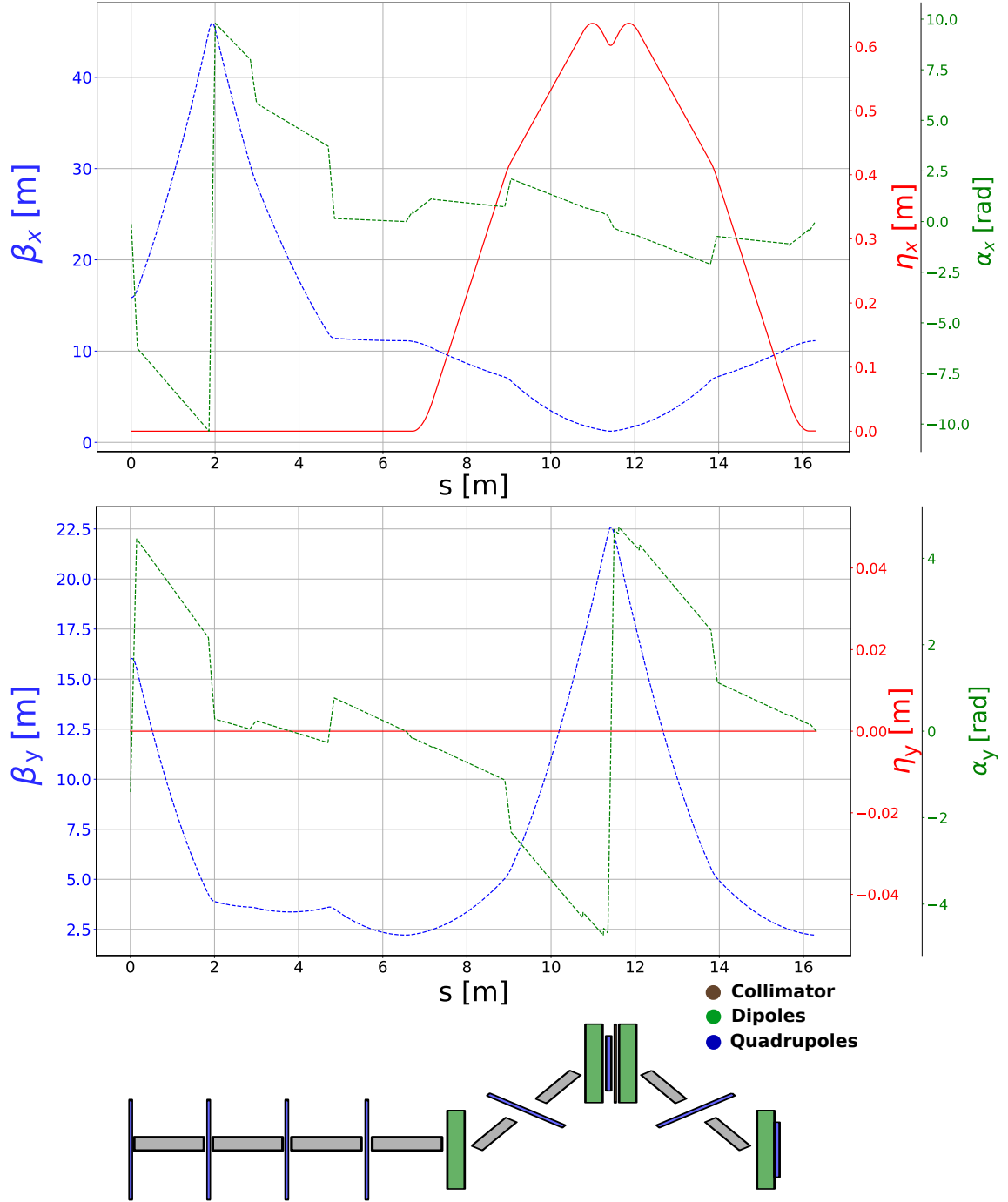


Figure 6.7: Transverse Twiss parameters variation along the designed collimation system

Upon exiting the momentum collimation chicane, positrons centered at 65 MeV/c remain, exhibiting a significantly reduced energy spread. All other energies outside this range are effectively dumped at the entrance of the collimator, as illustrated in the right panel of Fig. 6.8.

The positron beam parameters at the exit of the collimation chicane are summarized in Tab. 6.1.

At this stage of the positron injector layout, a successful design has been achieved

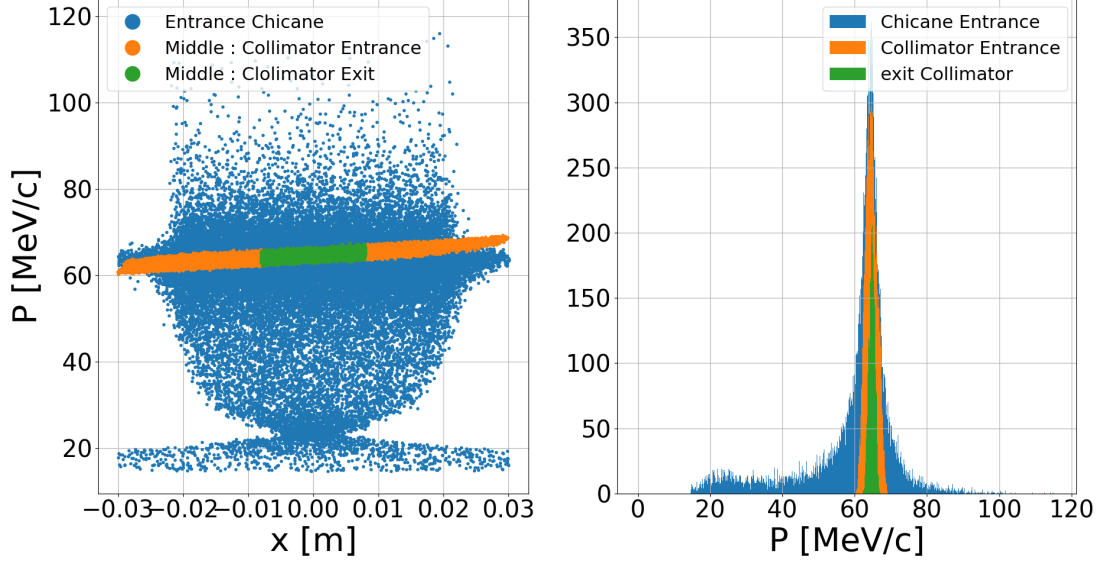


Figure 6.8: Momentum collimation process: Left panel, positron momentum collimation described in the  $p$  (MeV/c)- $x$  (m) plane at different locations, right panel, the positron momentum before and after the momentum collimation.

$P_0$ (MeV/c)	$\sigma_{\Delta p/p_0}$ (%)	$\sigma_t$ (ps)	$\epsilon_x$ (mm mrad)	$\epsilon_y$ (mm mrad)
65	1.3	10	0.12	0.18

Table 6.1: Positron beam parameters at the exit of the momentum collimation chicane showing a reduced energy spread

for capturing high positron polarization. Additionally, the requirement for positron energy spread has been met, and further reduction will occur during the 123 MeV acceleration phase. However, a remaining challenge involves reducing the bunch length, which presently exceeds the CEBAF injection limit of  $\sigma_z^{\text{Limit}} \leq 4$  ps.

## 6.2 Bunch Length compression

The optimization of the longitudinal positron phase space represents the next crucial step. This involves focusing on two main aspects. First, the reduction of energy spread must be pursued by accelerating the outgoing beam from the collimation chicane to 123 MeV. Second, the longitudinal length, commonly referred to as the bunch length, needs to be decreased.

Referring to Tab. 6.1, it becomes evident that the bunch length at the exit of the collimation chicane exceeds the anticipated acceptance of the CEBAF-NL. To be specific, after undergoing momentum collimation, the positron beam shows a length of 10 ps. Thus, designing an appropriate system is imperative to mitigate this issue.

The C100 cryo module will reduce the energy spread, delivering sufficient acceleration to transition the positron beam from 65 MeV at the exit of the preceding collimation chicane to 123 MeV. This acceleration is expected to result in a substantial energy spread reduction, estimated at 50%.

As observed earlier in Fig. 6.1, a charged particle passing through a dipole exhibits a direct connection between its longitudinal momentum component and the

bending radius. This relationship defines the particle's curved trajectory along the dipole, with the longitudinal momentum component characterized by:

$$p_z[\text{GeV}/c] = 0.299 B_0[T]\rho[m] \quad (6.17)$$

This indicates that particles with varying momentum will follow distinct paths (either longer or shorter) starting from the collimation chicane exit in the case of C<sup>+</sup>BAF. This variance arises due to the momentum spread of  $\sigma_{\Delta p/p_0} = 1.3\%$ , which consequently causes differences in their arrival times at a specific longitudinal position downstream of the dipole system. To put it simply, particles within the beam, enclosed by the 1.3% momentum spread, will exhibit distinct longitudinal coordinates ( $z$  in meters).

Control over the energy spread in the accelerator is achieved using a specialized accelerating component called the C100 cryomodule. One technique involves adjusting what is known as the "energy chirp," or the variation in particle energy along the length of a particle bunch. This tuning ensures that particles with lower energy at the beginning of the bunch travel along longer orbits, while those with higher energy at the end of the bunch take shorter orbits. As a result, the entire bunch of particles is compressed, thereby increasing the peak current of the positron beam—a key parameter for many applications.

For further compression of the particle bunch, a second chicane is introduced. This design relies on what is known as an "achromatic chicane," a specialized non-dispersive element, to effectively shorten the beam length.

Consideration is given to an achromatic symmetric chicane consisting of 4 identical sector dipoles. Thereafter, upon application of the achromaticity criterion, the bending angle generated by each dipole of length  $l_d$  can be characterized as follows:

$$\theta_0 = \frac{eB_0 l_d}{p_0} \quad (6.18)$$

The reference particle (on-momentum) is denoted with  $p_{z,0}$ , and as a result, the corresponding bending angle is  $\theta_0$ . Due to the identical nature of the four dipoles ( $\theta_2 = -\theta_1$ ,  $\theta_3 = -\theta_1$ , and  $\theta_4 = \theta_1$ ), the complete deflection experienced by an on-momentum particle along this chicane is given by:

$$\theta_{\text{chicane}} = \theta_1 + \theta_2 + \theta_3 + \theta_4 = 0 \quad (6.19)$$

For an off-momentum particle, the bending angle is defined as:

$$\theta = \frac{eB_0 l_d}{p + \Delta p_0} = \frac{\theta_0}{(1 + \Delta p/p_0)} \quad (6.20)$$

And the total deflection of the off-momentum particle is also 0.

Applying the achromaticity condition (described by Eq. 6.4), it follows that if the beam possesses zero dispersion at the entrance of the chicane, this zero dispersion will be maintained at the exit as well.

Consequently, within a chicane, particles originating in a linear trajectory at the entrance will preserve their linear arrangement at the exit, even when their energies vary. This definition of achromaticity implies that the total deflection experienced by particles with differing energy deviations along the magnetic chicane is null, regardless of the extent of their energy deviation from the nominal value  $p_0$ . As a

result, the chicane has its achromatic properties across all orders, unless anomalies are present in the magnets or imperfections in the geometry.

The chicane matrix in the longitudinal plane ( $z$ ,  $\Delta p/p_0$ ) at the first order is described by:

$$M_{\text{chicane}} = \begin{bmatrix} 1 & R_{56} \\ 0 & 1 \end{bmatrix} \quad (6.21)$$

As a result, the coordinates of the particles at the exit of the chicane experience the following transformation:

$$\begin{bmatrix} z^{\text{Exit}} \\ \Delta p/p_0^{\text{Exit}} \end{bmatrix} = \begin{bmatrix} 1 & R_{56} \\ 0 & 1 \end{bmatrix} \times \begin{bmatrix} z^{\text{Entrance}} \\ \Delta p/p_0^{\text{Entrance}} \end{bmatrix} \quad (6.22)$$

The longitudinal coordinate at the exit of the chicane is described by:

$$z^{\text{Exit}} = z^{\text{Entrance}} + R_{56} \Delta p/p_0^{\text{Entrance}} \quad (6.23)$$

Therefore, the expression for  $\Delta_z$  is formulated as  $\Delta_z = R_{56} \cdot \Delta p/p_0^{\text{Entrance}}$ , with  $R_{56}$  representing the chicane matrix element responsible for the adjustment in bunch length. By referring to Fig. 6.1, we can establish the variance in longitudinal coordinates between an on-momentum particle and an off-momentum particle. Operating under the assumption that the dipole length is insignificantly small in comparison to the chicane length, we can proceed to compute the ultimate longitudinal coordinate at the exit of the chicane in the following manner:

$$s_z = \frac{l_1}{\cos \theta} + L_2 + \frac{l_1}{\cos \theta} \quad (6.24)$$

Therefore, the  $\Delta z$  can be written as:

$$\Delta s_z = s_z - s_{z,0} = 2l_1 \left[ \frac{1}{\cos \theta} - \frac{1}{\cos \theta_0} \right] \quad (6.25)$$

Under the small angle approximation, the equation Eq. 6.25 can be approximated as follows:

$$\Delta s_z = -2l_1\theta_0^2 \left[ 1 - \frac{1}{1 + \delta^2} \right] + o(\theta^4) \quad (6.26)$$

Subsequently, the expression becomes  $\Delta s_z = -l_1\theta_0^2\delta + o(\theta^4, \delta^2)$  under the small angles approximation with  $\theta \ll 1$ .

Furthermore, recalling from Eq. 6.23 that  $R_{56} = \frac{\Delta s_z}{\Delta p/p_0}$ , the following formula can be expressed:

$$\frac{\Delta s_z}{\Delta p/p_0} = -2l_1\theta_0^2 = R_{56} \quad (6.27)$$

Eq. 6.27 primarily demonstrates how the longitudinal matrix element  $R_{56}$  relies exclusively on the drift space and the influence of the bend angle introduced by the dipoles. Its crucial role in shaping the bunch length is emphasized.

The compression factor formula based on  $R_{56}$  can be evaluated using a linear approximation. This involves differentiating the particle's longitudinal coordinate as described by Eq. 6.23:

$$dz_f = dz_i + d(R_{56}\delta) = dz_i \left[ 1 + R_{56} \frac{d(\delta)}{dz_i} \right] \quad (6.28)$$

By replacing  $\Delta p/p_0$  with  $\delta$ , the previous equation can be rewritten as:

$$dz_f = dz_i \left[ 1 + R_{56} \frac{d\delta}{dz_i} \right] \quad (6.29)$$

where  $d\delta = d(\frac{E-E_0}{E_0})$ , with  $E_0$  being the particle's mean energy, leading to:

$$dz_f = dz_i \left[ 1 + \frac{R_{56}}{E_0} \frac{d(E(z) - E_0)}{dz_i} \right] \quad (6.30)$$

$$dz_f = dz_i [1 + eR_{56}\delta] + R_{56}\delta' \quad (6.31)$$

The definition of  $\delta$  is given by  $\frac{1}{E_0} \frac{dE(z)}{dz_i}$ , where  $\delta$  represents the correlated energy deviation relative to  $E_0$ , and  $\delta'$  stands for the initial energy deviation at the entrance of the chicane. Additionally,  $h = \frac{\delta}{E_0}$  is introduced as the energy chirp, outlining the correlation between the beam's energy profile and its longitudinal coordinate.

To simplify the mathematics, expressing the final longitudinal particle coordinate as follows:

$$dz_f = dz_i [1 + hR_{56}] + R_{56}\delta' \quad (6.32)$$

Eq. 6.32 provides insights into the constrained rms bunch length at full compression. Specifically, as the compression factor  $C = \frac{1}{[1+hR_{56}]}$  approaches infinity when  $R_{56} = -\frac{1}{h}$ , the second term  $R_{56}\delta'$  remains, representing the minimum achievable rms bunch length in full compression mode. It's crucial to note that the initial value of  $\delta'$  governs the final bunch length; higher beam energies lead to a shorter minimum bunch length at the chicane's exit.

The analysis underscores that despite an optimized compression system, the potential for improvement is constrained by the initial injected bunch length at the compression chicane's entrance. This consideration adds another dimension to the argument for minimizing energy deviation upon exiting the collimation chicane.

The established compression factor, denoted as  $C = \frac{1}{[1+hR_{56}]}$ , establishes a connection between the energy chirp  $h$  and the longitudinal matrix chicane element  $R_{56}$ . As a result, including an accelerating section followed by a second chicane becomes imperative for achieving longitudinal beam compression. This sequential arrangement facilitates the compression of the beam along its longitudinal axis.

### 6.2.1 Investigation of the compression chicane

The compression factor, denoted as  $C$ , is described by the equation:

$$C = \frac{1}{[1 + hR_{56}]} \quad (6.33)$$

Equation 6.33 explains that to attain a minimal bunch length at the exit of the compression system, it is necessary to maximize the compression factor  $C$ . Notably, a simple mathematical demonstration reveals that when  $R_{56} = -\frac{1}{h}$ :

$$C = \frac{1}{[1 + hR_{56}]} \rightarrow \infty \quad (6.34)$$

The equation quantifies the energy correlation along the beam:

$$h = -\frac{eV_0}{E_f} k \sin \phi \quad (6.35)$$

Here,  $\lambda$  represents the RF wavelength, and  $V_0$  denotes the on-crest voltage gain of the Linac, responsible for accelerating the positron at a given phase value  $\phi_{\text{rf}}$ , transitioning from an initial energy  $E_i$  to a final energy  $E_f$ .

By substituting Eq.6.35 into Eq.6.34, the expression for the compression factor becomes:

$$C = \frac{1}{\left[1 + \frac{eV_0 R_{56}}{E_f} k \sin \phi\right]} \quad (6.36)$$

Furthermore, Fig. 6.9 provides an insightful visual representation of the compression factor's variation across the accelerating phase. This variation is particularly significant for a specific off-crest phase value. As illustrated, at  $\phi_{\text{rf}} = -97^\circ$ , an important beam compression factor of 20 is observed. This implies that the positron beam exiting the injector will have a significantly smaller bunch length, specifically 20 times smaller than the injected one originating from the first collimation chicane.

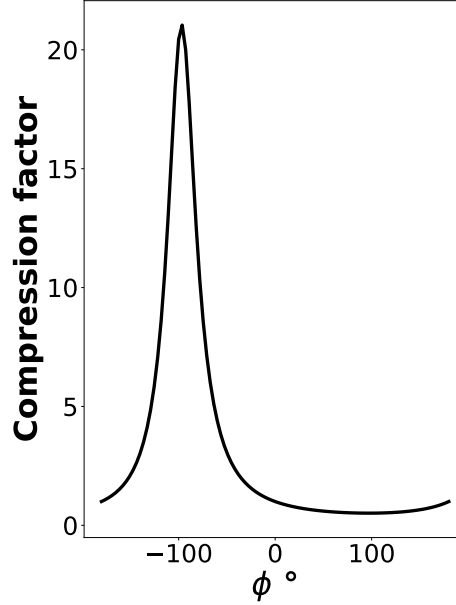


Figure 6.9: Energy Chirp Variation Across Accelerating Phase

This analysis highlights the critical importance of positioning the accelerating cryomodule ahead of the compression chicane. Precise tuning of this component is key to optimizing the compression factor and enhancing the efficiency of the longitudinal compression process.

The compression system can be simulated using an  $R_{56}$  value of  $-25$  cm. This can be achieved by configuring a second chicane with specific parameters, as determined by Eq. 6.27. Consequently, when operating at full compression factor, the following relationship is established:

$$h = -\frac{1}{R_{56}} = 3.8 \text{ m}^{-1} \quad (6.37)$$

This highlights the importance of selecting the appropriate phase within the accelerating cryomodule to achieve optimal beam compression. By choosing this phase,

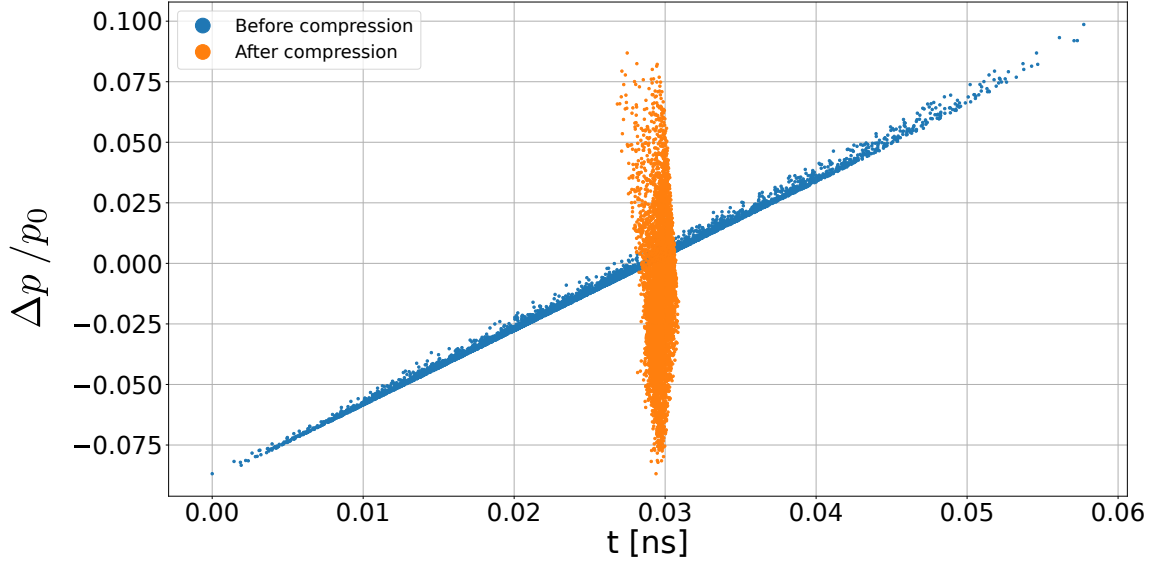


Figure 6.10: Longitudinal positron phase space before and after the compression process

an energy chirp of  $h = 3.8 \text{ m}^{-1}$  will be generated as the beam exits the cryomodule, considering a beam energy of 123 MeV. This energy chirp is directly connected to the specified value of  $R_{56} = -0.25 \text{ m}$ . The integrated compression system, which combines the accelerating module and the chicane, can be configured by substituting the chosen phase value into the equation in Eq. 6.36. This specific configuration is designed to achieve the maximum possible compression, denoted as  $C = 20$ . With this configuration in place, the simulation proceeds to evaluate the impact of such a system on the longitudinal positron phase space. The initial positron distribution from the first collimation chicane serves as the input for a C100 model. This model includes eight cavities, each spanning approximately 70 cm (3.5 wavelengths) in length. These cavities are paired with drift sections measuring 0.299 m in length. Following this arrangement, a specially designed achromatic chicane comes next, characterized by an  $R_{56} = -0.25 \text{ m}$ . This chicane is optimized to accommodate a 123 MeV positron beam and features a bending radius of  $B\rho = 0.41 \text{ T m}$ .

Figure 6.10 provides a clear visualization of the positron energy spread (vertical axis) in relation to the relative time coordinate (horizontal axis) at two critical locations: the exit of the C100 accelerating module (shown as blue dots) and the exit of the compression chicane (shown as orange dots). This representation effectively illustrates the evolution of the positron beam as it crosses the compression system.

Notably, the orange distribution at the exit of the second component exhibits a significantly reduced time extension compared to the blue distribution at the entrance of the C100 module. This observation corroborates our design strategy and aligns with our initial expectations. It confirms that coupling an accelerating process with a magnetic chicane leads to a fully compressed positron beam, as it originates from the collimation chicane.

Figure 6.11 illustrates the evolution of positron longitudinal characteristics, namely  $\sigma_t$ ,  $\Delta p/p_0$ , and the central momentum  $p_0$ . As observed, the accelerating module effectively reduces the energy spread over the initial four meters before the beam enters the second chicane. This reduction is significant; simultaneously, the positron energy rises to approximately 110 MeV.



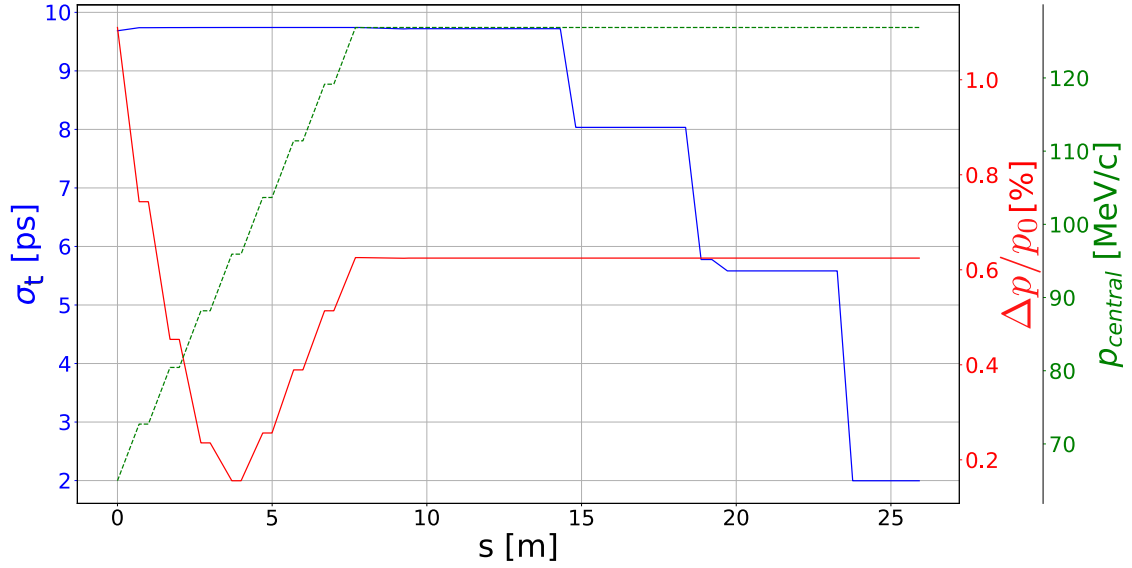


Figure 6.11: Progression of longitudinal positron beam characteristics in the optimized compression system

In the following stage, the latter portion of the C100 is used to achieve the targeted chirp value of  $h = 3.8 \text{ m}^{-1}$  at the exit of the C100. Unfortunately, this action results in an increase in energy spread.

At approximately 14 meters, the chicane begins (after a second matching section), and the bunch length  $\sigma_t$  exhibits continuous reduction until reaching a bunch length of 2 ps at its exit.

It is noteworthy that the energy spread remains constant, as previously established in Eq. (6.22), confirming that the energy spread along a chicane remains unchanged.

Considering the scenario of further minimizing the energy spread, additional reduction is emphasized. This approach prompts the exploration of the consequences of further reducing the energy spread.

Figure 6.12 illustrates the positron longitudinal phase space. In this description, the C100 module has been fine-tuned to achieve a smaller energy spread at its exit than the previous "Full compression case."

However, it becomes evident that the compression quality deteriorates in this context. The orange positron distribution demonstrates a pronounced extension along the x-axis, indicative of a larger bunch length.

Referring to Figure 6.13, it becomes evident that this second approach, focused on reducing the energy spread, results in an exit from the second chicane with a modest energy spread of 0.26%. However, this reduction comes with a drawback that leads to a bunch length of approximately 5 ps, larger than the previously achieved value.

Therefore, optimizing the compression section requires finding a balance between energy spread and bunch length that aligns with the exit requirements of the positron injector. The "Full compression" strategy proved more effective, yielding the desired outcomes and effectively meeting the longitudinal requirements of CEBAF.

With the efficacy of the compression section established, the focus now broadens to the overall characteristics of the positron injector. The subsequent section pro-

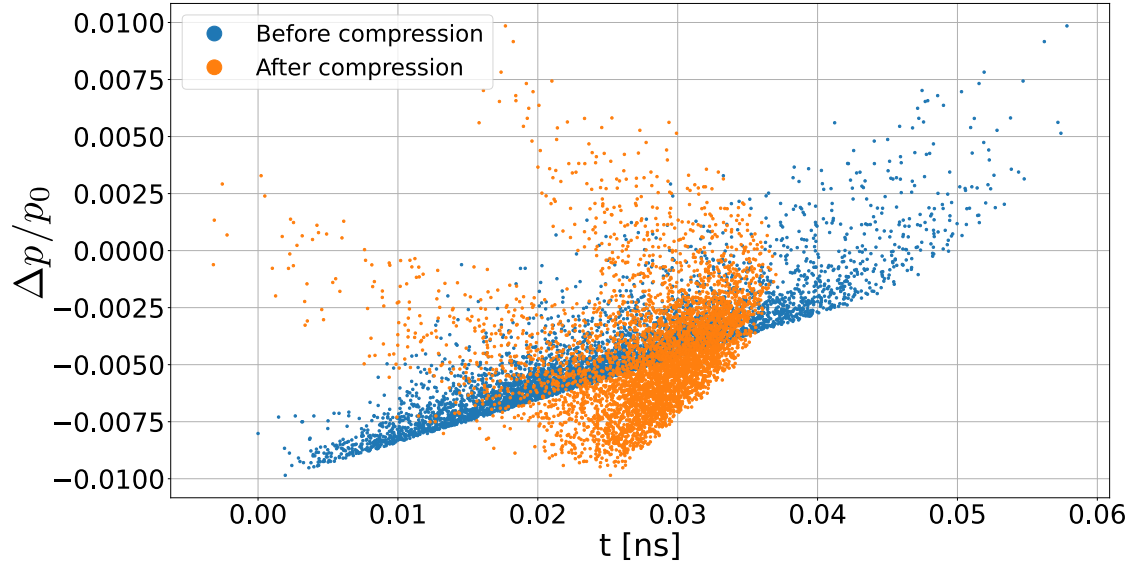


Figure 6.12: Longitudinal positron phase space before and after the compression process

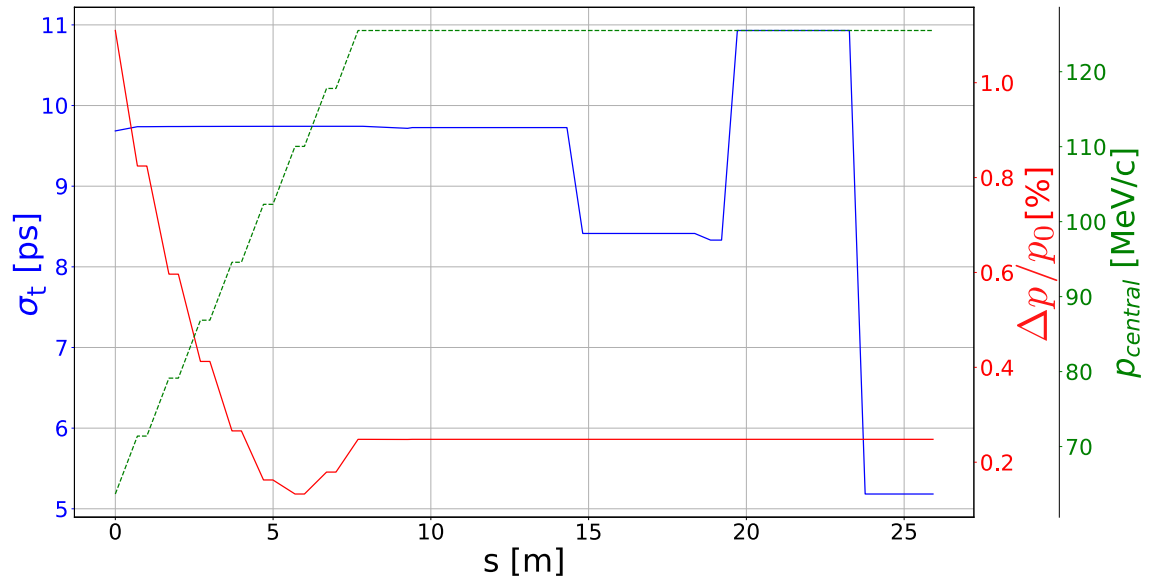


Figure 6.13: Progression of longitudinal positron beam characteristics in the optimized compression system

vides an integrated overview of the global positron injector characteristics along the entire designed layout, offering a comprehensive understanding of its performance and functionality.

### Positron injector characteristics

At this stage, all individual components of the positron injector have been designed. These elements are now assembled to form the complete layout of the positron injector.

A comprehensive simulation is conducted to track the path of the positrons from the moment they leave the target until they exit the compression chicane. The following figure illustrates the entire layout of the positron injector, encompassing all these stages: Conducting an ELEGANT simulation will provide insights into the

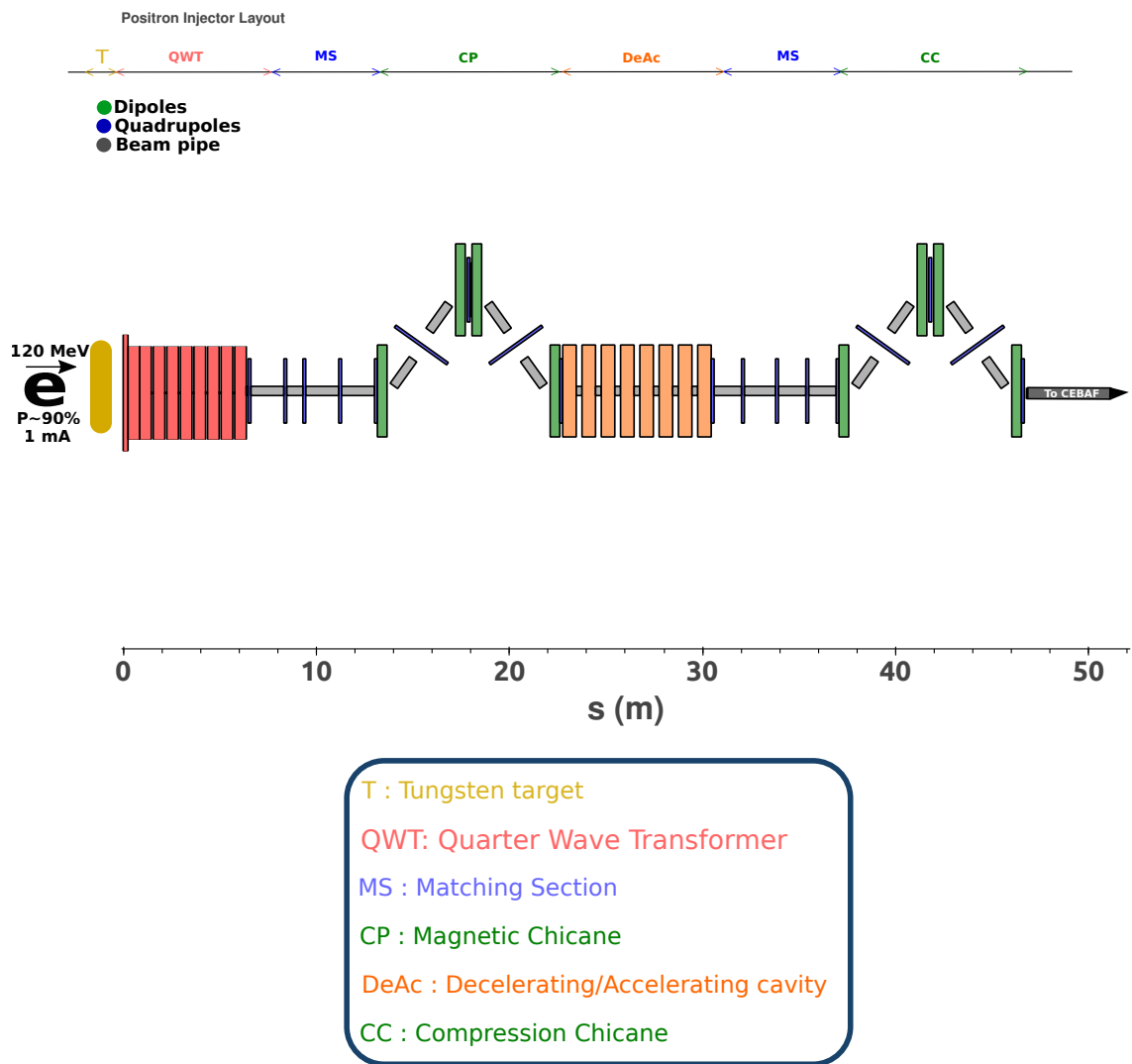


Figure 6.14: Schematic Layout of the Positron Injector Designed for the LERF Facility

behavior of crucial positron beam parameters throughout the positron injector. The aim is to assess positron efficiency, current, beam size, and emittance.

First, an analysis of the Twiss parameters along the length of the positron injector is conducted: Fig. 6.15 provides insight into the behavior of key optical parameters along the positron injector layout. The periodic nature of the betas is evident throughout the two incorporated magnetic chicanes, facilitated by the optimized matching sections. These sections enable precise beam control even when the dispersion function deviates from zero. Additionally, the dispersion is reset to zero at the exit of both chicanes, ensuring the injector's achromatic nature.

The subsequent figures illustrate the behavior of transverse beam properties across the designed injector. In Fig. 6.16, a substantial variation in  $\sigma_{x,y}$  is observed upon entering the injector. As discussed earlier, the employed collection system QWT transforms the beam from the target, resulting in a considerable increase in beam size and angular divergence, as indicated by notable jumps in  $\sigma_{x,y}$ . These jumps are reflected in the normalized transverse emittances  $\epsilon_{\text{Normalized},x,y}$ . A significant reduction in beam size is evident at the collimation region within the first chicane. This reduction is attributed to the collimation process, which selectively eliminates positrons located beyond the collimated energy spread, leading to particle loss and subsequent beam size reduction. A similar reduction occurs after exiting the collimation chicane. This trend continues after the C100 region, highlighting the positive effect of the second matching section in controlling transverse beam size. The addition of more quadrupoles could further enhance the control of the beam envelope.

Examining the lower portion of Fig. 6.16, the significant impact of the dispersion function introduced by the first chicane on the normalized horizontal emittance  $\epsilon_{\text{Normalized},x}$  is observed. The beam exits the collimator and behaves as a mono-energetic beam; the normalized transverse emittances remain constant along the C100, aligning with theoretical expectations.

In the pursuit of understanding the primary longitudinal characteristics of the positron beam, attention turns to Figure 6.17, which shows the evolution of key parameters: the central momentum  $p_0$  of the reference particle for the polarized mode ( $p_0 = 60$  MeV/c), the positron bunch length  $\sigma_t$ , and the positron energy spread  $\sigma_{\Delta p/p_0}$ .

Two distinctive acceleration regions are discerned in the top panel of the first figure. The initial acceleration occurs within the capture section, using 1 MV/m, where the central momentum accelerates from 60 MeV/c to 65 MeV/c. This stage helps to reduce the positron angular divergence. The second acceleration segment occurs after the collimation chicane, achieved through the C100 cryomodule, ending in the desired injection energy of 123 MeV.

Directing attention to the red curve, a significant reduction in energy spread is evident within the midpoint of the collimation chicane. This drop in energy spread at the 15-meter location is due to the successful momentum collimation, effectively minimizing the energy spread. Subsequently, the C100 module further reduces the energy spread.

Distinguishing between the top and bottom figures, the upper part highlights the optimized compression chicane. Here, the emphasis is on reducing the bunch length, resulting in an exit from the positron injector with  $\sigma_{\Delta p/p_0} = 0.6\%$  and  $\sigma_t = 2$  ps. This achievement aligns with the energy spread requirement for CEBAF-NL injection.

Conversely, the lower part presents an alternate configuration of the compression

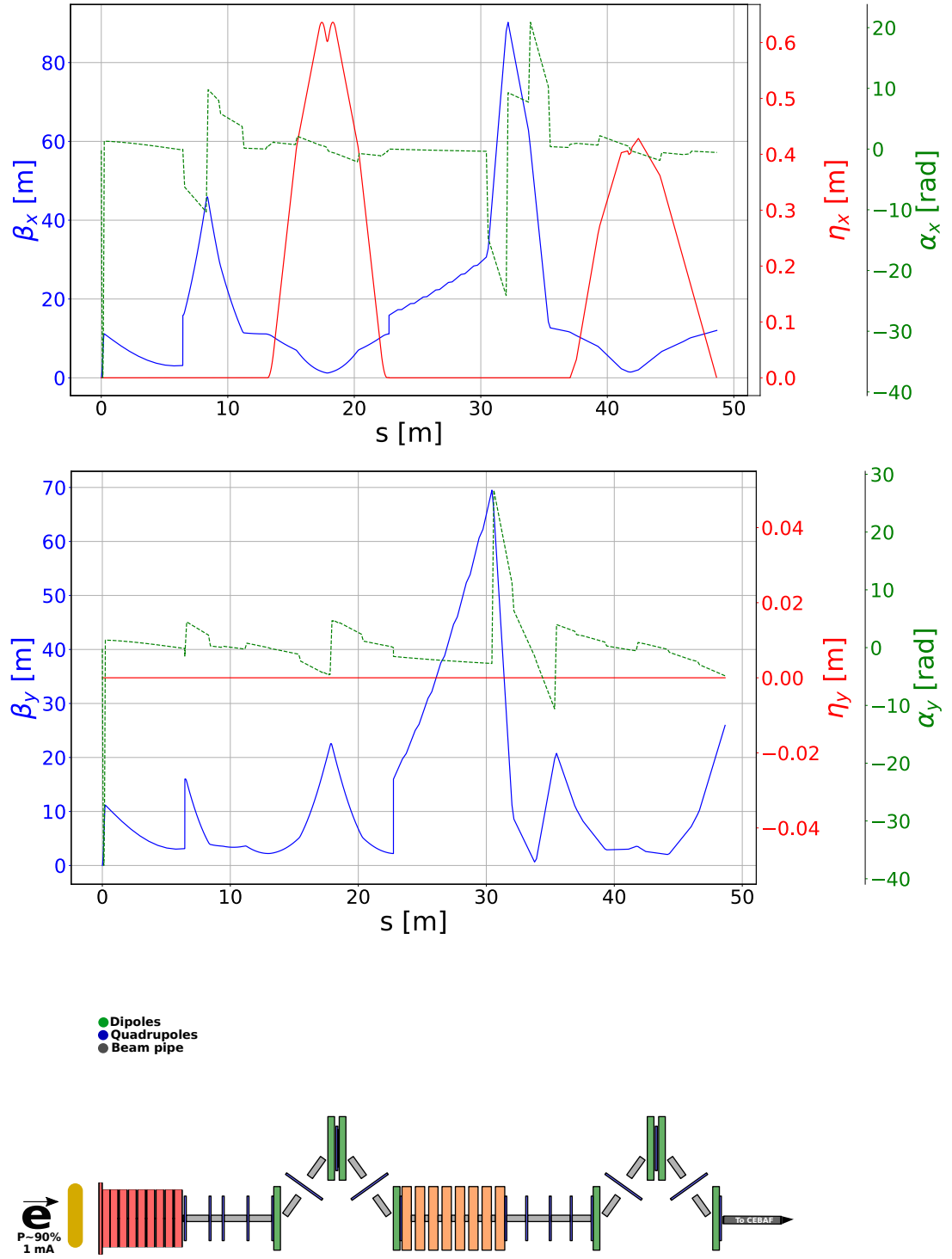


Figure 6.15: Twiss parameters variation along the designed positron injector for the polarized operational mode

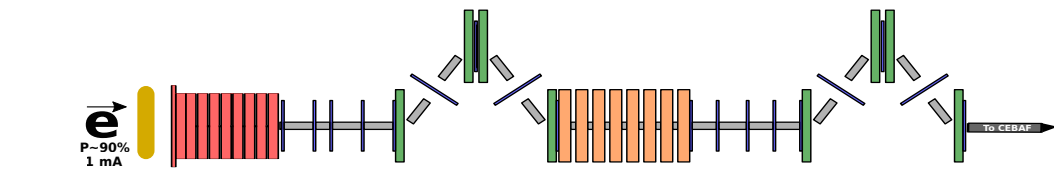
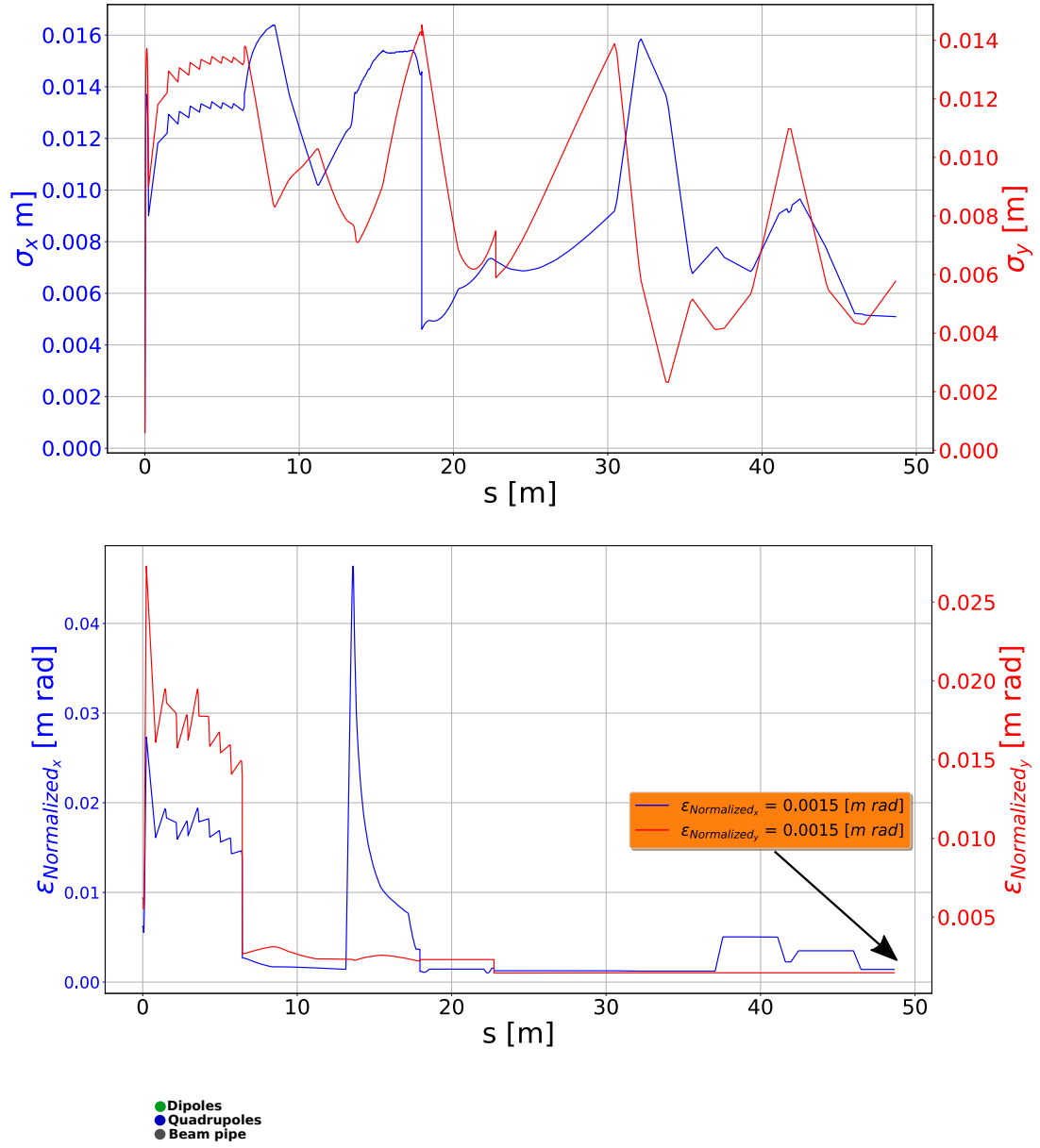


Figure 6.16: Evolution of transverse beam parameters along the positron injector: transverse beam sizes in x and y axes and normalized transverse emittances

system. In this scenario, both the C100 and the second chicane are optimized to minimize the energy spread, achieving an impressively tight beam energy spread of  $\sigma_{\Delta p/p_0} = 0.2\%$ . However, the corresponding trade-off leads to a bunch length of approximately  $\sigma_t = 5$  ps at the positron injector exit, a notable contrast to the former case where the bunch length remained below 2 ps.

From Fig. 6.18, the top panel provides insights into positron efficiency, central momentum, and positron current. As discussed earlier, two distinct accelerating stages are evident. A significant reduction in positron yield and current occurs within the capture section. This decline can be attributed to the optimized QWT collection system, which efficiently captures and transmits only a narrow energy spread, dumping many positrons along this section. The collimator stage also leads to a notable decrease in positron yield due to the collimation process. The behavior of the positron current, represented by the green curve, aligns with the observed efficiency pattern.

Exiting the tailored positron injector layout optimized for the polarized operational mode, the positron exhibits favorable parameters and notably improved current. These outcomes align closely with CEBAF injection requirements for CEBAF-NL.

The bottom panel of Fig. 6.18 illustrates the locations of positron loss within the injector. As discussed earlier, the highest lost density occurs at the initial segment of the QWT and continues throughout the second solenoid (capture section). These loss patterns introduce additional challenges concerning shielding and engineering considerations for the positron source.

An interesting phenomenon is also revealed in Fig. 6.18, highlighting the correlation between strong and weak magnetic fields within the QWT. This correlation selectively allows particles around 60 MeV to successfully traverse the capture section, underscoring the significance of optimization strategies.

After the collimation chicane, a high percentage of collimated positrons are successfully transmitted to the C100 and the compression chicane with minimal losses.

$$I_{e^+} = 170 \text{ nA.}$$

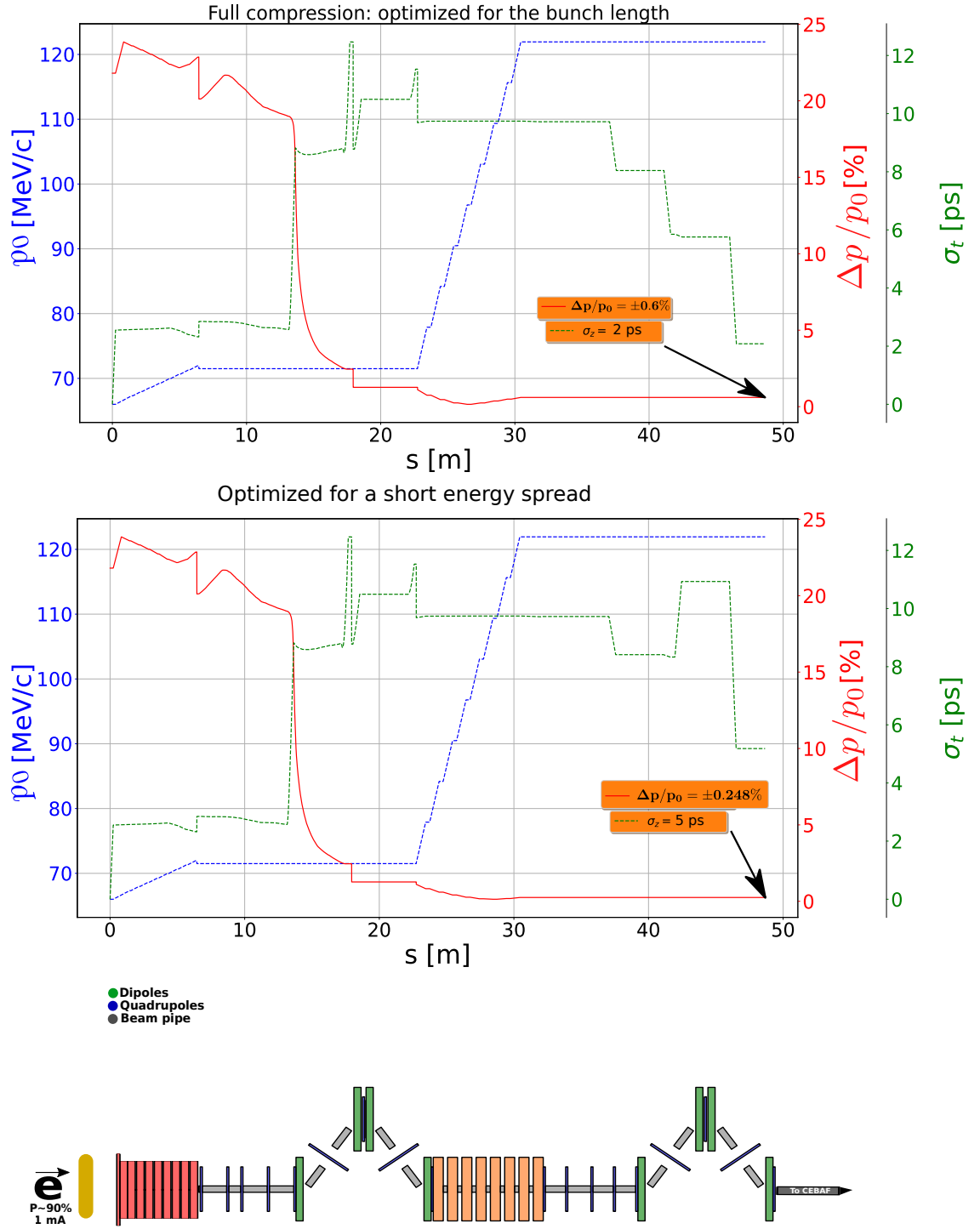


Figure 6.17: Evolution of Key Longitudinal Positron Characteristics Along the Designed Injector: Central Momentum  $p_0$  (Blue Curve), Bunch Length  $\sigma_t$  (Green Curve), and Energy Spread (Red Curve) for Two Distinct Compression Configurations



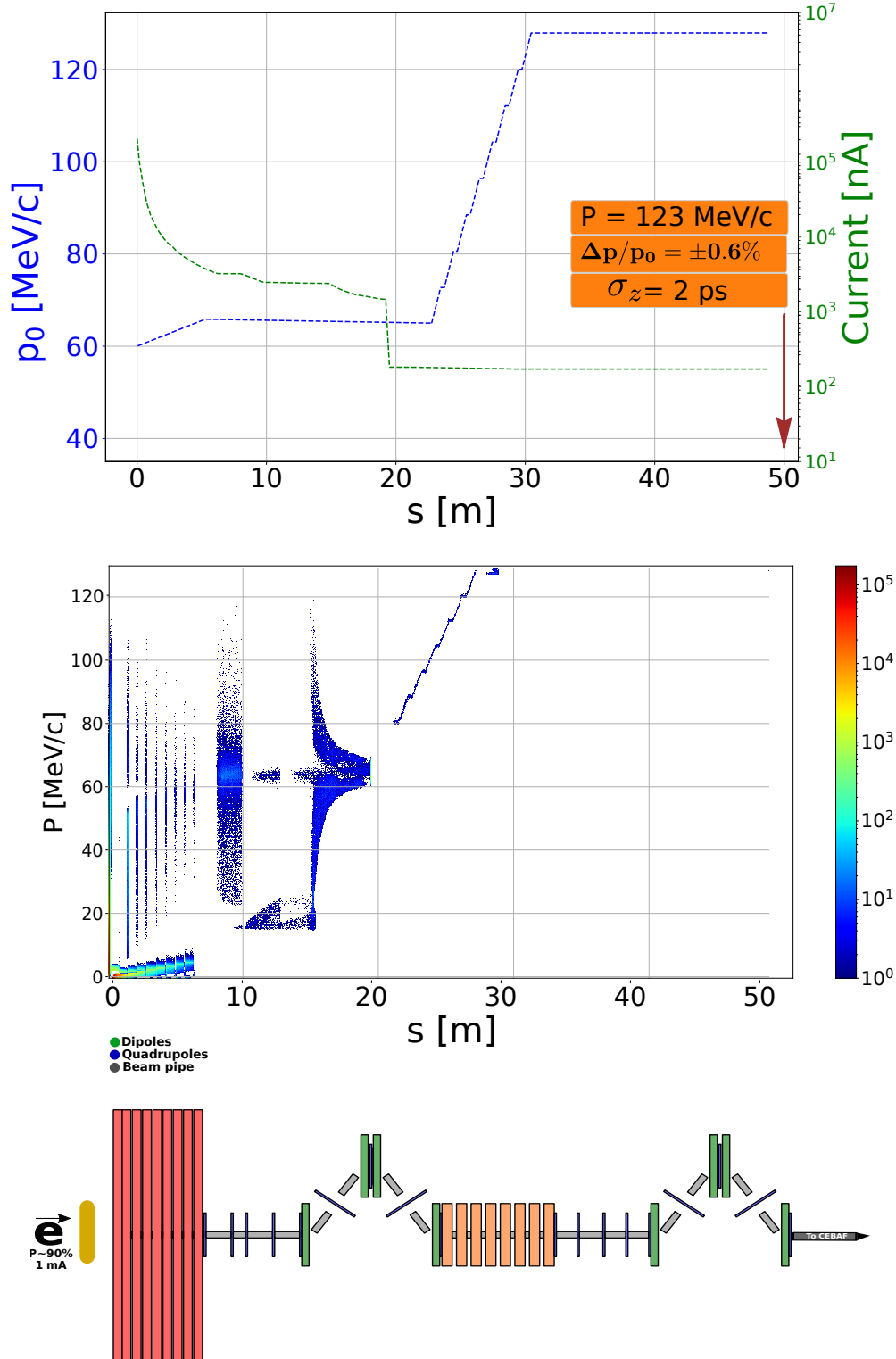


Figure 6.18: Positron beam physics characteristics along the layout, the central momentum is shown in blue color, and the green current shows the positron current, in the top panel figure, and in the bottom panel figure shows the lost positrons along the beam line

# Chapter 7

## Conclusion

In recent years, the potential of a highly polarized positron source has become increasingly evident at JLab, promising to pave the way to a new era of experiments by granting direct access to crucial nuclear parameters. Key experiments at JLab, such as the Deeply Virtual Compton Scattering (DVCS), underscore this necessity. DVCS allows researchers to explore the internal structure of nucleons, observing how virtual photons interact within these subatomic particles and consequently displaying their intricate dynamics. Moreover, it is worth noting that highly polarized positron sources have garnered global attention and have seen significant developments and successes worldwide, despite the inherent challenges they pose. Notably, institutions like MAMI and CERN are also exploring the potential of positron sources at their facilities. A significant step forward in this domain was marked by the success of the PEPPo experiment conducted at JLab in 2011 [26]. This experiment demonstrated the efficient transfer of polarization from JLab CW polarized electron beam to a generated positron beam. This transfer is achieved via the Bremsstrahlung process coupled with pair creation. The design principle of the new  $\text{Ce}^+\text{BAF}$  injector have a marked alignment with the evolution of the positron source.

This thesis presents a design for a CW polarized positron source, meeting the objectives through rigorous simulations. The research makes several significant contributions to the field, most notably achieving a simulated polarization of 65%, a positron current of 170 nA, and a positron energy of 123 MeV. This study not only contributes to the development of efficient positron sources but also highlights several critical requirements essential for advancements of positron sources. These requirements include beam power deposition in the target, addressing challenges in the high-field region of the collection system, ensuring its adjustability to operate efficiently at various positron energies, and the necessity for a high accelerating gradient to effectively reduce energy spread in the capture region.

This thesis had several goals. Firstly, this work aimed to give an initial evaluation of the positron beam quality, confirming that it meets the standards set by the CEBAF machine and the JLab experimental program. Secondly, its goal is to demonstrate the design of a new positron source that can achieve high polarization degrees. Specifically, future experiments at CEBAF need a positron beam with over 60% polarization. Thirdly, the objective is to optimize the current of the generated positrons. A minimum current of  $\geq 50$  nA is needed while maintaining a good positron polarization. On the other hand, at least  $\geq 1$   $\mu\text{A}$  is needed for a high positron yield regardless of polarization. These goals were successfully achieved,

paving the way for the exciting next level of R&D.

To meet these objectives, the thesis determined the optimal target thickness. This ensured a balance between positron polarization and yield. A specific thickness was identified that allows both polarized and unpolarized modes to operate optimally. In tandem with this, the design of a collection system was undertaken. A comparison between different variations and combinations of magnetic field profiles has been explored. The chosen design was successfully simulated to meet the small momentum acceptance in accordance with the CEBAF specifications. To further enhance the positron beam quality, a momentum collimation system using a magnetic chicane was designed and simulated. This system selects highly polarized positrons, meeting the energy spread prerequisites of CEBAF. Moreover, an accelerating cryo-module of the CEBAF-type was simulated to achieve the desired 123 MeV injection energy at the entrance of the CEBAF-NL. Concurrently, a second magnetic chicane was designed to compress the positron bunch length to under 4 ps, meeting the injection criteria.

This research presents a comprehensive start-to-end simulation, modeling a complete positron injector modeled in ELEGANT. The outcome exceeds the estimated requisite positron beam quality for JLab experimental halls and gives guidance on the feasibility of the positron project at JLab. This work also underlines some of the technical challenges, such as the urgent need to evaluate the thermal fatigue aspects resulting from high energy deposit in the production converter. This thesis also shows the need to engineer a capture section realistically following the optimized QWT configuration. Another key point is related to the distinct secondary nature of the positron beam. After generation at the target exit, the created positron beam displays a phase space completely different from the initial electron beam: such as a high yield at lower momenta and a wide transverse angular spread. Consequently, the quality of this beam at the injection region differs significantly from the standard primary electron beam typically injected into CEBAF. The work in this thesis was guided by the requirement for matching the CEBAF machine acceptances ( $E_i$ ,  $\Delta p/p_0$ ,  $\sigma_t$ ,  $\epsilon$ , FoM), which were thoroughly quantified.

This design can be implemented as a second injector inside the building of the Low Energy Recirculating Facility (LERF). The new positron injector at the LERF would require: a new high intensity and high polarization electron gun; several cryo-modules to accelerate the electron beam to 123 MeV; a positron production target, a capture section, a collimation chicane, an accelerating section, and a longitudinal compression system. Then the positron beam would be transported to the injection point at the CEBAF-NL entrance.

This thesis serves as an introductory step for the positron research program at JLab. While the simulations have shown promising results, it remains several engineering aspects requiring additional focus. The current design predominantly centers on optimizing the positron phase space throughout the positron injector. Future designs should address further considerations:

- Damping of the primary and secondary electron beam after the target;
- Refining design and enhance positron beam parameters, specifically to decrease normalized emittances arising from the beam secondary nature;
- Add realistic factors to the simulations, such as field errors and misalignments;

- Evolve the design to fit within engineering constraints and specifications.

Continuous research and development efforts are required to address these challenges and limitations. The primary focus would be enhancing positron generation efficiency, preserving polarization, managing power density, and ensuring compatibility with accelerator systems. Overcoming these hurdles is key for successfully designing future positron sources that rely on high-intensity and high polarization positron beams.

# Appendix A

Poster contribution to the  
International Particle Accelerator  
Conference | IPAC22

# CONCEPT OF A POLARIZED POSITRON SOURCE FOR CEBAF

S. Habet<sup>1,2</sup>, Y. Roblin<sup>2</sup>, R.M. Bodenstein<sup>2</sup>, S.A. Bogacz<sup>2</sup>, J. Grames<sup>2</sup>, A. Hofler<sup>2</sup>, R. Kazimi<sup>2</sup>,  
F. Lin<sup>2</sup>, M. Poelker<sup>2</sup>, A. Seryi<sup>2</sup>, R. Suleiman<sup>2</sup>, A. Sy<sup>2</sup>, D. Turner<sup>2</sup>, A. Ushakov<sup>1</sup>,  
C.A. Valerio-Lizarraga<sup>3</sup>, E. Voutier<sup>1</sup>

<sup>1</sup>Université Paris-Saclay, CNRS/IN2P3/IJCLab, 91405 Orsay, France

<sup>2</sup>Thomas Jefferson National Accelerator Facility, Newport News, VA 23606, USA

<sup>3</sup>Universidad Autónoma de Sinaloa, 80010 Culiacán, México

## Abstract

Polarized and unpolarized positron beams are essential for the future hadronic physics experimental program at the Thomas Jefferson National Accelerator Facility (JLab). The main challenge is to produce high duty-cycle and high intensity polarized positron beams. The JLab positron source uses the Polarized Electrons for Polarized Positrons (PEPPo) technique to create either a low intensity, high polarization positron beam ( $I > 100$  nA,  $P=60\%$ ), or a high intensity unpolarized positron beam ( $I > 3$   $\mu$ A), from an intense highly polarized electron beam ( $I=1$  mA,  $P=90\%$ ). The current design involves a new injector dedicated to positron production, collection, and shaping suitable for acceleration through the Continuous Electron Beam Accelerator Facility (CEBAF). The optimization of the layout and the performance of the positron source are explored in this paper.

## INTRODUCTION

Positron beams can be used to probe physics phenomena. For instance, high energy beams allow to investigate the structure of nuclei while low energy beams access the distribution of electrons inside materials [1]. One interest at JLab is the study of the partonic structure of the nucleon from the scattering of highly polarized electron and positron beams. For instance, the comparison between the two beam species allows to isolate the different components of the deeply virtual Compton scattering cross section, and provides more pertinent and sensitive experimental observables [2, 3].

In this context, we may refer to the PEPPo experiment [4, 5], which demonstrated at the CEBAF injector the efficient polarization transfer from longitudinally polarized electrons to positrons [6]. Initial beam electrons generate elliptical polarized photons within a tungsten target via bremsstrahlung. These polarized photons then create in the same target positron and electron pairs. The main concern of the JLab positron project is to generate high-duty cycle longitudinally polarized positron beams from a 120 MeV/c electron beam with as high as possible an efficiency. The essential difficulty is to keep a high positron efficiency all along the collection and transport line of the positrons to the main accelerator, and to permit polarized or unpolarized dual operation with a small momentum dispersion delivered to experimental halls. The positron injector layout design, the target thickness optimization, and the positron beam optics are described in the following sections.

## POSITRON INJECTOR LAYOUT

The positron injector is designed to provide an efficient number of positrons suitable for CEBAF injection. The transverse and longitudinal dynamics of the positron beam are optimized to stay within the acceptance limits. A positron collection system composed of high magnetic field lenses [7] is essential to decrease the large transverse momentum spread at the target exit. A conceptual layout of the injector is shown in Fig. 1. A moderate energy electron beam interacts within a tungsten target (T) to produce positrons that are collected with an Adiabatic Matching Device (AMD). A four quadrupoles matching section (MS) and a magnetic chicane (CP) select further the central momentum and the momentum bite of the positron population. A decelerating/accelerating section (DeAc) reduces then the momentum dispersion. Finally, a chirping cavity (ChC) correlates the momentum dispersion with the positron time-of-flight, and a second chicane (CC) compresses the positron bunch length to match with the CEBAF injection acceptance. We have determined the maximum bunch length acceptance is 4 ps, and our strategy is to further reduce this towards the nominal 12 GeV e- bunch length as possible, of 0.3 ps through compression techniques.

## POSITRON TARGET OPTIMIZATION

Geant4 [8] simulations are used to optimize the positron production considering a 120 MeV/c electron beam 100% longitudinally polarized hitting a tungsten target. The analysis of simulated data follows the evolution of the positron production efficiency  $\epsilon$  and of the Figure-of-Merit  $\text{FoM} = \epsilon P_{e^+}^2$  as function of the target thickness.  $\epsilon$  is the quantity of interest for an unpolarized positron source. The FoM further combines the average polarization to maximize the statistical precession of an experiment in the minimum amount of time. This investigation aims to optimize the target thickness for the production of unpolarized and polarized positrons. The Fig. 2 shows  $\epsilon$  (left) and FoM (right) simulations for a 4 mm thick target, within a selected momentum bite  $\Delta p/p = \pm 10\%$  at each central momentum  $p_0$  and within the angular acceptance  $\Delta\theta_{e^+}$ . The efficiency decreases when the angular aperture decreases, describing a large positron momentum spread in the transverse plane. The essential difference between unpolarized and polarized operation modes is the positron energy to be selected for optimum collection: about a sixth of the primary electron beam energy for optimized efficiency, and a half for optimized FoM. The maximum value

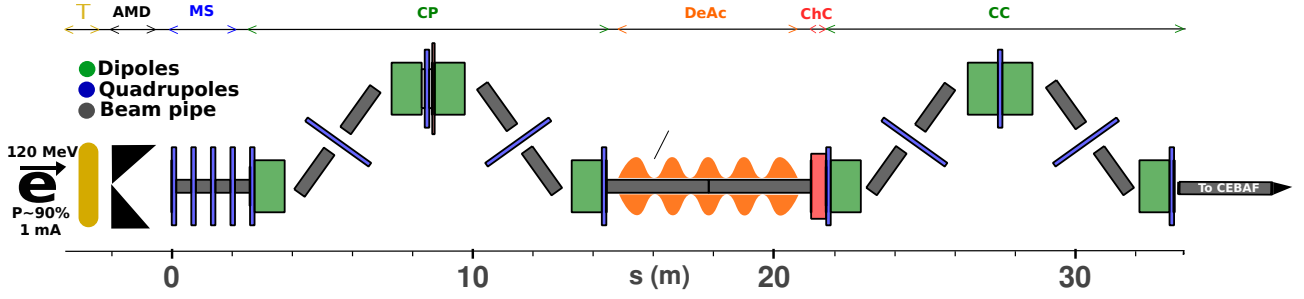


Figure 1: Conceptual layout of the positron injector for CEBAF.

of  $\epsilon$  and FoM determines the optimum target thickness. At 120 MeV/c, it is about 4 mm, however, depending on the angular acceptance and the operation mode. The absolute value of  $\epsilon$  and FoM are strongly affected by the angular acceptance and the momentum bite. These define the main parameters of the optimization of the positron injector.

## PRELIMINARY CHARACTERIZATION

### Momentum Selection

Figure 2 establishes the momentum selection procedure for unpolarized and polarized mode operation which is chosen at the  $p_0$  peak value of the efficiency or the FoM. In order to select the corresponding positron yield a conversion of the momentum dispersion from the longitudinal plane ( $\delta p/p, z$ ) to the transverse plane ( $\delta p/p, x$ ) was explored. A magnetic chicane is designed from two opposite doglegs constituted of dipoles centered around  $p_0$ . Since the positron beam is polychromatic, the dogleg will allow to reach the maximum dispersion at its exit. The dispersion generated by each dipole is calculated from the expression [9]

$$D(s) = S(s) \int_0^s \frac{1}{\rho} C(t) dt - C(s) \int_0^s \frac{1}{\rho} S(t) dt \quad (1)$$

where  $C(s)$  and  $S(s)$  are the parameters of the  $2 \times 2$  dipole transfer matrix. The dispersion function for each dipole can

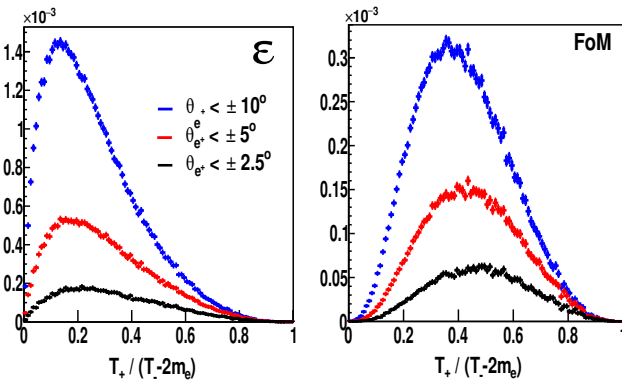


Figure 2: Positron production characteristics at 120 MeV/c off a 4 mm tungsten target, considering different angular acceptances and a  $\pm 10\%$  momentum bite.

be expressed as

$$D = \rho \left[ 1 - \cos\left(\frac{L}{\rho}\right) \right] \quad (2)$$

which quantifies the dogleg action on the beam in the  $(x, \delta p/p)$  plane. The positron beam envelope evolution along the dogleg is shown in Fig. 3. At the dogleg entrance (blue), the transverse coordinates  $x$  do not correlate with the momentum dispersion. At the middle of the chicane, the positron distribution (red) exhibits an essential correlation between  $x$  and  $\delta p/p$ . Therefore, a collimator centered at  $x = 0$  with appropriate aperture selects a given  $\Delta p/p$  of positron momentum. The distribution at the exit of the collimator (green) corresponds to a 5 mm radius collimator, selecting a  $\pm 10\%$  of positron momentum.

### Beam Size

Maximizing the positron selection efficiency after the collimator implies for the smallest beam size at the middle of the chicane. Thus a focusing-defocusing (FODO) lattice is introduced along the chicane. It consists of three quadrupoles, the first and the third are placed respectively at the entrance and exit legs of the chicane, the second at the middle of the chicane. The FODO aims at making a periodic  $\beta$ -function to obtain a minimum transverse beam size at the middle of the chicane. The periodicity condition requires  $\beta_{out} = \beta_{in}$

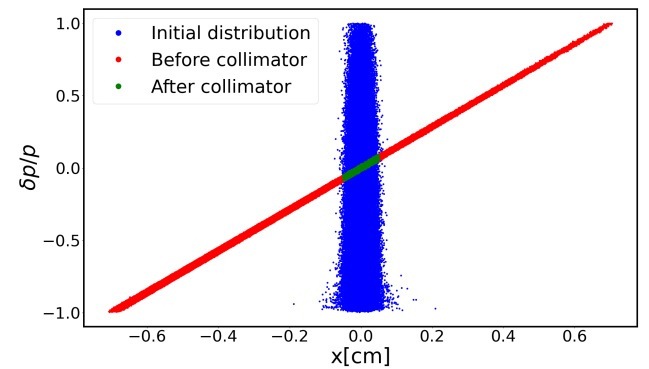


Figure 3:  $(\delta p/p, x)$  positron distributions at the entrance (blue) and middle of the chicane (red), and at the collimator exit (green).

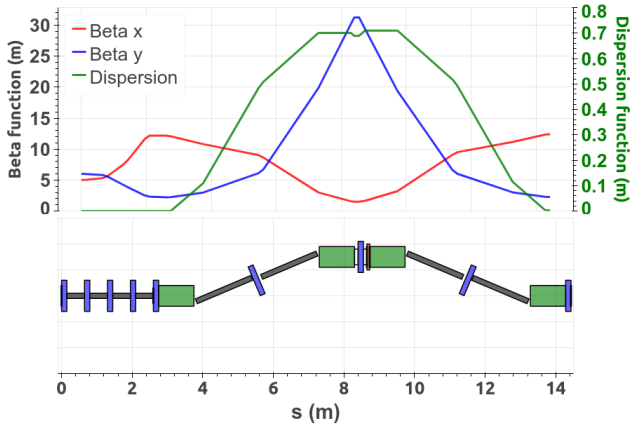


Figure 4: Variation of the optical  $\beta$ -function along the chicane.

where  $\beta$ 's are the positron beam twiss functions related to the transverse beam size at the entrance (in) and the exit (out) of the chicane. The evolution of the  $\beta$ -function along the chicane is shown in Fig. 4. The matching section prior to the first dipole intends to match the incoming optical parameters of the positron beam with the optical requirements at the entrance of the FODO lattice. The stability of the FODO lattice is also demonstrated by the periodicity of the  $\beta$ -function from the entrance to the exit of the chicane. As expected, the smallest  $\beta_x$ -function is obtained at the middle of the chicane, simultaneously with the largest dispersion. This allows an efficient momentum collimation.

## CHIRP AND COMPRESSION

The second chicane intends to compress longitudinally the beam. To reach an efficient compression, a correlation between  $\delta p/p$  and  $z$  is introduced by chirping the beam with an RF cavity. A second requirement is a magnetic chicane with appropriate properties to link the momentum dispersion to the longitudinal bunch length. The compression factor for a small momentum dispersion can be written as

$$C = \frac{1}{1 + \kappa R_{56}} \quad (3)$$

where  $R_{56}$  is the matrix element 56 of the chicane transfer matrix. It controls the longitudinal size of the beam according to

$$\Delta z = R_{56} \left( \frac{\delta p}{p} \right)_{in} \quad (4)$$

where  $(\delta p/p)_{in}$  represents the initial longitudinal momentum spread, and  $\kappa$  characterizes the beam chirp created by the cavity. The latter can be expressed as

$$\kappa = \frac{d}{dz} \left[ \frac{\delta p}{p} \right] = \frac{2\pi f}{c} \frac{eV_0}{E_0 + eV_0 \cos \phi} \sin \phi \quad (5)$$

where  $f$  is the cavity frequency (Hz),  $eV_0$  is the cavity acceleration (MeV),  $E_0$  is the central energy (MeV), and  $\phi$  is the cavity phase advance. Figure 5 shows the compression

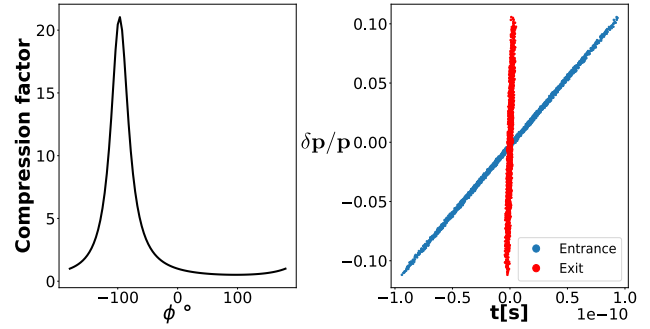


Figure 5: Variation of the compression factor vs the cavity phase advance (left), and full compression of the longitudinal beam length (right).

factor peak at  $\phi = -96.6^\circ$  (left), which describes the setting of the cavity with a proper chirp. The effect of full system on the  $(\delta p/p, t)$  beam profile, including the appropriate  $R_{56}$  chicane, exhibits a beam length at the exit of the chicane 23 times smaller than the entrance ones (Fig. 5 right).

## CONCLUSION

The generation and injection of cw positron beams suitable to the high performance will present a number of technical challenges which must be overcome. One of the challenges is to decrease the momentum dispersion of the collimated positron distribution from  $\delta p/p = \pm 10\%$  to  $\pm 2\%$ . A set of cavities at the exit of the first chicane will serve this purpose, and acceleration through the south linac will provide about ten times further reduction. The CEBAF arcs can also be tuned for more compression providing an additional chirp. An optimization will be performed to obtain a reduction factor suitable for CEBAF acceptances that are a bunch length of  $\Delta t = 4$  ps and a momentum spread of  $\delta p/p = \pm 2\%$ . Further studies about the capture magnet are also foreseen as different magnets may support different operation mode. The concept optimization is being explored with further analytical and simulation studies. Further, a new positron injector may be assembled at the Low Energy Research Facility (LERF) to develop a proof-of-principle, and then later maybe connected to the CEBAF accelerator through a new transport line.

## ACKNOWLEDGMENTS

This material is based upon work supported by the U.S. Department of Energy, Office of Science, Office of Nuclear Physics under contract DE-AC05-06OR23177. This work has received funding from the European Union's Horizon 2020 research and innovation program under grant agreement No 824093.

## REFERENCES

- [1] E. Voutier, "Physics potential of polarized positrons at the Jefferson Laboratory," *Nucl. Theor.*, vol. 33, pp. 142–151, 2014, doi:10.48550/arXiv.1412.1249



- [2] N. Alamanos, M. Battaglieri, D. Higinbotham, S. Niccolai, A. Schmidt, E. Voutier, “Topical issue on an experimental program with positron beams at Jefferson Lab,” *Eur. Phys. J. A*, vol. 58, no. 3, p. 45, 2022, doi:10.1140/epja/s10050-022-00699-6
- [3] A. Accardi *et al.*, “An experimental program with high duty-cycle polarized and unpolarized positron beams at Jefferson Lab,” *Eur. Phys. J. A*, vol. 57, no. 8, p. 261, 2021, doi:10.1140/epja/s10050-021-00564-y
- [4] J. Grames, E. Voutier *et al.*, “Polarized Electrons for Polarized Positrons: a proof-of-principle experiment,” Thomas Jefferson National Accelerator Facility, Newport News, VA, USA, Jefferson Lab Experiment E12-11-105, 2011.
- [5] E. Voutier, “The PEPPo Concept for a Polarized Positron Source,” in *4th Int. Particle Accelerator Conf. (IPAC’13)*, Shanghai, China, May 2013, pp. 2088–2090, <https://jacow.org/IPAC2013/papers/WE0AB203.pdf>
- [6] D. Abbott *et al.*, “Production of highly polarized positrons using polarized electrons at mev energies,” *Phys. Rev. Lett.*, vol. 116, p. 214801, 21 2016, doi:10.1103/PhysRevLett.116.214801
- [7] R. Boni, S. Guiducci, and M. Vescovi, “A new system for positron focusing at the Frascati linac,” INFN - Laboratori Nazionali di Frascati, Italy, Rep. LNF-81/6(R), Jan. 1981.
- [8] S. Agostinelli *et al.*, “GEANT4—a simulation toolkit,” *Nucl. Instrum. Meth. A*, vol. 506, pp. 250–303, 2003, doi:10.1016/S0168-9002(03)01368-8
- [9] H. Wiedemann, *Particle Accelerator Physics*. Springer Berlin Heidelberg, 2007, <https://books.google.com/books?id=S8CfmLe87RAC>

## Appendix B

Poster contribution to the  
International Particle Accelerator  
Conference | IPAC23

# POSITRON BEAMS AT Ce<sup>+</sup>BAF\*

J. Grames<sup>1</sup>, J. Benesch<sup>1</sup>, M. Bruker<sup>1</sup>, L. Cardman<sup>1</sup>, S. Covrig<sup>1</sup>, P. Ghoshal<sup>1</sup>, S. Gopinath<sup>1</sup>, J. Gubeli<sup>1</sup>, S. Habet<sup>1,2</sup>, C. Hernandez-Garcia<sup>1</sup>, A. Hofler<sup>1</sup>, R. Kazimi<sup>1</sup>, F. Lin<sup>3</sup>, S. Nagaitsev<sup>1</sup>, M. Poelker<sup>1</sup>, B. Rimmer<sup>1</sup>, Y. Roblin<sup>1</sup>, V. Lizarraga-Rubio<sup>4</sup>, A. Seryi<sup>1</sup>, M. Spata<sup>1</sup>, A. Sy<sup>1</sup>, D. Turner<sup>1</sup>, A. Ushakov<sup>1</sup>, C. A. Valerio-Lizarraga<sup>5</sup>, E. Voutier<sup>2</sup>

<sup>1</sup>Thomas Jefferson National Accelerator Facility, Newport News, VA, USA

<sup>2</sup>Université Paris-Saclay, CNRS/IN2P3/IJCLab, France

<sup>3</sup>Oak Ridge National Laboratory, Oak Ridge, TN, USA

<sup>4</sup>Universidad de Guanajuato, Leon, Gto., México

<sup>5</sup>Universidad Autónoma de Sinaloa, Culiacán, México

## Abstract

We present a scheme for the generation of a high polarization positron beam with continuous wave (CW) bunch structure for the Continuous Electron Beam Accelerator Facility (CEBAF) at Jefferson Laboratory (JLab). The positrons are created in a high average power conversion target and collected by a CW capture linac and DC solenoid.

## INTRODUCTION

The CEBAF accelerator has provided high energy spin polarized electron beams for almost 30 years. Today, JLab is exploring an upgrade which would provide high energy spin polarized positron beams to address new physics [1, 2].

A relatively new technique referred to as PEPPo (Polarized Electrons for Polarized Positrons) has been adopted [3] to generate the positrons. Here the spin polarization of an electron beam is transferred by polarized bremsstrahlung and polarized  $e^+e^-$  pair creation within a high-power rotating tungsten target.

In this scheme two accelerators are used (see Fig. 1). First, the Jefferson Lab Low Energy Recirculator Facility (LERF) building (see Fig. 2) is repurposed to take advantage of existing electrical, cryogenic, and shielding facilities. A high current  $>1$  mA spin polarized CW electron beam is produced, accelerated to an energy of 120 MeV and transported to the high-power target to generate the spin polarized positrons. Afterwards, the positrons are collected to maximize intensity or polarization, bunched and re-accelerated to 123 MeV. Finally their spin direction may be adjusted in a novel spin rotator. Once the positron beam exits the LERF it is transported from ground level through a new beam line to the CEBAF accelerator tunnel underground. There it is transported half-way around the accelerator and injected as a usual electron beam would from the existing CEBAF electron injector. The positrons are then accelerated to 12 GeV and may be extracted at any pass (intermediate energies)

\* This project is supported by the U.S. Department of Energy, Office of Science, Office of Nuclear Physics under contract DE-AC05-06OR23177; UT-Battelle, LLC, under contract DE-AC05-00OR22725 with the US Department of Energy (DOE); the European Union's Horizon 2020 research and innovation program under agreement STRONG - 2020 - No. 824093; the Programa de Fomento y Apoyo a Proyectos de Investigación code A1-022, from the Universidad Autónoma de Sinaloa.

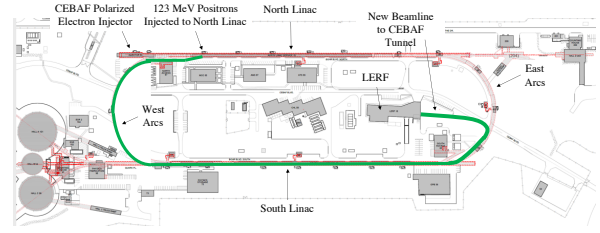


Figure 1: CEBAF and LERF accelerators. Green line shows the new 123 MeV transport beam line connecting LERF to CEBAF for high energy acceleration of positron beams.

to any of the four halls. The Ce<sup>+</sup>BAF design is optimized to provide users with spin polarization  $>60\%$  at intensities  $>100$  nA, and with higher intensities when polarization is not needed.

## LERF

### Polarized Electron Injector

The existing LERF injector provides the baseline layout with the superconducting quarter cryomodule (Capture Linac: SRF 10 MV) capable of accelerating up to 10 mA CW beams to 9 MeV/c [4]. Upstream of the Capture Linac, the layout will resemble that in CEBAF, albeit more compact starting with the polarized electron source, followed by a Wien spin rotator and a buncher cavity for longitudinal matching to the SRF 10 MV. Downstream of the SRF 10 MV, a three dipole magnet chicane injects the electron beam into the first of two full-length accelerating SRF cryomodules (60 MV each). The LERF electron gun will be

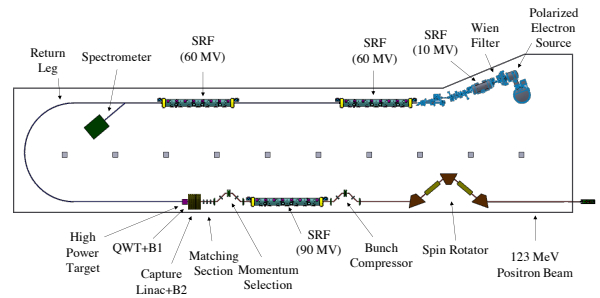


Figure 2: LERF layout of polarized  $e^-$  and  $e^+$  injectors.

a scaled-up version of the 130 keV inverted geometry gun used at CEBAF for many years [5]. The CEBAF gun reliably provides highly spin polarized electron beams 90% and average current of 200  $\mu$ A with 0.4 pC CW bunch trains (250/499 MHz). Due to excellent dynamic vacuum conditions and a biased anode limiting ionized residual gas from reaching the photocathode, charge lifetimes  $>400$  C with strained-superlattice GaAs/GaAsP are achieved [6, 7].

However, because the bremsstrahlung yield of positrons from electrons will be low ( $< 10^{-4}$ ) a much higher beam current  $>1$  mA is required with correspondingly higher bunch charge  $>2$  pC. We expect to operate the gun in a range of 300-350 kV to manage the higher bunch charge and allow direct injection to the SRF 10 MV. To meet the anticipated demands we expect to re-design the gun cathode electrode in two ways, (a) to have a larger spherical radius to achieve and safely maintain higher gradient and (b) to accommodate a larger laser beam spot size to extend the charge lifetime. Additionally the cathode must be free of field emission so we plan to include the capability of applying 50 kV beyond the required beam voltage for high voltage gas conditioning.

The higher bunch charges also pose challenges for the initial bunching and acceleration of the beam. Space charge forces will repel the electrons and reverse the bunching as the beam drifts, where space charge effects typically degrade beam quality. To prevent this, we have kept the distance between the gun and the first accelerating element as short as possible and plan to compress the electron bunch from 40 ps (determined by the optical pulsed) to about 2 ps within a few meters prior to the SRF QCM.

The final section of the electron injector shapes the transverse emittance to match the acceptance for two CEBAF style CMs which accelerate the beam energy to about 120 MeV. A separate contribution to this conference [8] describes the electron injector in detail.

### High Power Target for Positron Production

A conceptual design of the high power positron target has been developed. Tungsten has been chosen as the preferred target material. GEANT4 [9] simulations have been used to determine that a tungsten target thickness of 4 mm is optimal for maximizing the Figure-of-Merit [10] (FOM, defined as the product of the positron current and the square of their longitudinal polarization). The thermal power deposited by a 1 mA electron beam current of 120 MeV energy into 4 mm of tungsten has been estimated with FLUKA [11, 12] to be on the order of 17 kW. A typical target employed at JLab has less than 1 kW of electron beam power deposited into the target material. The only feasible cooling agent for the 17 kW target at Jefferson Lab would be water as the maximum cryogenic capacity for target cooling is less than 6 kW. Notably, the only JLab target that surpassed the 1 kW mark to date was the 2.5 kW liquid hydrogen target [13] for the Qweak experiment.

The design of the target has been done with ANSYS-Fluent [14] thermal simulations. Fluent calculations have shown that a static 4 mm thick tungsten target in a copper

frame cooled by an internal water channel could sustain about 1 kW of electron beam power safely. A 35 cm diameter and 4 mm thick tungsten target rotating at 2 Hz could safely dissipate the 17 kW beam power deposited in it while maintaining a maximum temperature below 1000 K. A con-

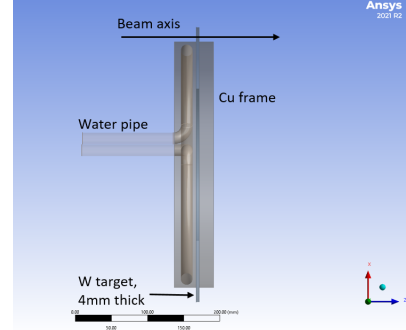


Figure 3: Side-view concept design of the rotating target.

cept of the rotating tungsten target is shown in Fig. 3, where the tungsten is an annular ring partially encased in a copper frame. The electron beam impinges onto the 4 mm tungsten annulus a few mm from the frame and 17.5 cm from the rotation axis. The conceptual design of the target will have to be engineered into a design that can be manufactured, operated and decommissioned safely. A detailed concept is evaluated in a separate contribution to this conference [15].

### CW Positron Beam Formation

The generation of positrons in a thick target creates an exceptionally broad distribution in transverse and longitudinal phase space. A high field ( $B_1$ ) quarter-wave transformer (QWT) located after the target decreases the transverse angular divergence of the positron distribution while also defining the central momentum of the positron polarization distribution to be collected. Following the high field region a low field ( $B_2$ ) solenoid is used to manage the positron beam through an RF capture section. The solenoid fields  $B_1$  and  $B_2$  are optimized to maintain the large 4D transverse phase space of the beam [16] through this region.

A positron momentum spread  $\delta p/p_0 < 1\%$  was chosen early on in the design in order to mitigate apertures in regions of large dispersion in the transport lines connecting the LERF to CEBAF. Although we have not settled on a final momentum spread this issue motivated us to include an RF capture section right after the QWT in our design studies in order to decrease the longitudinal energy spread as well as improve the transverse beam emittance.

Following the RF capture region the positron momenta is defined by a chicane beamline composed of quadrupoles and dipoles to create a correlation between positron energy and transverse position at its midpoint. After the chicane the positron beam is accelerated in a SRF CM to 123 MeV (an injection energy requirement for CEBAF 12 GeV) and transported through a bunch compression chicane to achieve a bunch length of a few picoseconds.

Table 1: Simulated Parameters of the Ce<sup>+</sup>BAF Injector

Ce <sup>+</sup> BAF Parameter	Status	Goal
$p_0$ [MeV/c]	60	60
$\sigma_{\delta p/p_0}$ [%]	0.68	$\pm 1$
$\sigma_z$ [ps]	3	$\leq 4$
Normalized $\epsilon_n$ [mm mrad]	140	$\leq 40$
$p_f$ [MeV/c]	123	123
$I_{e^+} (P > 60\%)$ [nA]	170	$> 50$

In this contribution the chicane was optimized for 60 MeV/c positrons (maximum polarized FoM) while passing a 1% energy spread. Results of recent CW polarized positron beam simulations are shown in Table 1 relative to our present design goals. We have met or exceeded all goals except for the normalized emittance, which can be met by reducing the acceptance and reducing the positron beam current or increasing the drive beam power. A reference to earlier work on this topic was reported in Ref. [17].

### Positron Spin Rotator

The precession of the electron beam polarization when accelerated at CEBAF to 12 GeV is more than 60 full revolutions. Experiments however most often require longitudinal or sometimes transverse spin polarization at their target. At CEBAF a  $4\pi$  spin rotator consisting of two Wien filters with intervening solenoid magnets [18] is used to orient the spin at the injector to control the final spin polarization at the experiment. This is convenient when the beam energy is 100 keV and the required Wien filter field strengths are modest (e.g.  $E = 1$  MV/m and  $B = 100$  G). However, the positron beam production energies at the LERF are 10's of MeV and the final beam energy is  $>100$  MeV, making a Wien filter impractical.

For Ce<sup>+</sup>BAF a higher energy spin rotator concept has been imagined. The proposed spin rotator scheme is shown in Fig. 4. Composed by interleaved dipole and solenoid fields the small anomalous gyromagnetic factor for positrons (or even electrons) means the spin rotation in the solenoids is more effective than in the dipoles at lower energies [19]. However, the dipole magnetic field is necessary to provide the desired spin rotation axis. Rotating the spin around the longitudinal solenoid and radial dipole fields, this spin rotator can provide a desired net spin rotation around the vertical axis in the horizontal plane. Notably in this design the dipole fields are arranged with net zero bending angle, leaving the beam trajectory intact and transparent to beam orbit perturbations. Further details of this design will be presented in a future presentation once on-going simulations are completed.

### 12 GeV Ce<sup>+</sup>BAF

Once the CW positron beam has been formed and the spin oriented it is ready for acceleration to higher energies. The

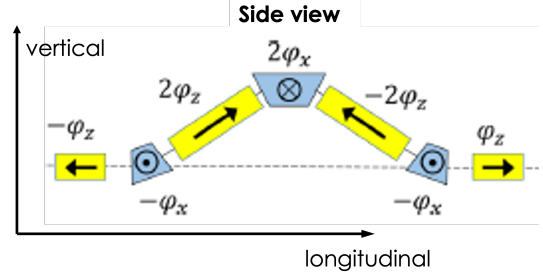


Figure 4: Spin rotator concept.  $\phi_x$ : spin rotation around the radial axis,  $\phi_z$ : spin rotation around the longitudinal axis.

positron beam is transported in a new tunnel connecting the east side of LERF to the south east corner of CEBAF near the entrance of the South Linac (Fig. 1). This new beamline features a double-bend achromat (DBA) to maintain small dispersion and a vertical achromatic translator to bring the beam to the elevation of the CEBAF South Linac tunnel near the ceiling. At this point a long FODO channel attached to the ceiling of the South Linac transports the beam to the west side of CEBAF where it is bent 180 degrees via a DBA-like lattice with low dispersion and is also isochronous. At the end of this long transport line a vertical achromat translator and horizontal bending magnets bring the beam to the start of the North Linac where it is injected. Additionally, each beamline also has a betatron matching section.

While this long beamline from LERF to CEBAF is designed for the 123 MeV/c positron beam it should also be suitable for an electron beam with energy up to 650 MeV/c to be compatible with a future upgrade of CEBAF to 22 GeV.

The CEBAF accelerator limits the maximum transverse emittance that one can transport because of the reduced acceptance at the extraction corners. We estimate that one can inject between 40 and 120 mm-mrad of normalized emittance at the front of the north linac. In terms of longitudinal acceptance, we are planning to change the optics configuration for the first two recirculation arcs (east and west sides) in order to have smaller dispersion functions and an easily tunable momentum compaction. With these new optics we should expect to inject up to a percent of energy spread in the front of the north linac and transport a beam that has a longitudinal bunch length around 1 mm. A separate contribution to this conference [20] is exploring the admittance of the electron injector and first recirculation pass of CEBAF.

### OUTLOOK

The Ce<sup>+</sup>BAF working group has developed a scheme to provide CEBAF with polarized positron beams with CW time structure. Early designs and simulated parameters combined with constraints are approaching the anticipated goals. Our focus in the coming months is to develop a white paper documenting in greater detail the technical approach and additional issues being addressed, but not reported in the length of these proceedings.

## REFERENCES

- [1] J. Arrington *et al.*, “Physics with CEBAF at 12 GeV and future opportunities,” *Prog. Part. and Nucl. Phys.*, vol. 127, p. 103 985, 2022. doi:10.1016/j.pnpnp.2022.103985
- [2] A. Accardi *et al.*, “An experimental program with high duty-cycle polarized and unpolarized positron beams at Jefferson Lab,” *Eur. J. Phys. A*, vol. 57, no. 8, 2021. doi:10.1140/epja/s10050-021-00564-y
- [3] D. Abbott *et al.*, “Production of Highly Polarized Positrons Using Polarized Electrons at MeV Energies,” *Phys. Rev. Lett.*, vol. 116, p. 214 801, 2016. doi:10.1103/PhysRevLett.116.214801
- [4] C. Hernandez-Garcia *et al.*, “Performance and modeling of the JLAB IR FEL upgrade injector,” 2004. <https://www.osti.gov/biblio/834871>
- [5] P. A. Adderley *et al.*, “Load-locked DC high voltage GaAs photogun with an inverted-geometry ceramic insulator,” *Phys. Rev. ST Accel. Beams*, vol. 13, p. 010 101, 1 2010. doi:10.1103/PhysRevSTAB.13.010101
- [6] P. Adderley *et al.*, “An overview of how parity-violating electron scattering experiments are performed at CEBAF,” *Nucl. Instrum. Methods Phys. Res., Sect. A*, vol. 1046, p. 167 710, 2023. doi:10.1016/j.nima.2022.167710
- [7] J. Yoskowitz *et al.*, “Improving the operational lifetime of the cebaf photo-gun by anode biasing,” Thomas Jefferson National Accelerator Facility (TJNAF), Newport News, VA, Tech. Rep., 2021.
- [8] R. Kazimi, A. Hofler, C. Hernandez-Garcia, G. P. Serrano, and J. Grames, “Polarized Electron Injector for Positron Production at CEBAF,” presented at IPAC’23, Venice, Italy, May 2023, paper WEPA035, this conference.
- [9] S. Agostinelli *et al.*, “GEANT4—a simulation toolkit,” *Nucl. Instrum. Meth. A*, vol. 506, pp. 250–303, 2003. doi:10.1016/S0168-9002(03)01368-8
- [10] S. Habet, A. Ushakov, and E. Voutier, “Characterization and optimization of polarized and unpolarized positron production,” Tech. Rep. JLAB-ACC-23-3794, 2023.
- [11] C. Ahdida *et al.*, “New Capabilities of the FLUKA Multi-Purpose Code,” *Front. Phys.*, vol. 9, p. 788 253, 2022. doi:10.1007/s11665-016-2457-x
- [12] G. Batistoni *et al.*, “Overview of the FLUKA code,” *Annals Nucl. Energy*, vol. 82, pp. 10–18, 2015. doi:10.1016/j.anucene.2014.11.007
- [13] J. Brock *et al.*, “The Qweak High Performance LH2 Target,” *arxiv.org, submitted to NIM-A*, pp. 1–52, 2023. doi:10.48550/arXiv.2303.07497
- [14] ANSYS. [www.ansys.com](http://www.ansys.com)
- [15] A. Ushakov, S. Covrig, J. Grames, S. Habet, C. L. Galliard, and E. Voutier, “Evaluation of a High-Power Target Design for Positron Production at CEBAF,” presented at IPAC’23, Venice, Italy, May 2023, paper WEPM120, this conference.
- [16] R. Chehab, “Etude de la production et du confinement d’un faisceau de positrons. Application à l’accélérateur linéaire d’Orsay,” Ph.D. dissertation, Université Paris-Sud, 1975.
- [17] S. H. Habet *et al.*, “Concept of a Polarized Positron Source for CEBAF,” in *Proc. IPAC’22*, Bangkok, Thailand, 2022, pp. 457–460. doi:10.18429/JACoW-IPAC2022-MOPOTK012
- [18] J. M. Grames *et al.*, “Two Wien Filter Spin Flipper,” in *Proc. PAC’11*, New York, NY, USA, Mar.-Apr. 2011, pp. 862–864. <https://jacow.org/PAC2011/papers/TUP025.pdf>
- [19] Y. N. Filatov *et al.*, “Polarization control in spin-transparent hadron colliders by weak-field navigators involving lattice enhancement effect,” *Eur. Phys. J. C*, vol. 81, 2021. doi:10.1140/epjc/s10052-021-09750-0
- [20] A. Sy *et al.*, “Degradation Beamline Design at the CEBAF Injector for Machine Acceptance Studies,” presented at IPAC’23, Venice, Italy, May 2023, paper MOPM081, this conference.



# Bibliography

- [1] J. E. Clendenin. High Yield Positron Systems for Linear Colliders. *Conf. Proc. C*, 8903201:1107, 1989.
- [2] D. J. Warner. NEW AND PROPOSED LINACS AT CERN: THE LEP (e+ e-) INJECTOR AND THE SPS HEAVY ION (Pb) INJECTOR. In *14th International Linear Accelerator Conference*, 1988.
- [3] M. Hüning and M. Schmitz. Recent changes to the e<sup>-</sup>/e<sup>+</sup> injector (linac II) at DESY. In *Proceedings of LINAC08*, Victoria, BC, Canada, 2008.
- [4] A. Mikhailichenko. CESR positron source. In *9th International Workshop on Linear Colliders*, 2002.
- [5] P. Valente. POSEYDON - Converting the DAΦNE collider into a double positron facility: a high duty-cycle pulse stretcher and a storage ring. *INFN-17-15-LNF*, 2017.
- [6] P. Guoxi. Progress of the BEPCII Linac Upgrade. In *Proceedings of the 21th Particle Accelerator Conference*, page 2416, 2005.
- [7] T. Natsui et al. Kek e<sup>+</sup>e<sup>-</sup> injector linac. In *Proceedings of the 65th ICFA Advanced Beam Dynamics Workshop on High Luminosity e<sup>+</sup>e<sup>-</sup> Colliders (eeFACT22)*, page 251, 2022.
- [8] T. Suwada et al. First application of a tungsten single-crystal positron source at the KEK B factory. *Phys. Rev. ST Accel. Beams*, 10(7):073501, 2007.
- [9] Chris A and al. The international linear collider technical design report - volume 3.ii: Accelerator baseline design, 2013.
- [10] S. Oğur and al. Linac and damping ring designs for the fcc-ee. 2019.
- [11] M. Poelker, J. Grames, J. Hansknecht, R. Kazimi, and J. Musson. Generation of electron bunches at low repetition rates using a beat-frequency technique. *Phys. Rev. ST Accel. Beams*, 10:053502, 2007.
- [12] J. Grames et al. Positron beams at Ce+BAF. presented at IPAC'23, Venice, Italy, May 2023, paper MOPL152, unpublished.
- [13] S. Habet et al. Concept of a Polarized Positron Source for CEBAF. In *Proc. IPAC'22*, number 13 in International Particle Accelerator Conference, pages 457–460. JACoW Publishing, Geneva, Switzerland, 2022.

- [14] S Habet, A Ushakov, and E Voutier. Characterization and optimization of polarized and unpolarized positron production. Technical Report JLAB-ACC-23-3794, 2023.
- [15] A. Ushakov, S. Covrig, J. Grames, S. Habet, C. Le Galliard, and E. Voutier. Evaluation of a high-power target design for positron production at CEBAF. presented at IPAC'23, Venice, Italy, May 2023, paper WEPM120, unpublished.
- [16] R. CHEHAB. Etude de la production et du confinement d'un, faisceau de positrons. Application à l'accélérateur linéaire d'Orsay. 1975.
- [17] J Benesch, A Bogacz, A Freyberger, Y Roblin, T Satogata, R Suleiman, and M Tiefenbach. 12 gev cebaf beam parameter tables. Technical Report JLAB-TN-18-022, 2018.
- [18] M. S. Fee, A. P. Mills, S. Chu, E. D. Shaw, K. Danzmann, R. J. Chichester, and D. M. Zuckerman. Measurement of the positronium  $1^3s_1$ - $2^3s_1$  interval by continuous-wave two-photon excitation. *Phys. Rev. Lett.*, 70:1397–1400, Mar 1993.
- [19] T. S. Stein, R. D. Gomez, Y.-F. Hsieh, W. E. Kauppila, C. K. Kwan, and Y. J. Wan. Total cross-section measurements for positrons and electrons colliding with potassium. *Phys. Rev. Lett.*, 55:488–491, Jul 1985.
- [20] P. Hautojärvi and A. Vehanen. *Introduction to Positron Annihilation*, pages 1–23. Springer Berlin Heidelberg, Berlin, Heidelberg, 1979.
- [21] P. Asoka-Kumar, K. G. Lynn, and D. O. Welch. Characterization of defects in Si and SiO<sub>2</sub> Si using positrons. *Journal of Applied Physics*, 76(9):4935–4982, 11 1994.
- [22] J. Grames, E. Voutier, et al. Physics with positron beams at jefferson lab 12 gev. *Jefferson Lab*, LOI12-18-004, 2018.
- [23] T. B. Hayward et al. Observation of Beam Spin Asymmetries in the Process  $ep \rightarrow e' \pi^+ \pi^- X$  with CLAS12. *Phys. Rev. Lett.*, 126:152501, 2021.
- [24] W Zhu. Improved Bethe-Heitler formula. *Nucl. Phys. B*, 953:114958, 2020.
- [25] S Golge. *Feasibility and conceptual design of a C.W. positron source at CEBAF*. PhD thesis, 08 2010.
- [26] (PEPPo Collaboration) D. Abbott et al. Production of highly polarized positrons using polarized electrons at MeV energies. *Phys. Rev. Lett.*, 116:214801, 2016.
- [27] H Olsen and L. C. Maximon. Photon and electron polarization in high-energy bremsstrahlung and pair production with screening. *Phys. Rev.*, 114:887–904, May 1959.
- [28] M. Borland et al. Elegant: A flexible SDDS-compliant code for accelerator simulation. *Proceedings of PAC2001*, pages 3514–3516, 2001.



- [29] A Abraham and P.M.G. Nambissan. Chapter 5 - positron annihilation spectroscopy for defect characterization in nanomaterials. In Sabu Thomas, Nandakumar Kalarikkal, and A Abraham, editors, *Design, Fabrication, and Characterization of Multifunctional Nanomaterials*, Micro and Nano Technologies, pages 123–146. Elsevier, 2022.
- [30] S Gambhir, John F. Valk, and E. Phelps. Molecular imaging of cancer with positron emission tomography. 2002.
- [31] R. Cherry, A. Sorenson, and E. Phelps. chapter 18 - positron emission tomography. In R. Cherry, A. Sorenson, and Michael E. Phelps, editors, *Physics in Nuclear Medicine (Fourth Edition)*, pages 307–343. W.B. Saunders, Philadelphia, fourth edition edition, 2012.
- [32] J. M. Kinser, M. A. G. Martinez, and J. A. Martin. Positron emission tomography (pet) radiopharmaceuticals. *Applied Radiation and Isotopes*, 50(1):11–19, 1999.
- [33] Simon Cherry. Fundamentals of positron emission tomography and applications in preclinical drug development. *Journal of clinical pharmacology*, 41:482–91, 2001.
- [34] F. M. Khan and J. P. Gibbons. *Khan’s the physics of radiation therapy*. Wolters Kluwer Health Lippincott Williams and Wilkins, 2010.
- [35] A Wu Chao, K Mess, Maury Tigner, and F Zimmermann. *Handbook of Accelerator Physics and Engineering*. WORLD SCIENTIFIC, 2nd edition, 2013.
- [36] R. Erickson. SLC DESIGN HANDBOOK. 1986.
- [37] J T. Seeman. The Stanford Linear Collider. *Ann. Rev. Nucl. Part. Sci.*, 41:389–428, 1991.
- [38] R Bossart, J P Delahaye, J C Godot, J H B Madsen, P Pearce, A J Riche, and Louis Rinolfi. The LEP Injector Linac. Technical report, CERN, Geneva, 1990.
- [39] LEP Design Report Vol.1: The LEP Injector Chain. 1983.
- [40] *LEP design report*. Report. CERN, Geneva, 1984. Copies shelved as reports in LEP, PS and SPS libraries.
- [41] G. Stange. An Inexpensive Positron Converter of High Reliability and High Yield. *IEEE Trans. Nucl. Sci.*, 26(3):4146–4148, 1979.
- [42] S E. Kopp. The CLEO III detector. *Nucl. Instrum. Meth. A, Spectrometers, Detectors and Associated Equipment*, 384(1):61–66, 1996.
- [43] V. A. Anosov, M. Billing, D. Kalchev, V. I. Kazacha, N. Y. Kazarinov, A. K. Krashykh, E. A. Perelshtein, M. Tigner, and A. T. Vasilenko. Electron - positron high efficiency converter. *JINR-E9-95-403*, 1995.
- [44] J. Barley, V. Medjidzade, and A. Mikhailichenko. New positron source for CESR. *CBN-01-19*, 2001.

- [45] G. V. Vignola et al. DAFNE, the Frascati  $\phi$ -factory. *Conf. Proc. C*, 930517:1993–1997, 1993.
- [46] G. Mazzitelli, A Ghigo, F Sannibale, P Valente, and G Vignola. Commissioning of the DAFNE beam test facility. *Nucl. Inst. Meth. Phys. Res. A*, 515(3):524–542, 2003.
- [47] P. Valente et al. Linear Accelerator Test Facility at LNF: Conceptual Design Report. *INFN-16-04-LNF*, 2016.
- [48] C.-A. Zhang. Performance of the BEPC and progress of the BEPCII. In *32nd International Conference on High Energy Physics*, page 15, 2004.
- [49] C.-A. Zhang et al. An overview of the BEPCII project. In *Proceedings of the 40th ICFA Advanced Beam Dynamics Workshop on High Luminosity  $e^+e^-$  Factories*, page 1, 2008.
- [50] K. Akai et al. Commissioning of KEKB. *Nucl. Instrum. Meth. A*, 499(1):191, 2003.
- [51] Gerald Aarons et al. ILC Reference Design Report Volume 1 - Executive Summary. 8 2007.
- [52] W. Gai. A 500 mev s-band low cost electron beam source for ilc keep alive source. Talk at KILC12, Daegu, Korea, 2012.
- [53] R. Chehab I. Chaikovska et al. Positron source for fcc-ee. In *Proceedings of IPAC2019, Melbourne, Australia*, 2019.
- [54] I. Chaikovska, R. Chehab, V. Kubytskyi, S. Ogur, A. Ushakov, A. Variola, P. Sievers, P. Musumeci, L. Bandiera, Y. Enomoto, M.J. Hogan, and P. Martyskin. Positron sources: from conventional to advanced accelerator concepts-based colliders. *Journal of Instrumentation*, 17(05):P05015, 2022.
- [55] I. Chaikovska et al. Positron Source for FCC-ee. In *Proc. 10th International Particle Accelerator Conference (IPAC'19), Melbourne, Australia, 19-24 May 2019*, number 10 in International Particle Accelerator Conference, pages 424–427, Geneva, Switzerland, 2019. JACoW Publishing. <https://doi.org/10.18429/JACoW-IPAC2019-MOPMP003>.
- [56] G. Stange. An inexpensive positron converter of high reliability and high yield. *IEEE Transactions on Nuclear Science*, 26(3):4146–4148, 1979.
- [57] C Liebig. Design and construction of an injector for an electron/positron linac optimized for positron yield and minimal particle loss. 2014.
- [58] T Behnke, E Garutti, I. Gregor, T Haas, U Kötz, I .Melzer-Pellmann, Norbert Meyners, Joachim Mnich, and F Sefkow. Test beams at desy. *EUDET-Memo-2007-11*, 2007.
- [59] Y. Funakoshi and all. The SuperKEKB Has Broken the World Record of the Luminosity. In *Proc. IPAC22*, number 13 in International Particle Accelerator Conference, pages 1–5. JACoW Publishing, Geneva, Switzerland, 2022.

- [60] C. Leemann, D. Douglas, and G. Krafft. The continuous electron beam accelerator facility: Cebaf at the jefferson laboratory. *Annu. Rev. Nucl. Part. Sci.*, 51:413–50, 2001.
- [61] J. Grames and M. Poelker. *Polarized Electron Sources*, pages 261–284. Springer International Publishing, Cham, 2023.
- [62] C. K. Sinclair, P. Adderley, B. M. Dunham, J. Hansknecht, P. Hartmann, M. Poelker, J. S. Price, P. M. Rutt, W. J. Schneider, and M. Steigerwald. Development of a high average current polarized electron source with long cathode operational lifetime. *Phys. Rev. ST Accel. Beams*, 10:023501, 2007.
- [63] T Satogata, Yves Roblin, M Tiefenback, and D Turner. 12 GeV CEBAF Transverse Emittance Evolution. In *6th International Particle Accelerator Conference*, page WEBD1, 2015.
- [64] J. Rosenzweig and L. Serafini. Transverse particle motion in radiofrequency linear accelerators. *Phys. Rev. E*, 49:1599–1602, 1994.
- [65] R. Boni, S. Guiducci, and M. Vescovi. A new system for positron focusing at the Frascati LinAc. 1981.
- [66] J. Grames et al. Two Wien Filter Spin Flipper. In *Proc. PAC’11*, pages 862–864. JACoW Publishing, Geneva, Switzerland.
- [67] E. Haug and W. Nakel. *The Elementary Process of Bremsstrahlung*. World Scientific lecture notes in physics. World Scientific, 2004.
- [68] Y-S Tsai. Pair production and bremsstrahlung of charged leptons. *Rev. Mod. Phys.*, 46:815–851, Oct 1974.
- [69] H Olsen and L.C. Maximon. Photon and electron polarization in high-energy bremsstrahlung and pair production with screening. *Phys. Rev.*, 114:887–904, 1959.
- [70] W H. McMaster. Matrix representation of polarization. *Rev. Mod. Phys.*, 33:8–28, Jan 1961.
- [71] W Stein, A J. Sunwoo, V Bharadwaj, D. C. Schultz, and J C. Sheppard. Thermal shock structural analyses of a positron target. *PACS2001. Proceedings of the 2001 Particle Accelerator Conference (Cat. No.01CH37268)*, 3:2111–2113 vol.3, 2001.
- [72] R H. Helm. Adiabatic approximation for dynamics of a particle in the field of a tapered solenoid. 1962.
- [73] G. Steffen and A. L. King. High Energy Beam Optics. *American Journal of Physics*, 34(11):1071–1071, 1966.



# Résumé en français

Les accélérateurs de particules sont des outils essentiels pour sonder les lois fondamentales de l'univers. Ils manipulent des particules chargées dans des faisceaux utilisés dans des secteurs variés tels que la médecine, l'industrie et la recherche. Ces applications exigent des faisceaux de haute qualité, caractérisés par leur intensité, leur taille et leur énergie. Avec l'évolution de la technologie, les attentes des utilisateurs de faisceaux ont également évolué. Dans la communauté des accélérateurs de particules, les leptons, en particulier les électrons et les positons, jouent un rôle significatif. Ils offrent une fenêtre unique pour sonder la matière à son niveau le plus fondamental. Le développement de faisceaux de positons accélérés a connu des avancées notables ces dernières années, tirées par l'innovation et la recherche rigoureuse.

L'importance des expériences avec les positons est soulignée par leurs aperçus profonds des interactions de ces particules avec les matériaux aux échelles atomique et subatomique. Par exemple, des expériences avancées utilisant des faisceaux de positons ont permis des études sur des phénomènes comme l'excitation à deux photons du positonium. Cette découverte a propulsé le domaine de la spectroscopie d'annihilation de positons comme une technique capable de caractériser les matériaux à une échelle granulaire et subatomique.

Dans ce contexte, cette thèse décrit la conception d'une nouvelle source de positons polarisés pour le Thomas Jefferson National Accelerator Facility (TJNAF) pour la physique nucléaire. La communauté physique de JLab a un fort intérêt pour l'utilisation de faisceaux de positons dans les expériences. Le programme de physique hadronique au JLab vise à étudier en détail la structure des hadrons. Les faisceaux de positons polarisés offrent un outil unique pour certaines expériences, notamment la diffusion Compton virtuelle (DVCS).

Le DVCS est intéressant car il fournit une fenêtre sur la structure interne du proton, en particulier la distribution des quarks et des gluons à l'intérieur du nucléon. L'utilisation d'un faisceau d'électrons et de positons polarisés dans les expériences DVCS offre plusieurs avantages, permettant de mesurer l'asymétrie de spin du faisceau, ce qui est intrinsèquement lié à des GPD spécifiques, éclairant la distribution des quarks et des gluons à l'intérieur du nucléon.

Les études précédentes ont exploré la faisabilité d'introduire une source de positons à onde continue pour le Continuous Electron Beam Facility (CEBAF). Plusieurs options de conception pour un injecteur de positons ont été étudiées. Les sources de positons construites partagent des caractéristiques communes en raison de la nature pulsée des linacs. Les études ont montré que l'espace des phases du faisceau de positons est plus grande que celle du faisceau d'électrons existant.

La conception de la cible de positron est également un défi significatif. Des solutions proposées impliquaient soit une cible rotative, soit une cible liquide. Fi-

nalement, bien que la gestion de la grande quantité d'énergie déposée sur la cible présente un défi de R&D, il est possible qu'avec les modifications appropriées, la réalisation d'un courant de positons de  $1\ \mu\text{A}$  est à portée de main.

Cette thèse constitue une avancée notable dans la conception et l'amélioration d'une source de positons pour le CEBAF. À travers des simulations approfondies, Grâce à des simulations détaillées, une polarisation de positons simulée de plus de 65% a été atteinte, accompagnée d'un courant de positons excédant 170 nA. Ces accomplissements prouvent non seulement la viabilité pratique du projet des positons, mais mettent aussi en lumière son impact futur possible sur le fonctionnement de JLab. En s'attaquant méthodiquement aux défis et aux contraintes existants, cette étude contribue au progrès significatifs dans le domaine des positons et de leur utilisation en recherche.